Development of a Desktop High-Resolution MRI for Microflow Visualization

by

Ramin Sahebjavaher

BASc., The University of British Columbia, 2006

A THESIS SUBMITTED IN PARTIAL FULFILLMENT OF

THE REQUIREMENTS FOR THE DEGREE OF

Master of Applied Science

in

THE FACULTY OF GRADUATE STUDIES

(Electrical and Computer Engineering)

THE UNIVERSITY OF BRITISH COLUMBIA

(Vancouver)

October 2008

Abstract

Research in lab-on-a-chip (LOC) technology involving microfluidics is a growing field aiming at the development of miniaturized biomedical systems with rich functionality. In order to design effective LOC microfluidic systems, the flow fields and the fluids inside LOC devices need to be carefully characterized. High-resolution magnetic resonance imaging (MRI) offers a powerful non-intrusive technology for this application. In this thesis, the design and implementation of a prototype for a desktop high-resolution MRI instrument, consisting of a magnet, gradient coils, gradient amplifiers, and radio frequency (RF) electronics, is presented. To reduce the size and cost of this MRI instrument, a permanent magnetic configuration with a magnetic flux density of 0.6 T is designed with off-the-shelf NdFeB permanent magnets. The coils of the triaxial gradient module are developed using a novel lithography technique. This gradient module is capable of generating gradient fields as high as 2.83 T/m with custom made current amplifiers. The radio frequency (RF) probe is integrated with the gradient module and is connected to the RF electronics which are made using off-the-shelf components. Pulse sequences and signal processing for acquiring static images and velocity profiles are described. The performance of this instrument in terms of static and dynamic image resolution are presented. As a preliminary test, the velocity profile of water flowing inside a small tube was measured with a nominal resolution of 40 μm. The instrument is designed for a static resolution of better than 30 μm and a velocity resolution better than 50 μm/s. Improvements to the current instrument in addition to theoretical limitations are also detailed.

Table of Contents

List of Tables

List of Figures

Acknowledgements

I am most grateful to both of my advisors Dr. Boris Stoeber and Dr. Konrad Walus for their guidance and encouragement that they have provided throughout the duration of my M.A.Sc. None of this work could have been accomplished without the countless productive meetings (often me randomly showing up at their offices) we had. It has been a privilege working with both them on such an interesting and challenging project.

I would like to thank all the technicians and machinists especially Markus Fengler, Glenn Jolly and Bernhard Nimmervoll who have always given me excellent practical advice. My deepest thanks to: Dr. Walter Hardy for the many meetings and practical help he gave me to get my first NMR signal; Dr. Piotr Kozlowsky, Dr. Alex Rauscher and Dr. Alex MacKay for their extensive help with my many MRI questions; and Dr. Carl Michal and his students for teaching me how to tune and match my RF probe, and providing useful tips for my receiver design. A special thank you to my brother Dariush who has significantly contributed, with his hard and outstanding work, to the design and implementation of the gradient amplifiers.

Thank you to all my friends and lab mates (Iman Mansour, Mahmood Valizadeh, Hamed Valizadeh, Pirooz Darabi, Amir Entezarmahdi, Vahid Bazargan, Reynald Hoskinson, Larsen Dittrich, Daniel Buescher, Holger Knell, Benjamin Mustin, Stefan Hampl, and many of whom I failed to mention) for their help and encouragement. A big thank you to Veis Dokhani for the futuristic sketch of the proposed instrument. And finally, and most importantly, I would like to thank Shaghayegh Khayambashi for her love and encouragement that pushed me to always perform at my best.

Dedication

This thesis is dedicated to my parents who, with their endless inspiration, guidance and support, have taught me to lead my life to achieve beyond what I think I am capable of.

Chapter 1 - Introduction

1.1.1 Motivation

Research in lab-on-a-chip (LOC) technology involving microfluidics is a rapidly growing field aiming at the development of miniaturized biomedical systems with enabling functionality. These integrated devices can handle and manipulate minute amounts of biological samples to perform various tasks on a single microchip. These tasks range from sample preparation to detection of chemical or biological agents including DNA sequencing [1-3]. Conventionally, these experiments are performed in a lab requiring a considerably larger sample volume and longer analysis time. Characterization of fluid flow at these length scales is an essential step in the design of LOC devices. The behaviour of fluids at the microscale can differ from 'macrofluidic' behavior in that factors such as surface tension and viscosity start to dominate the system [4]. The presence of cells, biological molecules or other substances typically transported through lab-on-a-chip devices results in very complex fluid flows with unique properties [1], especially when these objects reach the dimensions of their flow environment. In order to design effective LOC microfluidic systems, these fluids need to be visualized for careful characterization at these length scales.

In the simplest form, a LOC device consists of a microchannel, an inlet and an outlet as shown in Figure 1. Many different microfabrication methods have been developed for such integrated systems [3]; Soft lithography is one of the least expensive fabrication techniques which typically employs materials such as Polydimethylsiloxane (PDMS) for microstructures, that is bonded on a glass or silicon substrate [3].

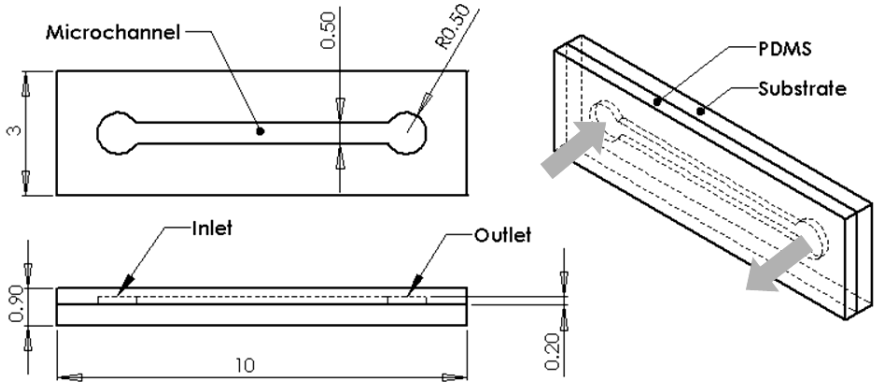

Figure 1. Simplest form of a sample microfluidic microchannel with one inlet and one outlet. (dimensions are in mm)

The fluid sample that is injected from the inlet port, passes through the microchannel, and exits from the outlet port as shown in Figure 2. The objective of this work is to visualize the flow field (i.e., the velocity profile) inside the microchannel, and to extract rheological information, such as viscosity, from the flow profile.

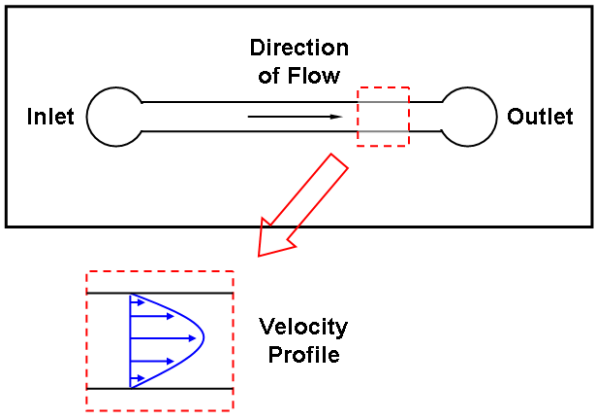

Figure 2. Velocity profile of a Newtonian fluid passing through the microchannel.

Conventionally, instruments such as micro particle image Velocimetry (micro PIV) are used for visualization of flow in microfluidic structures [5-8]. A schematic of a typical micro PIV setup is

shown in Figure 3. First, small seed particles are added to the fluid of interest which would follow the flow. The measurement is performed under a microscope that is usually equipped with two pulsed laser sources and a high-resolution camera. The lasers are pulsed consecutively with a certain delay while the camera is recording the images. A correlation between consecutive images reveals a two dimensional (2D) velocity profile indicating the magnitude and direction of flow at various points in the microfluidic channel. More recent developments include a scanning micro PIVs which can create pseudo three dimensional (3D) images of the flow by combining several 2D slices [6]. The velocity profile can then be extracted by signal processing techniques [7].

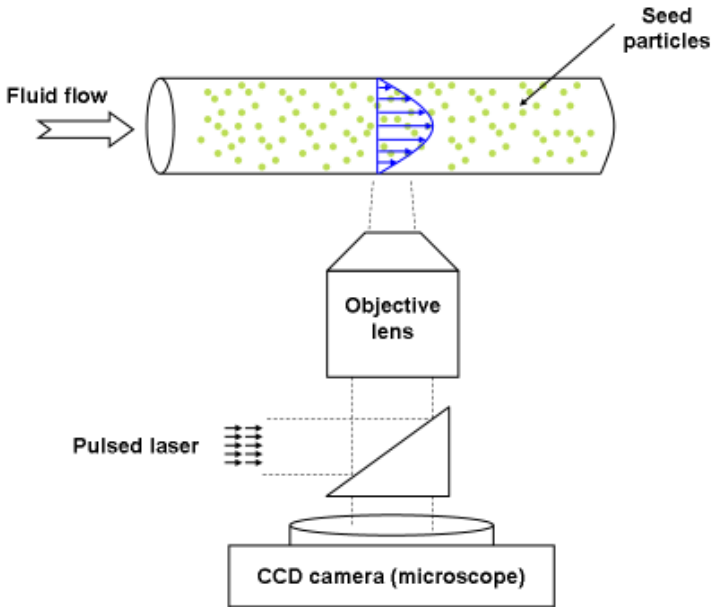

Figure 3. Schematic view of a typical micro PIV setup.

This technique produces high resolution images (sub micron) at relatively high speeds (delays of tens of millisecond). For the measurement to be successful, however, the seed particles need to be carefully chosen such they are small enough, so that their presence does not significantly

affect the flow pattern, and large enough that the particle are visible by the optics either by scattering or fluorescence detection mechanisms [7]. The size of the seed particle also needs to be large enough so that the Brownian motion does not introduce significant errors in the measured velocity profiles. As the seed particles affect the flow to some extent, it is necessary to average the velocity fields to reduce theses errors. In addition, this technique requires that the microfluidic structure and the sample to be transparent (at least partially) to the lasers so that the particles can be detected by the camera. This is usually the case when transparent materials such as PDMS or glass are used for the microfluidic structure. If, however, opaque samples or material are used for fabrication of microfluidic structures, then the micro PIV measurements are not possible. For structures made out of silicon it is possible to use infrared light sources as silicon is semi-transparent to infrared light, at the expense of reduced resolution [8]. For opaque materials the only other option for visualizing flow is to use X-ray sources and specialized detectors [9]. The main limitation using this technique is that the imaging plane is not well defined. In other words the resulting image is an average value of the signal at different depths which again limits the resolution.

The objective of this work is to overcome the limitations posed by micro PIV by using magnetic resonance imaging (MRI) techniques.

MRI is a non-invasive imaging method that uses magnetic fields and radiofrequency (RF) pulses to interact with nuclear spins in order to collect information regarding the sample under investigation. Nuclear spins such as hydrogen (H_1, also referred to as proton) are almost always present in fluid samples (e.g., water and oil) used in microfluidics experiments. It is possible to encode spatial and temporal information into the spins to detect diffusion, relaxation, velocity, acceleration (and even higher order dynamics) of a fluidic sample [10-12]. Through a Fourier

transform and further signal processing the encoded information are presented to the researcher in form of a simple 1D plot, or 2D and even 3D images. MRI flow imaging is commonly used for blood flow imaging for clinical diagnosis and is referred to as MRI angiography (MRA) [12-15]. For more information regarding the principles of magnetic resonance and velocity encoding techniques refer to Section 1.4 of this work. MRI is commonly used in steady or periodic flow due to limitations in temporal resolution (long acquisition times) of conventional MR imaging, however, recent advances in encoding and detection schemes and coil design have enabled fast flow imaging [16] of even turbulent flows [16, 17]. MRI has advantages in terms of being non-invasive (as it does not require injection of seed particles that would affect the flow) and not being adversely affected by optical opaqueness (many multiphase mixtures are optically opaque). A disadvantage of MRI technique is that the resolution cannot be much less than one-hundredth of the sample size due to signal-to-noise constraints [18]. In most MRI machines used for microscopy the spatial resolution is limited to about 10 μm which is far worse than the resolution of better than 1 μm obtained by micro PIV measurements. However, it turns out that MRI is very sensitive to detecting motion more accurate than conventional techniques. This is because the motion measurements techniques are not subject to the constraints of static imaging. Bonn *et al.* [18] report that sample displacements of less than 1 μm and velocities as small as 10 μm/s can be measured in MRI facilities in which the static imaging resolution cannot be better than 1 mm. This accuracy of flow measurement makes MRI particularly suitable for fluid mechanics research at the micron scale. Disadvantages of MRI techniques in general include experimental complexity, cost, and the large size of conventional superconducting magnets. For these reason the microfluidic research using MRI has been limited to researchers who have access to specialized MRI facilities. One important limitation of MRI is that ferromagnetic materials

cannot be present in the microfluidic structure as it will distort the magnetic field.

The advantages and disadvantages of conventional and MRI fluid visualization instruments are summarized in Table 1.

Table 1. Advantages and disadvantages of micro PIV and micro MRI fluid visualization instruments at micro scale.

	Advantages	Disadvantages
micro PIV (conventional)	▪ High spatial resolution (< 1 μm) ▪ Fast acquisitions (< 10 ms)	▪ Requires seed particles ▪ Only transparent structures ▪ Inherently 2D
micro MRI (proposed method)	▪ No seed particle ▪ Additional information (diffusion, relaxation time, etc) ▪ High spatial resolution (<10s μm) ▪ High sensitivity to flow(<10s μm/s) ▪ 3D	▪ Long acquisitions ▪ No ferromagnetic material ▪ Complexity ▪ Cost ▪ Size

In summary, available instrumentation, such as micro PIV, have limited velocity resolution, are inherently intrusive techniques that affect the flow with the required seed particles, and require a transparent microfluidic channel and fluidic samples. High-resolution magnetic resonance imaging (MRI) is a powerful technology that is able to characterize fluid flow in 3-dimensions, is

non-intrusive, and does not require transparent channels or fluidic samples.

1.1.2 Objective

The objective of this work is to develop a desktop MRI fluid visualization instrument that is inexpensive so that it can be used by engineers and researchers working in the microfluidic research. The most expensive and massive component of an MRI instrument is the main magnet. Conventionally, superconductive magnets are used which, including their accessories (refrigeration), occupy a complete room. The rooms are usually specifically designed to withstand the large weight of the magnet and to shield the large stray magnetic fields. To reduce the cost and size (desktop) of the proposed instrument it was decided to utilize a permanent magnetic configuration. Permanent magnets are very compact, have relatively small stray magnetic fields, and do not require refrigeration. For more information regarding magnet types and design of permanent magnets refer to Chapter 2.1.

The envisioned instrument would be placed in a corner of a research lab. The researcher would insert a sample microfluidics chip inside the proposed instrument, setup the desired information encoding scheme and press start. After the acquisition, the images can be post-processed to highlight the desired information and be displayed to the researcher. An artistic rendition of the proposed instrument is shown in Figure 4. The magnet is inside a magnetically shielded and thermally insulated enclosure on a workbench. The instrumentation to control the flow is attached to the side of this enclosure. The electronics and the computer are located underneath the desk. The user would place the chip in an insert that is used to accurately position the chip inside the magnet. The insert is also used to hold and transfer all the tubes and cables from the chip to the instrumentation outside of the magnet enclosure.

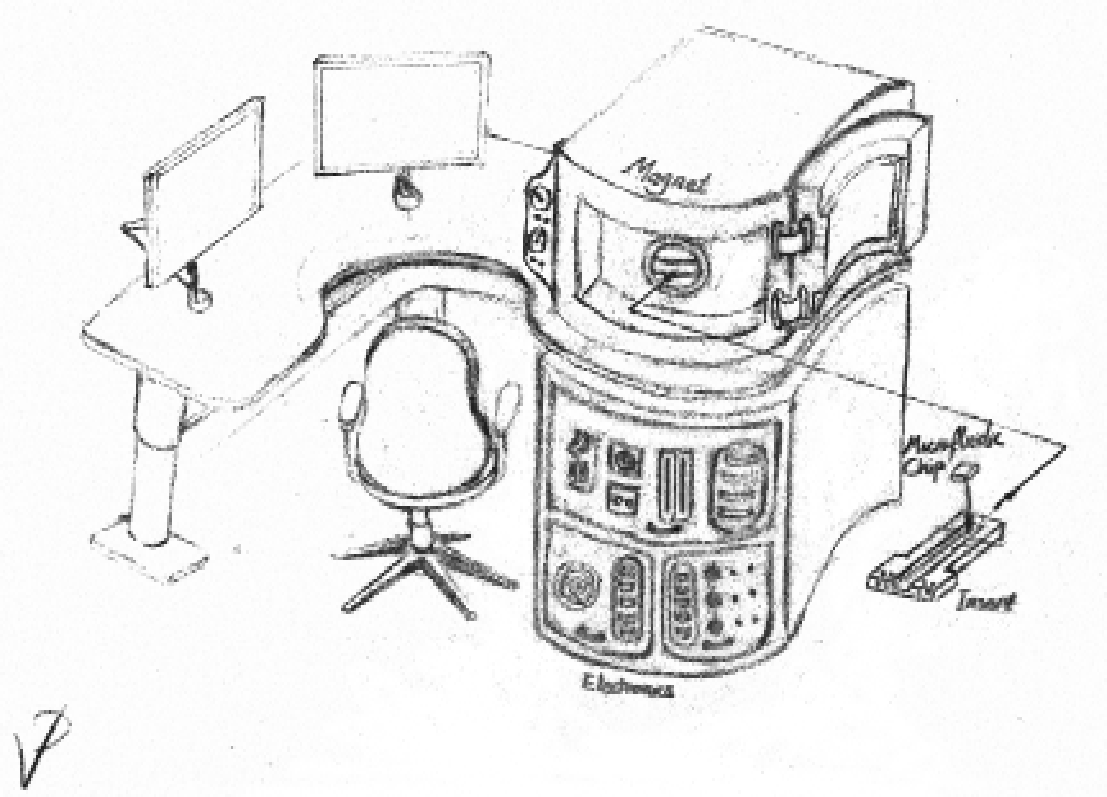

Figure 4. Artistic rendition of the futuristic MRI instrument for visualization of flow in microfluidic chips (courtesy of V. Dokhani).

The proposed instrument will be an important research tool for scientists and engineers working in the growing area of microfluidic research and development including biomedical microsystems for bioanalysis and drug discovery applications for label-free flow imaging. This instrument has further applications in imaging of cells and other biological organisms within the channels and will provide direct benefits to the biotech industry.

1.2 MRI Fluid Measurement at Microscale - Prior Art

To this date, no magnetic resonance imaging instrument has been designed solely for the purpose of measuring of flow fields. Most research groups have conducted velocity encoded imaging experiments either on clinical or general purpose imaging machines without any major modifications to the standard hardware [5, 10, 16-22]. This is especially true for velocity imaging of fluids in 'macroscale' and also clinical imaging of blood flow. For imaging at the microscale, however, there are a limited number of research groups who have modified parts of a standard MRI machine to optimize their performance for flow imaging. For example Sun *et al.* [21] have constructed a thermostatted glass rheometer that is optimized for use in a MRI machine as a 'plug-and-play' module. Rheological tests on aqueous solutions of sucrose and xanthan gum were performed, which were in good agreement with measured results by classical rheometer. They used a 2 T Oxford Instruments superconducting magnet and a general purpose Bruker console. The gradient coils were custom made which were driven by off-the-shelf Techron gradient amplifiers. They also had a custom made quadrature birdcage-type RF coil. A maximum fluid speed on 275 mm/s was measured inside a 4 mm diameter tube. The spatial resolution was 39 x 39 μm^2 need the wall of the tube. A quantitative velocity resolution was not reported.

Bosshard [19] reports very fast imaging of velocity profiles of tubes 4.8 mm in diameter at 200 frames per second (fps) at the expense of lower spatial resolutions of 1 mm x 2 mm in a 2D image. Using conventional imaging with an acquisition time of approximately 13 min, resolutions of 10 x 10 μm^2 can be attained. The maximum velocity in the tube was 1120 mm/s; the velocity resolution is not reported. In this research, a 4.7 T commercial Bruker/GE

superconducting system was used. Only the sample holder was custom made.

Perlo *et al.* [23] have measured the velocity profile of a fluid flowing in small tubes in a highly in-homogeneous magnetic field of a single sided magnetic configuration with a field of 0.23 T. They show a 1D plot of velocity for a tube of 3 mm with a spatial resolution of 0.3 mm and a 2D velocity profile inside a 6 mm diameter tube with a resolution of 0.5mm. The maximum velocity at the center was 20 mm/s; the velocity resolution was not reported. The spectrometer was custom made from off-the-shelf components.

Uludag *et al.* [24] made a tubular heated rheometer to determine viscosity over a range of shear rates of melted polymers. They use commercial General Electric systems with TecMag spectrometers, a 0.6 T Oxford superconducting magnet and water-cooled gradient amplifiers. Velocities up to 36 mm/s were tested in a tube with 12.7 mm in diameter. A spatial resolution of 0.25 mm and a velocity resolution of 0.9 mm/s are reported.

Goloshevsky *et al.* [25, 26] have made integrated planar gradient coils with an RF coil using microfabrication techniques. They utilized a 0.6 T superconducting magnet with commercial spectrometer and gradient amplifiers. The 1D velocity profile of a 1.02 mm tube with a nominal spatial resolution of 10 μm and a velocity resolution of 0.13 mm/s is presented. The maximum velocity inside the tube was of 51.5 mm/s.

Callaghan [11, 27, 28] is probably the most prominent researcher in fluid mechanics who has used and developed spectroscopic NMR and MRI imaging techniques to make rheological measurements of fluids. He and his research group have made a number of setups using commercial magnets, gradients and RF electronics to measure diffusion and flow fields in macroscale and microscale. In his papers and books he suggest that 10 μm spatial resolutions are

possible with small samples and probes.

1.3 Thesis Overview

The rest of this thesis is organized as follows:

In Chapter 1.4, the principles of magnetic resonance imaging are briefly reviewed.

Chapter 2 is broken down into four sections that describe the design, construction and characterization of the main components of the proposed MRI instrument. The main components are: the magnet (section 2.1), gradient coils (section 2.2), gradient amplifiers (section 2.3) and the radio frequency (RF) electronics (section 2.4).

The overall system design and synchronization of the main components is detailed in Chapter 3.

Pulse sequence design for static and velocity imaging, including preliminary velocimetry results obtained using the proposed instruments, are presented in Chapter 4.

The conclusion and future work are covered in Chapter 5.

1.4 Principles of Magnetic Resonance Imaging

The flowing section gives a semi-classical description of the pulsed magnetic resonance phenomenon. It also includes static and velocity encoded imaging sequences and a discussion of the limitations for MRI techniques for static and velocity imaging.

1.4.1 Magnetic Dipole Moment

Fundamental properties of nuclear particles are mass, charge and spin. Fermionic spin is a vector quantity that can have values of ±½ [14]. The angular momentum

$$\mathbf{S} = \hbar \mathbf{I} \tag{1}$$

is proportional to the net nuclear spin $\boldsymbol{I} = \pm ½$ and the reduced Plank's constant $\hbar = 1.055 \cdot 10^{-34}$ J·s [29]. The magnetic dipole moment

$$\boldsymbol{\mu} = \gamma \mathbf{S} \tag{2}$$

can be calculated from the angular momentum [29] using the gyromagnetic ratio $\gamma = 2\pi \cdot (42.5764 \text{ MHz/T})$ for a proton (H_1). Therefore, the magnetic dipole moment can be re-written as

$$\boldsymbol{\mu} = \gamma \hbar \mathbf{I} \, . \tag{3}$$

In atoms with a zero net nuclear spin (paired spins), no magnetic dipole moment exists. For atoms that have a non-zero net nuclear spin (un-paired spins), such as hydrogen, a magnetic dipole exists that interacts with an externally applied magnetic field $\boldsymbol{B_0}$ [30]. The collective interaction of magnetic dipole moments with an external magnetic field gives rise to the magnetic resonance signal.

1.4.2 Bulk Magnetization

At equilibrium, dipole moments either align (low-energy state) or anti-align (high-energy state) with an externally applied magnetic field [30]. In a large sample of hydrogen for example, not all dipole moments align with the applied external magnetic field. The bulk magnetization is the net dipole moment of a sample at equilibrium is given by

$$\mathbf{M}_{0,V} = \sum\nolimits_{V} \boldsymbol{\mu}_i \, . \tag{4}$$

Each aligned dipole moment cancels out an anti-aligned dipole in the sample. The bulk magnetization is zero if there is an equal number of aligned and anti-aligned dipole moments in a sample. Only with a non-zero magnetization is the nuclear magnetic resonance (NMR) signal detectable. The ratio of aligned versus anti-aligned dipole moment is given by the Boltzmann statistics for the ratio of aligned (low-energy) dipole moments n^+ to the anti-aligned (high-energy) dipole moments n^- for an external magnetic field $\boldsymbol{B}_0$ [T],

$$\frac{n^-}{n^+} = e^{-\frac{\gamma \hbar B_0}{k_B T}} \tag{5}$$

the Boltzmann constant $k_B = 1.381 \cdot 10^{-23}$ J/K, and the absolute temperature T [K] [30]. It follows that with an external magnetic field of 0.6 T at room temperature, for every 10^6 anti-aligned dipole moments there are approximately $10^6 + 4$ aligned dipole moments. It is this excess of only four dipole moments out of every million that results in a non-zero bulk magnetization that can be used for the detection of a magnetic resonance (MR) signal. This is the main reason why nuclear magnetic resonance techniques have inherently low sensitivity.

The magnetization of a sample with N hydrogen atoms can be derived as [29]

$$\mathbf{M}_{0,V} = \frac{N \gamma^2 \hbar^2 \mathbf{B}_0}{4 k_B T}. \tag{6}$$

At thermal equilibrium, $\boldsymbol{M}_0$ and $\boldsymbol{B}_0$ point the same direction. It is customary to assign the direction of $\boldsymbol{B}_0$ to the z-axis as shown in Figure 1. If the bulk magnetization is disturbed out its equilibrium condition, precessional behaviour of the magnetization is observed. This means that the bulk magnetization will tend to recover to its thermal equilibrium condition (i.e., align with

the magnetic field). During this recovery, energy is dissipated into surrounding environment which is discussed in the next section.

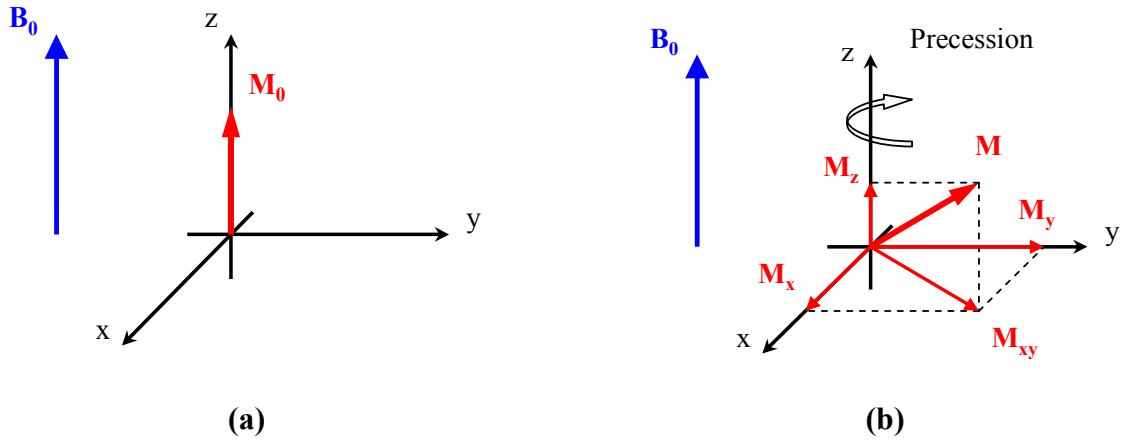

Figure 1. Direction of bulk magnetization and external field (a) at equilibrium and (b) after it is disturbed.

1.4.3 Bloch Equations

The precessional dynamics of the magnetization is defined by the Bloch equation [31]

$$\frac{d\mathbf{M}}{dt} = \mathbf{M} \times \gamma \mathbf{B} - \frac{(M_z - M_0)\mathbf{k}}{T_1} - \frac{M_x \mathbf{i} + M_y \mathbf{j}}{T_2}, \tag{7}$$

where *i*, *j* and *k* are unit vectors in the Cartesian coordinate system. The first term describes the path the bulk magnetization follows after a disturbance (excitation) in order to align with the external magnetic field $\boldsymbol{B}_0$. It also includes the precessional frequency

$$\omega_0 = \gamma B_0, \tag{8}$$

which is also called the Larmor frequency. The Larmor frequency is the frequency at which the

bulk magnetization precesses about the axis of the external magnetic field. For example, an external magnetic field $\boldsymbol{B}_0 = 0.6$ T results in a precessional frequency of $\omega_0 \sim 25$ MHz.

The other two terms in (7) refer to the relaxation processes. The second term refers to the longitudinal (M_z) relaxation towards thermal equilibrium, which is characterized by the T_1 (spin-lattice) time constant. T_1 depends on the sample material, temperature, and the magnetic field strength [32].

The last term refers to the transverse magnetization (M_{xy}) decay characterized by the T_2 (spin-spin) time constant. The T_2 relaxation corresponds to decoherence of the transverse bulk magnetization. Detailed description and analysis of Bloch equation and the relaxation mechanisms are covered elsewhere [28-32].

In practice, another time constant called the T_2* is also considered with (7)

$$\frac{1}{T_2^*} = \frac{1}{T_2} + \gamma \Delta B_0 \,. \tag{9}$$

It takes into account non-ideal conditions, especially the non-homogeneity of the static magnetic field $\Delta \boldsymbol{B}_0$.

Assuming a sample with bulk magnetization of $\boldsymbol{M}_0$ in a homogenous magnetic field along the z-axis, if $\boldsymbol{M}_0$ is excited out of equilibrium onto the x-axis, the precessional path would be similar to the path shown by the Bloch simulations shown in Figure 2.

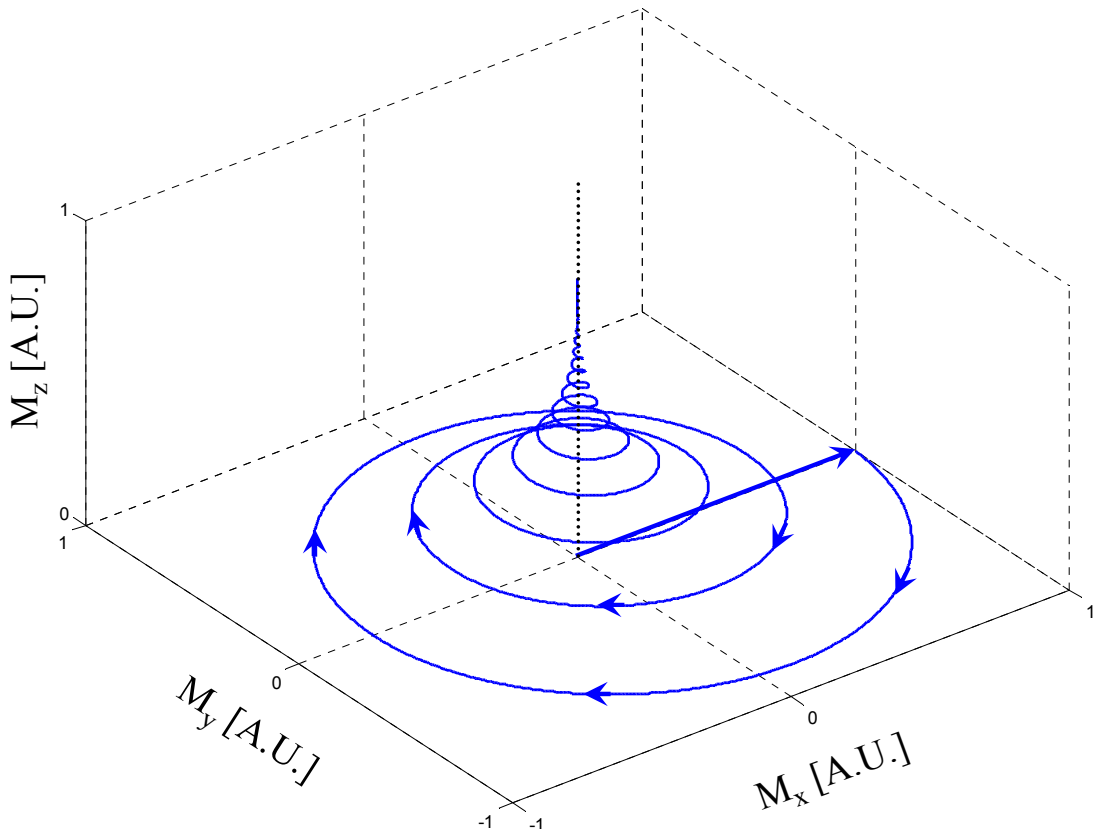

Figure 2. Relaxation bulk magnetization after a 90° excitation onto the x-axis. In this simulation T_1 = 40 ms and $T_2 = T_2^*$ = 10 ms. (B_0 directed along in z-direction)

Starting from the x-axis, the bulk magnetization vector $\boldsymbol{M_0}$ starts precessing about the z-axis (parallel to the magnetic field) at the Larmor frequency ω_0. The transverse bulk magnetizations $\boldsymbol{M_x}$, $\boldsymbol{M_y}$ decay according to the spin-spin time constant T_2 = 10 ms while the longitudinal relaxation $\boldsymbol{M_z}$ recovers at a slower rate T_1 = 40 ms as shown in Figure 3. After about $5 \cdot T_1 = 200$ ms thermal equilibrium is reached and the magnetization vector points towards the external magnetic field $\mathbf{B_0}$.

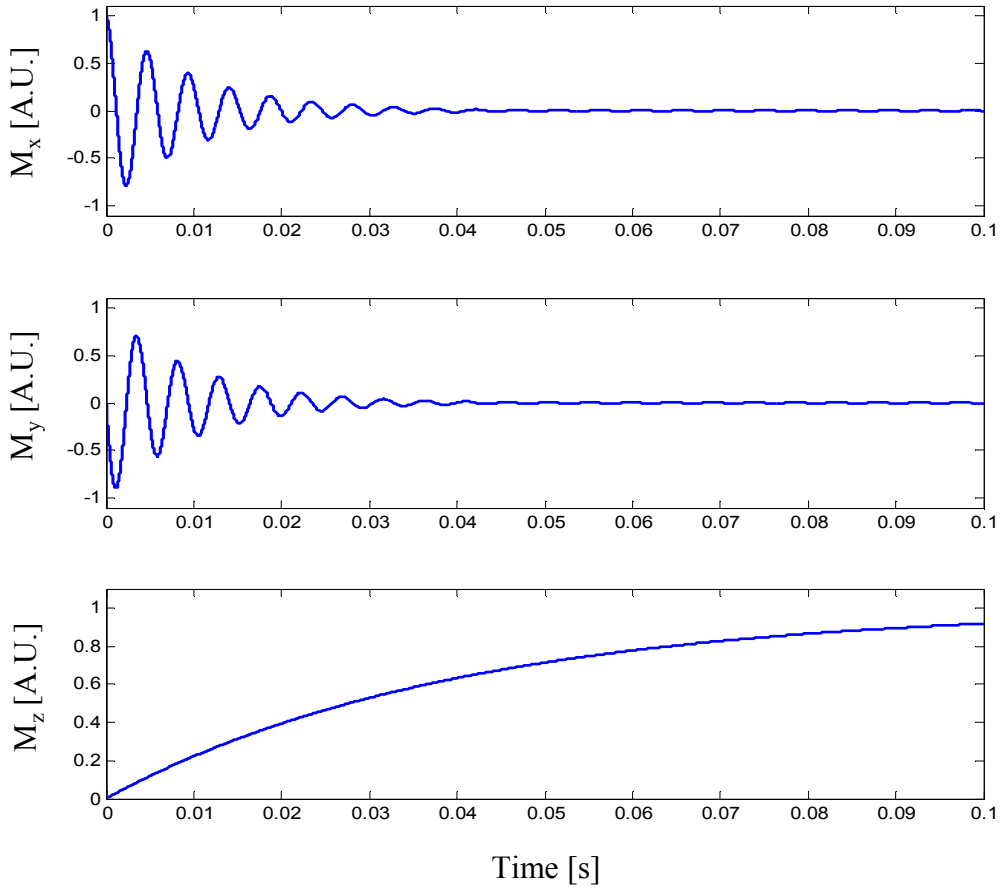

Figure 3. The three components of the bulk magnetization after a 90° excitation onto the x-axis.

The T_2* time constant is the dominant factor in determining the received signal decay. Basically, the spins of the sample experience slightly different magnetic fields at various locations of the magnet. This results in some spins precessing faster than others. After the initial excitation, all the spins are more or less in phase resulting in a large bulk transverse magnetization. A snap shot after the initial excitation is shown in Figure 4a. After a short time delay however, the spins start to acquire phase shift which results in a reduced overall bulk transverse magnetization (see Figure 4b and c). In other words, the phase coherence of the nuclei is lost.

1.4.4 Excitation

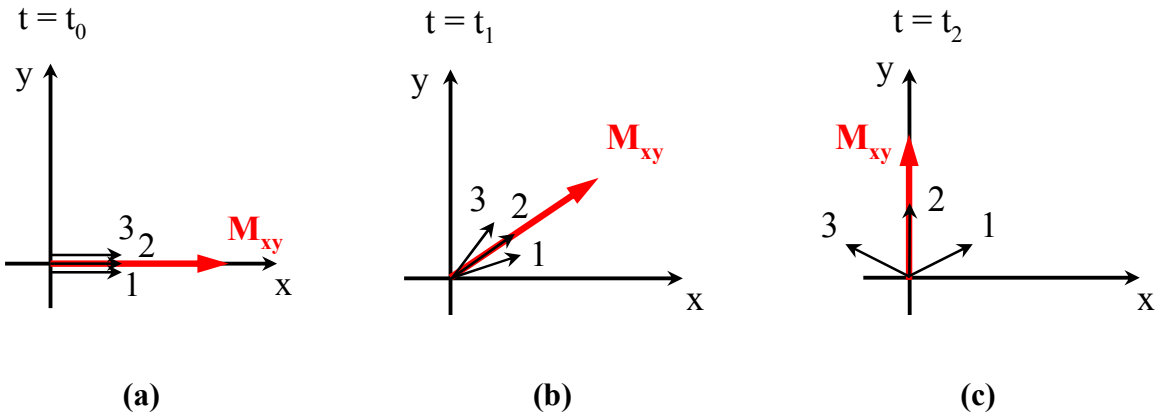

Figure 4. Effect of T_2 (and T_2*) on the phase coherence of the magnetic resonance signal. The three numbered arrows indicate the magnetization of three spins. The spin marked as 1 experiences a slightly lower magnetic field, which also makes it precess slower, compared to spins marked as 2 and 3. In (a) all spins are in phase and result in a large M_{xy}. As time passes (a → b → c) the spins go out of phase and their net magnitude M_{xy} is reduced. (B_0 is pointing into the page)

To excite (flip) the bulk magnetization from its equilibrium position, a time varying magnetic field B_1 is applied that is perpendicular to the main static magnetic field B_0. The frequency of B_1 is chosen to be the Larmor frequency ω_0 (hence the term resonance) and the amplitude is usually two to three orders of magnitude less than the main magnetic field B_0. Due to the high frequency of the excitation signal, it is called the radiofrequency (RF) signal. The circularly polarized component of the bulk magnetization

$$\mathbf{B_1}(t) = B_1(\cos(\omega_0 t)\mathbf{i} - \sin(\omega_0 t)\mathbf{j}) \tag{10}$$

corresponds to the projection of the path shown in Figure 2 onto the x-y plane. By controlling the amplitude, phase and duration of the pulse, the magnetization can be excited to almost any arbitrary direction. In the rotating frame (about the z-axis), the excitation signal can be

interpreted as changing the effective magnetic field [29]

$$\mathbf{B}_{\text{eff}} = (\mathrm{B}_0 - \frac{\omega}{\gamma})\mathbf{k} + \mathbf{B}_1(\mathrm{t})\mathbf{i} \tag{11}$$

experienced by the sample. The rotating frame is a coordinate system that rotates about the z-axis (parallel to the magnetic field $\boldsymbol{B_0}$) with a rotational speed ω. For example, the excitation field $\boldsymbol{B_1}$ which is a function of ω according to (10) appears stationary in the rotating frame shown Figure 5a. The static magnetic field $\boldsymbol{B_0}$ is along the z-axis with excitation field $\boldsymbol{B_1}$ applied along the x-axis. The effective excitation field $\mathbf{B}_{\text{eff}}$ is shown in Figure 5a. According to (11), if ω is very close to ω_0 the effective magnetic field would almost exclusively be in the direction of excitation field B_1, even thought its amplitude is only a fraction of that of B_0. The magnetization is flipped about the effective magnetic field $\mathbf{B}_{\text{eff}}$ according to the left hand rule (if the left-hand thumb is aligned in the direction of $\boldsymbol{B}_{\text{eff}}$, the spins are flipped in the direction of other fingers). For example, a 90° excitation on applied on the x-axis flips the magnetization onto the y-axis when the frequency is set at the Larmor frequency as shown in Figure 5b.

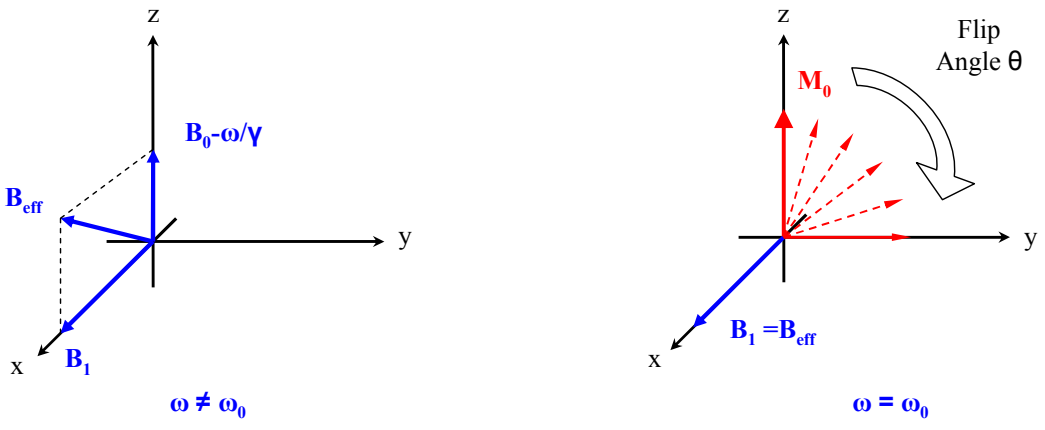

Figure 5. Effective magnitude (a) and the corresponding flip angle (b) of the bulk magnetization in the rotating frame of reference.

For a “hard” rectangular RF pulse, a 90° flip is achieved when $\mathbf{B_1}$ is applied on the x-axis at resonance (Larmor) frequency for a specific duration so that the magnetization is excited onto the y-axis. The required time,

$$t_{90^\circ} = \frac{\theta}{\omega} = \frac{\pi/2}{\gamma B_1}, \tag{12}$$

typically ranges from 10 μs to 1 ms for a 90° flip angle depending on the excitation coil and the RF electronics. A rectangular pulse (in the time domain) is commonly used to excite the whole sample. To excitation a specific region of the sample, various RF excitation pulses exist [15]. The RF pulse sequence used for imaging is explained later in this work.

One way to recover the T_2* de-coherence of the magnetic resonance signal mentioned in section 1.4.3 is to apply a second RF excitation, the 180° pulse, to rephase the spins [33] as shown in Figure 6. This is accomplished by flipping all the spins either about the x-axis or the y-axis after a short time delay τ (shorter than T_2) after the initial 90° pulse. After 2τ, the spins rephase and the result is a spin echo as shown in Figure 6.

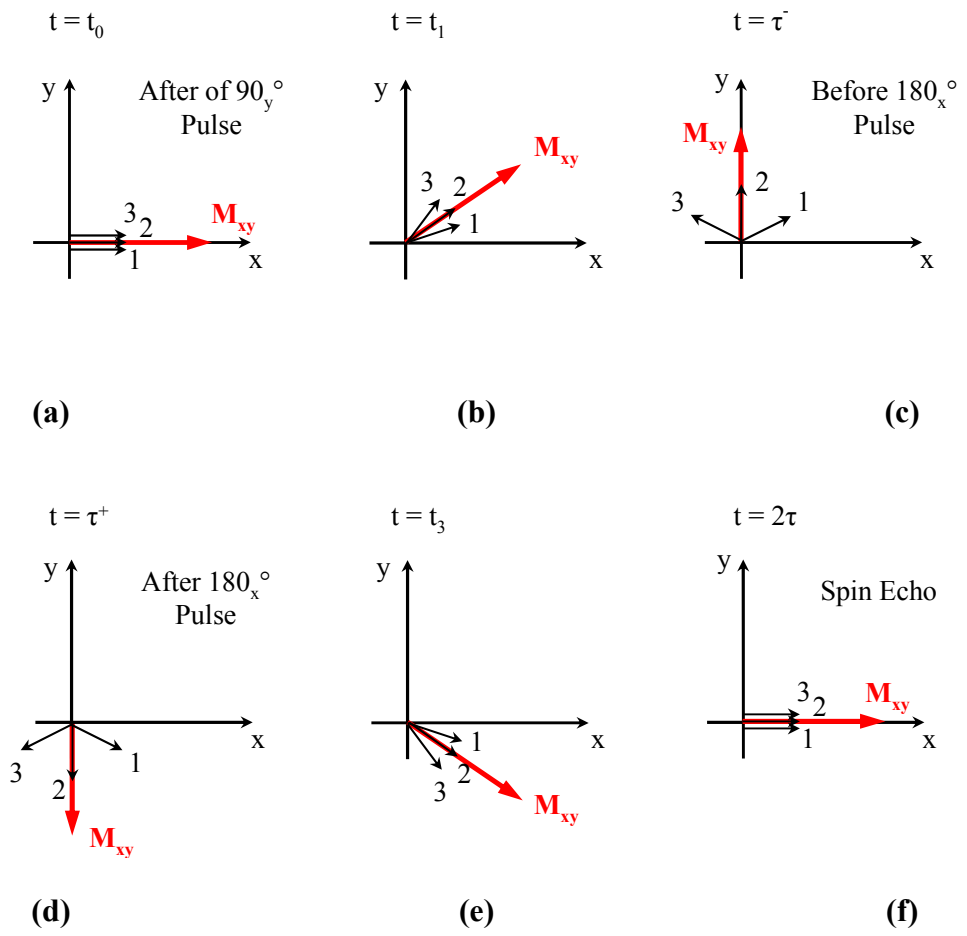

Figure 6. Spin Echo: starting with $90_y°$ flip (a) the T_2* decay from in-homogeneities of the magnet de-phase the signal (b). At time τ the $180_x°$ pulse is applied (c) and the phases are rotated about the x-axis (d). The spins start to rephrase (e) and form an echo (f) at time 2τ with a reduced amplitude due to the intrinsic T_1 and T_2 relaxation times. (B_0 is pointing into the page)

Excitation sequences need to be separated far enough apart in time to allow the longitudinal magnetization to align with the main static magnetic field. The repetition time TR is commonly chosen to be 3-5 times the expected value of T_1.

1.4.5 Detection of Magnetic Resonance Signal

To detect the MR signal, a coil perpendicular to the main magnetic field B_0 is used to pick-up the

changing magnetic flux produced after the transverse ($\boldsymbol{M}_{xy}$) bulk magnetization is excited out of equilibrium. The magnetic flux of the transverse bulk magnetization Φ_M

$$\Phi_{\mathrm{M}} = \int_{\mathrm{Sample}} \mathrm{d}^3\mathbf{r}\, \mathbf{B}_{\mathrm{Receiver}}(\mathbf{r}) \cdot \mathbf{M}(\mathbf{r}, \mathrm{t}) \tag{13}$$

can be calculated, where **r** [m] is the position of the magnetization vectors, $\boldsymbol{B}_{receiver}(\boldsymbol{r})$ [T/A] is the magnetic flux density generated by the coil at position $\boldsymbol{r}$ per unit current, and $\boldsymbol{M}(\boldsymbol{r},t)$ is the transverse component of the bulk magnetization. The change of the magnetic flux

$$\mathrm{emf} = \mathbf{V}_{\mathrm{receiver}} = -\frac{\mathrm{d}}{\mathrm{dt}}\Phi_{\mathrm{M}} \tag{14}$$

induces a voltage in the receiver coil. From (13) and (14) the voltage in the receiver coil can be re-written as

$$\mathbf{V}_{\mathrm{receiver}} = -\frac{\mathrm{d}}{\mathrm{dt}} \int_{\mathrm{Sample}} \mathrm{d}^3\mathbf{r}\, \mathbf{B}_{\mathrm{Receiver}}(\mathbf{r}) \cdot \mathbf{M}(\mathbf{r}, \mathrm{t} = 0) \tag{15}$$

where the voltage induced in receiver coil $\mathbf{V}_{\mathrm{receiver}}$ [V] has the maximum amplitude immediately after a 90° excitation (at t = 0 , $\boldsymbol{M}_{xy}$ is maximum).The signal decays as a function of time according to the relaxation times. The signal is demodulated and further processed in the receiver and sent to the computer to generate an image as will be explained later.

1.4.6 Gradient Fields

According to (8), the frequency of the MR signal depends on the magnetic flux density in a linear fashion. Under a linearly varying main magnetic field $\mathbf{B_0}$, the sample experiences a different magnetic field as a function of location, which in turn results in location-dependent Larmor frequencies. The corresponding MR signals of different frequencies now correspond to

different locations in space.

The function of the gradient field is to modulate the main magnetic field linearly in one direction in space. Usually three gradients are employed to encode the signal in 3-dimensions. The resulting flux density

$$\mathbf{B} = \mathbf{B}_{0,z} + \mathbf{G}_{\mathbf{r}} \cdot \mathbf{r} \tag{16}$$

of any point in space depends on the three gradients

$$\mathbf{G}_{\mathbf{r}} = \frac{dB_z}{dx} + \frac{dB_z}{dy} + \frac{dB_z}{dz} \tag{17}$$

that are applied. Gradient fields have units of [T/m] and are generated by gradient coils.

An example of the use of a gradient applied over a disc shaped object is shown in Figure 7. When no gradients are applied, the sample experiences a homogenous field; therefore, the resulting MR signal ideally contains a single frequency as shown in Figure 7a. If a gradient is applied over the object, however, the received MR signal has a frequency spread that corresponds to the projection shape of the object as shown in Figure 7b.

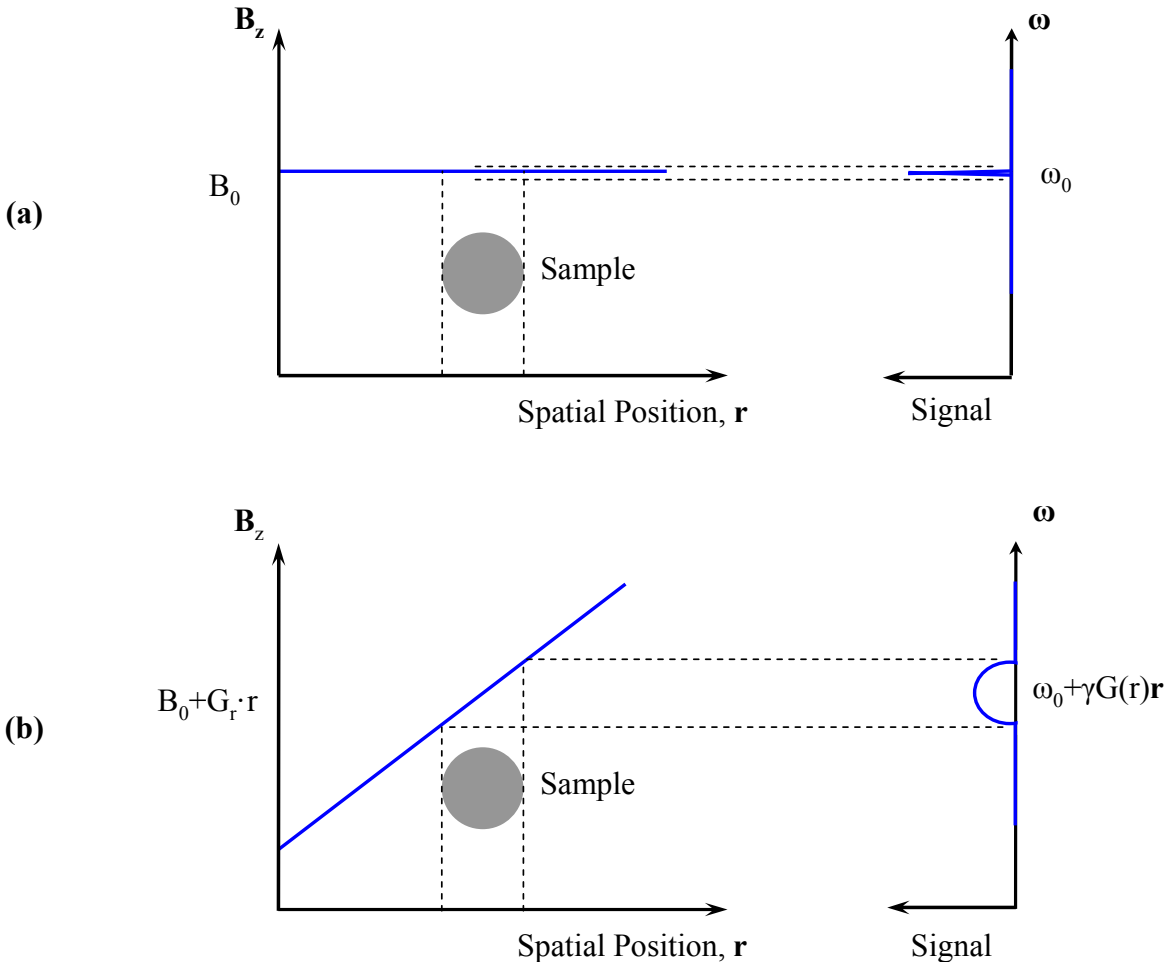

Figure 7. Ideally, when no gradient field is applied (a) a single frequency is present. When a gradient is applied (b) a spread of frequencies that corresponding to the shape of the sample will be present.

The applied gradients change the local Larmor frequency and, thus, encode spatial position into the frequency of the detected MR signal. The precessional frequency with the application of gradient is

$$\omega(\mathbf{r},t) = \gamma\,(B_0 + \mathbf{G}(t)\,\mathbf{r})\,. \tag{18}$$

The phase difference in the MR signal relative to the signal at $\boldsymbol{r} = 0$ can be calculated as

$$\phi(\mathbf{r}, t_0) = \mathbf{r}.\left(\gamma \int_0^{t_0} \mathbf{G}(t')dt' \right). \tag{19}$$

The term inside the brackets

$$\mathbf{k}(t_0) = \gamma \int_0^{t_0} \mathbf{G}(t')dt' \tag{20}$$

is a function of the applied gradients and time. The vector quantity ***k*** is the reciprocal space vector with units of m^{-1}. By applying an adequate sequence of gradients with correct timing, a sample can be encoded to highlight hydrogen density, T_1 relaxation, T_2 relaxation, mass diffusion and even mass transport (i.e., flow) in three dimensions.

Another application of the gradients is for selective excitation of the sample. To excite a cross-sectional slice of certain thickness for example, a gradient field is applied along with a RF excitation of a specific bandwidth. To excite slice, the frequency component of the excitation pulse needs to be of rectangular shape. A rectangular shape in the frequency domain corresponds to a Sinc (sin x/x) in time domain. The slice thickness

$$\Delta z = \frac{BW_{Sinc}}{\gamma G_{Slice}} \tag{21}$$

depends on the amplitude of the slice selection gradient G_{Slice} and the bandwidth of the selective RF pulse BW_{Sinc}. Various types of pulses exist which are discussed in detail in [15]. The use of selective excitation is further discussed in the following sections.

1.4.7 The Signal Equation

For an object (sample to be imaged) with a spatially varying magnetization density of *M(r)* the

MR signal before the detection coil

$$\text{Signal}_{\text{MR}}(t) = \int_{\mathbf{r}} M(\mathbf{r}') e^{-j(\omega_0 t + \phi)} d^3\mathbf{r}' \tag{22}$$

includes contributions of all precessing transverse magnetizations in the volume (assuming the relaxation terms are ignored). The term with ω_0 can be removed by setting the reference frequency of the demodulator to be at baseband ω_0. The signal equation can then be re-written in terms of $\boldsymbol{k}$

$$\text{Signal}_{\text{MR}}(\mathbf{k}_{(t)}) = \int_{\mathbf{r}} M(\mathbf{r}') e^{-j\mathbf{r}'\cdot\mathbf{k}(t)} d^3\mathbf{r}'. \tag{23}$$

According to (19) and (22) the signal of a slice of thickness Δz is

$$\text{Signal}_{\text{Slice}}(\mathbf{k}_{(t)}) = \Delta z \int_x \int_y M(x,y) e^{-j\left[k_x(t)x + k_y(t)y\right]} dxdy. \tag{24}$$

The signal equation has the form of a Fourier transform (FT), thus an image I(x,y) can be formed by taking the inverse FT of the signal equation

$$I(x,y) = FT^{-1}\left(\text{Signal}_{\text{Slice}}(\mathbf{k}_{(t)})\right), \tag{25}$$

$$I(x,y) = \Delta z \int_{k_x} \int_{k_y} \text{Signal}_{\text{Slice}}(\mathbf{k}_{(t)}) \cdot e^{j\left[k_x(t)x + k_y(t)y\right]} dk_x dk_y, \tag{26}$$

$$I(x,y) = M(x,y)\Delta z. \tag{27}$$

The cross-sectional 2D image is a representation of the spin density of a slice of the sample.

1.4.8 Imaging Principles

Two implementations of spatial encoding can be derived from (26) namely *phase encoding* and

frequency encoding [12]. Frequency encoding includes the application of a constant gradient over the sample resulting in MR signal of different frequencies corresponding to the projection of the sample, as shown in Figure 7. Phase encoding involves a gradient is applied only for a short time *t* to introduce phase shifts

$$\Phi(\mathbf{r},t) = \gamma\,(B_0 + \mathbf{G}(t)\,\mathbf{r})\,t \tag{28}$$

in the MR signal. The phase encoding gradient is usually assigned to the y-axis while the frequency encoding gradient along the x-axis. A sequencing diagram of the RF and gradient pulses is shown in Figure 8 as a function of time. For example, in Figure 8a the 90° pulse is applied first followed by the phase encoding gradient. The time the MR signal is sampled is indicated by the data acquisition plot. In *phase encoding* the gradient (phase gradients, G_{phase}) is applied before the sampling the MR signal starts, as shown in Figure 8a. During the acquisition of the MR signal $G_{phase} = 0$ [T/m], thus according to (20) $\boldsymbol{k}_y(t) = \boldsymbol{k}_{phase}(t)$ does not change during the sampling window. This ensures that each sample of the MR signal will have the same phase encoding $\boldsymbol{k}_{phase}$ as seen in Figure 8a. When the phase gradient is applied, the phase of the MR signal changes linearly according to (20). This experiment is repeated for different durations or amplitudes for the phase encoding gradient so that each experiment has a different phase encoding.

In *frequency encoding* the gradient is applied while the MR signal is sampled as shown in Figure 8b. Again the, 90 RF pulse is applied first, then after a time delay the frequency encoding gradient is applied for a specific duration. According to (20), $\boldsymbol{k}_{frequency}(t)$ changes linearly during the acquisition of the MR signal, this ensures that each sampled signal has a slightly different phase increment associated with it. In principle, the phase and frequency encoding techniques are

the same. The only difference between the frequency encoding and phase encoding is that $\boldsymbol{k}_x(t) = \boldsymbol{k}_{frequency}(t)$ is different for each sample of the MR signal as shown in Figure 8b. In other words, the frequency encoding gradient alters the local magnetic field according to (18), which results in a spatial variation in the Larmor frequencies of the magnetization vectors of the sample.

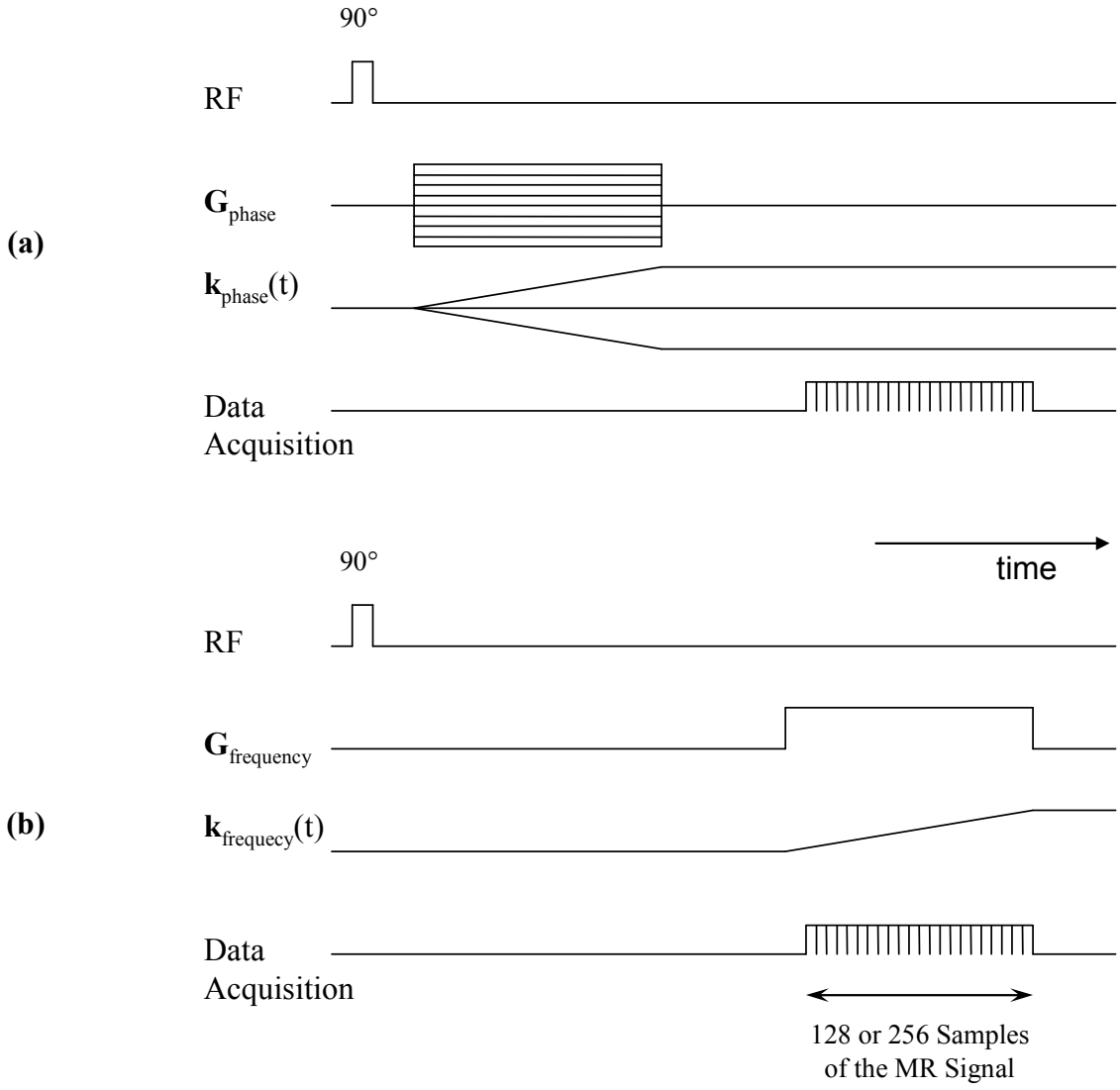

Figure 8. In phase encoding (a) k(t) stays constant during acquisition of the MR signal whereas in frequency encoding (b) k(t) varies during sampling.

According to (26), a two dimensional inverse Fourier transform of the MR signal would yield an image. To generate a meaningful image, the MR signal needs to be sampled at specific **k**(t) locations. In practice, the data is collected on a Cartesian grid in **k**-space for computational efficiency. One of the earliest pulse sequences used to cover the complete k-space is called the spin-warp imaging sequence [34, 35]; where phase and frequency encoding are used.

The more common spin echo pulse sequence for a 2D slice is Figure 9.

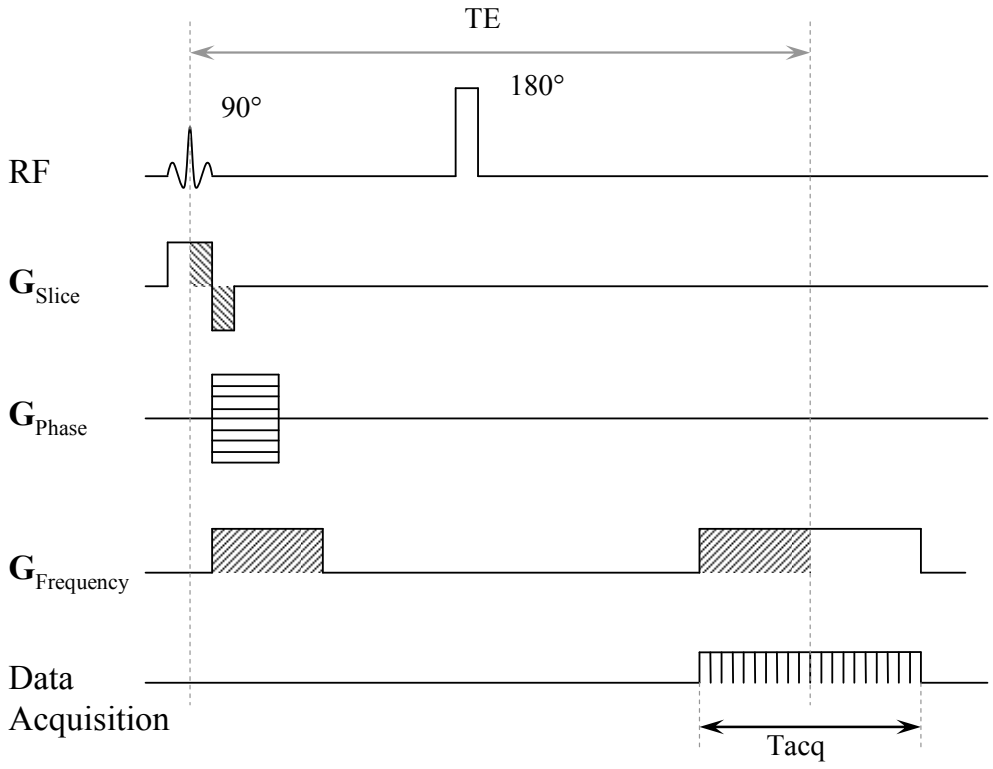

Figure 9. Spin echo (SE) imaging sequence.

In the spin echo (SE) imaging sequence, a 180° pulse is applied after the initial 90° pulse after a time delay *TE*/2; thus the MR signal forms at time *TE*. The selective 90° pulse is applied along with a slice-selection gradient to excite the nuclei in a slice. This is necessary to generate a cross-sectional slice of the sample. After the end of the RF pulse, the slice-selection gradient is

reversed for a half of the time of the RF pulse to rephase all the spins of the selected slice. The frequency encoding gradient is applied during data acquisition for the same duration as the data acquisition. $G_{frequency}$ is also applied before the 180° pulse for a duration of half the acquisition time. The first part of the frequency encoding gradient de-phases the nuclei so that the second part of the frequency encoding gradient, which works in conjunction of the 180° pulse, rephases the spin exactly at the time TE as explained previously (see Figure 6). The entire horizontal line in k-space is sampled in a single repetition of the SE pulse sequence which is the frequency-encoding implementation discussed before. The phase encoding gradient is applied between the 90° and 180° pulses. At each repetition of the SE pulse sequence the phase gradient is applied with different amplitude to increment the phase. This results in vertical shifts in k-space at each repetition. This is the phase-encoding implementation mentioned before. After several repetitions the SE waveform (usually 128-512), the complete k-space is covered.

The simplified trajectory in 2D k-space is shown in Figure 10b for a simplified SE pulse sequence in Figure 10a. Consider the first iteration of this pulse sequence when the phase encoding gradient is zero. The point 0 (in Figure 10a and Figure 10b) is the time just before the de-phasing pulse of the frequency encoding gradients is applied. The de-phasing pulse of the frequency encoding gradient, marked as 4, shifts the current position in k-space horizontally. Thus, at the end of the of both pulses before the 180° pulse, the position in k-space has moved to the point marked as 3,4 that lies on the horizontal $k_y = 0$. After the 180° pulse, the current position in k-space moves to 6 by the trajectory marked as 5 in Figure 10b. Next, when the frequency encoding gradient is applied between points 6 and 7 while the MR signal is sampled, as shown in Figure 10a. The sampled MR signal corresponds to a single horizontal line (from 6 to 7) in k-space as shown in Figure 10b at $k_y = 0$. Now, the iteration restarts with a different

phase encoding step. Consider an iteration in which the phase encoding gradient is maximum. The point 0 (in Figure 10a and Figure 10b) is the time just before the phase and frequency encoding gradients are applied. The phase encoding gradient marked with as number 1 shifts the current position in the k-space vertically (upwards); The de-phasing pulse of the frequency encoding gradient, marked as 4, shifts the current position in k-space horizontally. Thus, at the end of the of both pulses before the 180° pulse, the position in k-space has moved to the point marked as 1,4. After the 180° pulse, the current position in k-space moves to 6 by the trajectory marked as 5 in Figure 10b. Next, when the frequency encoding gradient is applied between point 6 and 7 while the MR signal is digitized, as shown in Figure 10a. The digitized MR signal corresponds to a single horizontal line (from 6 to 7) in k-space as shown in Figure 10b at $k_y = k_{Phase,max}$. If this pulse seqcuence is repeated for different phase encoding steps, the entire k-space can be covered as shown in Figure 10c. A 2D inverse Fourier transform of the k-space would yield a cross-sectional static image of the sample (Figure 10d). For more information on various implementations to cover the k-space, refer to the book by Bernstein *et al.* [15].

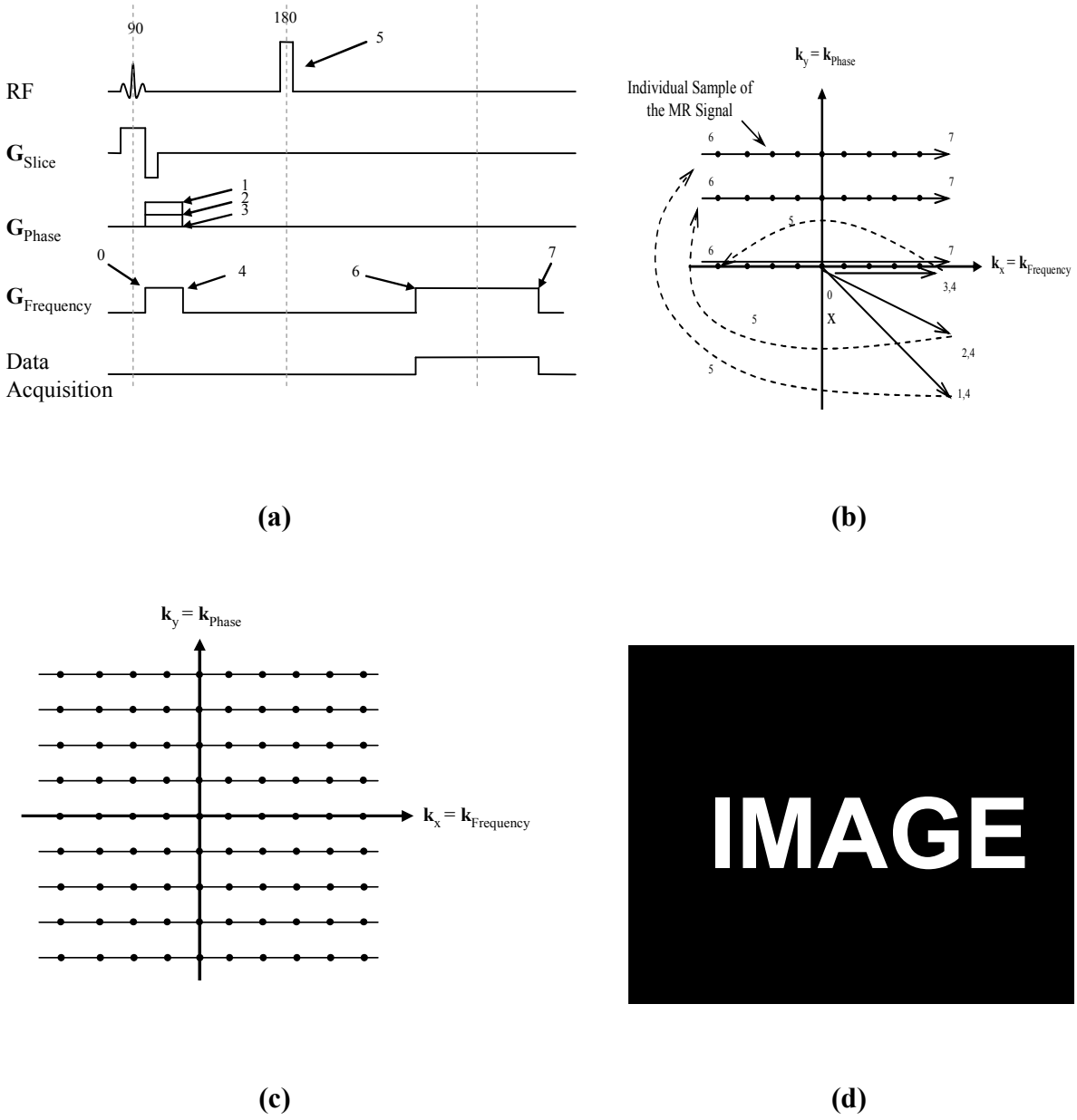

Figure 10. A standard SE imaging sequence is shown in (a) with its trajectory in k-space (b). An inverse 2D Fourier transform of the k-space (c) yields and image (d).

Another commonly used pulse sequence is the gradient recalled echo (GRE) sequence as shown in Figure 11. The primary difference between SE and GRE is that the MR echo in the SE sequence is formed by a 180° pulse while in the GRE sequence it is formed by a gradient echo. A

gradient echo forms whenever spins are de-phased by applying a gradient for time *t* and then re-phase by applying the gradient in the reverse direction for 2*t*.

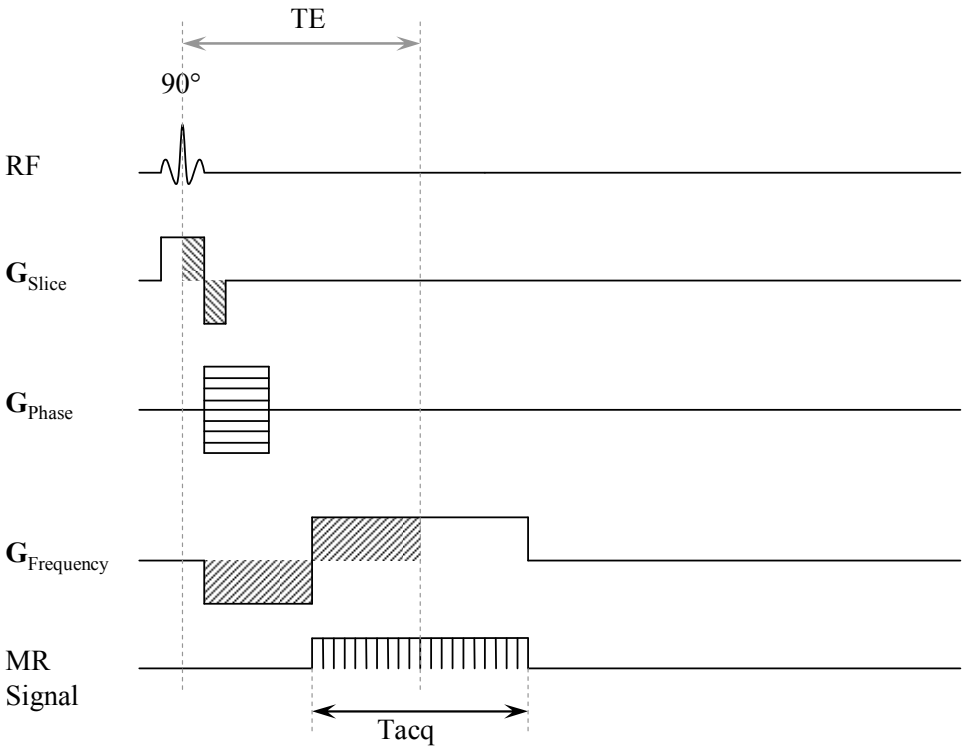

Figure 11. Gradient recalled echo (GRE) imaging sequence

1.4.9 Flow Imaging

Two commonly used techniques exits to encode velocity information: time-of-flight (TOF) and phase-contrast (PC). These methods are extensively described in [15, 29] and are mostly developed for the clinical sector to detect blood flow for magnetic resonance angiography (MRA) applications.

In one implementation of the TOF technique, an additional 180° pulse is applied with a certain

delay $t_{Inversion}$ before the imaging sequence. A sample inversion SE pulse sequence to visualize flow in one dimension is shown in Figure 12. For example, if a pulse sequence with $t_{Inversion} = 0.6 \cdot T_1$ is used [30], the stationary spins do not generate a MR signal. The non-stationary spins, however, experience the inversion pulse with a slightly different timing compared to stationary spins. Thus moving spins generated an MR signal proportional to their velocity. A phase encoding can be added the sequence shown in Figure 12 along with slice selection gradients and selective RF pulses to generate a TOF flow encoded two dimensional image.

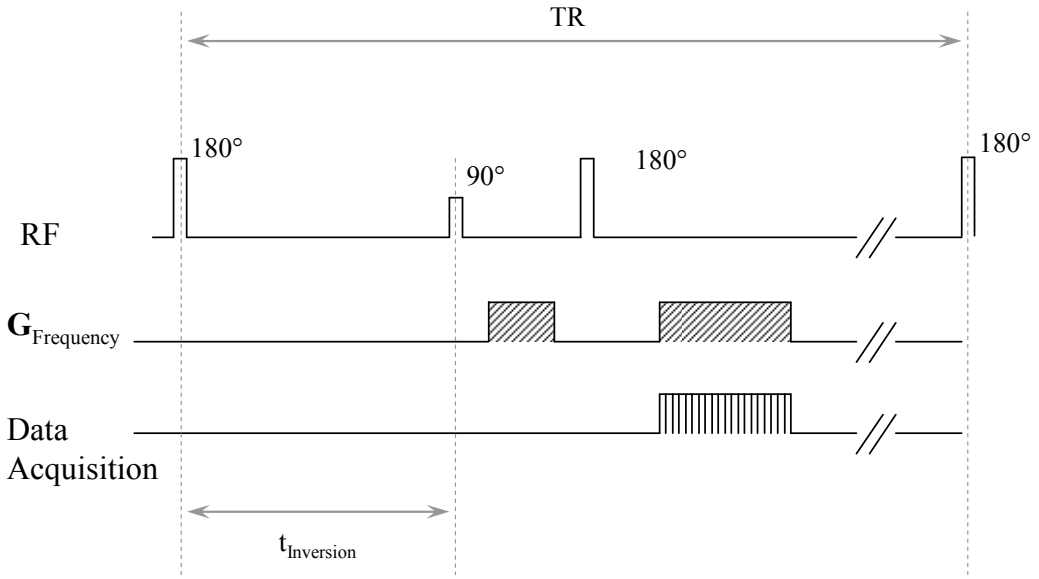

Figure 12. Inversion saturation SE sequence for 1D flow imaging.

An even simpler TOF pulse sequence to visualize fast flows is shown in Figure 13. This pulse sequence is a one-dimensional SE pulse sequence with no slice selection. Stationary spins that experience both the 90° and 180° pulses generated a strong spin echo pulse. Moving spins that flow fast enough, exit the excitation/detection area and do not experience one of both the RF pulses. In that case, a reduction of the spin echo signal is observed semi-proportional to the flow.

The pulse sequence shown in Figure 13 is repeated twice, once when all the spins are stationary and once when the spins are moving. A difference between the magnitudes of their Fourier transform is an indication of the velocity profile inside the sample. This technique is used as a proof-of-concept test of the experimental setup of this work.

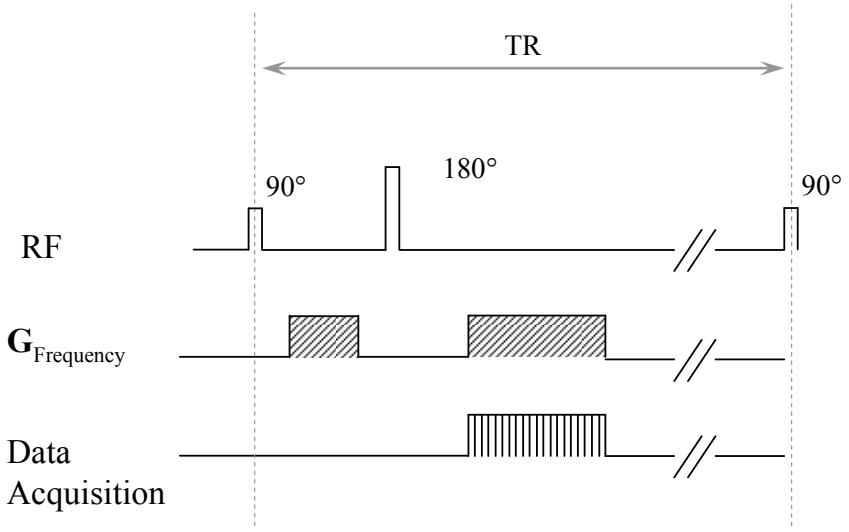

Figure 13. Simplified SE for 1D imaging of fast flow.

Phase contrast methods are widely used because they are much more sensitive to slow flows. For this reason, phase contrast (PC) techniques need to be implemented in this setup to measure the flow rates that are more commonly encountered in microfluidics chips. Unlike TOF based techniques that are dependent on relaxation effects, signal drop out in regions or complex flow, phase-based techniques are self calibrating since phase is directly proportional to motion, and is independent of other parameters, such as relaxation rates, geometry of the sample, and inflow effects [12]. The primary disadvantage of PC techniques is that, when the induced phase change is greater than 2π, phase warp occurs and causes aliasing artifacts in the velocity encoded

images. This problem, however, can be compensated to some extent by carefully adjusting the pulse sequence and also through post processing the images.

As mentioned in sections 1.4.6 and 1.4.9, phase information is used to encode position. If position is generalized and is let to be also a function of time, then phase encoding can be extended to include higher order motions such as velocity. Assuming a flow with constant velocity, the position of the nuclei of the sample are given as

$$\mathbf{r(t)} = \mathbf{r}_0(\tau) + \mathbf{v}_0(\tau)\cdot(t-\tau) \tag{29}$$

The coefficients represent $\boldsymbol{r_0(\tau)}$ and $\boldsymbol{v_0(\tau)}$ position and velocity at time τ. Referring to (19), the phase of the MR sample can be rewritten as

$$\phi_{MR}(\mathbf{r},t) = \gamma\int_0^t \mathbf{G}(t')\cdot\mathbf{r}(t')\,dt' \tag{30}$$

$$\phi_{MR}(\mathbf{r},t) = \gamma\left[\mathbf{r}_0(\tau)\int_0^t \mathbf{G}(t')\,dt' + \mathbf{v}_0(\tau)\int_0^t \mathbf{G}(t')\cdot(t'-\tau)\,dt'\right] \tag{31}$$

which can be simplified using n-th moment of the gradient pulse sequence

$$\mathbf{M_n}(t,\tau) = \int_0^t \mathbf{G}(t')\cdot(t'-\tau)^{(n)}\,dt' \tag{32}$$

to read

$$\phi_{MR}(\mathbf{r},t) = \gamma\left[\mathbf{r}_0(\tau)\cdot\mathbf{M_0}(t,\tau) + \mathbf{v}_0(\tau)\cdot\mathbf{M_1}(t,\tau)\right]. \tag{33}$$

The phase

$$\phi_{MR}(t) = \phi_r(t,\tau) + \phi_v(t,\tau) \tag{34}$$

is the combination of the phase accumulation due to static position components and also dynamic components (only velocity here). Assuming a uni-polar gradient similar to the one depicted in Figure 14a is applied (i.e., $M_0(t,\tau) \neq 0$). According to (33), if velocity or higher order phase terms are negligible, the measured phase ϕ_{MR} is a measure for position. If the higher order terms, such as ϕ_v, are not small in comparison to ϕ_r then errors appear in the image as ghosts and blurriness. Now assume that a bi-polar gradient which has positive and negative gradient lobes with equal areas is used (i.e., $M_0(t,\tau) = 0$ and $M_1(t,\tau) \neq 0$). As shown in Figure 14b the phase developed during the positive lobe cancels out the phase developed during the negative lobe for stationary spins. For moving spins, however, the developed phase does not cancel out because they experience a different gradient, and therefore a different phase shift, due to their change in location. The developed phase is an indication of the velocity of the spins. The mathematics to generate a velocity encoded image are presented next.

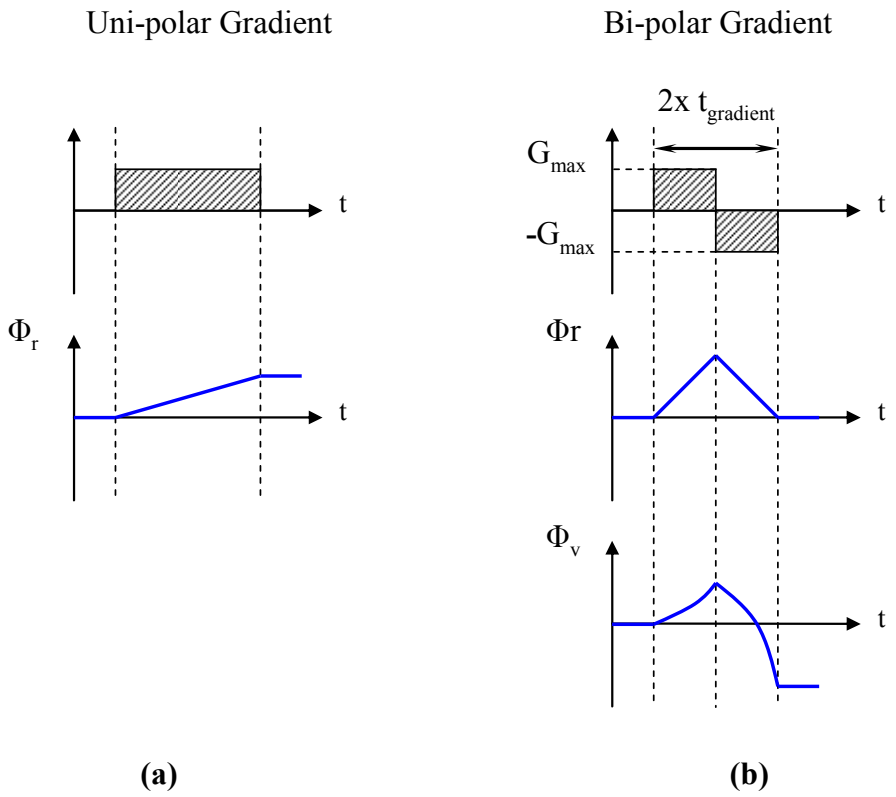

Figure 14. When spins do not have any dynamic components, a uni-polar gradient is used to encode their position (a). By applying a bi-polar gradient (b), phase accumulation from stationary components is eliminated and non-stationary spins will have a velocity dependent phase shift.

For a rectangular bi-polar gradient with amplitude G_{max} and total pulse duration of $t_{gradient}$ the phase change

$$\phi_{MR}(\mathbf{r},t) = -\gamma\,\mathbf{v}_0(\tau)\,G_{max}\,t^2_{Gradient} \tag{35}$$

of a nucleus moving with speed v_0 follows from (31). The maximum velocity

$$V_{max} \le \frac{\pi}{\gamma\,G_{max}\,t^2_{Gradient}} \tag{36}$$

can be calculated from the above equation noting that the allowable phase change for unambiguous measurement has to be $-\pi < \Phi_{MR} < \pi$. Ideally, if a bi-polar velocity encoding gradient is applied along one of the spatial axes, the velocity component in the same direction can be estimated [12, 29] in a single experiment. In practice, this is not feasible due to errors induced by eddy currents and other sources of phase error. Therefore, two acquisitions each with a different first moment $M_1(t)$ are applied to make accurate velocity estimates. If the phases of the reconstructed images are subtracted the velocity image is acquired. The subtraction process also removes the common mode errors due to eddy currents and other sources of error. This technique is known as the phase contract (PC) MR. The basic concept of PC imaging is to superimpose the velocity-encoding gradients onto the basic imaging sequences, such as SE and GRE, that were described in 1.4.8 and to reconstruct a series of velocity encoded images [30]. Various velocity encoding gradient (VEG) configurations and encoding technique exist to encode velocity in all spatial direction which are covered in [15]. An example velocity encoding sequence is shown in Figure 15 where a GRE imaging sequence is used along with a velocity-encoded gradient in a single direction. First, a slice is excited by the 90° pulse and the slice selection gradient, G_{slice}. The phase and frequency encoding are exactly as explained for the standard GRE imaging. Two velocity encoding gradients (VEG) were applied in the slice selection direction to detect flow perpendicular to the cross-sectional slice. In the first iteration of this pulse sequence, VEG1 is applied and the MR data is recorded for a single phase encoding step. Then, for the same phase encoding step, VEG2 is applied and the data is recorded. This process is repeated until all the phase encoding steps are complete and the entire k-space can be covered.

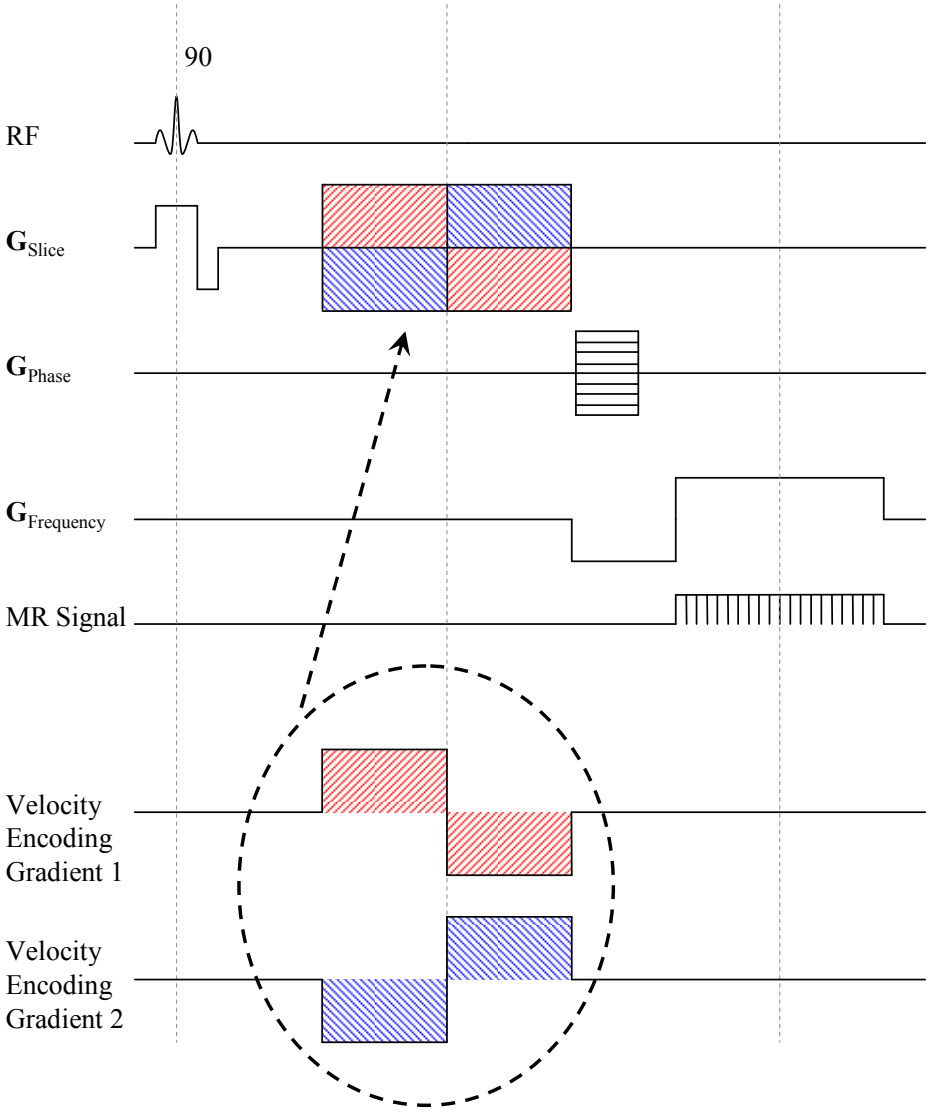

Figure 15. Gradient recalled echo (GRE) velocity encoding imaging sequence. The experiment is repeated twice: first using VEG1 and then VEG2.

The signal equation

$$\text{Signal}_{\text{2D-Slice-Velocity}}(\mathbf{k}_{(t)}) = \int_x \int_y M(x,y) e^{-j\left[k_x(t)x + k_y(t)y\right]} e^{-j\phi_v} dxdy \tag{37}$$

for a velocity encoded image is derived from (24), (34). After taking an inverse 2D Fourier transform the resulting image becomes

$$I(x,y) = FT^{-1}\left(\text{Signal}_{\text{2D-Slice-Velocity}}(\mathbf{k}_{(t)})\right), \tag{38}$$

$$I(x,y) = M(x,y) e^{-j\phi_v}. \tag{39}$$

A velocity dependent phase shift appears in the image that is independent of the GRE sequence. The velocity parameter can be extracted by subtracting the phases

$$\Delta\phi_{MR} = \measuredangle\left[I_1(\mathbf{r})\right] - \measuredangle\left[I_2(\mathbf{r})\right] = \phi_{v,1} - \phi_{v,2} \propto v_0(\tau) \tag{40}$$

of the two images to find the velocity component

$$\Delta\phi_{MR} \propto v_0(\tau). \tag{41}$$

Many other techniques exist to acquire velocity component in all spatial directions [12, 15].

1.4.10 Limitations of MRI Techniques

The limitations of MRI techniques are in terms of materials that can be present in the sample to be imaged and the resolution limitations due to signal to noise ratio and the performance of the experimental instrumentation.

A central limitation for any magnetic resonance imaging instrument is that no ferromagnetic material can be present in or even close to the sample for proper imaging. In addition, the amount of conductive material in the sample volume must be limited for successful imaging. Due to thed pulse nature of MRI techniques, the magnetic field becomes distorted by the eddy currents that are generated in the conductive material close or inside the sample.

The dominant and fundamental limiting factor for high resolution microscopy is the signal-to-noise ratio. Various formulas to estimate SNR, following a 90° flip, exist in the literature [36] the most accepted one is given by Abragam [37]

$$\mathrm{SNR} = \frac{K\eta M_0}{NF_R}\left(\frac{\mu_0 Q\omega_0 V_C}{4k_B T_C \Delta f}\right)^{1/2}, \tag{42}$$

where K is a numerical factor close to unity that depends on the coil geometry, η is the filling factor, V_C is the coil volume, Q is the quality factor, T_C is the temperature of the probe, Δf is the bandwidth of the receiver and NF_R is the noise factor of the receiver (a measure of how much noise is introduced by the receiver itself). Assuming the instruments and the sample are at room temperature, using (6) the SNR is re-written as

$$\mathrm{SNR} = \left(\frac{K \cdot n_v \gamma \hbar^2 \mu_0^{1/2}}{4k_B T_R}\right) \cdot \left(\frac{\omega_0^{3/2} \cdot V_s^2 \cdot Q^{1/2}}{NF_R \cdot V_c^{1/2} \cdot \Delta f^{1/2}}\right) \tag{43}$$

The variables in the first bracket are mostly physical constants while the variables in the second bracket are defined by the properties of the instrument and components. The most important design variable that affects the SNR is the frequency term which is defined by the magnetic field strength. In other texts, even a higher dependence ($\omega_0^{7/4}$) has been suggested [38, 39] due to inter-dependence of variables of (43). Once the magnetic field is known, SNR can be optimized

by a coil with a small enough volume, *Vc,* to encapsulate the sample *Vs*. The smaller the sample, the less spins exist, and the smaller the signal becomes. The receiver has to have minimal noise factor NF_R and the coil should have the largest practically feasible quality factor. The receiver bandwidth has to be chosen carefully to match the expected frequencies from the chosen pulse sequence. Another way to increase SNR is to average the received MR signal. SNR is proportional to the square root of the number of averages.

The definition of a coordinate system for a fluidic sample that is flowing inside a tube with the diameter $D_i = 2 \cdot L_y$ is shown in Figure 16. The tube is along the x-axis (left of Figure 16) and the cross-sectional view (right hand side of Figure 16) is shown in the z-y plane.

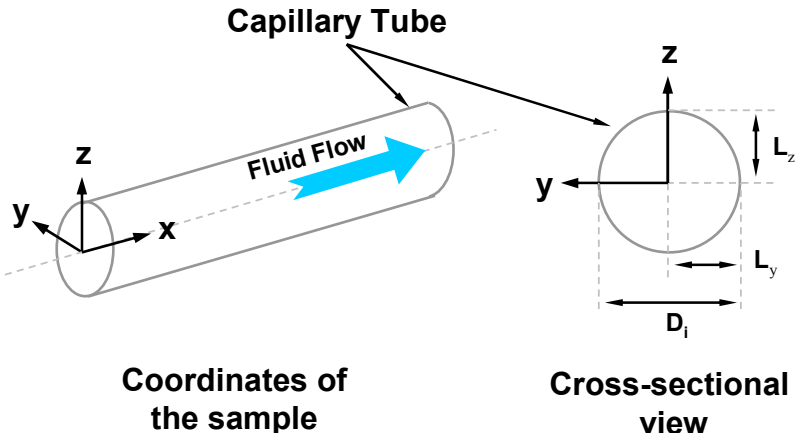

Figure 16. Definition of the coordinate system.

For static imaging of a sample shown in Figure 16, the limiting factors in terms of positional accuracy can be calculated by differentiating the Larmor equation (18) as

$$x = \frac{1}{G_x}\left(\frac{\omega}{\gamma} - B_0\right)$$

$$\Delta x \geq \left|\frac{\partial x}{\partial B_0}\Delta B_0\right| + \left|\frac{\partial x}{\partial G_x}\Delta G_x\right| + \left|\frac{\partial x}{\partial \omega}\Delta\omega\right| \tag{44}$$

$$\Delta x \geq \frac{1}{G_y}\Delta B_0 + L_y\frac{\Delta G_y}{G_y} + \frac{1}{\gamma G_y}\Delta\omega \tag{45}$$

For high resolution, (45) requires high field homogeneity, large gradients with good linearity, and sensitive distinction of signals that have comparable frequencies.

The other fundamental limiting factor comes from the uncertainty principle [28] which states that

$$T_{acq} \geq \frac{1}{\Delta\omega}. \tag{46}$$

This principle can be re-written as

$$\Delta x \geq \frac{1}{\gamma G_x T_{acq}} \tag{47}$$

where the acquisition time is T_{acq}. Equation (47) calls for large gradients with minimal acquisition times.

For accuracies of better than tens of microns, diffusion also becomes a limiting factor which is given by [40]

$$\Delta x \geq \sqrt{2DT_{acq}} \tag{48}$$

where a typical diffusion constant of water at room temperature is $D = 2\cdot10^{-9}$ m^2/s. Equation (48) indicate that the acquisition time must be minimized so that diffusion is not the limiting factor of

spatial resolution. Another important point is that a trade-off that exists between (47) and (48) where the optimal value for the acquisition time can be calculated.

The nominal resolution of the image

$$\Delta x = \frac{D_i}{N_{samples}} \tag{49}$$

is also dependent on the sample size, and the number of phase and frequency encoding steps, $N_{samples}$. A trade-off exists between the selected field-of-view that defines the largest sample that can be imaged and the resolution for a given imaging time. A higher resolution necessitates a smaller FOV for a given imaging time.

The resolution for velocity encoded images, if the PC techniques are used, can be derived from (31) where the developed phase of a moving nucleus is

$$\Phi_{MR} = -2\pi\gamma G_x \tau^2 V_\tau. \tag{50}$$

The velocity accuracy

$$\Delta V = \left|\frac{\partial V}{\partial \Phi_{MR}}\Delta\Phi_{MR}\right| + \left|\frac{\partial V}{\partial G_x}\Delta G_x\right| \tag{51}$$

$$\Delta V = \frac{1}{2\pi\gamma G_x \tau^2}\Delta\Phi_{MR} + \frac{\Phi_{MR}}{2\pi\gamma G_x^2 \tau^2}\Delta G_x \tag{52}$$

is found by differentiating (50). To minimize the velocity errors the above equations indicate that large gradients with high linearity must be applied for a long pulse duration τ. Furthermore, it is necessary to increase the phase encoding steps such that the phase error $\Delta\Phi_{MR}$ is minimized.

It is also worth mentioning the maximum velocities that can be detected using PC techniques in

MRI. One limitation is in terms of maximum phase shift found from (36) is given as

$$V_{max} \leq \frac{\pi}{\gamma G_x \tau^2},$$

which can be corrected for to some extent in software [41]. The second limitation is related to the length of the detection coil $L_{Receiver}$. If the flow is faster than

$$V_{max} < \frac{L_{Receiver}}{TE} \tag{53}$$

the excited slice moves out of the detection area and therefore the MR signal is lost. TE is the echo time.

Chapter 2 - Components of the High-Resolution MRI

2.1 Magnet

The requirements, design, and characterization of the magnet are described in the following section.

2.1.1 Magnet Requirements

Important characteristics of a magnet for magnetic resonance applications are: the magnetic field strength, homogeneity, temporal stability and access.

Field Strength: The signal-to-noise ratio, SNR, is proportional to the Larmor frequency as

$$\mathrm{SNR} \propto \omega_0^{\alpha} \tag{54}$$

where, $\omega_0 = \gamma B_0$, which increases rapidly as the magnetic flux density B_0 is increased ($^3/_2 < \alpha < {}^7/_4$).

Homogeneity: The decay of the MR signal is dominated by the T_2* time constant

$$T_2^* \approx \frac{1}{\gamma \Delta B_0} \tag{55}$$

which has to be maximized by reducing the flux density variations ΔB_0 in the volume of interest. This is equivalent to improving the homogeneity, $\Delta B_0/B_0$ of the magnet. In addition, the accuracy of the spatial localization

$$\Delta x_{\mathrm{homogeneity}} = \frac{1}{G_x} \Delta B_0 \tag{56}$$

is dependent on the homogeneity as described in Chapter 1.4.

Temporal Stability: There are two reasons why the magnetic field needs to be stable. One is related to using averaging to increase the SNR of the MR signal from a large number of acquisition cycles. This is only possible if the magnetic field is stable over the whole imaging time. The second reason is that even if no averaging is employed, the image may get distorted if the magnetic field fluctuates for two consecutive but slightly different (e.g., phase incremented) pulse sequences.

Access: The gap or bore of the magnet has to be sufficiently large to accommodate the sample, gradient and RF coils.

2.1.2 Magnet Design

Resistive, superconducting and permanents magnets are the three main types of magnets used for MRI.

Resistive magnets, or electromagnets, generate the magnetic field using a coil through which a current is driven. The magnetic flux return path can be air or magnetic material. Typical whole body MRI scanners have flux densities less than 0.4 T. A constant large amount of electrical power (typically 50 kW) is required to maintain the field. Most of the power is dissipated in the windings as heat necessitating elaborate cooling systems. The field homogeneity and temperature stability is relatively poor compared to superconducting magnets. This is because the variation of the field is limited by the current regulation of the power supply in an electromagnet; whereas the power supply is disconnected from a superconducting magnet after it is energized. Advantages of resistive magnets include the ability to be switched off easily, lower fringe fields compared to superconducting magnets and better temperature stability compared to permanent

magnets. Electromagnets have much lower capital and operating cost than superconducting magnets [13, 30].

In ***Superconducting magnets***, the coils are made of superconducting materials which have zero resistance at cryogenic temperatures. As long as the windings are kept below their critical temperature (between 1.9 to 70 °K), the current flow producing the magnetic field continues without application of electrical power. These magnets can produce fields up to 11 T for animal and small sample imaging and between 0.5 T to 3.0 T for whole body human imaging. Superconducting magnets offer superb homogeneity and stability (temporal and temperature). The disadvantages include high capital and operating cost [13, 30] (due to cryogenic liquid boil off), large fringe fields (which requires a magnetically shielded room), and their large size and weight. In addition, the magnetic field cannot be turned off easily because of the large energy stored inside magnetic field.

Permanent magnets are constructed from magnetized hard magnetic material such as AlNiCo, Samarium-Cobalt and most recently Neodymium-Iron-Boron. Magnetic fields up to 0.4 T have been used for whole body imaging, but for imaging of smaller volumes fields up to 1.0 T for imaging have been demonstrated [42]. Permanent magnets are lower cost when compared to superconducting and resistive magnets in terms of capital and operating costs. They occupy less space and weigh less for low to mid fields compared to the other magnets including their accessories (refrigeration system for superconducting magnets and cooling system for electromagnets). The fringe fields are less than superconducting magnets thus no magnetically shielded room are required. On the other hand, permanent magnets have poor homogeneity and temperature stability as the magnets have a large temperature coefficient.

The choice of the MRI magnet is application dependent. If the highest field, best homogeneity and temporal stability with a large access are desired the superconducting magnets would be the only choice. The trade-off here is cost and the required space for installing the magnet. If cost is an issue and lower field, poorer homogeneity and stability can be tolerated, then an electromagnet is suitable when a variable field is desired. The trade-off here is the cost associated with operating the cooling unit and supplying the electrical power. Permanent magnets are chosen when a variable field is not necessary. In that case permanent magnets are preferred to electromagnets as they occupy less space, require no electrical energy to generate the magnetic field, cost less, and have a larger access. However, the performance in terms of temperature stability is poorer than other magnets. The advantage and disadvantages of the various magnets is summarized in Table 2.

Table 2. Advantages and disadvantages of magnets used for MRI.

	Resistive Magnet	**Superconducting Magnet**	**Permanent Magnet**
Advantages	• **High magnetic fields** • **Variable field** • **Good homogeneity**	• **Very high magnetic fields** • **High homogeneity** • **Superb temporal stability** • **Large access**	• **Low capital cost** • **No operating cost** • **Large access**
Disadvantages	• **High capital cost** • **High operating cost** • **Size**	• **Very high capital cost** • **High operating cost** • **Size** • **Not easily turned off**	• **Moderate magnetic fields** [43] • **Poor temperature stability** • **Poor homogeneity** • **Always ON**

Permanent magnets are the ideal choice for this work because

- the goal is to demonstrate a prototype of a *desktop* MRI instrument that is relatively *inexpensive*.

- the samples to be imaged (microfluidic chips) are of relatively small size. Therefore, it is possible to generate high fields with permanent magnets for smaller gap sizes. Therefore, the magnetic field for this work will be on permanent magnets.

2.1.2.1 Permanent magnets: magnetic materials

The relationship between magnetic field strength (H) and magnetic flux density (B) is shown in terms of a hysteresis (BH) curve as shown in Figure 17. Magnetic materials are characterized by the second quadrant of the intrinsic hysteresis curve. In Figure 17, B_r is the residual magnetic flux density, H_c is the coercivity field and H_{ci} is the intrinsic coercivity.

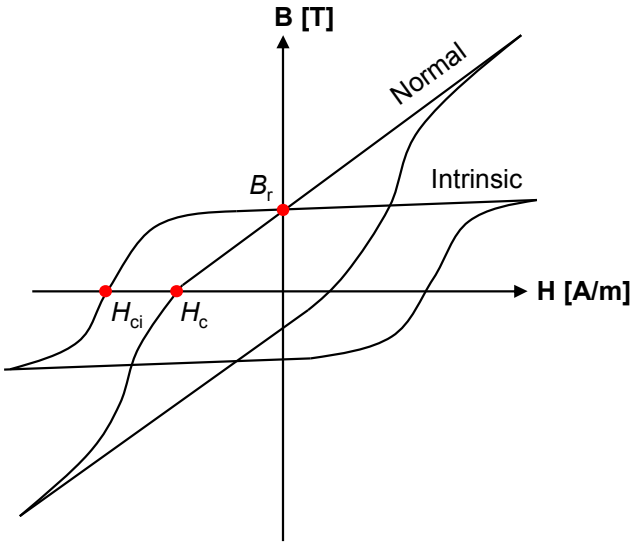

Figure 17. Magnetic materials are characterized by their intrinsic and normal B-H hysteresis curves.

The two types of magnetic material are soft and hard magnetic materials. Hard magnetic materials have a much larger H_c (> 700 kA/m) value than soft magnetic materials (H_c < 100 kA/m). Therefore, a hard magnetic material retains its magnetism after being magnetized, whereas a soft magnetic material looses most of its residual magnetism after the magnetizing field is removed. Permanent magnets are made of hard magnetic materials which retain their magnetization after being magnetized. A summary of permanent magnetic material and typical properties is listed in Table 3. The performance of permanent magnetic material is reported in terms of their energy per unit volume BH_{max}. As seen in Table 3, NdFeB materials have the highest energy density per unit volume compared to other materials. The temperature coefficient parallel to the magnetization direction of the hard magnetic material $\alpha_{parallel}$ is given as a percentage per unit temperature. A high temperature coefficient results in poor temperature stability of a permanent magnet as it will become very sensitive to temperature fluctuations. Unfortunately, the NdFeB material has one of the highest temperature coefficients compared to

other permanent magnetic material.

Table 3. Properties of commonly available hard magnetic material [44]**.**

	Ferrite (Ceramic 8)	**AlNiCo (Alnico 5)**	**SmCo (REC-26)**	**NdFeB (HS-42AV)**
B_r [T]	**0.4**	**1.25**	**0.9**	**1.31**
H_{ci} [kA/m]	**262**	**51**	**1,600**	**1,110**
$(BH)_{max}$ [kJ/m^3]	**30**	**43.8**	**159**	**334**
$\alpha_{parallel}$ [%/°C]	**-0.18**	**-0.02**	**-0.05**	**-0.12**

Soft magnetic materials are used for the flux path of the magnetic configurations because of their high relative magnetic permeability μ_r. The relative magnetic permeability is the slope of the intrinsic curve of the magnetic material in the BH diagram. A steeper slope corresponds to a larger μ_r. The leakage of a magnet can be reduced by selecting a soft magnetic material with a high μ_r as described later. A summary of soft magnetic material suitable for application with static magnetic field with their typical magnetic properties is listed in Table 4. The saturation limit of each material is indicated by the $B_{saturation}$ value.

Table 4. Properties of commonly available soft magnetic material (Annealed 1 mm thick stamped sheet). [45].

	Iron	Silicon-Iron Alloy (TRAFOPERM N3)	Nickel-Iron Alloy (PERMENORM 5000 V5)	Cobalt-Iron Alloy (VACOFLUX 50)
Initial μ_r	**1,000**	**1,000**	**9,000**	**1,000**
Max μ_r	**4,000**	**3,000**	**135,000**	**9,000**
H_c [kA/m]	**<0.05**	**0.02**	**0.004**	**0.14**
$B_{saturation}$ [T]	**2.2**	**2.03**	**1.55**	**2.35**

Nickel-Iron alloys have extremely high relative permeability with high magnetic flux saturation limits which make them ideal as pole materials. The thickness of these materials is limited to around 2 mm and must be annealed at 1200 °C in presence of a pure hydrogen gas after machining [46]. These relatively expensive specialized materials may not be available in small quantities or in specific shapes. Low-carbon steel (or iron) is a much less expensive and readily available soft magnetic material and has a relative magnetic permeability of about 4,000 with a saturation limit of 2.2 T.

2.1.2.2 Geometric configurations of magnetic circuits using permanent magnets

Two main types of permanent magnetic configurations exist: Iron-cored and Halbach.

The Iron-cored magnetic configuration is a classical design where the magnetic flux passes through the permanent magnets, two opposing poles (making the air gap) and the yoke (flux return path). The yoke, and especially the poles, must be made of soft magnetic material preferably with high relative magnetic permeability. For MRI applications the C-shaped and H-

shaped magnets are used for their superior homogeneity and relatively open access. Various C-shaped configuration of the soft and hard magnetic material exist, a selection of which were simulated for the purposes of this work are depicted in Figure 18.

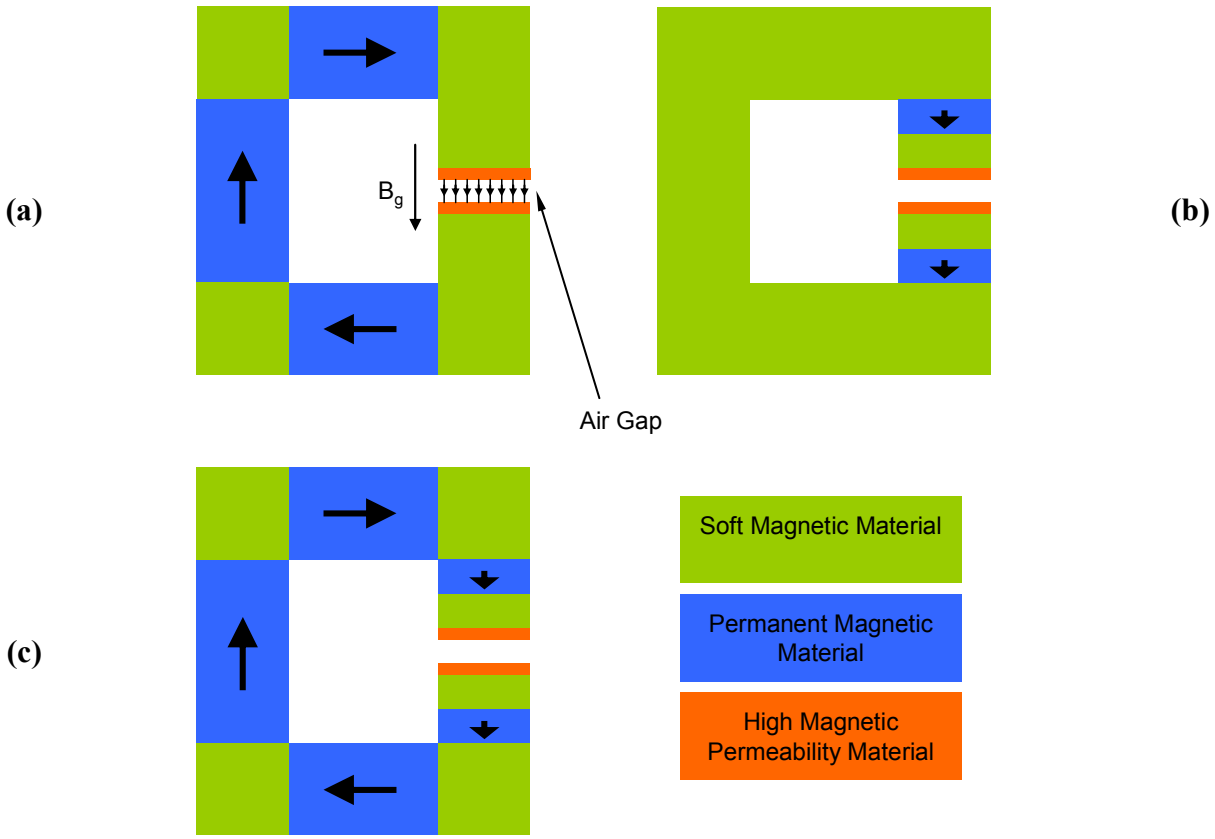

Figure 18. C-shaped permanent magnet configurations. The leakage is highest for (a) and the field is highest for (c).

The direction of magnetization of the hard magnetic material (permanent magnets) is indicated by an arrow (tail: S, tip: N). The return path (i.e., the yoke) is made of soft magnetic material such as low carbon steel. The poles are also made of soft magnetic material with high permeability such as Nickel-Iron (49%) for increased homogeneity.

The magnet efficiency

$$n_L = \frac{\phi_{gap}}{\phi_{Total}} \tag{57}$$

is a figure of merit for magnets where Φ_{gap} [Wb] is the flux traveling through the air gap and Φ_{Total} [Wb] is the total magnetic flux produced by the permanent magnets. The total magnetic flux can be calculated as explained later in this chapter. The magnet efficiency n_L depends on a number of factors including the geometric configuration and the gap ratio of the gap width to the cross-sectional area. Magnetic efficiencies can only be estimated using empirical data which were not available to the author; therefore, the magnet efficiencies were estimated using simulations. In the C-shaped configurations in Figure 18, n_L increases as poles are placed closer together and the air gap decreases. If the magnets are placed very close to the air gap, however, the homogeneity is compromised. To achieve highest magnetic flux density for a given gap size, configuration in Figure 18c is preferred.

H-shaped magnets are very similar to C-shaped magnets except that the return path is symmetric which results in simpler overall mechanical design. The cases that were simulated for the purposes of this work are shown in Figure 19. The lowest magnetic flux density is generated by the configuration shown in Figure 19a; also this configuration has the lowest efficiency n_L. The magnetic flux density is highest for Figure 19c. Configuration Figure 19b has comparable magnetic flux density to the one shown in Figure 19c, and has a much simpler mechanical design. The homogeneity of H-shaped configurations is higher than C-shaped ones because of their symmetry in design. Also due to their symmetry, H-shaped magnets are less susceptible to variations in room temperature as the geometrical changes due to temperature are symmetric. It

was observed in the simulations that the homogeneity of the configuration shown in Figure 19a was better than the homogeneity of the magnetic configuration shown in Figure 19b and Figure 19c, because the magnets are further away from the poles.

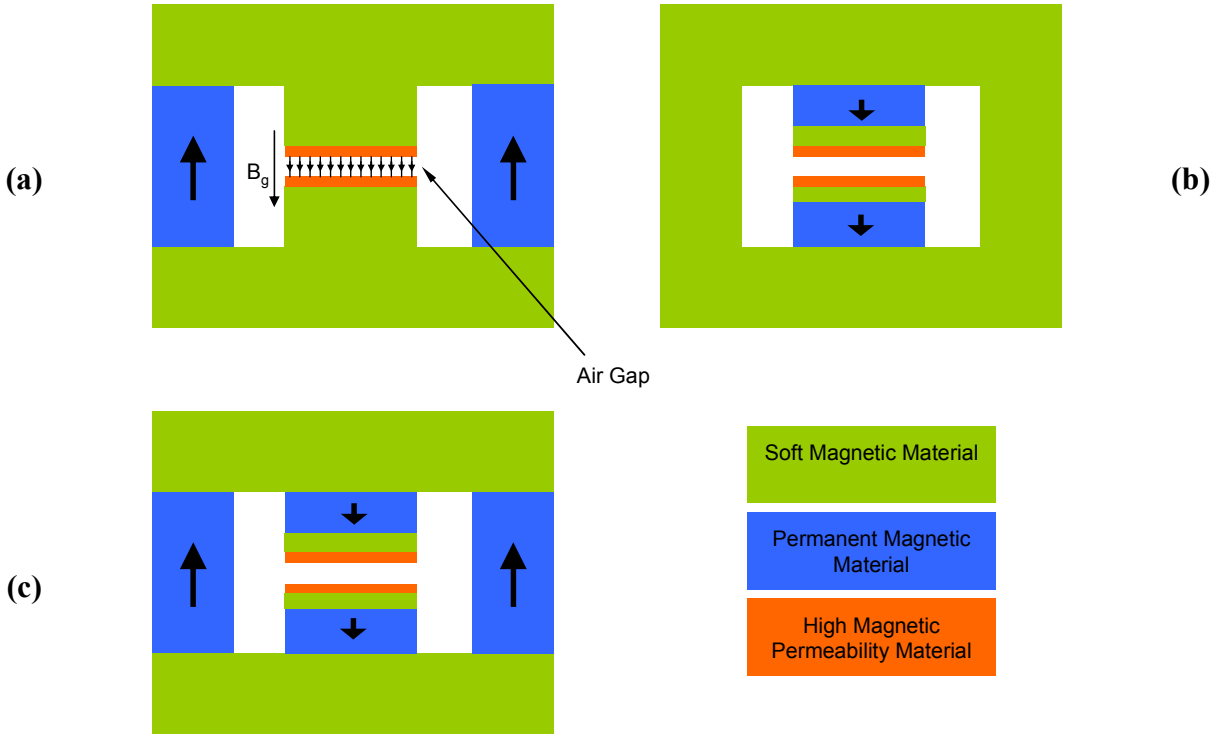

Figure 19. H-shaped permanent magnet configurations. The leakage is highest for (a) and the field is highest for (c).

The other category of permanent magnetic configuration is the Halbach cylinder design (see Figure 20). To generate a dipole field only a special case of the Halbach is considered [47]. Basically, the magnetic material surrounds the air gap and is ideally magnetized in such a way to create a homogenous magnetic field in the air gap. In practice, the magnetization pattern is approximated by number of discrete permanent magnets. The greater the number of the permanent magnets, the better the approximation resembles the ideal case Figure 20a. Halbach

magnets have the potential to generate much higher fields than iron-cored magnets. The homogeneity is usually less than iron-cored magnets and access to the air gap is very limited. The discrete components can be a number of magnetized rods that extend out of the page (Figure 20-b, Figure 20-d) and are rotated to resemble the magnetization of that of an ideal Halbach pattern. Alternatively, the discrete components can be of shapes that do not extend all across the magnet (Figure 20-c, Figure 20-e). The discrete magnetized blocks are assembled in stacked rings to cover the out-of-page dimension. Simulations of Halbach designs were not performed in this work.

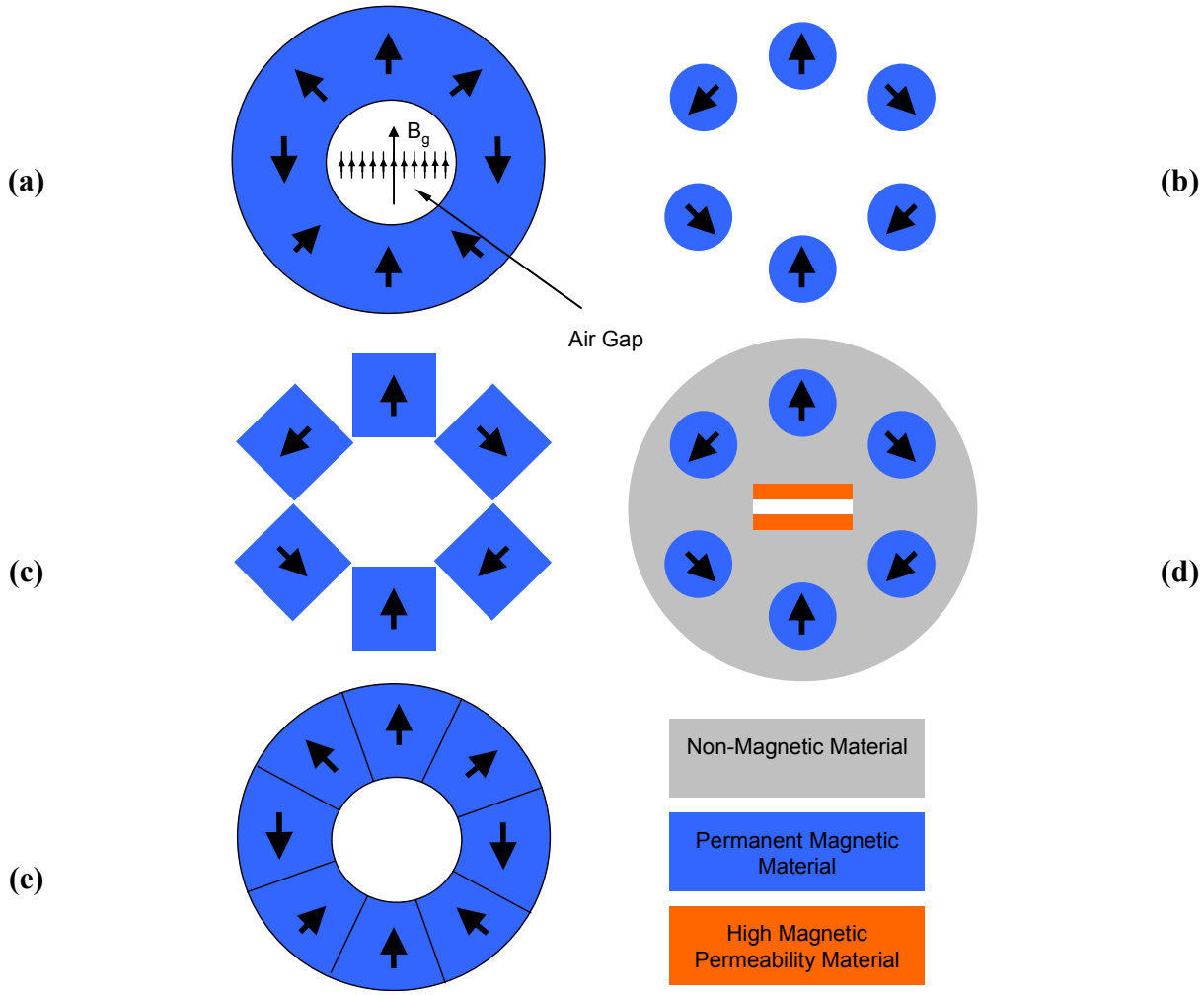

Figure 20. Halbach permanent magnet configurations. Ideally a hard magnetic material is magnetized as seen in (a). Due to practical limitations, the magnetization pattern is approximated by discrete magnets (b-e). Materials with high magnetic permeability can be used to in crease homogeneity (d).

2.1.2.3 Prior art on Permanent Magnets for MRI Applications

A summary of available magnets from MRI manufacturers is given in Table 5 for comparison. Most whole-body imaging machines have a homogeneity between 5-50 ppm and a field of view of typically 400 mm in one dimension. The temperature stability is usually better than 0.1 ppm/hour.

Table 5. Clinical whole-body MRI permanent magnets available as of 2008.

Company	Product	B [T]	Size [m x m x m]	Weight [tonnes]
Siemens	Magnetom Concerto	0.2	2.3x2.1x1.6	11
	Magnetom C	0.35	2.3x2.1x1.6	16
General Electric	Signa Profile	0.2	2.3x2.1x1.6	10
	Signa Ovation Excite	0.35	2.1x2.6x2.2	19
Hitachi	AIRIS Elite	0.3	0.8x1.1x0.73	15
	AIRIS II	0.3	0.8x1.1x0.73	15
	MRP-7000	0.3	NA	NA
Millennium Tech Inc.	Virgo	0.35	2.1x1.4x2.1	17

In terms of the prior art on permanent magnets, there is great deal of information available regarding the design and the experimental results for magnets that are used for research purposes. This is not true, however, for magnets used in clinical MRI instruments manufactured by private companies. Therefore, the literature review presented here is mostly gathered form

academic searches and patents.

Permanent magnets for clinical applications: An iron-cored H-shaped magnet made of NdFeB material, for whole-body imaging, with a field of 0.2 T homogeneity of 30 ppm over 350mm diameter-spherical-volume (DSV) that weighs 9,000 kg is given by Miyamoto *et al.* [48]. Another H-shaped iron-cored low-field PM is given by Kose *et al.* [49] for imaging of the Trabecular Bone. The reported field is 0.21 T, 50 ppm homogeneity over 120mm DSV and a gap of 160 mm. The magnet weighs approximately 500 kg and is installed in a 2 m by 2 m space. An iron-cored PM for human head surgery is presented by Katznelson *et al.* [50]. This patent describes the design of a magnet with a field of 0.1 T, homogeneity of 10 ppm and a field-of-view (FOV) of 200 mm DSV. A patent filed by Lee *et al.* [51] for whole-body imaging apparatus describes a Halbach configuration with design objectives requiring minimum 0.1 T field, variation of over a DSV of 400 mm less than 0.5 mT and stability no worse than 5 ppm/s.

Permanent magnets with smaller footprint (i.e., miniature magnetic resonance machines imaging [52]) are also used for imaging extremities in clinical setting, animal research, spectroscopy and flow.

Halbach designs: The design and construction of a 0.31 T Halbach NdFeB magnet consisting of multiple rings for applications in NMR spectroscopy is presented by Raich *et al.*[47]. The homogeneity is 700 ppm over 18 mm DSV with a gap of 73 mm. A Halbach configuration for spectroscopy application with a field of 0.6 T, homogeneity 42 ppm over an air gap region of 3 mm x 3 mm x 5 mm is presented by Moresi *et al.* [53]. The permanent magnet material is $SmCo_{17}$ and the pole pieces are constructed out high permeability material ($\mu_r > 10{,}000$). The magnet is a cylindrical in shape with a diameter of 0.09 m and length of 0.23 m. The temperature

stability of the magnet is a reported -300 ppm/°C. Another Halbach permanent magnet is made for imaging mice by Shirai *et al.* [42]. They report a magnetic field of 1.0 T with 10 ppm homogeneity over 30 mm DSV. The magnet is approximately 980 kg with dimensions of 0.58 m (W) x 0.48 m (H) x 0.52 m (L) for the magnet and gap of 24 cm (W) x 9 cm (H) x 48 cm (L). The temperature sensitivity of this magnet was -1200 ppm/°C which is compensated for using an NMR lock. Multiple Halbach magnets are described by Kumada *et al.* [43, 54, 55], which are not specifically designed for MRI applications, have demonstrated fields exceeding 6 T for a 2 mm gap. The magnets weigh approximately of 340 kg. The homogeneity is worse than 4000 ppm with little room for any field corrections.

Iron-cored designs: A desktop iron-cored C-shaped PM out of NdFeB magnetic blocks was designed by Wright *et al.* [56-58] with a magnetic field of 0.21 T with a 100 mm gap and homogeneity of 20 ppm over approximately 7 mm DSV. The approximate dimension of this magnet is 0.2 m (W) x 0.41 m (H) x 0.2 m (L). A H-type magnet for educational purposes with a field of 0.08 T, homogenous region of 10 mm DSV and a gap of 44 mm is made by Sahakian *et al.*[59] using off-the-shelf NdFeB PM blocks. The size of the magnet is approximately 0.13 m (W) x 0.13 m (H) x 0.25 m (L). An H-shaped desktop PM for MRI purposes was designed by Kose *et al.* [49] with a field of 1.02 T, homogeneity of over 150 ppm 3 mm DSV and weight of 1.7 kg. The magnet was found useless due to the poor homogeneity performance. Permanent magnets have been also developed for the food industry one of which is described by Li *et al.* [60]. They report the design of an NdFeB H-type PM with a field of 1.3 T, homogeneity of 92 ppm over 80 mm with dimensions of 0.3 m (W) x 0.05 m (H) x 0.2 m (L). An iron-cored 1.0 T PM made out of NdFeB material is constructed by Haishi *et al.* [61]. The reported air gap is 61 mm with homogeneity of 12 ppm over a 20 mm DSV. The dimensions of the magnet are

0.62 m (W) x 0.75 m (H) x 0.75 m (L) and it weighs 1,400 kg. The pole pieces are made of silicon steel plates that have radial cuts on them to suppress eddy currents from the switching gradients. The reported temperature coefficient for the magnet is -1200 ppm/°C which makes imaging practically impossible if no corrections where made during the imaging sequence. This problem was rectified by implementing a NMR lock to correct for the shift in resonance frequency.

As for the development of magnets, Podol'skii [62-64] compares magnetic configurations for different applications including the Halbach, iron-cored, and a hybrid called the novel magnet system (NMS). The results suggest that depending on the application different magnets are suitable. For example, the Halbach design is more weight efficient for higher fields but is more complex to manufacture and it is more sensitive to temperature variations. In a similar study [65] where Halbach and C-shaped iron-cored magnets are compared, the results suggests that iron-cored weigh less compared to other magnetic configurations in applications requiring a large cross-sectional gap with a shorter gap length. In addition, the assembly and manufacture of iron-cored magnets is significantly simpler than Halbach designs.

A number of research groups [66-68] have focused on optimizing the pole shapes of the magnets to correct for coarse inhomogeneities. As a first prototype only simple pole shapes have been considered in this work.

2.1.2.4 Theory and Basic Calculations

Two permanent magnetic configurations were designed and tested in this work. iron-cored permanent magnetic configurations were chosen because of their:

- simpler design, construction and assembly
- larger access (more open design than Halbach magnets)
- lower cost (magnet are purchased off the shelf)

Magnetic configurations are analyzed using their equivalent magnetic configuration. Detailed information about this section is described in elsewhere [69, 70]. Table 6 presents the electrical circuit analogy to the magnetic circuits.

Table 6. Electrical and magnetic circuit analogy.

Electrical Circuit Parameter	Magnetic Circuit Parameter
Electromotive Force (Voltage), EMF	**Magnetomotive Force (F_m), MMF**
Resistance, *R*	**Reluctance, R**
Current, I	**Flux, Φ**

The flux

$$\Phi = \frac{H\ell}{R} = B \cdot A \tag{58}$$

of a magnet is found by calculating the reluctance

$$R = \frac{\ell}{\mu_0 \mu_r A} \tag{59}$$

where *l* and A refer to the length and cross-sectional area of the material. The magnetic permeability of free space μ_0 (= $4\pi \cdot 10^{-7}$ N/A^2) and relative magnetic permeability of the material

μ_r are constants.

If the magnetic material has relatively linear characteristics (such as NdFeB material) in the second quadrant of its BH curve, it can be modeled as a voltage source with a series resistor as shown in Figure 21.

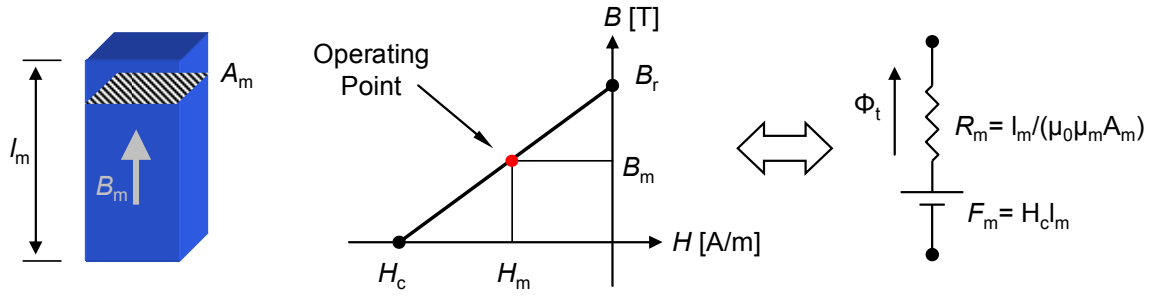

Figure 21. A permanent magnet can be modeled as a voltage source F_m with an internal resistance R_m.

The equivalent voltage and resistance of a permanent magnet can be calculated by knowing the material properties (the intrinsic BH curve) and the geometry. For example, a single NdFeB permanent magnetic block with an area, A_m, of 51 mm x 51 mm, a length l_m of 25.4 mm and coercive field H_c = 1100 kA/m can be modeled as a voltage source with an magnetomotive force of

$$F_m = H_c l_m = 110 \cdot 10^3 \cdot 25.4 \cdot 10^{-3} \approx 2800 \quad \text{A}, \tag{60}$$

and a resistance of

$$R_m = \frac{l_m}{\mu_0 \mu_m A} = \frac{25.4 \cdot 10^{-3}}{4\pi \cdot 10^{-7} \cdot 1.05 \cdot (51 \cdot 10^{-3})^2} = 7.4 \cdot 10^6 \quad \frac{\text{A}}{\text{Wb}} \tag{61}$$

where the typical relative magnetic permeability, $\mu_{m,}$ of a NdFeB magnet is 1.05. Therefore, the permanent magnet is modeled as

$$F = F_m - \Phi_t R_m . \tag{62}$$

With this technique the magnetic configuration of interest can be modeled. The specific magnetic configurations chosen in this work is depicted in Figure 22 along with their equivalent magnetic circuits. The magnetic flux path is represented by a dotted line Φ. The flux Φ_t is the total magnetic flux generated by the PM. The reluctances R_m, R_c, R_g, and R_l refer to the reluctance of the magnet, the iron core, the air gap and the leakage, respectively. A_c refers to the cross-sectional area of the iron core.

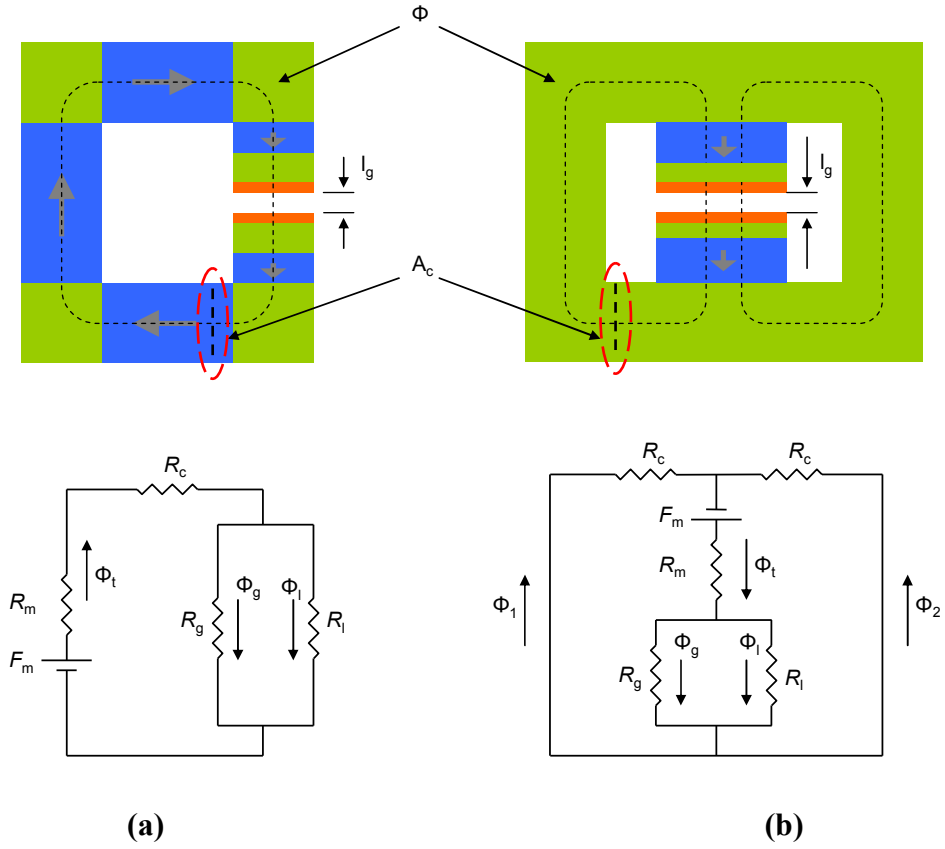

Figure 22. C-shaped (a) and H-shaped (b) permanent magnet configurations chosen for this work and their corresponding equivalent magnetic circuit.

The effective cross-sectional area of the air gap $A_{g\text{-effective}}$ is larger than the nominal area A_g as depicted in Figure 23, because the magnetic flux lines fringe away from the magnetic poles. As a rule of thumb, the effective area of the gap is increased by the length of the gap as shown in Figure 23. Saturation occurs when the magnetic flux density exceed the saturation flux density of the soft magnetic material. For example, a region of the magnet where saturation typically occurs is shown in Figure 23. Leakage of the magnetic flux lines mainly occurs as a result of these saturations.

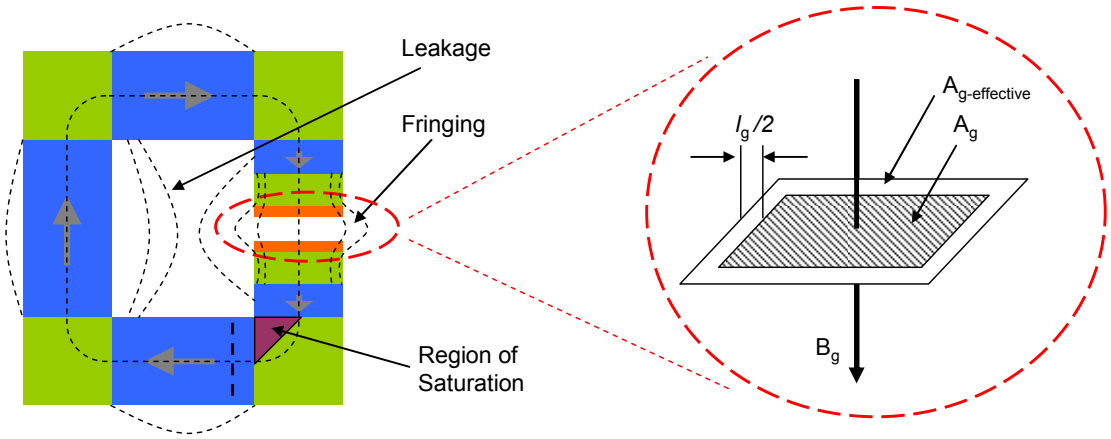

Figure 23. The fringe field and region of saturation of the C-shaped magnetic configuration along with its effective gap is shown.

Using (59), and assuming the reluctance of the iron core, R_c, to be negligibly small, the magnetic flux density at the gap, for all configurations, can be calculated

$$B_g = \mu_0 H_c \left(\frac{1}{\frac{1}{n_L} \times \frac{A_{g\text{-effective}}}{A_m} + \frac{l_g}{l_m} \mu_m} \right). \tag{63}$$

The leakage factor is complicated to model analytically and ranges between 2% - 91% according to Moskowitz [70]. Simulations of the selected configurations show a magnet efficiency between 40% - 85%. The C-shaped magnetic configuration similar to that shown in Figure 22a has a leakage factor about 47% according to simulations described later. According to (60) the magnetic flux density in the gap is then

$$B_g = B_r \left(\frac{1}{\frac{1}{n_L} \times \frac{A_{g\text{-effective}}}{A_m} + \frac{l_g}{l_m} \mu_m} \right) = 1.47\text{T} \left(\frac{1}{\frac{1}{0.47} \times \left(\frac{37\text{ mm}}{51\text{ mm}} \right)^2 + \frac{7\text{ mm}}{381\text{ mm}} 1.05} \right) = 1.29 \quad \text{T}, \tag{64}$$

, where the effective gap area is a square of length and width of 37 mm, the area of the magnet is a square of length and width of 51 mm , the gap length is 7 mm and the total magnet length is 381 mm. For an H-shaped magnet with a magnet efficiency of 68% (simulation is presented later) the magnetic flux density in the gap becomes

$$B_g = B_r \left(\frac{1}{\frac{1}{n_L} \times \frac{A_{g\text{-effective}}}{A_m} + \frac{l_g}{l_m} \mu_m} \right) = 1.32\text{T} \left(\frac{1}{\frac{1}{0.68} \times \frac{(144\text{ mm})^2}{(127\text{ mm})^2} + \frac{16.5\text{ mm}}{51\text{ mm}} 1.05} \right) = 0.59 \quad \text{T}, \tag{65}$$

where the effective gap is a disc with a 144 mm diameter, the area of the magnet is a 127 mm diameter disc , the gap length is 16.5 mm and the total magnet length is 51 mm.

2.1.2.5 Simulation of the selected magnetic configurations

To better estimate the maximum magnetic flux density and homogeneity inside the gap, selected designs were simulated in three dimensions using the AC/DC module of COMSOL MultiPhysics 3.3a. In addition multiple simulations were carried out to assess the sensitivity of a magnet to manufacturing tolerances. Pole plates out of material with high relative magnetic permeability were excluded in the final design to minimize cost. The final design of the C-shaped magnetic configuration is displayed in Figure 24 with the approximate dimensions. The 2” (W) x 2” (L) x 1” (H) permanent magnetic blocks are off-the-shelf NdFeB N50 grade

(strongest available) with a residual flux density of $B_r = 1.47$ T (Applied Magnets, 1111 Summit Avenue Suite #8, Plano, TX 75074, USA). The soft magnetic material is low carbon steel (AISI 1010)[1]. The poles are designed to be adjustable to correct for the parallelism of the poles faces due to manufacturing tolerances. The top pole pivots in the horizontal direction and the bottom pole pivots in and out of the page. Similar adjustment mechanisms are also described in [71, 72]. The air gap is approximately 7.5 mm in length and has a nominal dimension of 30 mm by 30 mm. The non-magnetic enclosure (Aluminum T6061) holds the magnetic pieces in place.

[1] Courtesy of George Clark for donating the soft magnetic material.

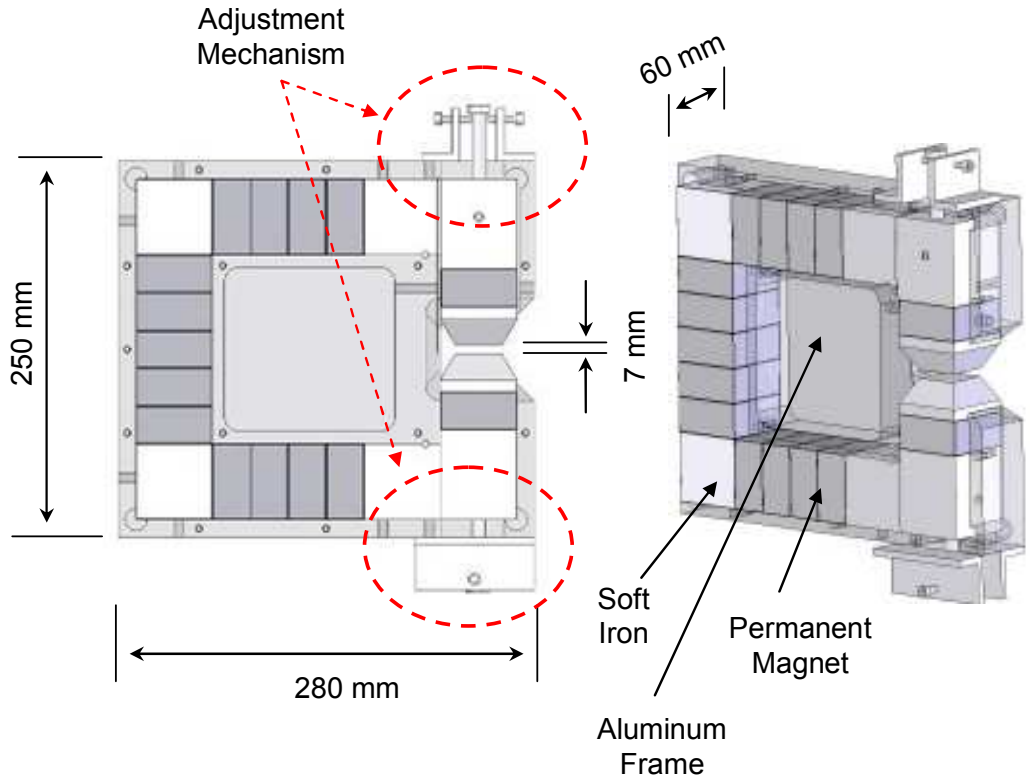

Figure 24. Final design of the C-shaped permanent magnet.

The final design of the H-shaped magnet with approximate dimensions is shown in Figure 25. The 5" (D) x 1" (H) permanent magnetic discs were also purchased off-the-shelf from the same distributor. The material is NdFeB of grade N42 and a residual flux density of $B_r = 1.32$ T. The return path is a low carbon steel plate (AISI 1018). The distance between the pole faces (i.e., the gap) and also the parallelism is adjustable using four bolts on the top plate. The gap is adjustable between 5 – 20 mm and is set to 16.5 mm throughout this work. The aluminum blocks on the side are used to support the force exerted by the adjustment bolts. The steel acts as both the return path and the mechanical structure.

The magnets were drawn using SolidWorks and imported to the magnetostatics sub-module of COMSOL for steady-state conditions. The relative magnetic permeability of iron is set to 4000,

the residual magnetic flux density of the C-shaped magnets is 1.47 T and the residual magnetic flux density of the H-shaped permanent magnet is 1.32 T. The boundary conditions of the outer boundaries are set to 'zero potential' and the inner boundaries are set to continuity. A free mesh was used for the overall structure of the magnet and was refined to 0.2 mm on the pole faces. A steady state solver (GEMRES) was used.

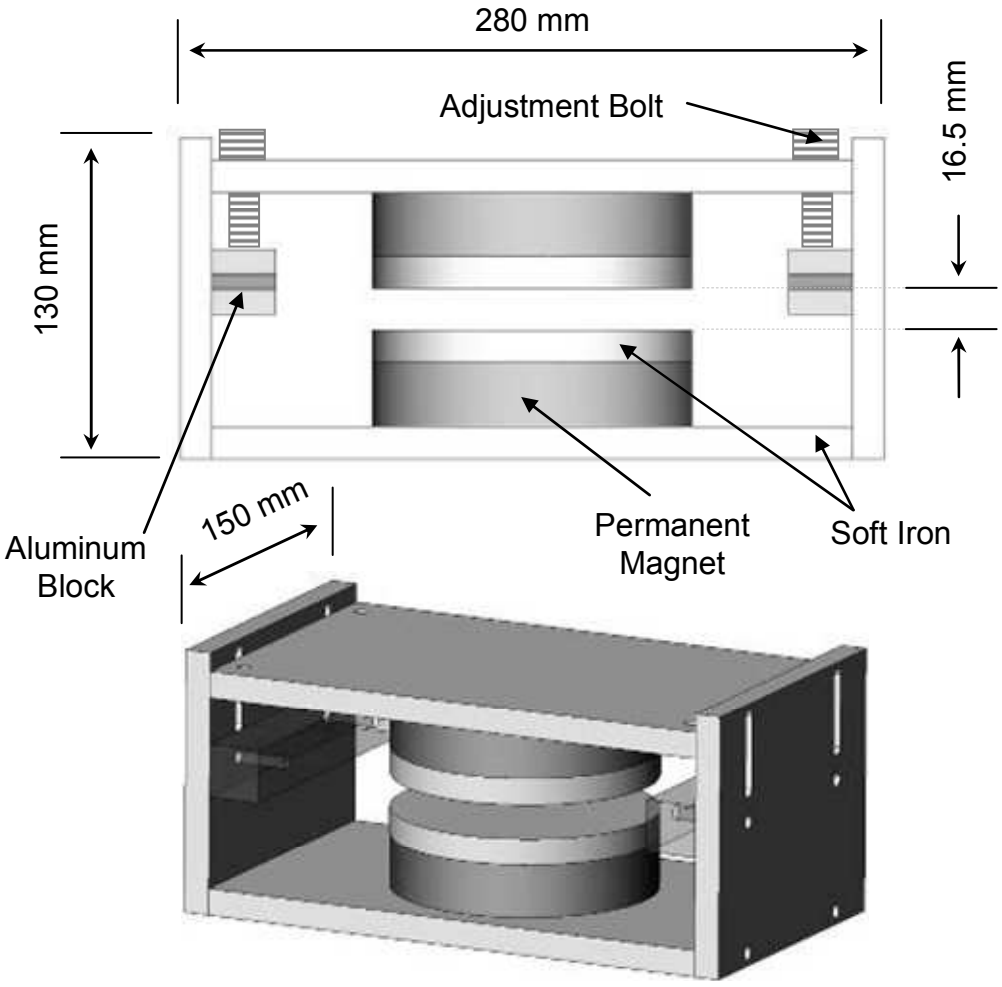

Figure 25. Final design of the H-shaped permanent magnet.

The results of these magnets are summarized in Table 7. The magnetic field and homogeneity is

evaluated in the center of the gap.

Table 7. Specification of the magnet based on results from simulations.

	C-shaped	H-shaped
Gap [mm]	**7.5**	**16.5**
B_0 [T]	**1.282**	**0.595**
$\Delta B/B_0$ [ppm]	**50**	**50**
Along x-axis [mm]	**10**	**13**
Dimensions [m x m x m]	**0.28L x 0.25H x 0.07W**	**0.28L x 0.13H x 0.15W**
n_L	**47%**	**68%**

Sample simulation results showing the distribution of the magnetic flux for each magnet is depicted in Figure 26 and Figure 27. The leakage and fringing effects are also depicted. The fringing in the C-shaped magnet is relatively small at the air gap. However, regions with a magnetic flux density of higher than 2.2 T saturate the soft iron cores; the leakage in the H-shaped magnet is mainly due to the saturation of the core which, according to simulations, can be easily solved by choosing a thicker plate which was not done due to time constraints. In Figure 26a and Figure 27a the arrows represent the magnetic flux lines. The magnet is also coloured based on the absolute magnetic flux density which ranges from 0.2 T to 2 T. The region of saturation are indicated in the figures. In Figure 26b and Figure 27b the magnetic flux is shown in terms of isosurfaces at 100 mT and 200 mT which highlight the leakage and fringing of the magnetic field. The fringing is larger in the H-shaped magnet because the iron cores are

saturated.

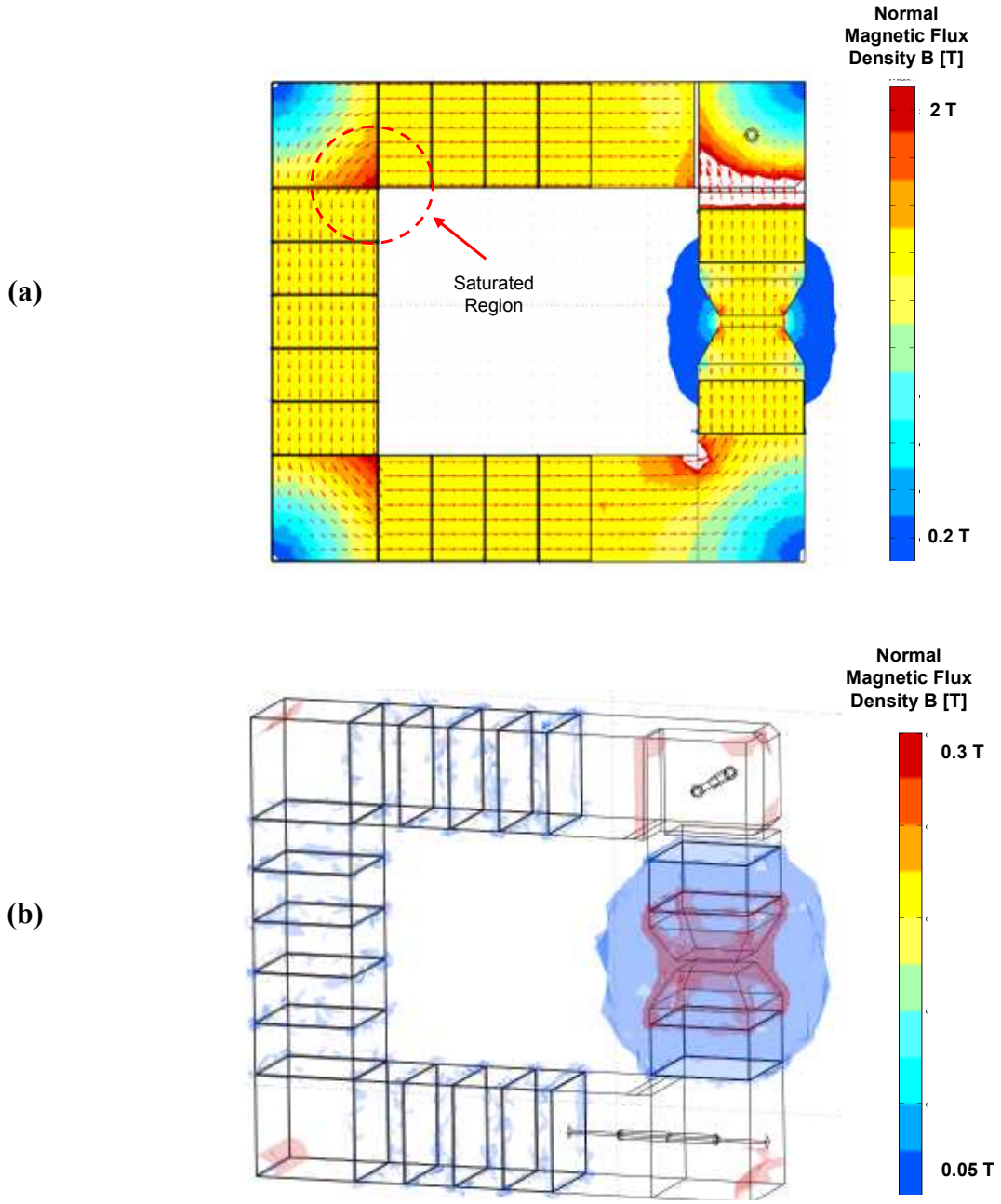

Figure 26. Distribution of magnetic flux density in the final C-shape design (a) and the leakage and fringing effects (b) are shown.

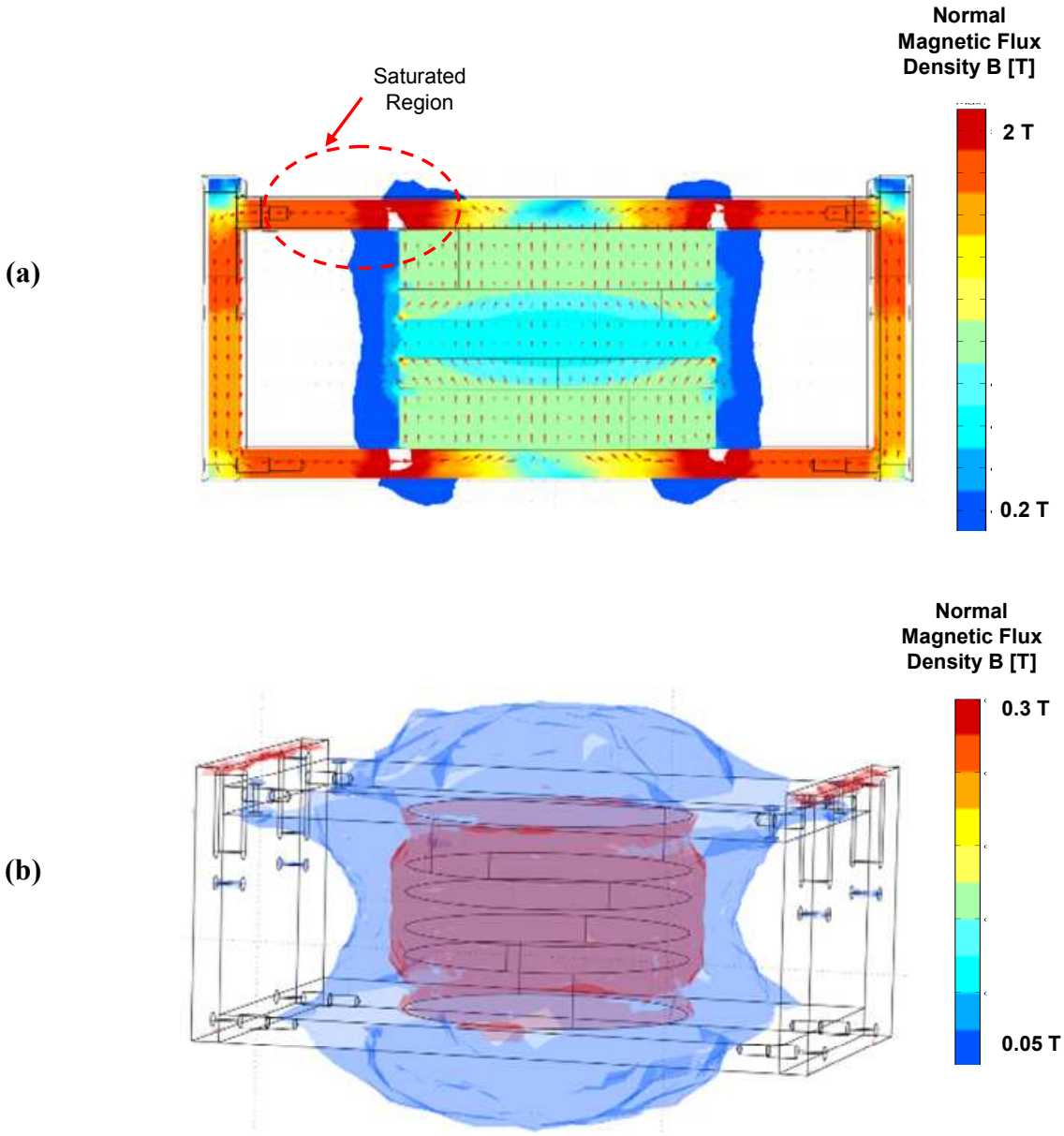

Figure 27. Distribution of magnetic flux density in the final H-shape design (a) and the leakage and fringing effects (b) are shown.

2.1.3 Magnet Characterization

A photo of each manufactured magnet is shown in Figure 28. The C-shaped is shown in Figure 28a before the magnet was re-machined to incorporate the adjustment bolts.

(a)

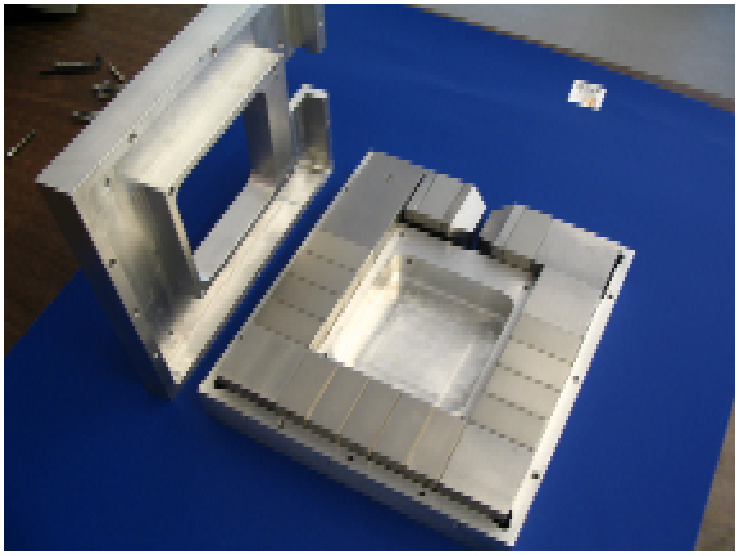

(b)

Figure 28. Manufactured C-shaped (a) and H-shaped (b) magnets.

The summary of the measured performance of both magnets is displayed in Table 8. The field and homogeneity were evaluated in the middle of the gap of each magnet.

Table 8. Specification of the magnet based on results from measurements.

	C-shaped	H-shaped
Gap [mm]	**7.5**	**16.5**
B_0 [T]	**1.205**	**0.589**
$\Delta B/B_0$ [ppm]	**500**	**150**
along x-axis [mm]	**10**	**13**
n_L	**44%**	**67%**

For measuring the field of the C-shaped magnet a Hall-effect gaussmeter (F. W. Bell 4000, Sypris Test & Measurement, 6120 Hanging Moss Road,Orlando, FL 32807 USA) with a digital resolution of 1 mT was used. The resolution of this commercial probe is not high enough to make meaningful plots (see Figure 29b) of the magnetic field in order of part-per-million (ppm) and an analog output was not available. Therefore, a hall effect (SH-400 model from F.W. Bell) component was used along with a homemade electronics to measure the magnetic flux density. The probe generates a voltage proportional to the magnetic flux density. Data was taken every 1.0 mm and measured voltage averaged by an Agilent 34401A digital multimeter for 2 seconds and read from the display. The magnetic flux density across the gap of the C-shaped magnet is shown in Figure 29a. The solid line represents the simulation and the crosses represent the measured data. The data from simulation was corrected by a scaling factor (x 1.028) to account

for a number of uncertainties including the magnetization of the permanent magnets and relative magnetic permeability of the iron poles. In addition, the hall-effect probe with homemade electronics had an offset about 2 mT which was compensated for during calibration. The calibration was performed by recoding the magnetic field at a few locations in the magnet using the commercial probe, and then recording the voltage of the hall-effect probe (with homemade electronics) at the same locations. An error of up to 5% was present with this calibration scheme as there were errors in placing the probes exactly in the same locations. In addition, the data sheet of this probe reports a non-linearity error of 1%. The homogeneity of the C-shaped magnet along the X and Y axes is plotted in Figure 29-B. The magnetic flux density varies by approximately ±1 mT over ±8 mm in the X and Y axes at the middle of the gap. The variation of the magnetic flux density from one pole face to the other (i.e., along the Z-axis) is negligible according to simulation. This was confirmed with the commercial gaussmeter. However, measurements using the homemade probe show variations up 10 mT along the Z-axis. Since the sensor was relatively large (2 mm) compared to the gap (7.5 mm) this error was attributed to small amount of magnetic material being present inside the homemade probe, which resulted in a measurement error as the probe came close to the pole faces. In general the measured values for the maximum magnetic flux density and the shape of the field inside the gap were very well explained by the simulation results. However, the estimated homogeneity is different from measured homogeneity by a factor of 10 for the C-shaped magnet. This error arises from manufacturing tolerances such as the air gaps in the magnetic circuit, surface finish of the pole faces, and the ability to adjust for the parallelism of the poles. Other researchers have reported an error factor of a 100 [53] for a Halbach design. The addition of high permeability magnetic plates as Alloy 49 would improve homogeneity by a factor between 2 and 3 depending on the

thickness of the plates. The magnet efficiency is also close to the expected value from simulation.

(a)

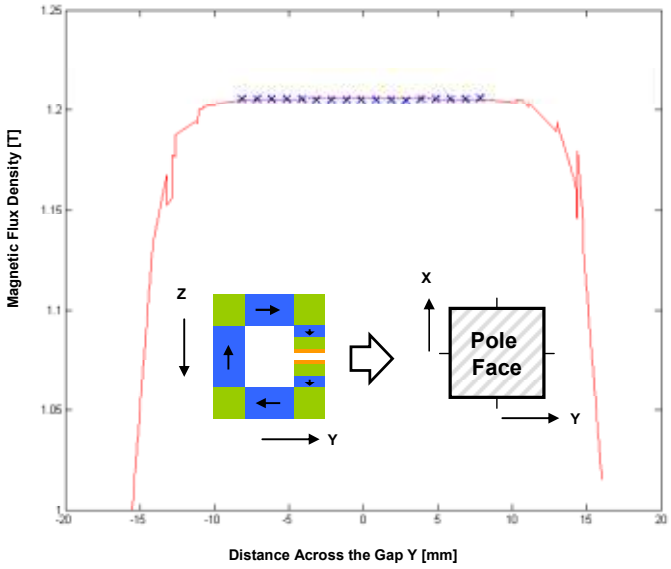

(b)

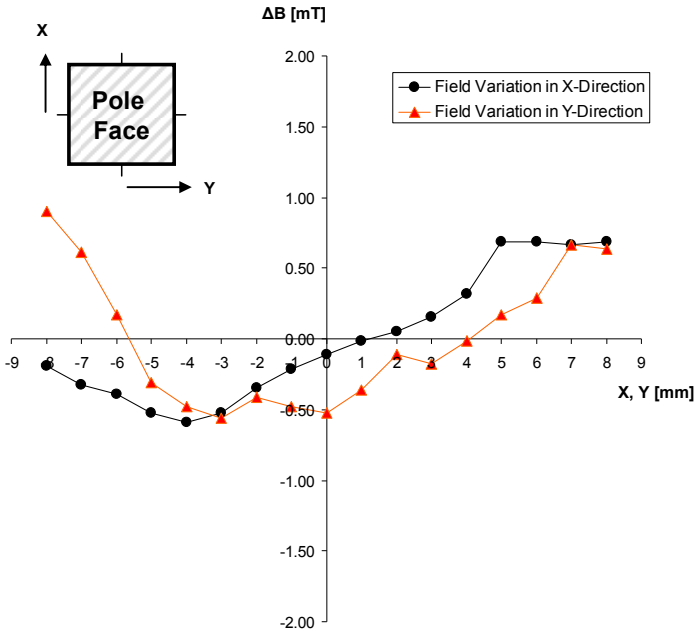

Figure 29. Magnetic flux density along the gap of the C-shaped magnet (a). The solid line represents simulation values and the crosses show measurement data points. The variation of the magnetic flux density along the center of the x and y axes are shown in (b).

The magnetic flux density along the gap of the H-shaped magnet is shown in Figure 30a. The

Hall-effect probe used for this measurement was an F.W. Bell 6010 model with an analog output. The datasheet of this probe claims an absolute accuracy of better than 1 mT with an uncertainty of ±1%. Data was taken every 3 mm at 5 kS/s for a duration of one second. The solid line represents corrected (x 1.0125) data from simulation and the error bars represent the measured data. The homogeneity of the H-shaped magnet in the middle of the gap (Z = 0 mm) is shown in Figure 30b as contour lines. The measured variation of the magnetic flux density from one pole face to the other is negligible (as expected from simulation) for the region of interest and therefore not presented here. Again, the results from simulation match the measured data very well except for homogeneity which is different from measurements by a factor of 3. According to simulations performed in this work, the magnet efficiency of the H-shaped PM can be significantly increased (form 67% to 85%) if the iron plates are made thicker to prevent them from saturation.

(a)

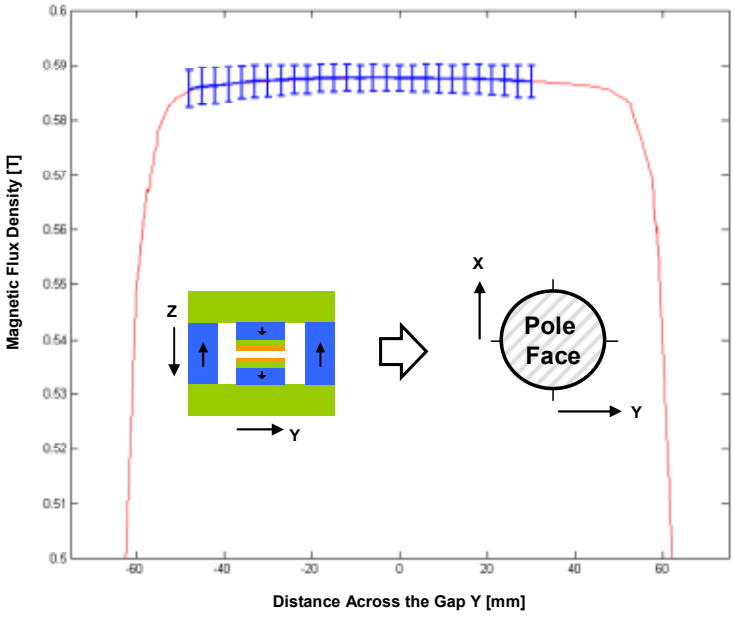

(b)

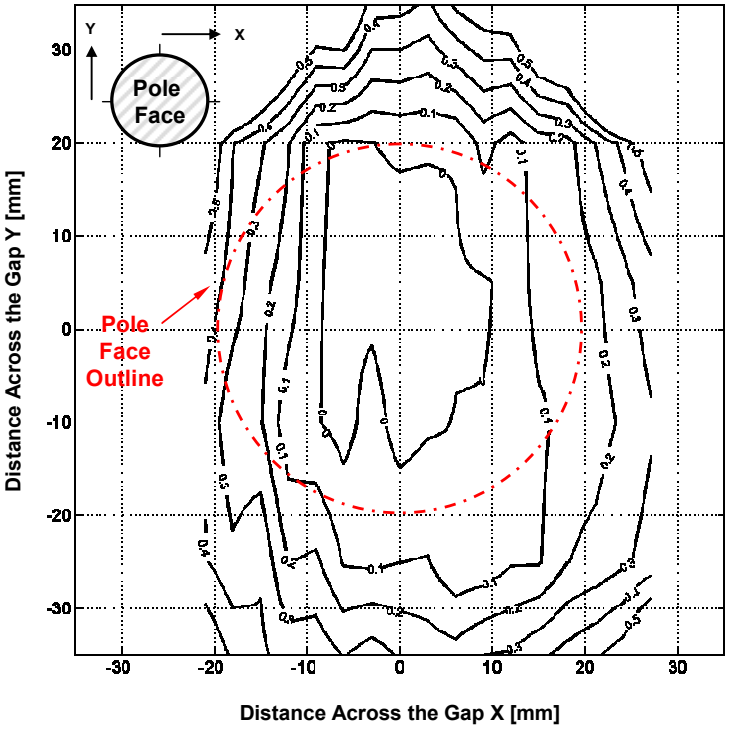

Figure 30. Magnetic flux density along the gap of the H-shaped magnet (a). The solid line represents corrected simulation values and the crosses show measurement data points. The variation of the magnetic flux density along X and Y axes in the middle of the magnet (Z = 0 mm) is shown in as contour lines (b).

The homogeneity of the C-shaped magnet would result in a T_2* decay of approximately 40 μs according to equation (55). An MR signal this short would be very challenging to pick-up due to practical limitations. After the application of the excitation signal the receiver goes through a recovery phase (> 50 μs in the experimental setup of this work) which would make detection of the MR signal with a short decay time very challenging. The more important challenge is the tuning of parameters such as frequency, amplitude, and pulse duration of the excitation, tuning and matching of the receiver probe, adjustment of the receiver gains with no MR signal present and at the same time seeking the most homogenous section of the air gap. For example, the carrier frequency can be estimated by knowing the magnetic flux density of the C-shaped magnet. Assuming a measurement accuracy of 1%, the uncertainty in the carrier frequency would be over 500 kHz. Depending on the RF electronics, if the carrier frequency is offset more than a certain amount (say 50 kHz) at Larmor frequency (about 51 MHz here), no MR signal would be observed even if T_2* was much longer than the recovery time of the receiver. As a result of these challenges and time constraints the application of the C-shaped magnet for the purpose of making a desktop imaging device was not further pursued. The homogeneity of the H-shaped magnet and the large access is much better suited as a first prototype of a desktop fluid flow visualization instrument. In addition, the homogeneity would improve for smaller samples as the variation of the magnetic field across a smaller sample is less. The trade-off however is the observed amplitude of the MR signal as a smaller number of protons exist to contribute to the signal.

In terms of stability, the variation of the magnetic flux density was observed along with a measurement of the temperature of the magnet. As the fluctuations in the field are rather small, the magnetic flux density was measured by recording the frequency shift of the MR signal. The

temperature fluctuations of the magnet along with its shift in resonance frequency were measured over a period of 6 hours, as shown in Figure 31a. The drift in the magnetic resonance shift correspond to the changes in temperature of the magnet. Note that the resonance frequency shift in Figure 31a was inverted about the x-axis for ease of comparison. The shift in magnetic resonance vs the temperature of the magnet is shown Figure 31b where the temperature coefficient of the magnet was -707 ppm/°C. Other groups have reported -300 ppm/°C [53] and -1200 ppm/°C [42]. The fluctuation due to temperature is mainly due to the large temperature coefficient of the NdFeB magnets (-0.12%/°C, Table 3) which suggest a maximum temperature coefficient of -1200 ppm/°C for the whole magnetic structure according to (63). The fluctuations of the magnetic field due to geometric changes of the magnet (because of variations in temperature) are two orders of magnitude lower in amplitude compared to the temperature coefficient of the permanent magnets.

(a)

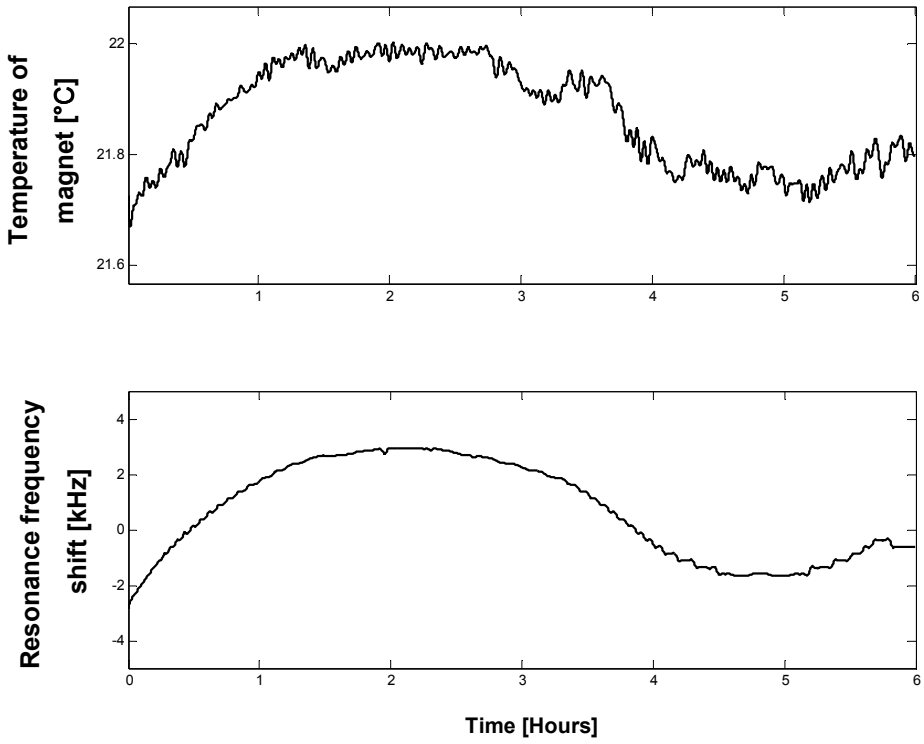

(b)

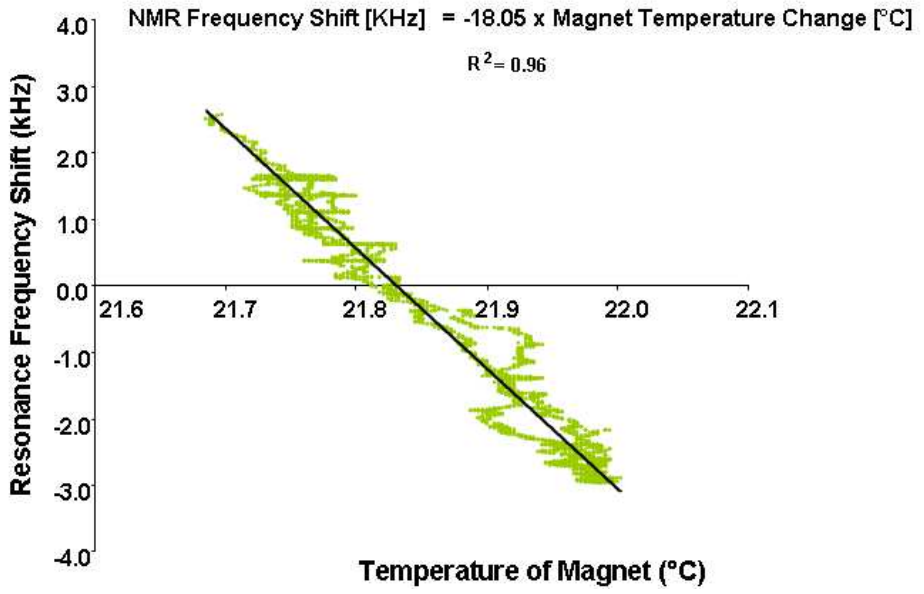

Figure 31. Fluctuation of the magnetic flux density and the room temperature in 6 hours (a). The temperature coefficient is -707 ppm/°C (b).

The temperature stability of this magnet is rather poor for MRI purposes and imaging would be not practical unless corrections are applied either to the magnetic field or the carrier frequency [73-75]. Compensation of the magnetic field in this work is applied to the magnetic field by the means of coils wound on the each of the poles of the magnets. The homogeneity is optimized when the distance between the two coils is equal to their diameter; this configuration is called the Helmholtz coil. The current *I* in both coils flow in the same direction. The magnetic flux density of a Helmholtz coil in the middle of the two coils is given by [76]

$$B = (4/5)^{3/2} \frac{\mu_0 \mu_r N}{r} I. \tag{66}$$

The radius *r* is equal to the radius of the disc shaped permanent magnet and μ_r is the relative magnetic permeability (= 1.05) of NdFeB material. The number of turns was arbitrarily chosen as 8. From (66) and the Larmor equation, the expected frequency shift per amperes for the described Helmholtz coil is 4.8 kHz/A. The recorded frequency shift of the magnetic resonance signal is shown in Figure 32 as a function of current inside the coils. The measured value for this coefficient (= 5.2 kHz/A) is reasonably close to the estimated value given by (66). A typical magnetic resonance shift during the whole day is about ±15 kHz; by regulating a current up to ±3 A in this coil it is possible to compensate for drift in temperature as it will be discussed in Chapter 3.

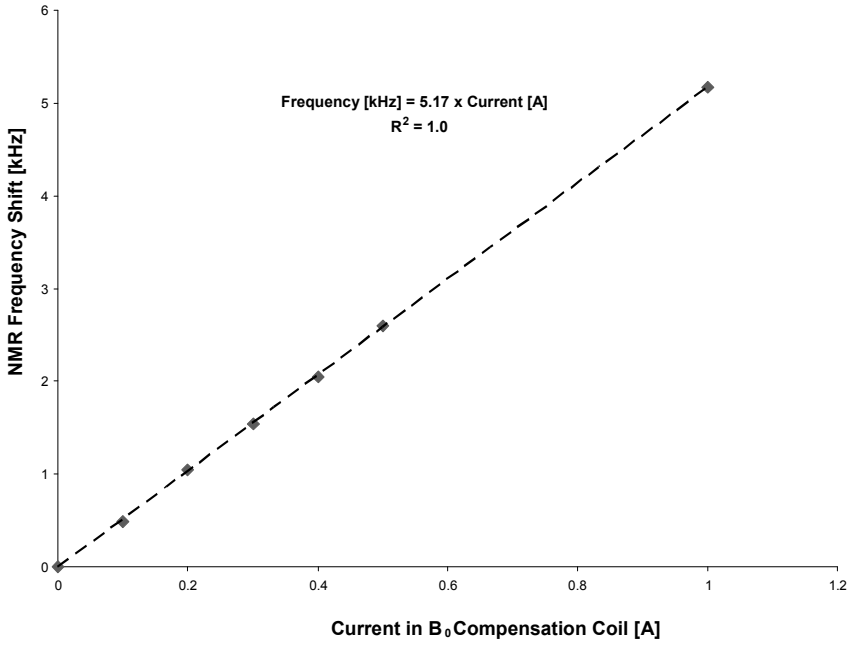

Figure 32. Effect of flow of current in the B_0 compensation coils.

The implementation and the sequencing of the disturbance compensation of the permanent magnet are further discussed in Chapter 3.

2.1.4 Summary of Magnets

In summary, two permanent magnets (C- and H-shaped) were designed based analytical equations and simulations, constructed and characterized. The C-shaped magnet has a measured field of 1.205 T with a 7.5 mm gap and a homogeneity of 500 ppm over 10 mm. Due to the small gap and poor homogeneity, this magnet was not used for magnetic resonance imaging. The H-shaped magnet has a measured field of 0.589 T with a 16.5 mm gap and a homogeneity of 150 ppm over 13 mm. The measured temperature coefficient of this magnet is -707 ppm/°C; Helmholtz coils were added to this magnet which can be used to compensate the magnetic drift. The H-shaped magnet is used in this work for magnetic resonance imaging.

2.2 Gradient Coils

The design and characterization of the gradient coils is described next.

2.2.1 Gradient Coil Requirements

As the strength of the gradient field (G_x) is increased, the spatial resolution given by

$$\Delta x = \frac{1}{G_x}\Delta B_0 + L_x\frac{\Delta G_x}{G_x} + \frac{1}{\gamma G_x}\Delta\omega \tag{67}$$

of the image is improved (see Chap 1.4). Linear gradient fields (i.e., small deviations, ΔG_x) are also necessary to avoid image distortions. To achieve a resolution of about 30 μm, a gradient of greater than 0.67 T/m with a linearity of 3% is needed assuming that L_x = 1 mm and ΔB_0 = 20 μT.

The resolution is also limited by the uncertainty principle as

$$\Delta x \geq \frac{1}{\gamma G_x T_{acq}}. \tag{68}$$

To improve resolution, both the acquisition time, T_{acq}, and the gradient field strength have to be maximized. However, increasing the acquisition time leads to greater spin diffusion and is related to the resolution as

$$\Delta x \geq \sqrt{2DT_{acq}} \tag{69}$$

for the molecular diffusion constant D. To avoid problems encountered with diffusion, the acquisition time has to be minimized, which is in conflict with equation (68) where longer T_{acq}

are preferred. From equations (68) and (69), if the acquisition time T_{acq} is less than 5 ms, in order to achieve a resolution of approximately 30 μm, a gradient of at least 0.6 T/m is needed. In this case, the resolution limited to approximately 5 μm due to self-diffusion, assuming a typical self-diffusion coefficient $D \approx 2.2 \cdot 10^{-9}\ m^2/s$ for water at room temperature [36]. To keep the acquisition time short, the duration of the applied gradient field has to be minimized which requires that that the gradients are switched rapidly. Typically the rise time needs to be better than 5% of the total duration of the gradient pulse. So, for a gradient pulse duration of 1 ms, a 100 μs rise time is typical.

To obtain optimal performance in terms of velocity resolution (as derived in chapter 1.4)

$$\Delta V = \frac{1}{2\pi\gamma G_x \tau^2}\Delta\Phi_{MR} + \frac{\Phi_{MR}}{2\pi\gamma G_x^2 \tau^2}\Delta G_x, \tag{70}$$

large gradients of high linearity that are pulsed for long durations are necessary. To obtain a velocity resolution of 50 μm/s, a gradient strength of 0.68 T/m and a linearity of better than 5% is needed if we assume a gradient pulse duration τ of 2 ms and maximum phase shift $\Phi = \pm\pi$. The variation in Φ is determined by the number of phase encoding steps (=128) which results in phase steps of $\Phi = \pi/128$.

Therefore, the requirements of the gradient coils are:

- High gradient field strength (> 0.68 T/m)
- High linearity (< 3%)
- Fast switching speed (< 100 μs).

2.2.2 Gradient Coil Design

The design and simulation of the gradient coils is described in the following section.

2.2.2.1 Basic Theory: Gradients

The orientation of the gradient fields inside relative to the static magnetic field is shown in Figure 33. The main magnet generates a vertical magnetic field along the z-axis. The three gradient coils generate a linearly dependent magnetic field in the z-direction (Figure 33-b). For example, the gradient in the x-direction, G_x, generates a magnetic field in the z-direction that is linearly dependent on x as illustrated in Figure 33-c. Similarly, the gradients in y and z are illustrated in Figure 33-d and Figure 33-e respectively. In other words, the gradients are defined as

$$\mathbf{G_r} = \frac{dB_z}{dx} + \frac{dB_z}{dy} + \frac{dB_z}{dz}.$$

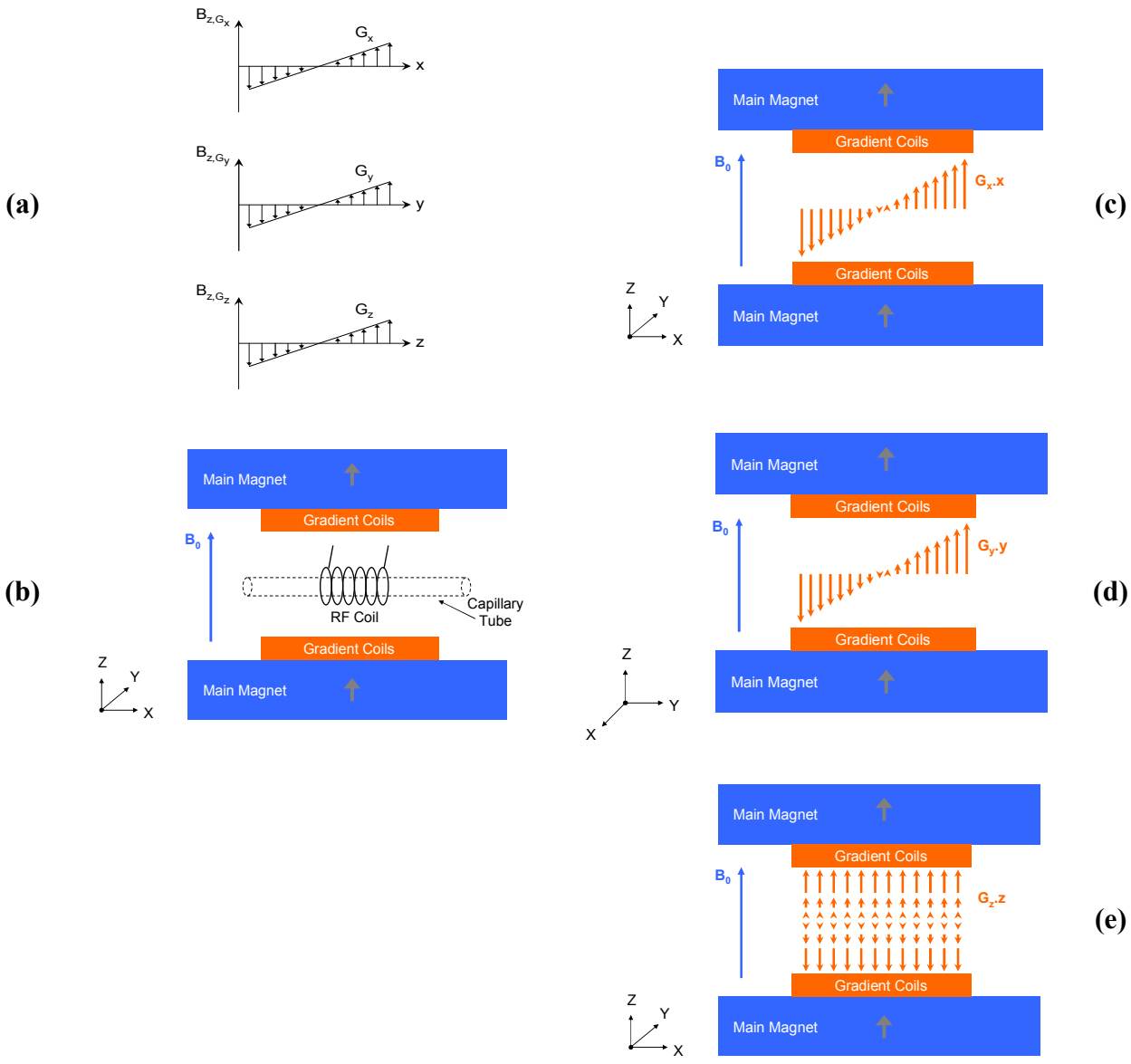

Figure 33. The direction of the field generated by the gradient coils (a); location of the gradient coils and the probe (b); The gradient field in x, y, and z directions are shown in (c), (d) and (e), respectively.

The gradient field along the z-axis, G_z, is generated using a Maxwell coil configuration. This configuration consists of two current carrying loops with a radius *a* and separation *d*. The electrical current is passed through the coils in opposite directions as illustrated in Figure 34.

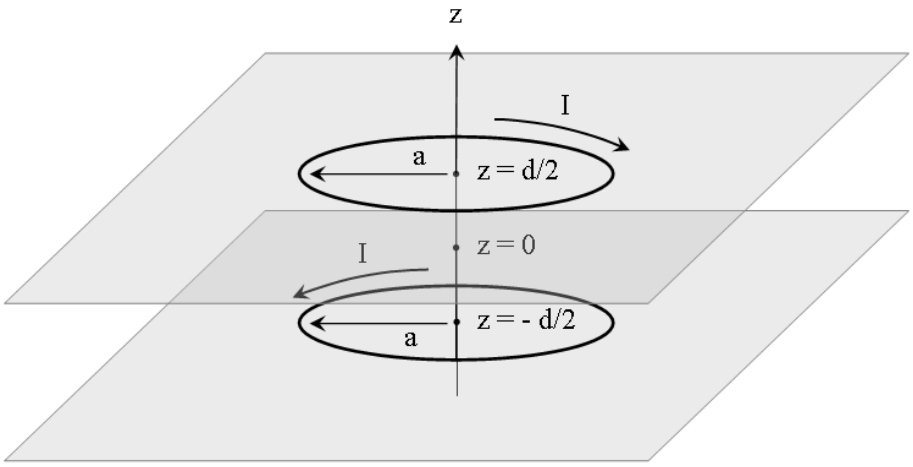

Figure 34. Maxwell gradient coil.

The magnetic field along the z-axis is [76]

$$B_z = \frac{\mu_0 n I a^2}{2}\left[\frac{1}{\left(\left(\frac{d}{2}a - z\right)^2 + a^2\right)^{3/2}} - \frac{1}{\left(\left(\frac{d}{2}a + z\right)^2 + a^2\right)^{3/2}}\right], \tag{71}$$

where μ_0 is the permeability of free space ($4\pi \cdot 10^{-7}$ N/A^2), I is the electrical current and n is the number of turns for each loop. If the separation is chosen to be

$$d = \sqrt{3} \cdot a ,$$

the gradient fields are linear up through the fourth power [76] and the magnetic field gradient of this configuration is found by taking the derivative of (71) with respect to z

$$G_z = \frac{48\sqrt{3} \cdot \mu_0 n I}{7^{5/2} a^2} \approx 0.64 \frac{\mu_0 n I}{a^2}. \tag{72}$$

This approximation is true for a imaginary sphere of 0.6*a* in radius in the center of this coil (at $z = 0$ in Figure 34) for a linearity of 5% [77].

The gradient fields along the x and y axes are generated using the "rectangular loop" coils described by Anderson *et al.* [78]. Other configurations exist that are described elsewhere [13, 32, 76]. The rectangular loop configuration is suitable for this work due to its compact design. This design consists of four current carrying loops with a width *w*. The coils are located on two planes separated by $2z_0$, each holding two of the loops of length *L*. The centers of the two loops on each plane are separated by $2y_c$. This gradient configuration is illustrated in Figure 35.

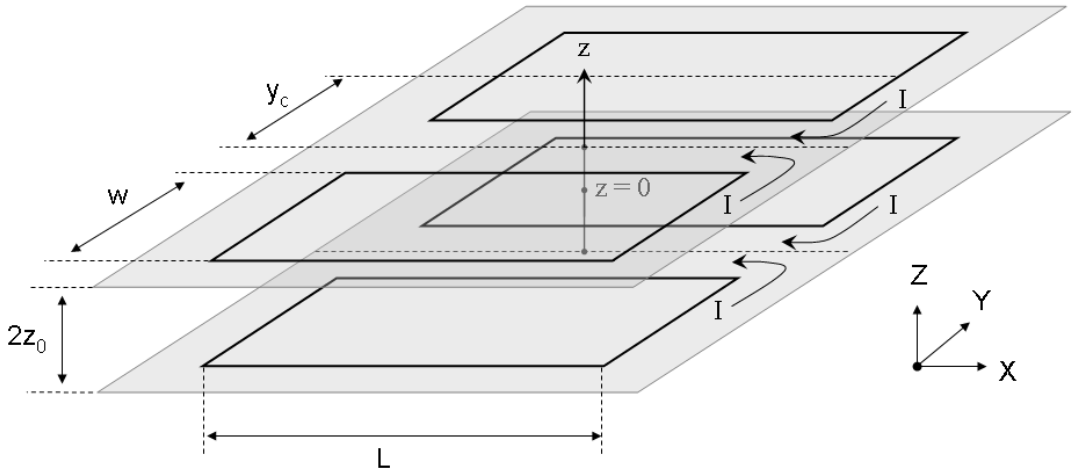

Figure 35. Rectangular loop gradient coil.

The gradient in x and y are very similar; the only difference is that they are rotated by 90° with respect to each other. The maximum gradient field with vanishing second order terms can be achieved by choosing $w/z_0 = 1.55$ and $y_c/z_0 = 1.19$ [78]. The gradient field is estimated using

$$G_x = G_y \approx 0.46 \frac{\mu_0 nI}{z_0^2}. \tag{73}$$

The gradient field is linear to within 5% for a imaginary cube of $0.4z_0$ on each side in the center of the coils (at z = 0 in Figure 35) [77]. The length of the coil *L* has to be long enough compared to the size of the gradient so that it can be approximated as being infinitely long.

2.2.2.2 Prior Art: Gradients

Typical values for gradients range from 0.001 to 0.01 T/m for clinical imaging while for microscopy 1 T/m is more typical. Much larger gradients (up to 250 000 T/m) can be obtained over a very small volume near ferromagnetic tips of newly developed NMR force microscopes [77]. The literature review of this work was focused on gradients used for microscopy only.

Callaghan *et al.* [79] describe the design of a Maxwell gradient coil with a sensitivity of 1.65 T/m/A which was successfully tested up to 40 T/m (at a current of 24 A) for diffusion measurements. The uniformity over a sphere of 2 mm and 3 mm in diameter is about 2.5% and 8% standard deviation, respectively. The coil consists of 23 turns of 0.36 mm diameter enameled copper that is potted in epoxy. The coil has an inductance of 15.3 μH and a resistance of 0.8 Ohms. The gradient rise and fall time are reported to be on the order of 50 μs. Wright *et al.* [56] report rectangular loop planar gradient coils with a sensitivity of 0.0045 T/m/A that were tested up to 0.045 T/m (at current of 10 A). The gradients are linear enough for imaging a region of 25.4 mm with a resolution of 100 μm. They are etched from 8 oz copper clad printed circuit boards. Another paper also by Wright *et al*. [80], reports the design of a Maxwell coil with elongated loops with a sensitivity of 1.26 T/m/A is reported. This gradient coil was tested up to 52 T/m (at a current of 41 A) for diffusion measurements and consists of 23 turns of 0.36 mm diameter enamel-coated wire. The uniformity of the gradient over a 2 mm diameter sample is ±2% standard deviation. The coil has an inductance of 21 μH and a resistance of 1.7 Ohms and

has a rise time about 125 μs.

Casanova *et al.* [81] report two gradient coils of rectangular loop type each with 20 turns and a sensitivity of 0.02 T/m/A and 0.012 T/m/A; the gradients were used up to 0.4 T/m and 0.24 T/m (at a current of 20 A), respectively. The reported resistance is 0.8 Ohm and the rise time is about 50 μs. The linear region of the gradients is a sample of 6 x 8 mm^2. Seeber *et al.* [77] report the design and testing of a triaxial gradient module. The z-gradient is a Maxwell pair and the transverse gradients (G_x and G_y) are rectangular loop gradients as described by Anderson *et al.* [78]. The G_z has a sensitivity of 0.095 T/m/A and was tested up to 9.4 T/m (at a current of 99 A) with an estimated linearity of 5% in a sphere with 1.5 mm radius. The G_x and G_y gradient have a sensitivity of 0.25 and 0.14 T/m/A and were tested up to 40 T/m (at a current of 160 A) and 20 T/m (at current of 142 A), respectively. The linearity of the gradients is estimated to be within 5% in a region of $(600\ \mu m)^3$. The gradient are made using a single turn of a gauge 24 copper wire (diameter = 0.51 mm) embedded in slots machined in printed circuit boards. The gradients have inductances in the order of 0.1 μH with a rise time of about 15 μs. Another triaxial gradient system is developed by Haishi *et al.*[61] where gradient sensitivities of G_z =17 T/m/A, G_x =12 T/m/A and G_y =11 T/m/A are reported. The gradients are used up to G_z = 0.026 T/m, G_x = 0.029 T/m and G_y= 0.028 T/m. Details on the linearity, electrical properties and the dynamic response of these gradient coils were not given.

Shen *et al.* report gradients of Golay type [82] with sensitivities about 0.0005 T/m/A with a linearity of better than ±5.4% over a spherical region with a radius of 80 mm. The coils are made using 13 turns of 2.5 mm diameter copper wires. Details on electrical properties and the dynamic response of these gradient coils are not provided. Design and calibration of multilayer gradient coils of Maxwell type are described by Bowtell and Robyr [83]. The reported gradient has a

sensitivity of 1.73 T/m/A which was tested up to 52 T/m (current of 30 A). The gradient is linear within 5% over a standard 5 mm NMR tube. The coil consists of 120 turns of 0.224 mm diameter copper wire and has an inductance of 50 μH and a resistance of 1.8 Ohms.

2.2.2.3 Proposed Design of the gradient Module

From equations (72) and (73) it follows that in order to satisfy the high gradient strength requirement, it is necessary to minimize the coil dimension and to pass as large an electrical current as possible through the coil while increasing the number of turns. The dimensions of the gradient coils are limited by the required homogeneity over the sample. The larger the gradient coils are compared to the sample, the more uniform the gradient fields become. To increase the strength of the gradients further, a choice between the number of turns of the coils and the maximum current has to be made. However, the larger the number of turns the higher the inductance of the gradient coils becomes. This limits the switching speed thus a low number of turns is preferred. In summary, the size of the gradient coils is chosen based on the size of the sample. The number of turns is chosen based on the desired gradient strength. Current of approximately 5-20 amperes are relatively easy to generate using off-the-shelf solid-state electronics. Therefore, the number of turns for the gradients of this work were chosen by taking this in consideration.

The three described gradients are stacked on top of each other as shown in Figure 36. The Maxwell coil (G_z) is located at the two opposite sides of the gradient module (which is referred to as the insert in this work) and the other two rectangular loop gradient coils (G_x and G_y) are sandwiched in between the sample and the G_z gradient coils. Each x and y gradient coil consists of three turns and is made from a 0.01 inch thick sheet of copper with a width of 1.5 mm. Each

coil is rated for a 20 A peak current for a duty cycle of less than 10% assuming a maximum current density of 5 A/mm^2 for copper. The current rating could be increased if the coils are cooled so that the heat generated by the resistive power dissipation is removed.

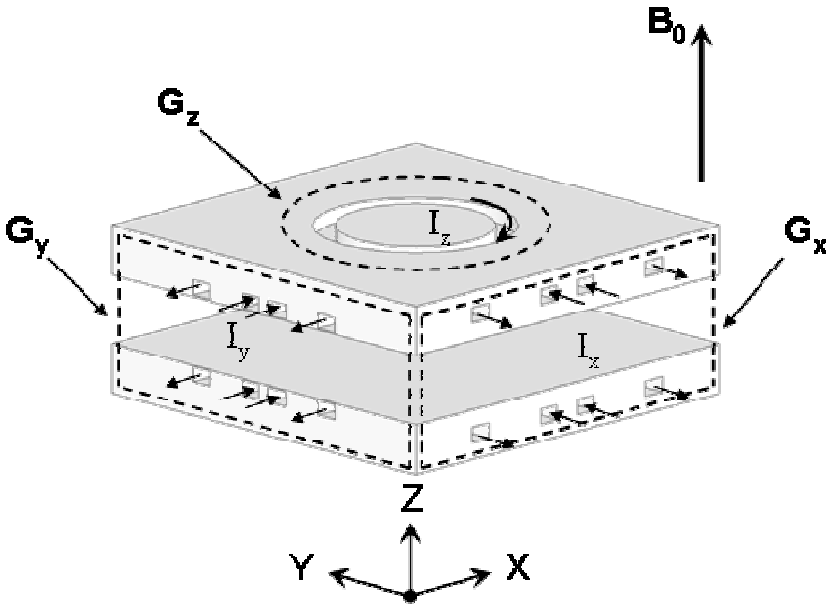

Figure 36. The positioning of the three gradient coils: G_x, G_y and G_z.

A clearance (size of the gap) of 9.53 mm was chosen to fit the RF probe. The gradient coils are assembled on the outer faces of the enclosure that consists of two back-to-back 3/16 inch (4.76 mm) thick plates of polypropylene. The enclosure is further described in section 2.4 along with the integrated radio frequency probe.

2.2.2.4 Simulation

Equations (72) and (73) assume that the size of the wire is relatively small to the overall dimensions of the coil such that it can be approximated as an infinitely long current path. To better understand the effects of current paths with a rectangular cross-section where the size of

the wire is relatively large compared to the overall dimensions of the gradient coils, the gradient fields were simulated in 2D in COMSOL MultiPhysics. The AC/DC module was utilized to perform static and transient electromagnetic simulations. The boundary conditions of the outer boundaries were set zero potential while the inner boundaries where set to continuity. The various simulated configurations for G_z (Figure 37) and for G_x or G_y (Figure 38) vary based on the possible choices for placement of the current paths as illustrated by the cross-sections in the figures. The simplest configuration (Figure 37a and Figure 38a) is a vertical stack such that the three turns can be assumed as one single loop with three times the current. A configuration where the coils are stacked horizontally is also considered and shown in Figure 37c and Figure 38c. Figure 37b and Figure 38b illustrate a configuration in which the gradient coils are interlaced. For example, the G_z coil in Figure 37b could be interlaced with the gradient G_x in Figure 38-b so that the order of the current paths from bottom to top would be: $G_{x1} \rightarrow G_{z1} \rightarrow G_{x2} \rightarrow G_{z2} \rightarrow G_{x3} \rightarrow G_{z3}$. The horizontal spacing remains fixed in this configuration because the effective area of the current paths is considered. The alternative has also been considered in Figure 37d and Figure 38d where each loop is considered as a separate loop and is spaced as described by Anderson *et al.* This was also simulated for the configuration of interlaced gradient as illustrated in Figure 37e and Figure 38e.

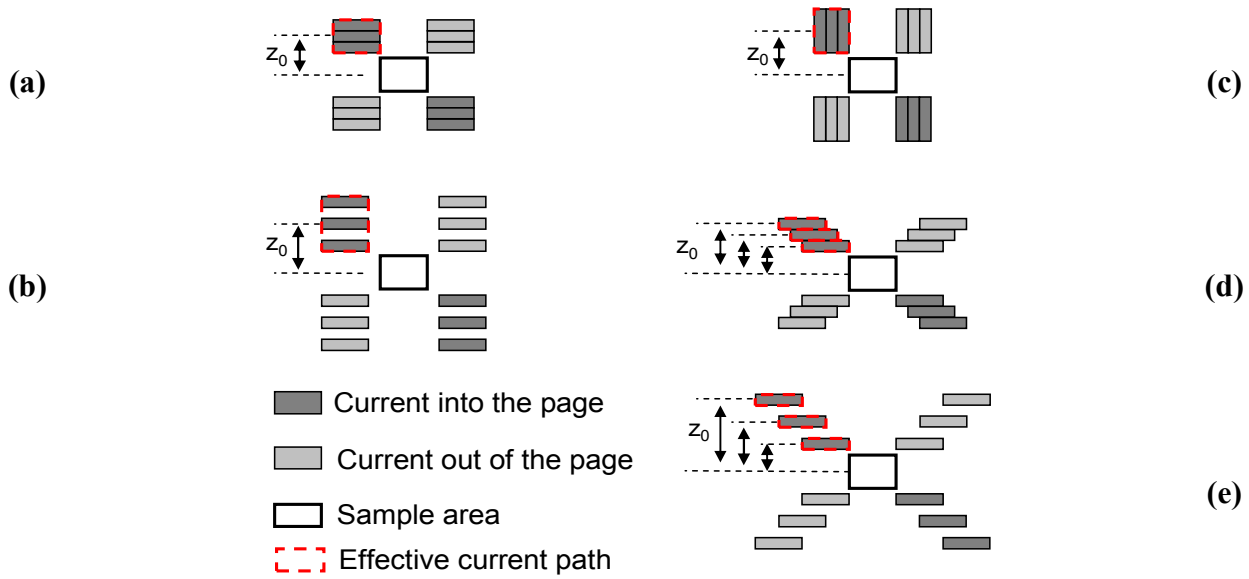

Figure 37. Simulated current path configurations for the Maxwell gradient.

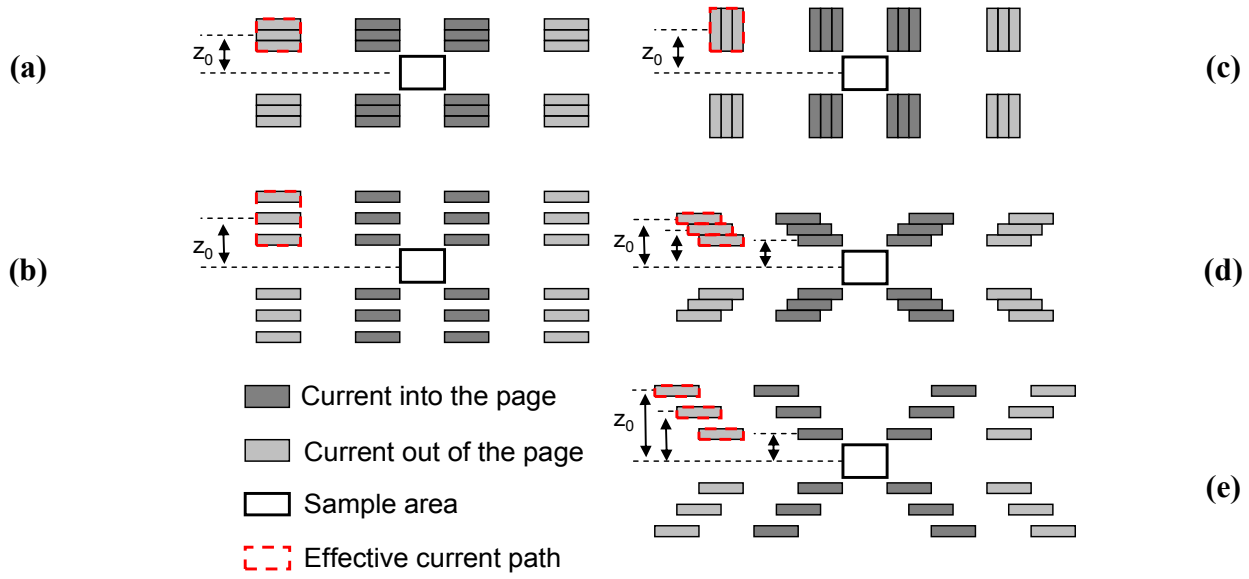

Figure 38. Simulated current path configurations for the "rectangular loop" gradient.

The simulations were performed assuming a current of 20 A with the copper coils extending 30 mm into the page. The results of the best gradients based on simulated gradient strength linearity and ease of fabrication are chosen for this work and are presented next. For G_z, the configuration in Figure 37a is chosen while for G_x and G_y the configuration in Figure 38a were chosen.

The results for the z gradient are shown in Figure 39. The contour plot of the magnetic flux density is shown in Figure 39a where an axial symmetry exists at x = 0 mm. The current paths are two sets of three turn loops that are positioned as previously described. The magnetic flux density in the z-direction was evaluated at x = 0.1 mm (G0), x = 1 mm (G1) and x = 2 mm (G2) for z = ±2.5 mm which is shown in Figure 39b. The gradient field strength is about 0.71 T/m with linearity better than 0.5% for a square of 2 mm on each side.

The results for the y gradient are shown in Figure 40. The contour plot of the magnetic flux density is shown in Figure 40a. The current paths are two sets of three turn loops that are positioned as previously described. The magnetic flux density in the z-direction was evaluated at z = 0 mm (G0), z = 1 mm (G1) and z = 2 mm (G2) for y = ±2.5 mm which is shown in Figure 40b. The gradient field strength is about 1.2 T/m with linearity of about 3% for a square of 2 mm on each side. The results for the x gradient are very similar to the y gradient and therefore not presented here. The results show a gradient field of 0.85 T/m and linearity better than 3% for a square of 2 mm on each side for the y-gradient.

(a)

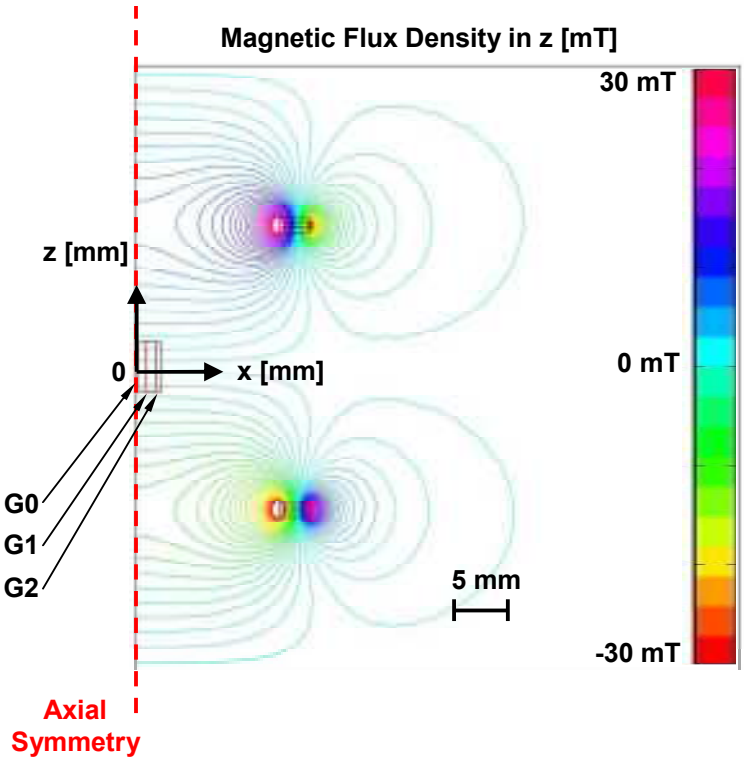

(b)

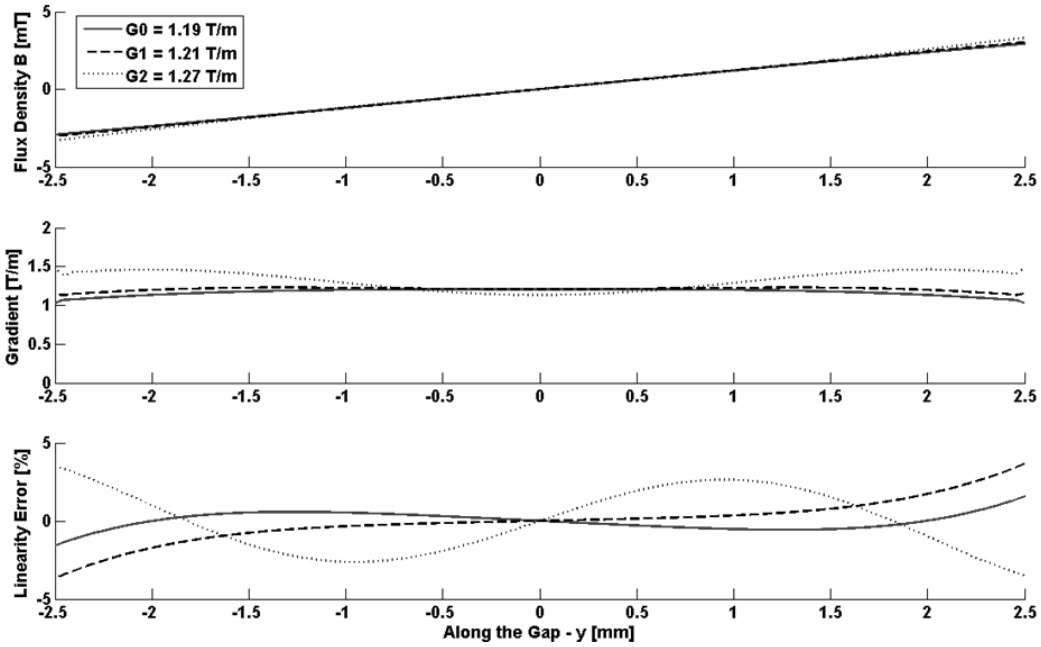

Figure 39. Simulation results of G_z: (a) shows the magnetic field contours; (b) and (c) show the gradient field strength and linearity.

(a)

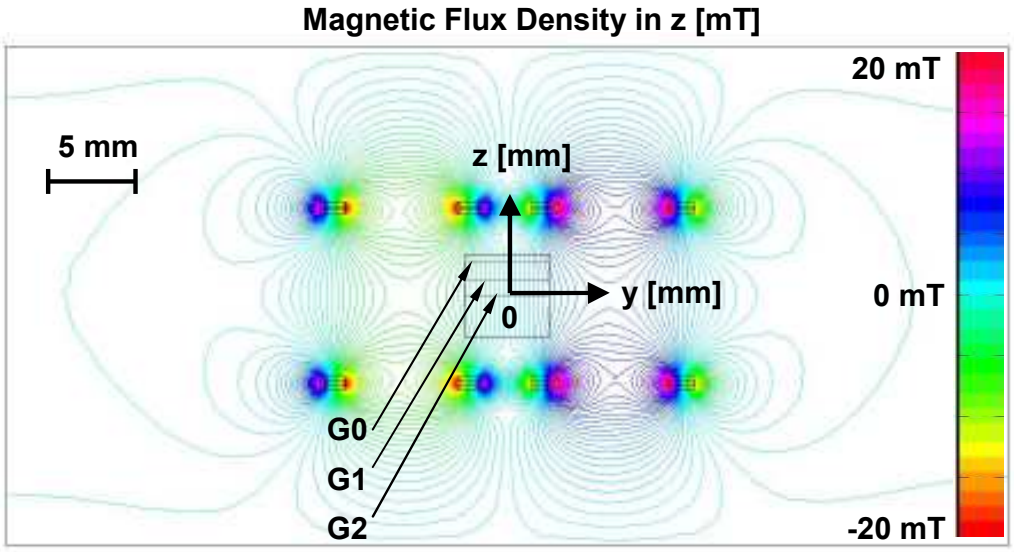

(b)

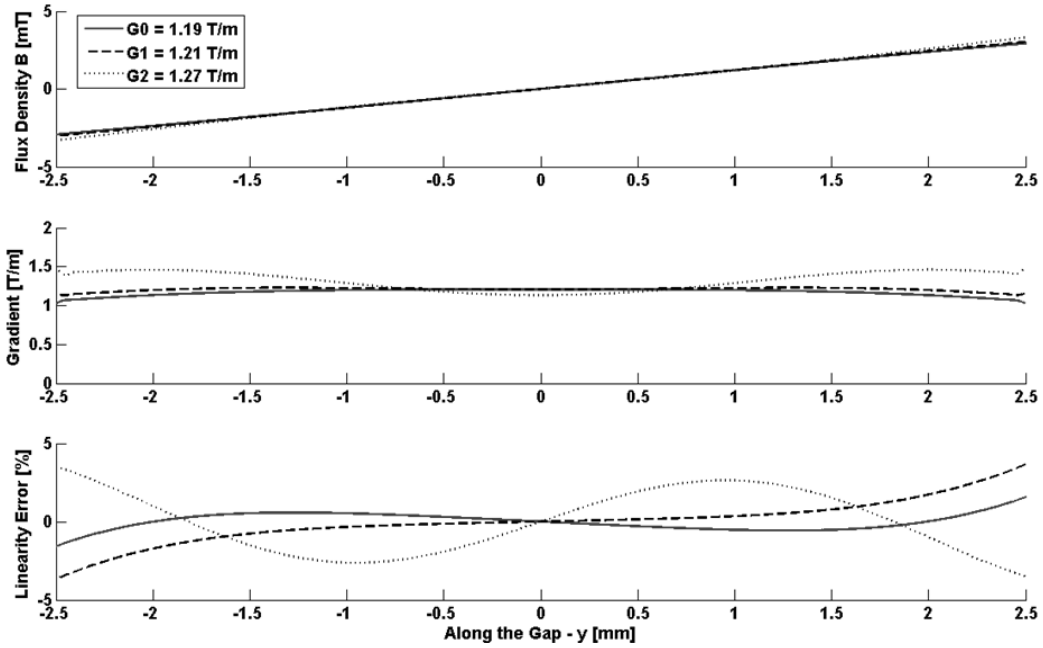

Figure 40. Simulation results of G_y: (a) shows the magnetic field contours; (b) and (c) show the gradient field strength and linearity.

Transient simulations were performed for the G_z gradient coil with and without the presence a nearby conductive medium (the pole of the main magnet) which is shown in Figure 41a. In Figure 41a, the pole is coloured according to the induced eddy current in the out-of-plane direction which ranges from 1 A/m^2 to 2 MA/m^2. As seen in Figure 41a, the highest level of eddy currents exist near the surface of the pole faces (conductive) close to the gradient coils. The simulations for the transient response are shown in Figure 41b. The magnetic field was evaluated at a point marked in Figure 41a as a function of time. In the first case in Figure 41b, the rise time is set to 10 μs. When no conductive pole is present, the magnetic field rapidly increases to its steady-state value with a rise time defined by the input. When a conductive pole is present, eddy currents oppose the rapid increase of the magnetic field which leads to a longer rise time of the magnetic field. As the rise time of the input is increased, less eddy currents are generated and the magnetic field follows the input more closely (as seen in Figure 41b for the cases where the rise time is 50 μs and 100 μs). The rise time of the gradient coil is on the order of microseconds if no conductive medium is present; if the conductive medium is placed 2 mm from the coil the rise time ranges from 10 μs to 100 μs. As expected the rise time is increased by the conductive medium which would resist the change in flux due to generation of eddy currents.

(a)

(b)

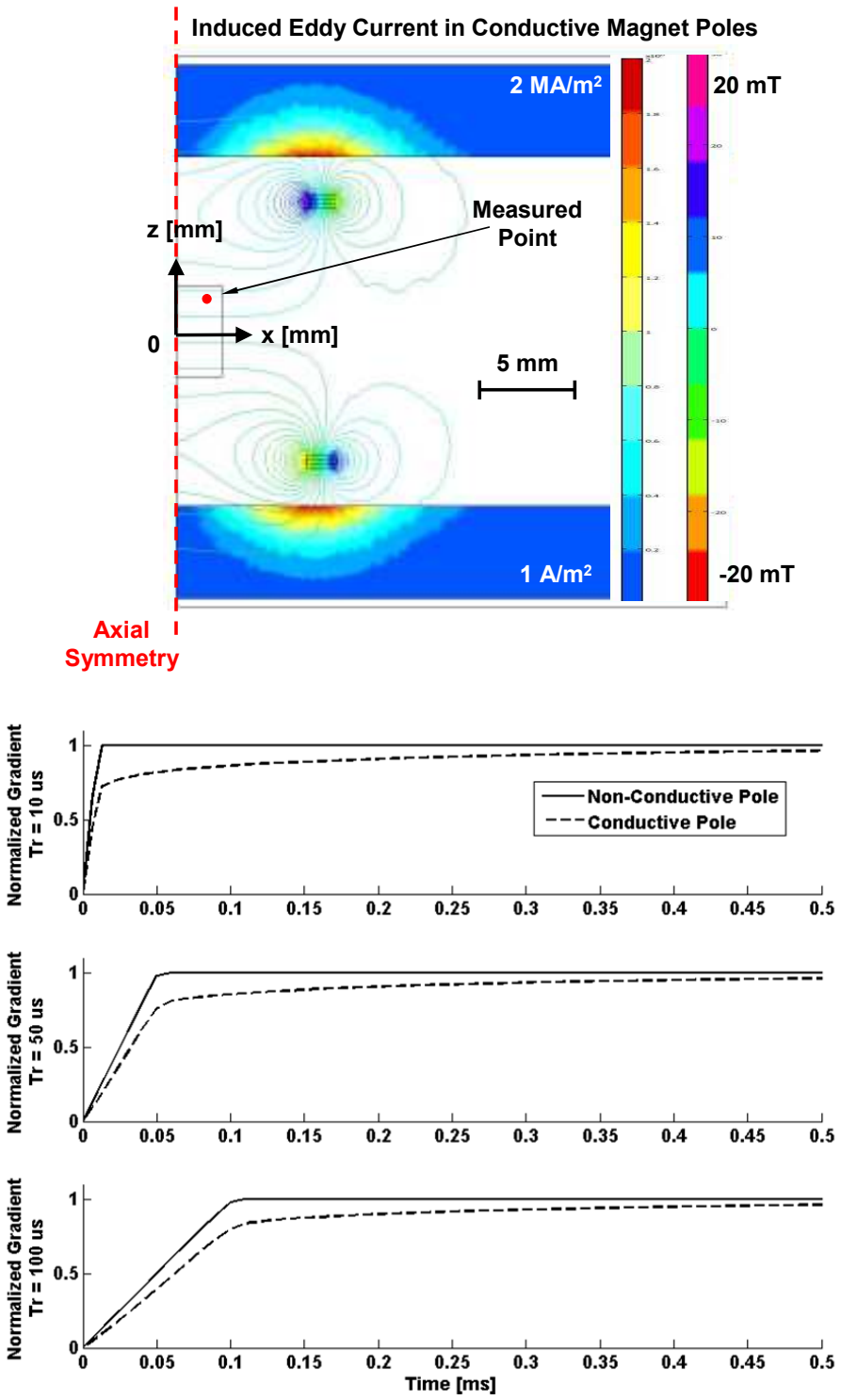

Figure 41. Simulation of the transient response of the G_z gradients in the presence of conductive and non-conductive poles. The induced currents are shown in the poles in plot (a); the transient response of the labelled point is shown in (b) with driving currents that have rise times of 10, 50 and 100 microseconds.

The positions of the current paths of the final design of the three gradient coils are shown in Figure 42.

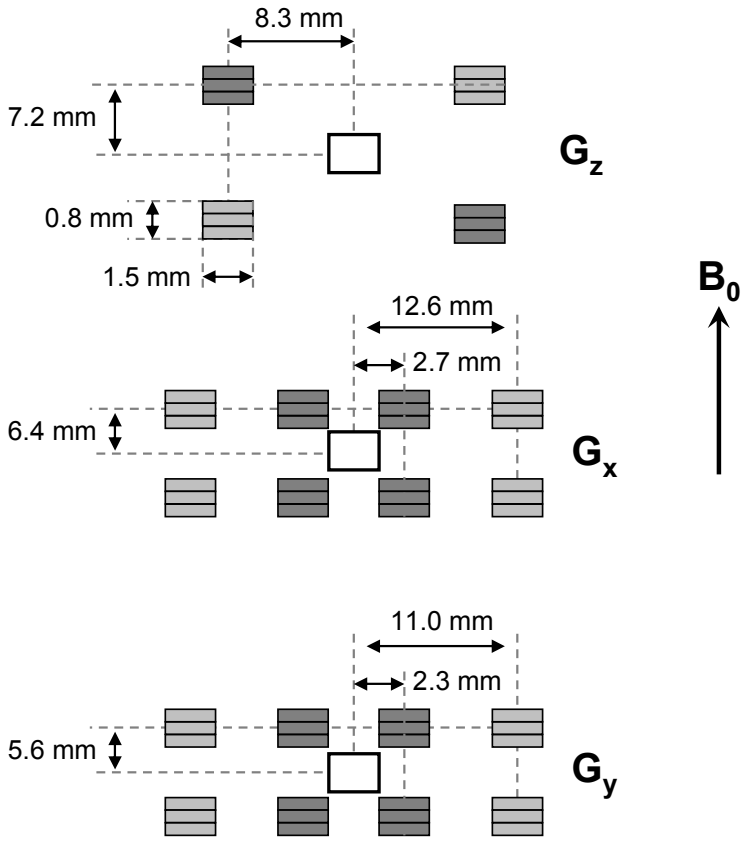

Figure 42. Dimensions of the final design of the three gradient coils are shown. All the conductors have the same width of 1.5 mm and height of 0.25 mm.

The performance parameters extracted form the results of the simulations of the gradient coils are listed in Table 9.

Table 9. Specification of the gradient coils. The clearance between the gradients is 9.5 mm and the total insert thickness is 16 mm. (number of turns n = 3)

	G_x	G_y	G_z
Gradient Sensitivity [T/m/A]	**0.0425**	**0.055**	**0.0355**
Gradient Strength [T/m] at I = 20 A	**0.85**	**1.2**	**0.71**
Linearity for a cube of 2 mm on each side [%]	**< ± 3**	**< ± 3**	**< ± 0.1**

The gradient coils are etched from a sheet of copper using the fabrication technique described in Appendix A. The gradient coils are made from copper parts stacked on top of each other to make up the three turns. All the coils have four aligning holes which are used for accurate placement of all the coils (G_x, G_y and G_z) on both sides of the insert. The mask used for the fabrication of all the coils is shown in Figure 43-a and the assembly drawing in Figure 43-b; the electrical connections points of the gradient coils are also shown.

(a)

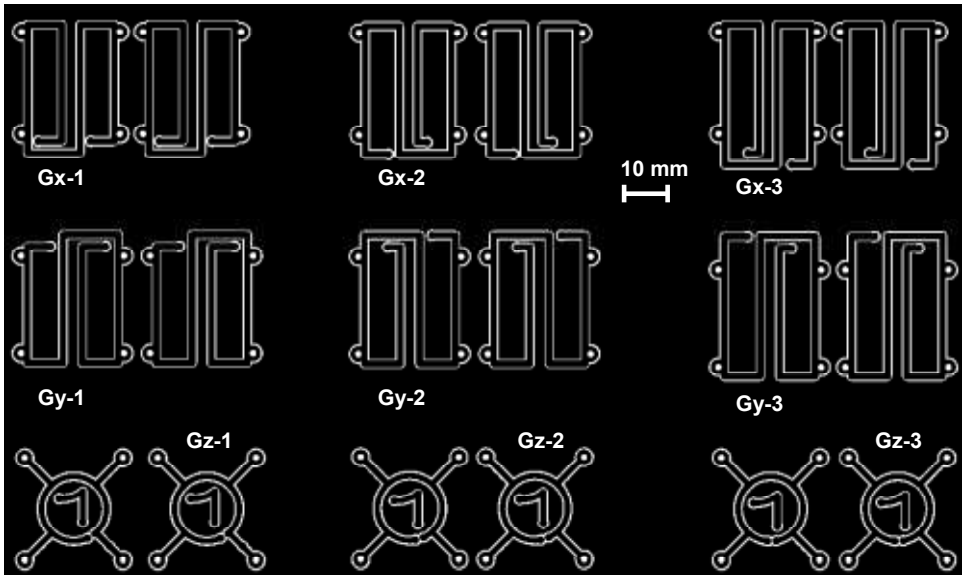

(b)

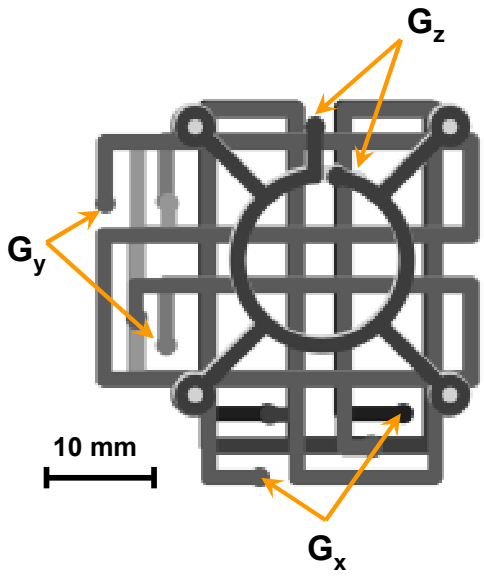

Figure 43. Mask (a) and the assembly (b) of the gradient coils.

A photograph of each individual current path after the etching process is shown in Figure 44-a. The top and angled side views of the assembled current paths before the final epoxy coating are shown in Figure 44-b. The copper strips are used for soldering connection wires between the

coils on top and bottom side of the Insert.

(a)

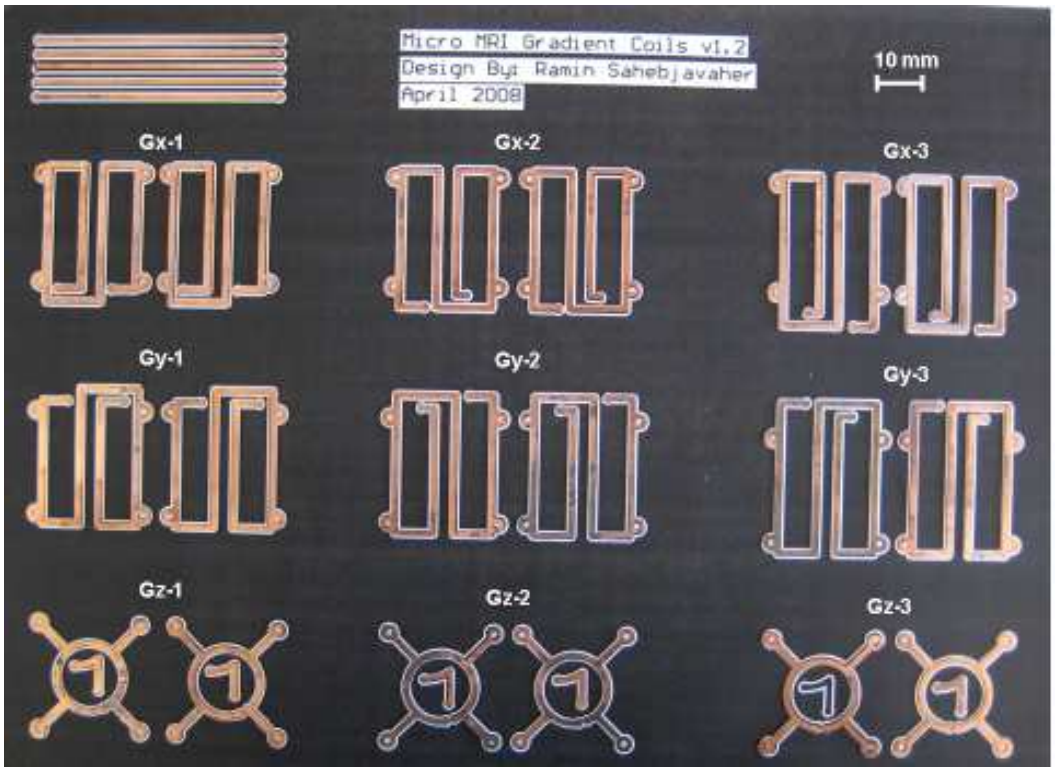

(b)

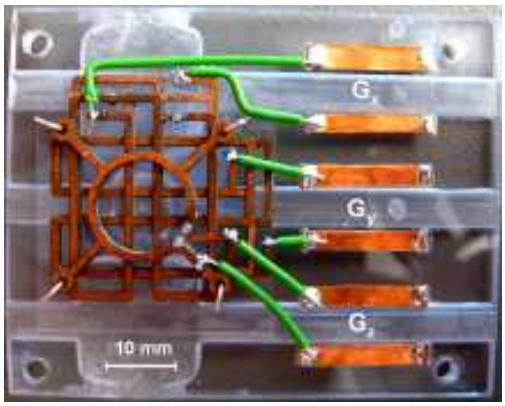

Figure 44. Photograph of the fabricated (a) and the assembled (b) gradient coils (only the top piece of the insert is shown).

Photos of the completed insert with integrated triaxial gradient coils and the RF probe are shown in Figure 45.

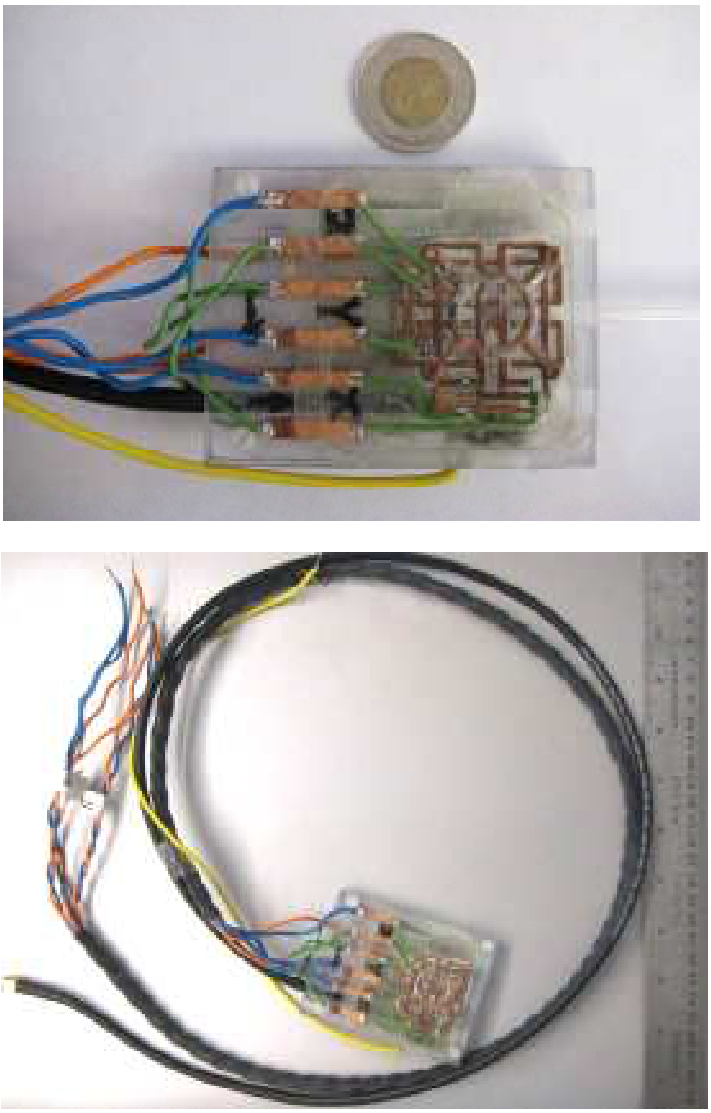

Figure 45. Top view of the insert module with integrated probe and gradients

2.2.3 Gradient Coil Characterization

The gradient coils are connected using a 1.2 m long twisted wire (AWG 18) which are used to make connections to the measuring equipment and later to the current amplifiers. The measured electrical properties of the gradient coils are listed in Table 9. The measurements were performed while the insert was located outside the main magnet.

Table 10. Measured electrical properties of the gradient coils including connecting wires.

	G_x	G_y	G_z
Resistance [Ohm]	**0.384**	**0.392**	**0.374**
Inductance [μH]	**2.35**	**2.04**	**2.06**

The electrical properties are within reasonable agreement with theory and other similar gradient coils summarized in the literature review.

In order to verify the gradient field strength, the bandwidth of the MR signal of a disk shaped sample was measured for various gradients strengths for the G_x, G_y and G_z gradient coils. Ideally, the shape of the obtained spectrum would have an oval shape if the sample has a circular cross section. The cross-section of the sample for the Gy and Gz gradients are roughly circular while the shape of the sample for the Gx gradient would be of rectangular shape if a selective excitation was used. Since slice selection was not used for these experiments (due to time constraints), the shape of the spectrum does not necessarily represent the cross-sectional shape of the sample. However, knowing the dimensions of the imaging area and recording bandwidth of the spectrum for various input currents, the gradient sensitivity can be obtained.

The sample is in a polyethylene tubing with an outer diameter OD = 2.39 mm and inner diameter ID = 1.67 mm. The sample is tab water diluted with $CuS0_4$ (40mM) to reduce the T_1 time

constant to about 30 ms [53]. A spin echo pulse with TE = 6 ms and TR = 102 ms was used. The pulse sequence is shown in Figure 46. The seconds half of the spin echo pulse is recorded, averaged for 256 times. The data is later phase corrected and Fourier transformed in MATLAB (MathWorks).

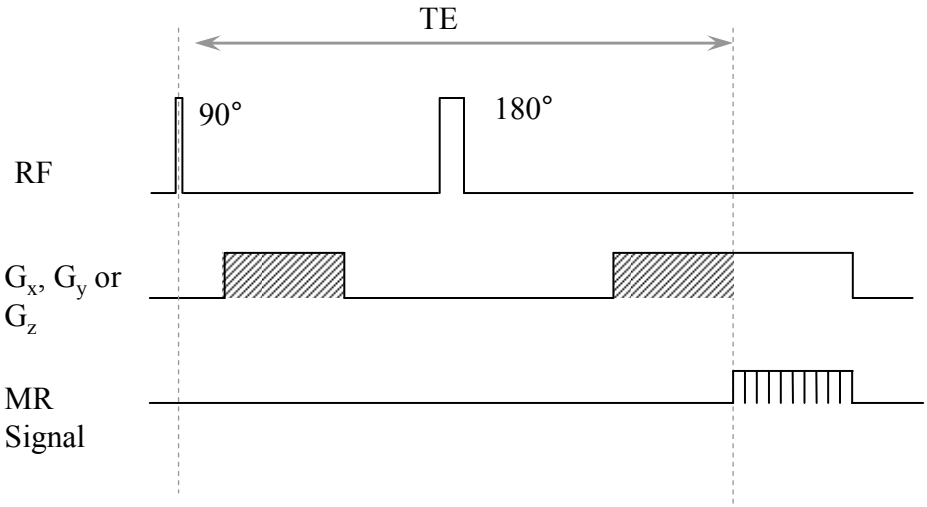

Figure 46. Pulse sequence used to verify the strength of the gradient coils.

The spectrum for the G_x gradient for field strengths up to 0.121 T/m are illustrated in Figure 47-a. As expected, the bandwidth of the MR signal is increased as the gradient field strength is increased. For the lowest current setting (I = 0.24 A) which would result in a bandwidth smaller than the homogeneity of the magnet and an increase in the echo amplitude is observed. This suggests that the gradient in this direction can be used later to actively shim the magnet by introducing a constant offset current in this gradient. Due to limitations of the bandwidth of the IF amplifier (~30 kHz) and poor SNR for larger gradients, the maximum gradient field that could be tested using this technique was limited to about 0.2 T/m for all the gradient coils. For higher field strengths, the gradients can be calibrated using a technique described by Wright *et al.* [80].

To calibrate the gradients for high gradient fields, a SE pulse sequence similar to that shown in Figure 46 is used where the RF pulse remains the same but the gradient pulse is different. Basically, immediately after the initial RF pulse a large gradient is applied in the positive direction, which is then followed by a low gradient field in the negative direction; the area of the low amplitude gradient is adjusted until the observed echo has maximum amplitude. By comparing the areas of the high and low amplitude gradient pulses, the strength of the high amplitude gradient can be estimated. The spectrums for the G_y (tested up to 0.161 T/m) and G_z (tested up to up to 0.150 T/m) gradients are illustrated in Figure 47-b and Figure 47-c, respectively.

(a)

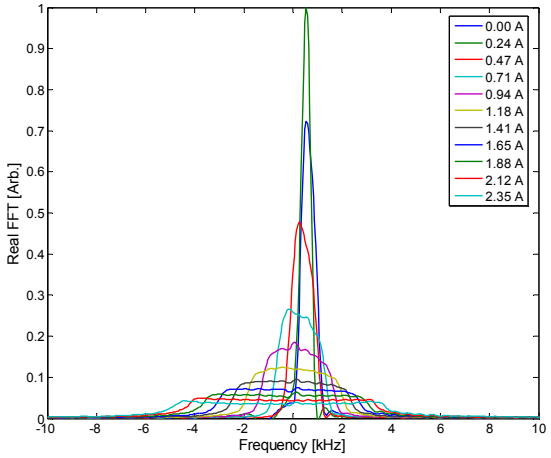

(b)

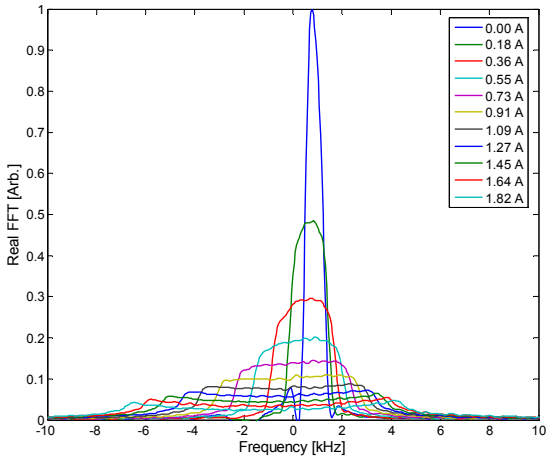

(c)

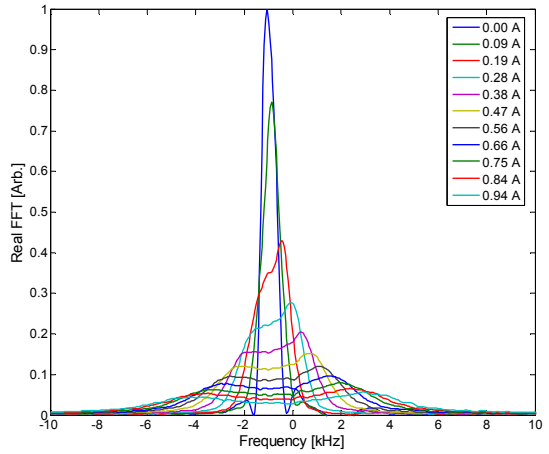

Figure 47. Bandwidth of the MR signal for different gradient field strength are shown for the three gradients G_x, G_y and G_z in (a), (b) and (c), respectively.

Again, the bandwidth increases as the gradient strength is increased. The tests performed without

compensating for the drift in resonance frequency due to magnetic field disturbances caused by temperature fluctuations. The experiments typically take between 2 to 20 minutes depending on the number of current steps and the number of averages. A frequency shift between 50-400 Hz/min is typical. This partially explains the shift in resonance frequency observed in the spectrum of all the gradients in Figure 47. Another reason for this shift that the sample is not perfectly centered in the insert which would impose a linear shift in the spectrum as a function of field strength.

The bandwidths of the MR signals are extracted from plots in Figure 47 and plotted versus the input current and shown in Figure 48. As expected, the bandwidth increases linearly with increased current (resulting in increased gradients). The slope of the each graph shows the sensitivity of the G_x, G_y and G_z gradient coils.

(a)

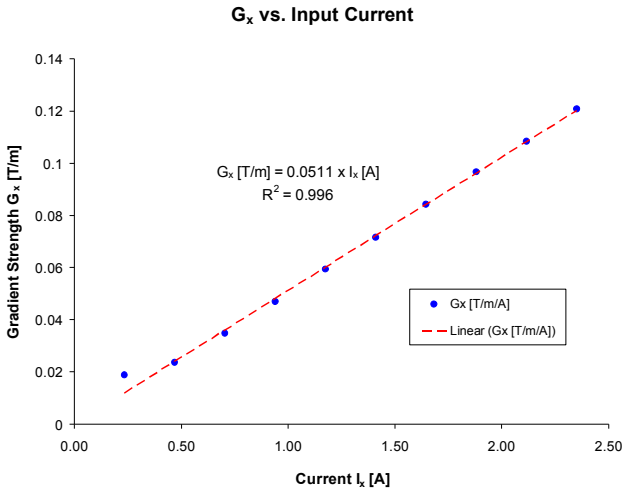

(b)

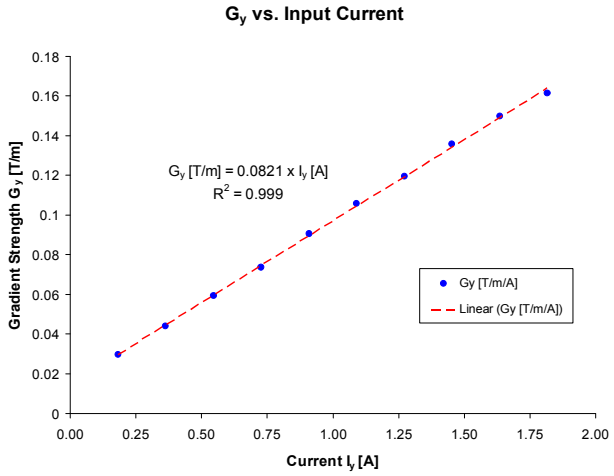

(c)

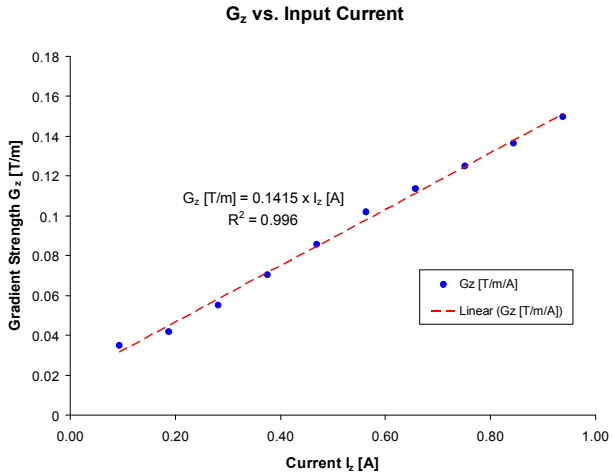

Figure 48. Gradient strength vs the input current of the gradients G_x, G_y and G_z are shown in (a), (b) and (c) respectively.

The estimated error in the measured sensitivity of the gradients can be as high as 25% due to uncertainties in the measured signal bandwidth (varies depending on the signal amplitude), inner diameter of the tube, and applied current.

The measured values for sensitivity of the coils are reasonably close to that of the simulation given above for the G_x and G_y gradient coils considering the tolerances of the insert assembly and the measurement errors. However, the gradient sensitivity obtained for the G_z gradient is off by a factor of about 3 compared to the results obtained in simulations. The measured strength of the gradient field is significantly larger than expected from simulations because the coil is exceedingly close (< 2 mm) to the iron pole (with $\mu_r = 4000$) of the main magnet, which was not considered in the simulations during the design stage. This was later verified by simulation which suggests a linearity of better than ±3%. Fortunately, the increased gradient strength is an advantage as discussed in the beginning of this section. The measured sensitivity and maximum gradient strength on the gradients is summarized in Table 11.

Table 11. Measured gradient sensitivity and strength of the triaxial gradient module.

	G_x	G_y	G_z
Gradient Sensitivity [T/m/A]	**0.0511**	**0.0821**	**0.1415**
Gradient Strength [T/m] at I = 20 A	**1.02**	**1.64**	**2.83**

There are two ways to measure the linearity of the gradients:

- A Hall-effect probe is used to measure the field at different positions, or
- An MRI image is formed of a calibration phantom that would indirectly indicate the linearity of the gradients.

If the first technique is used, the size of the Hall-effect probe has to be much smaller than

the region over which the gradients are uniform. Such small Hall-effect probe was not available for this study. As for the second technique, a cross-sectional image of a sample could not be taken due to time constraints. Therefore, the linearity of the gradient was not evaluated.

To check whether eddy currents would pose a significant problem in this setup, first a pickup coil was used to measure the induced voltage in the sample area during the switching of the gradients. The induced voltage of the coil is shown for the rising and falling edges of the 15 A current pulse into the G_z gradient in Figure 49. The G_z gradient was the only gradient tested for eddy currents as this gradient is the closest coil to the pole face of the magnet with the largest expected eddy currents. This experiment was performed once the insert was located outside the main magnet and once when the insert was inside the magnet. No significant change in the shape of the pick up voltage was observed which suggests that eddy currents are relatively small.

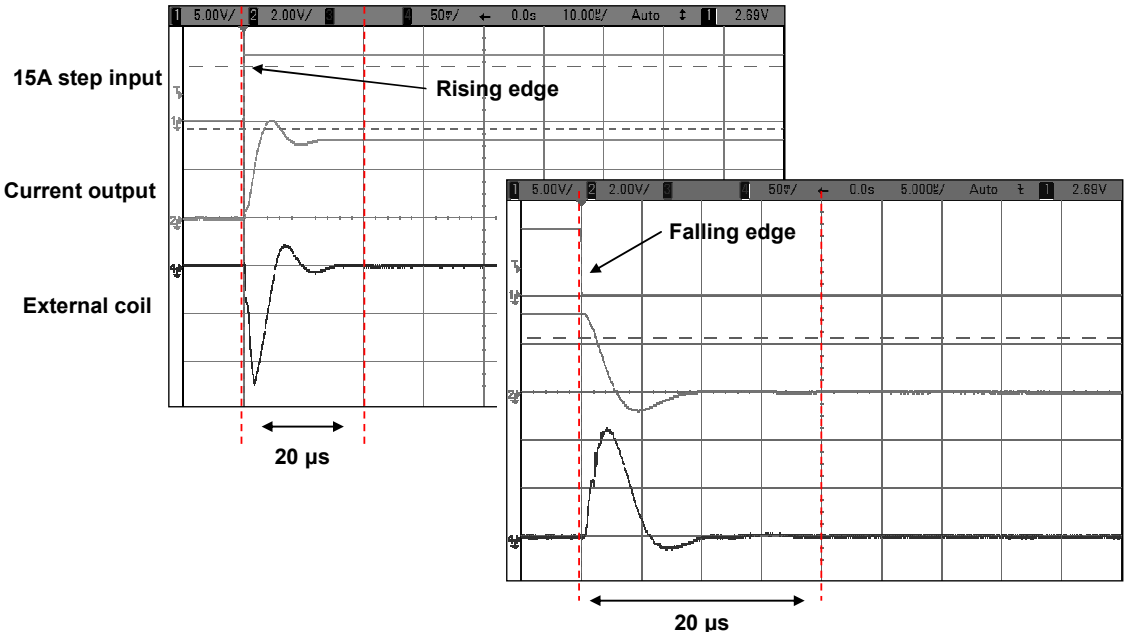

Figure 49. Magnetic flux detected by a pickup coil inside the probe area during a gradient pulse.

To obtain a better sense of the effect of the eddy currents, an eddy current pulse sequence is used as illustrated in Figure 50. A gradient field is applied for a certain duration (5 ms) and then switched off. After a short time delay (T_{delay}) a 90° RF pulse is applied and a Fourier transform of the resulting FID signal is recorded. This experiment is performed for various values of the delay and it is expected that as the delay becomes smaller, the spectrum of the FID signal becomes increasingly distorted. The time delay at which the FID signal starts to become distorted indicates the duration of the eddy currents inside the poles of the magnets [15, 84]. The longer the duration of the eddy currents, the slower the gradients can be applied. which is not desirable for high resolution microscopy.

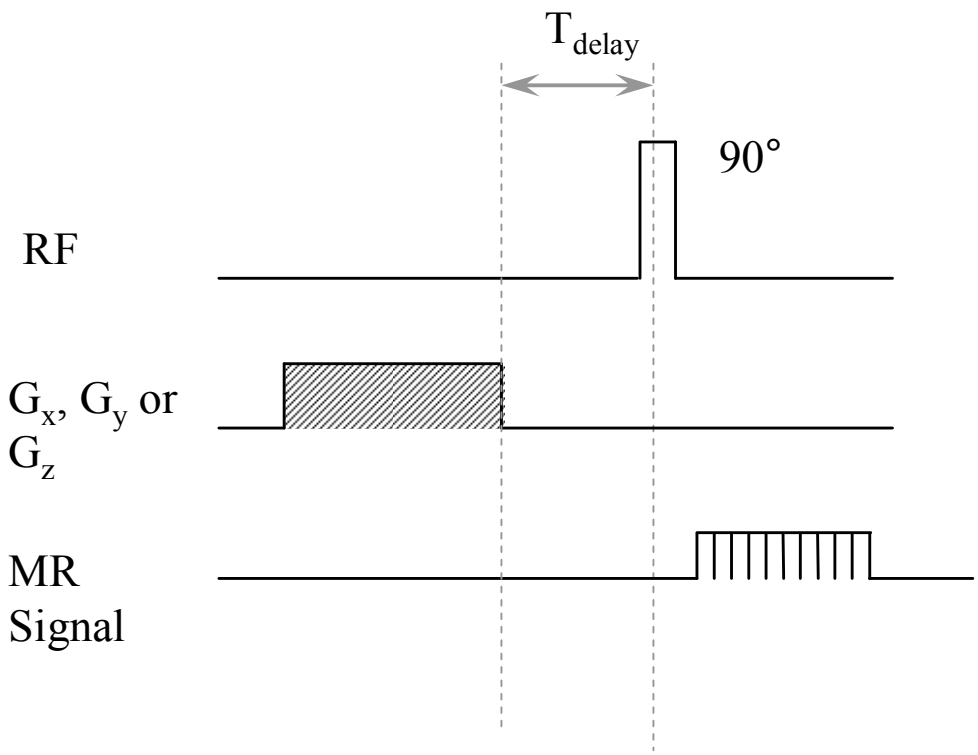

Figure 50. Pulse sequence to detect the effect of eddy currents.

The recorded MR signal (with a dead time of 60 μs) was processed offline using MATLAB. The in-phase phase corrected MR signal and the resulting spectrum are shown in Figure 51 where G_z = 0.28 T/m. The experiment is performed for three time delays: 100 μs, 15 μs and 1 μs. The spectrum is not distorted for time delays larger than 100 μs.

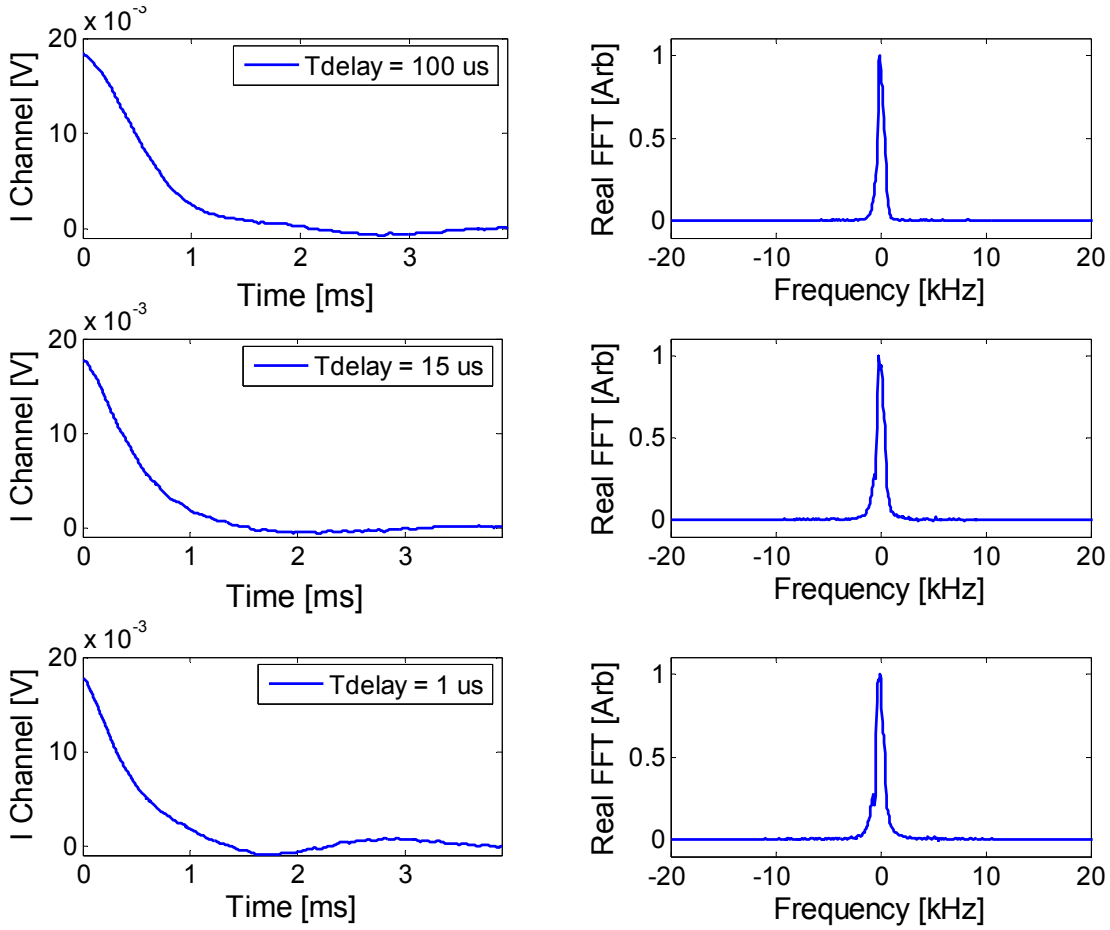

Figure 51. FID signal immediately after the removal of the gradient pulse. (G_z = 0.28 T/m)

For shorter time delays however, the spectrum becomes increasingly distorted. This is more clearly shown in Figure 52 where a fixed time delay of 25 μs is chosen while the gradient strength is increased from 0.28 T/m to 1.84 T/m.

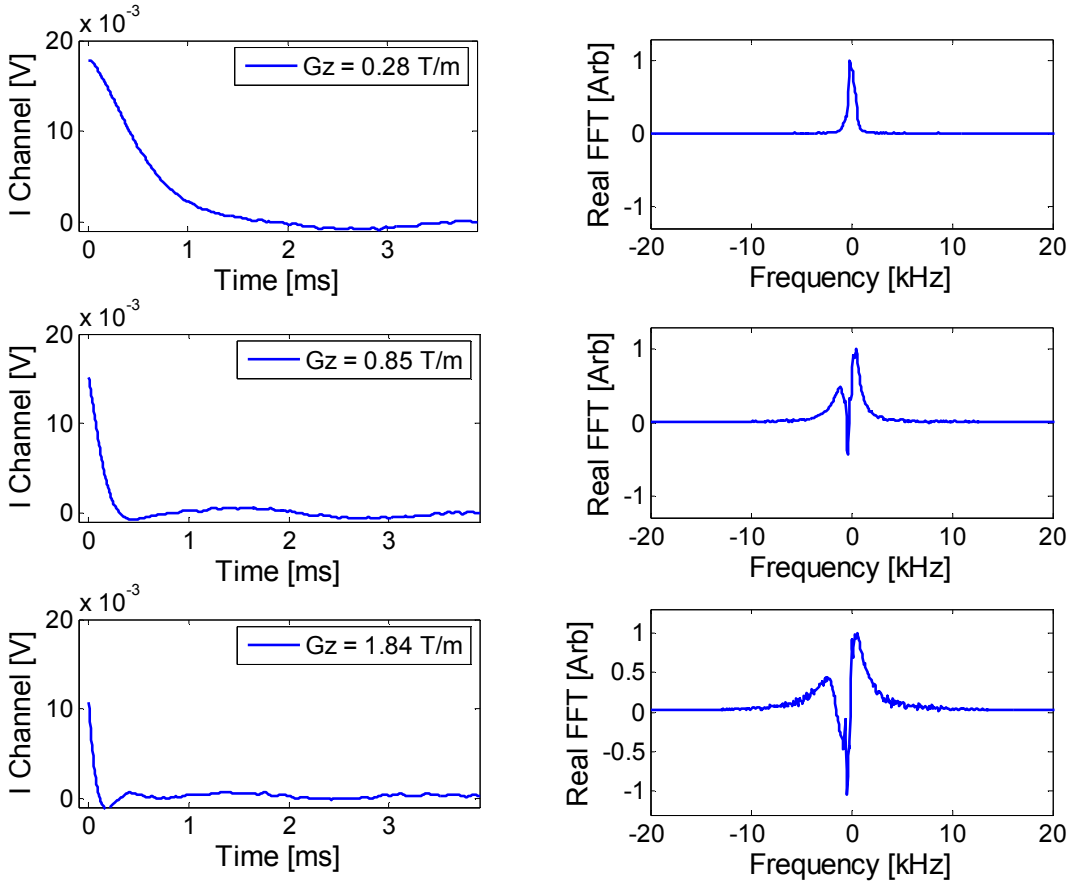

Figure 52. FID signal immediately after the removal of the gradient pulse. (delay = 25 µs)

Experimental data suggests that for gradients of about 1 T/m the eddy currents last about 100 µs. This is still acceptable considering that practically no measures where taken to reduce the eddy currents using known techniques such as reducing the rise times and employing pre-emphasis techniques [80]. Another common technique to suppress eddy currents is to introduce a thin plate with slits between the poles and the gradients [42]. More sophisticated techniques exist to actively shield the gradients using more complex gradient coil [76]. Offline image processing techniques for reducing image distortions due to eddy currents also exist and are thoroughly discussed by Bernstein *et al*. [15].

2.2.4 Summary of Gradient Coils

A triaxial gradient coil module with gradient strengths of G_x = 1.02 T/m, G_y = 1.6 T/m and G_z = 2.83 T/m has been designed, constructed and characterized. The linearity of each gradient is better than ±3% and the switching speeds of better than 20 μs have been achieved. Eddy currents would only adversely affect the signal when the z gradient is switched faster than 100 μs only for large gradients (> 0.6 T/m). The performance of this module would allow for imaging of a region of $(2\ mm)^3$ with a static image resolution of approximately 30 μm and a velocity resolution of about 50 μm/s.

2.3 Gradient Amplifiers

The design and characterization of the amplifiers that drive the magnet compensation coil and the three gradient coils are described next. The design of amplifier was mainly based on data sheets found on manufacturers websites[2, 3, 4, 5] and the microelectronics reference book by Sedra and Smith [85]. The design is also similar to a high current amplifier designed by an undergraduate student [86] for the purposes of this work.

2.3.1 Gradient Amplifier Requirements

The amplifiers drive the desired current through the gradient coils. The designed gradient coils (refer to Chapter 2.2) require currents of up to 20 amperes to generate gradients of 0.68 T/m (required for a static resolution of 30 μm and velocity resolution of 50 μm/s). The gradients are driven in bi-polar mode meaning that the current is amplified for positive and negative pulses. The gradients also need to be switched with a settling time less than 100 μs. This requires that the gradient amplifier have a rise time less than 20 μs that is equivalent to a bandwidth (BW) of greater than 50 kHz. The gradients are applied for a short time for each repetition which is referred to as the duty cycle (see Figure 53), and the duty cycle is typically below 2%. Another requirement is that input range of the amplifier has to match the output voltage range of the data acquisition/generation card (= ±10 V).

---

[2] ON Semiconductor (www.onsemi.com).

[3] Texas Instruments (www.ti.com)

[4] International Rectifier (www.irf.com)

[5] Cirrus Logic, formerly know as Apex Power Technology (www.cirrus.com)

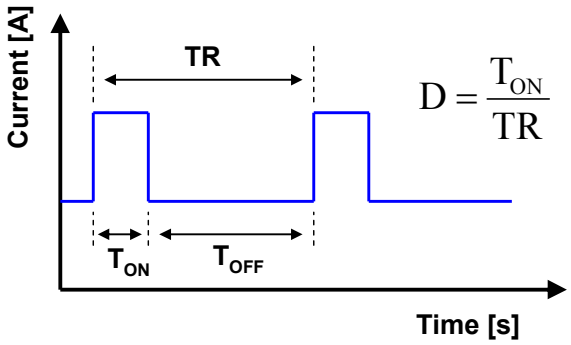

Figure 53. The duty cycle is defined as the ratio of the ON time of the pulse to its period (= repetition time, TR).

Therefore, the requirements of the gradient amplifiers are:

- Output currents up to ±20 A
- Fast switching speeds (rise time less than 20 μs, BW > 50 kHz)
- Duty cycle of at least 5%
- Input range of ±10 V.

2.3.2 Gradient Amplifier Design

There are two power amplifier architectures: linear and switching. Switching amplifiers, though more efficient, are not considered appropriate for the application of this work mainly because of the high switching noise [87]. Typically, switching amplifiers operate in pulse-width-modulation (PWM) mode at the industry standard of 20 kHz, which is appropriate for applications with a bandwidth lower than 2 kHz. Even if an amplifier with a switching frequency of 200 kHz were to be made the bandwidth would be less than 20 kHz which is lower than what is needed to drive the gradient coils. More importantly, however, the higher switching noise would be picked up by the RF probe (considering that the gradient coils are millimetres away from the probe) and

significantly deteriorate the minuscule (typically between 0.2 to 10 μV in this work) MR signals. Therefore, a linear amplifier solution is chosen for this work even though it presents significant design challenge. Integrated high current OP amps (such as the PA52 by APEX Power technologies with peak output of 80 A) are commercially available for linear amplifiers but are expensive (about CAD 700 each) considering that four amplifiers are needed. Thus it was decided to design the amplifiers mainly from discrete components.

Four amplifiers have been designed three of which are used to drive the gradient coils and one to drive the B_0 compensation coil. All amplifiers are very similar in design except for the amplifier for the B_0 compensation coil which is designed for ±5 A. Each amplifier is made of three stages as depicted in Figure 54. The power and driver stage are made from discrete components and the current controller is an operational amplifier (OP amp) that controls the response of the current in the load and corrects for any offsets and drifts from the power stage.

The load is the gradient coil with a resistance of approximately R = 0.5 Ohms (with 0.35 Ohm gradient coils and 0.15 Ohm due to connections) and an inductance of approximately L = 3 μH. The maximum voltage at the load can be estimated (~13 V) at I_{max} of 20 A using

$$V_{max} = R\,I_{max} + L\frac{\Delta I}{\Delta t} = 0.5 \cdot 20 + 3 \cdot 10^{-6}\frac{20}{20 \cdot 10^{-6}} = 13V \tag{74}$$

where ΔI is the change in current (20 A) and Δt is the rise time (20 μs). A higher output voltage is desired as overdriving the voltage would result in faster rise times. A voltage compliancy of ±26 V for the amplifier is chosen which is twice the maximum voltage at the load. A significant voltage drop (typically 7 V) exists in the power stage of the amplifier and requires using a supply voltage approximately 33 V.

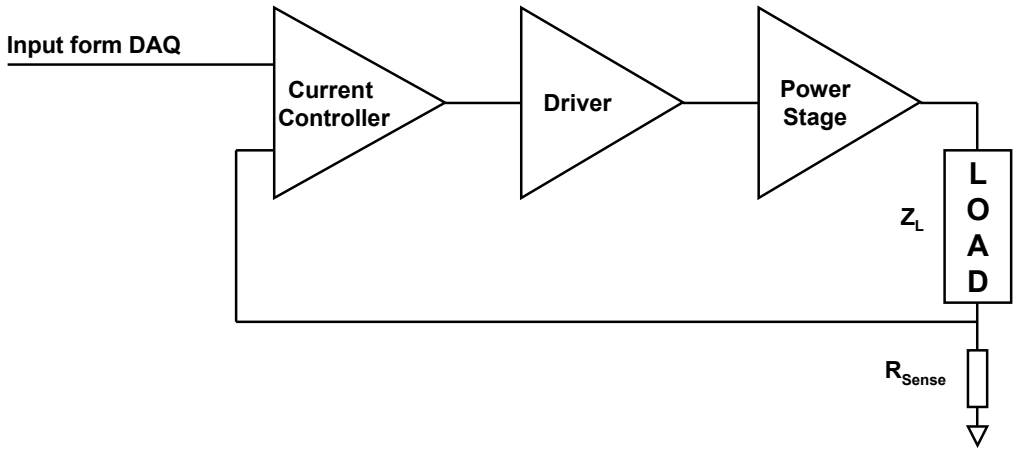

Figure 54. The schematics of the three stages of the gradient amplifier: the power stage, the driver of the power stage and the current controller is shown.

The amplifier is designed to operate in class AB (i.e., push-pull) mode using Bipolar Junction Transistor (BJTs). Amplifier design with BJTs is preferred over Metal-Oxide-Field-Effect Transistors (MOSEFTS) for this work because they are lower cost and have simpler driving circuitry. The simplified schematic of the power stages is shown in Figure 55. The two complementary power BJTs (MJ11028 and MJ11029) are used to drive the current through the load. The power BJTs have a high DC gain (h_{fe}> 400) with a high current capability (up to 50 A) and a maximum V_{CE} voltage of 60V. The complementary BJTs are in fact Darlington pairs that increase the gain and also the input impedance of the BJTs. The load current measured as a voltage using a non-inductive current sense resistor (0.05 Ohm, 20 nH) and sent as a negative feedback to the current controller.

The V_{BE} multiplier, consisting of a transistor and four resistors, biases the power BJTs to eliminate the cross-over distortion for input voltages (from the driver) less than the forward biasing voltage $V_{BE2} = V_{BE3}$ (~0.65 V) of the BJTs. The degree of cross-over distortion is controlled by the selection of the *R1* and *R2* resistors. The V_{BE} multiplier shifts the input (from the driver) by a voltage equal to

$$V_{CE1} = (1 + \frac{R1}{R2}) V_{BE1} \approx 4 \times V_{BE1}. \quad (75)$$

Typically, the resistor values are selected to make V_{CE1} between 2.5V and 4V. One of the resistors (*R1*) is a potentiometer used to adjust the biasing. For more information about class AB amplifier design and biasing refer to microelectronics reference book by Sedra and Smith [85].

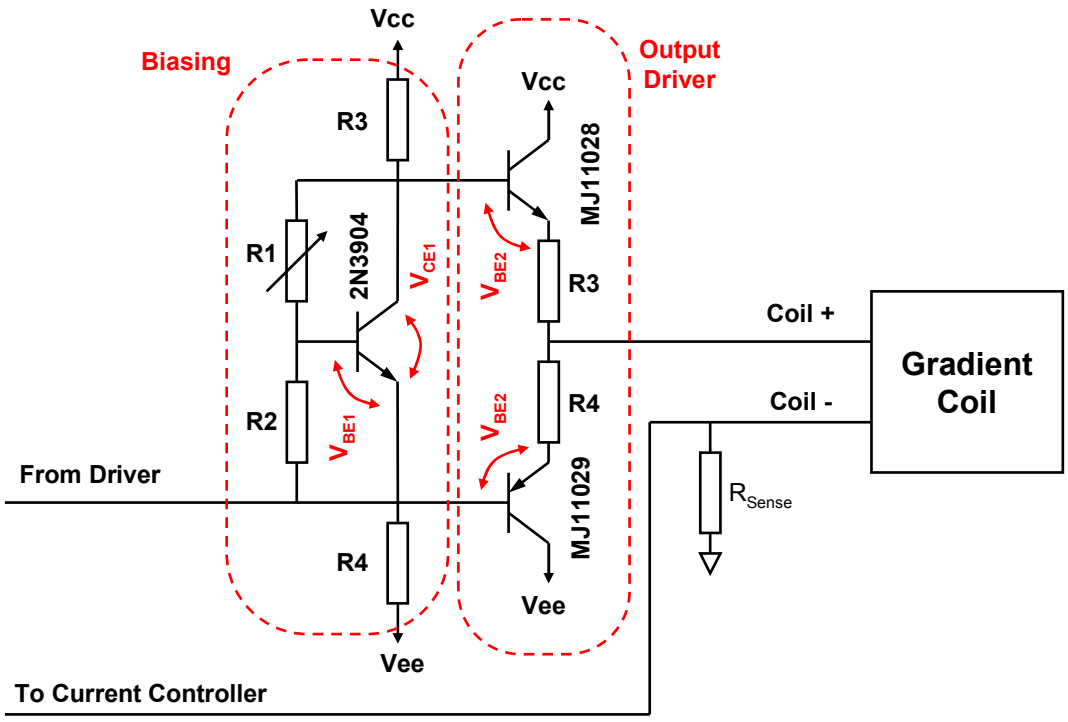

Figure 55. Simplified schematic of the power stage.

The rest of the resistor values are chosen based on simulations performed in Cadence PSPICE by trial and error and considering tradeoffs between the power rating of each component, supply voltage and the maximum current passed through the load.

The power stage is driven by the driver stage which is illustrated in Figure 56. The driver stage also consists of a class AB amplifier similar to the power stage and is driven by the current amplifier. The complementary transistors (BD675 and BD676) are also Darlington pairs with a high gain (h_{fe}> 750), current capabilities up to 4 A and a max voltage of 45V. The biasing is also performed using a V_{BE} multiplier. The bandwidth of this stage can be extended (up to 30%) by introducing a bootstrapping capacitor (C1) to increase the open loop gain.

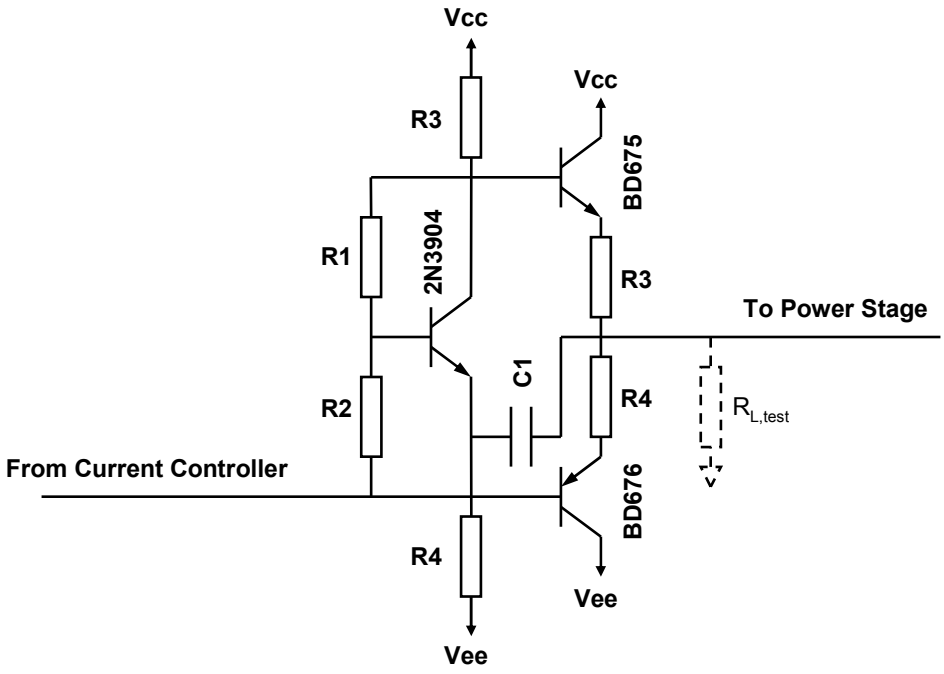

Figure 56. Simplified schematic of the driver stage.

The components of the driver stage were chosen based on simulations assuming a dummy load that has the same the input impedance as the power stage.

To control the dynamic response of the current passed through the load and also to correct for linearity and offset errors in the power stage, a current controller is implemented using an OPA453 amplifier as shown in Figure 57. The feedback is the voltage sensed by the current sensing resistor. The op amp is the weakest link in the chain in terms of bandwidth performance. Thus, it is important to select an op amp with high bandwidth, high slew rate and wide output voltage swing (requires high voltage supply). The gain-bandwidth product of the selected op amp is 7.5 MHz and has a slew rate of 28 V/μs and maximum voltage supply of ±40 V (voltage swing is $V_{supply} - 4$), which is more than sufficient for the purposes of this work.

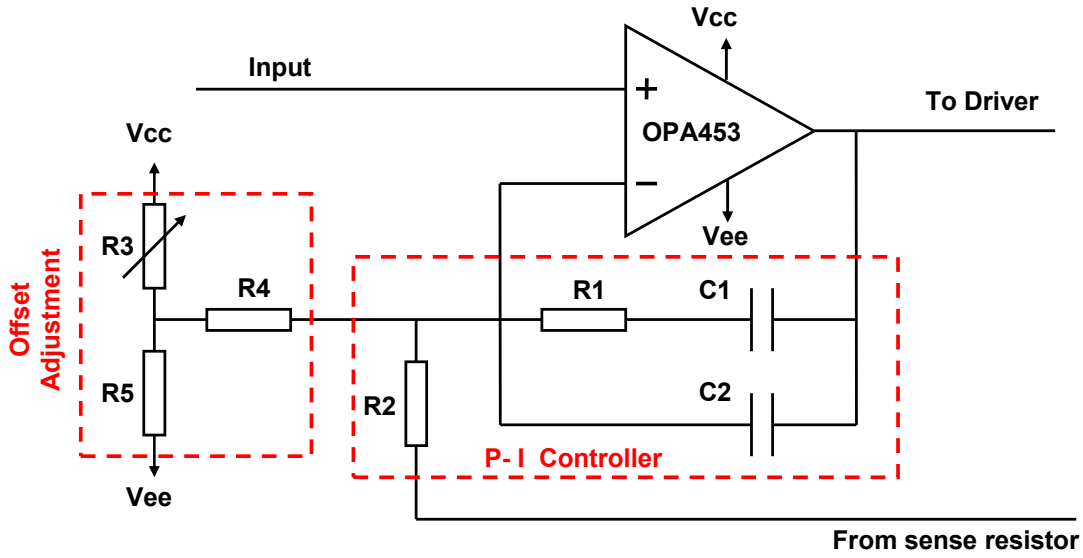

Figure 57. Simplified schematic of the current controller.

The proportional-integral controller is implemented with the combination of resistors (R1 and R2) and capacitors (C1 and C2). The transfer function in the s-domain is

$$TF = \frac{s^2(C1 \cdot C2 \cdot R1 \cdot R2) + s(C1 \cdot R2 + C2 \cdot R2 + C1 \cdot R1) + 1}{s^2(C1 \cdot C2 \cdot R1) + s(C1 + C2)} \tag{76}$$

with poles at

$$Poles = 0, -\frac{(C_1 + C_2)}{R_1 C_1 C_2}. \tag{77}$$

By selecting proper values for the *R1*, *C1*, and *C2*, the rise time can be minimized while reducing the oscillations in the output are reduced or eliminated. To remove any residual offset that might appear in the final implementation, a offset adjustment circuit using a voltage divider is used as shown in Figure 57.

In order to monitor the current of the load (shown in Figure 58), another op amp is used to drive

the oscilloscope probe with the gain of the OP amp being 5 V/V (corresponds to an overall gain 4 A/V). The current monitor can also be used in the feedback loop to increase the voltage from the sense resistor. This feature is not utilized for the purposes of this thesis, but it would be useful for future gradient coils that might have a different load impedance. The current monitor is implemented using the OP37 with a gain bandwidth of 40 MHz and a slew rate of 10 V/μs with a maximum supply voltage of 22V. The fast response of this OP amp ensures that no delay is observed in the monitoring signal.

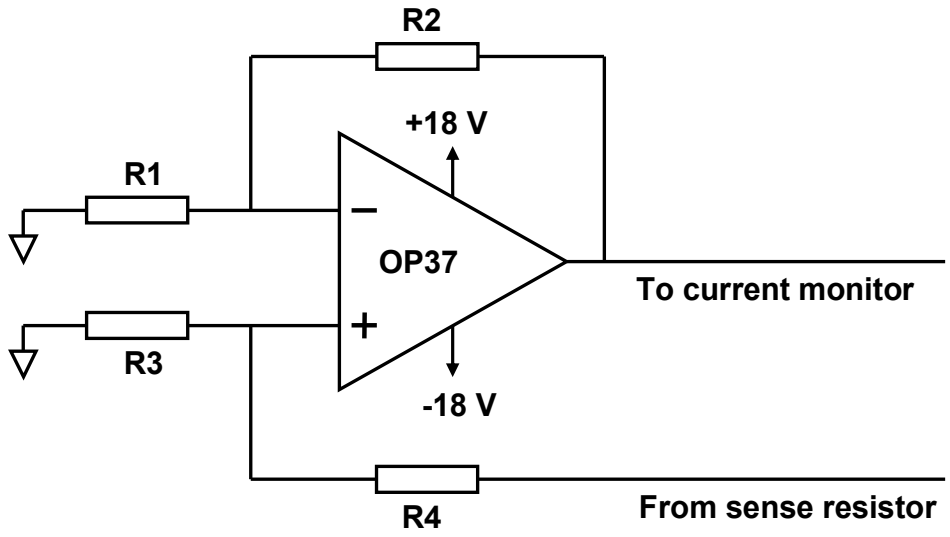

Figure 58. Schematic of the current monitor.

The gain of this OP amp is found as

$$\text{Gain} = \frac{1 + R2/R1}{1 + R4/R3}, \tag{78}$$

and by selecting the resistors (R1 = 2 kΩ, R2 = 10 kΩ, R3 = 10 kΩ, R4 = 2 kΩ) gain of 5 is obtained; this values was chosen because this op amp is not stable for gains of 5.

Each of the described stages was simulated separately and its performance was verified. Then, all the stages were connected to each other and simulated again. The final component values are shown in the screenshot of the simulation shown in Figure 59. The power, driver and current controller stages are marked as shown. The input voltage is adjusted to the specified rage of the data acquisition (DAQ) board to ±10 V using a voltage divider. The circuitry for the current monitor is not shown.

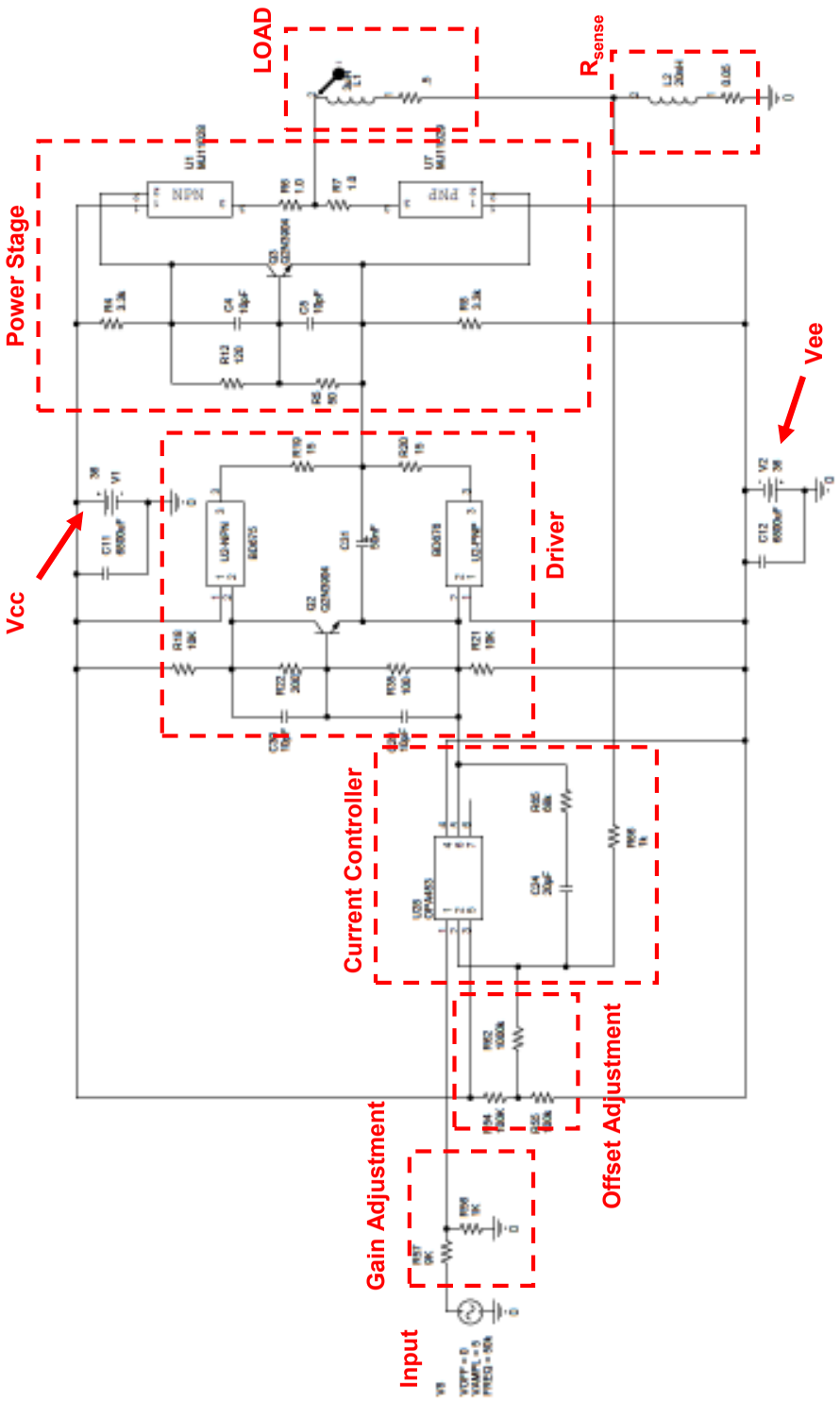

Figure 59. Screenshot of the final values obtained by simulation.

The steady-state output current versus the input voltage of the amplifier is shown in Figure 60. The input voltage is shown on the horizontal axis and ranges between ±10V corresponding to an output current (vertical axis) saturating at ±20 A. Therefore, the total gain of this amplifier (the slope) is 2 A/V, which can be adjusted using the potentiometer at the input of this amplifier (to 1A/V). The saturation of the amplifier will be lower if the supply voltage is decreased. The amplifier is designed to operate with a supply voltage between ±20 - ±36 volts.

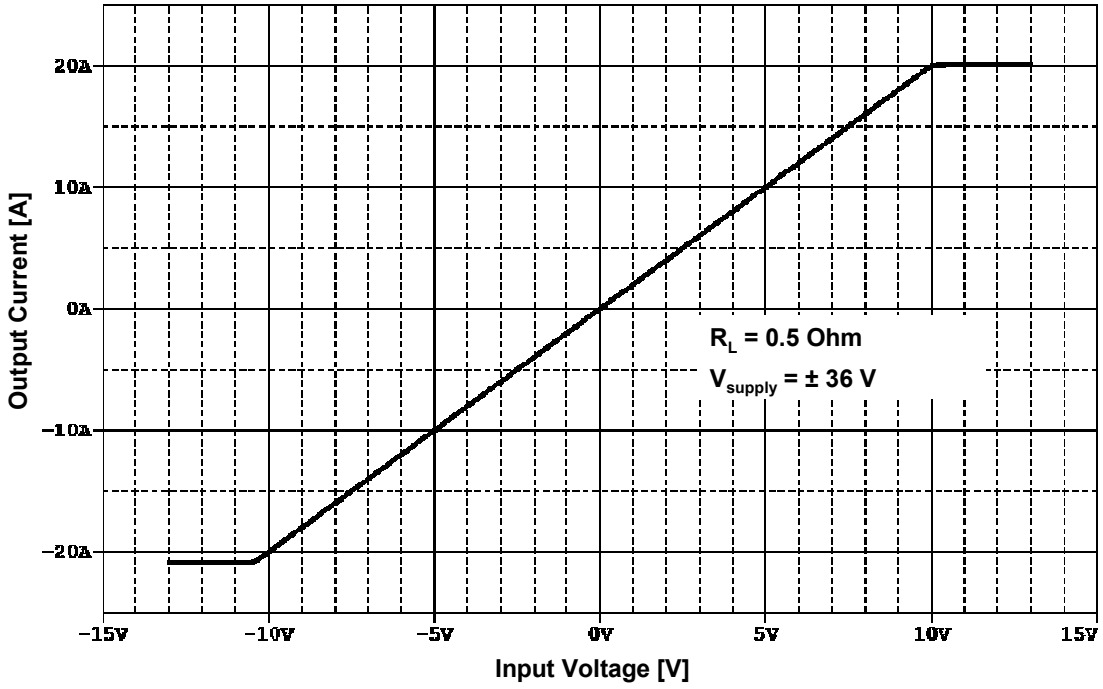

Figure 60. Simulated steady-state output current versus the input voltage. The input voltage range is set to the maximum range of the DAQ (= ±10 V). The maximum output current is ±20 A.

A sample sinusoidal response of a 10 kHz sine wave with a ±10 A amplitude of simulations is shown in Figure 61. The output of resembles a perfect sine wave and there are no visible indication of any offset or cross over distortion. The phase shift at this frequency is less than 3 degrees.

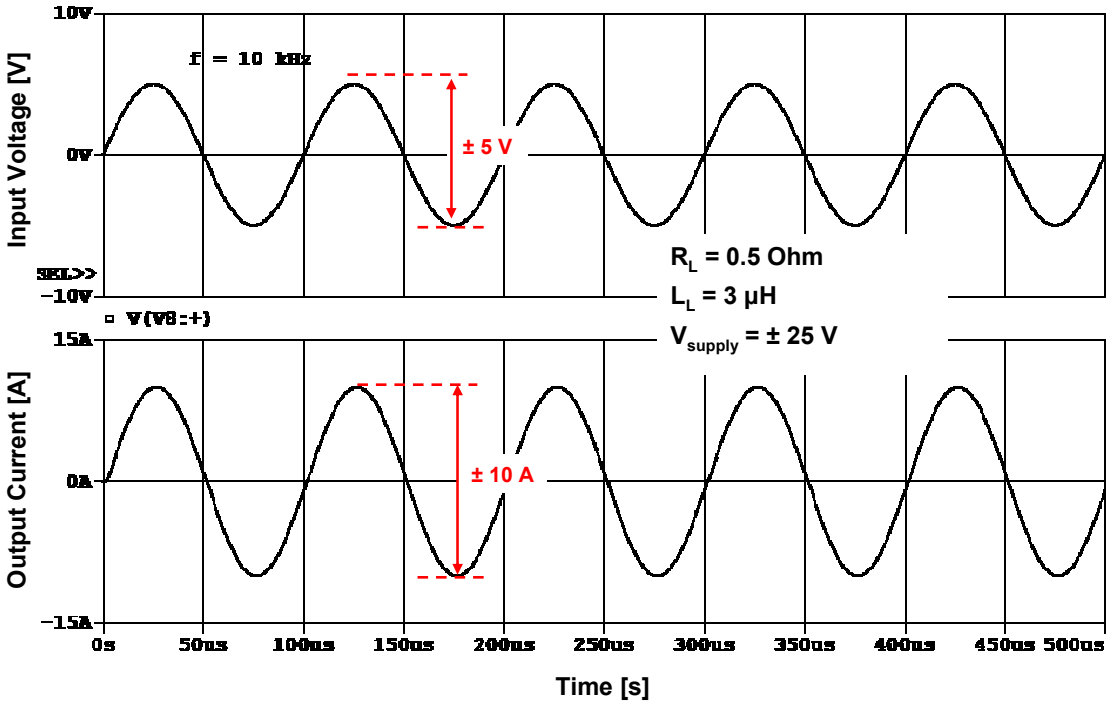

Figure 61. Simulation of a 10 kHz sinusoidal input with ±5 V amplitude (top) resulting in a sinusoidal output of amplitude ±10 A (bottom).

A sample pulse response with +20 A amplitude and pulse duration of 20 µs of simulations is shown in Figure 62. The output current closely follows the input with minimal overshoot, rise time of 4 µs and fall time of 3 µs. The settling time is less than 10 µs. The performance characteristics exceed the required switching and current levels needed to drive the gradient coils.

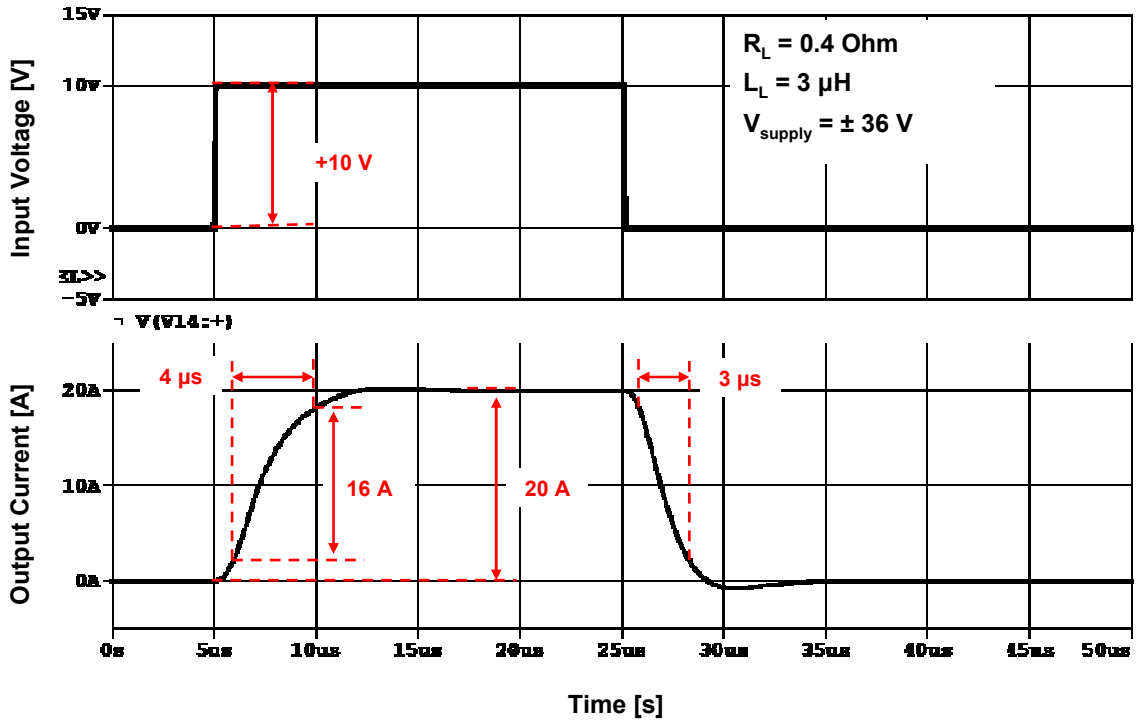

Figure 62. Simulation of a +20 A pulse (bottom) for +10 V input (top). The rise and fall times indicates that this amplifier exceeds the performance requirements necessary for very fast gradient switching.

The amplifier that drives the B_0 compensation coil has similar characteristics to the other amplifiers. The maximum current capability is ±5 A with a bandwidth of more than 50 kHz.

Similar to most linear amplifiers the limiting factor in terms of duty cycle and current rating is the power dissipation of the power stage. The maximum mean dissipation power of a linear amplifier in this case can be found using [87]

$$P_d = \frac{2}{\pi} I_{max} V_s = \frac{2}{\pi} \cdot 20 \cdot 36 \simeq 460 W, \tag{79}$$

where V_s is the supply voltage (= 36 V). The maximum mean dissipation power considering a

duty cycle of 20% is about 90 W for each amplifier. Therefore, based on theory only, the total power dissipation of four amplifiers would be 360 W which does not take into account the any DC current or non-idealities in the biasing of the power stage.

The power dissipation of each component of the power stage (for one amplifier) in steady-state conditions (DC current) was simulated and the result is shown in Figure 63. The top plot shows the power dissipation versus the input voltage while the bottom plot shows the output current versus the input voltages. The resistors (R3 and R4 in Figure 55) dissipated power proportional to the square of the output current and the BJTs have a peak dissipation of about 210 W in the midrange of the input (±6 V).

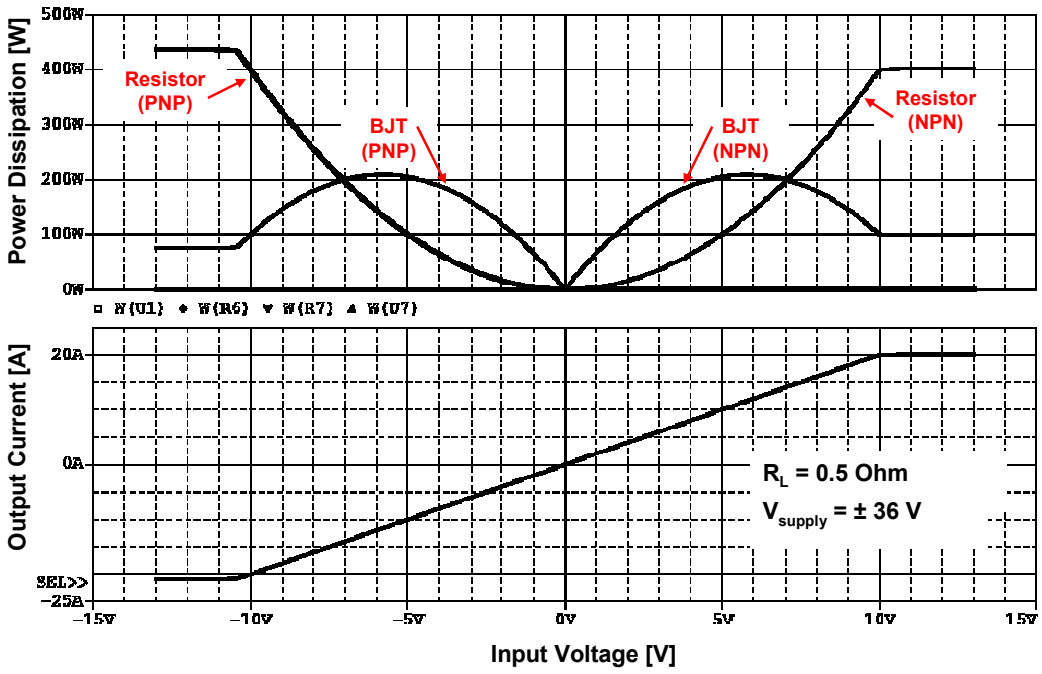

Figure 63. Simulation of the steady-state power dissipation (top) of the most critical components of the power stage for as full range ±10 V input (bottom).

The simulated average power dissipation for a 50 kHz sine wave with a ±10 A amplitude is shown in Figure 64. The output of the amplifier is shown in the bottom plot while the power dissipation of the main components of the power stage is shown in the top plot. The total average power dissipation of a single amplifier is shown as a bold line in the top plot that saturates at about 195 W. Therefore, the heat sink of this amplifier has to able to dissipate at least 200 W to ensure its proper operation. The total power dissipation of four amplifiers is about 800 W based on simulations. It is noted that the power dissipation is considerably less for lower supply voltages and higher load impedances. For example if the voltage of the power supply is reduced from ±36 V to ±30 V, the power dissipation for ±10 A sinusoid with output would be 160 W.

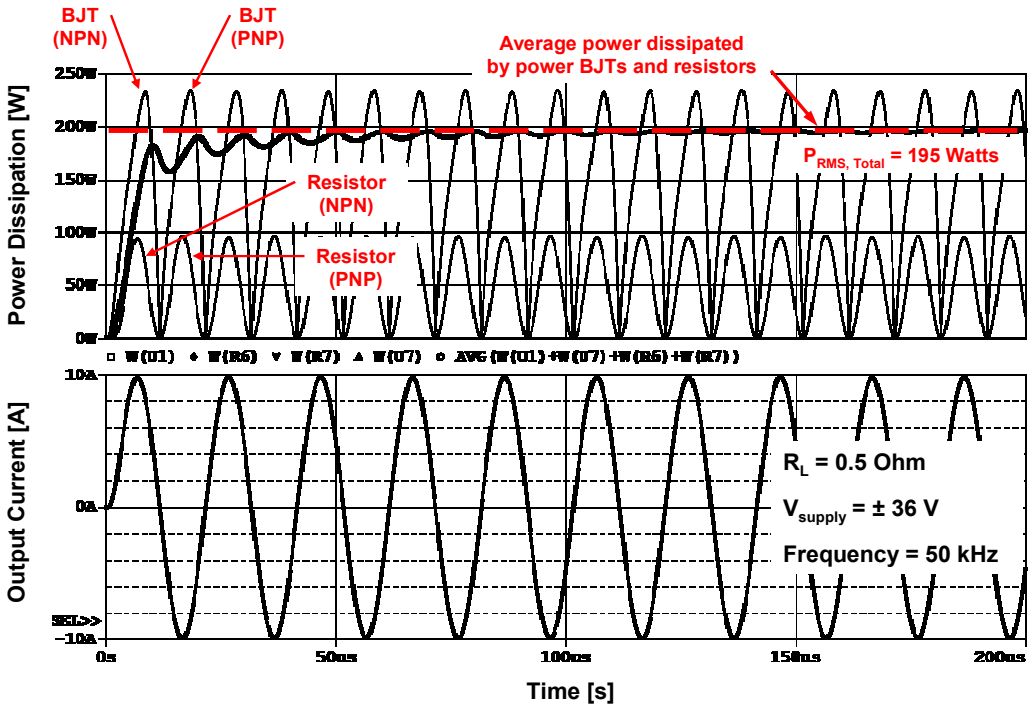

Figure 64. Simulation of the power dissipation (top) of the most critical components of the power stage for a 50 kHz ±10 A sine wave (bottom). The average dissipated power of the combined resistors and BJTs of the power stage is shown as the bold line saturating at about 195 W for each amplifier.

With a heat sink capable of dissipating 200 W of thermal power, ideally, a duty cycle of 40% can be achieved for 20 A pulses. This values is calculated by adding the power dissipation of the NPN BJT (100 W) and resistor (400W) at 20 A (input of 10 V) from Figure 63. The duty cycle is then 200/(100+400) = 40%.

The schematic layout of the thermal design is shown in Figure 65. The power BJTs (TO-3 package) are attached on the top and resistors (TO-246 package) to the bottom of a ½" thick aluminum plate. The collector connection of the BJTs is connected to its case which has to be electrically isolated (but thermally conducting) from the aluminum plate. As shown in cross-sectional view in the top-left in Figure 65, a Mica layer is typically used for this purpose. The pins of the BJTs are not long enough to pass through the aluminum plate; therefore, pin connectors were used to make electrical contact. The connections to the collector (case of TO-3) were transferred to the bottom using a #6 bolt using a semiconductor mounting kit that contains all the necessary fittings, as shown in the cross-sectional view in Figure 65. The power resistors are bolted to the aluminum plate and aligned in such a way that one of the pins of each opposing resistor can be bent downwards to make a direct wire connection to the load (see cross-sectional view in Figure 65 bottom-left). The aluminum plate serves as the mechanical support and the heat-conducting medium between the PC cooling fan and power stage. A copper (with thermal conductivity at least twice as large as aluminum) plate can be used for better performance. The Freezer 7 Pro PC[6] cooling fan was chosen for its superior heat removing performance (up to 200W) with a 0.17 °C/W resistance and its relatively low cost.

[6] Zalamn Cooling Innovations (www.zalman.com)

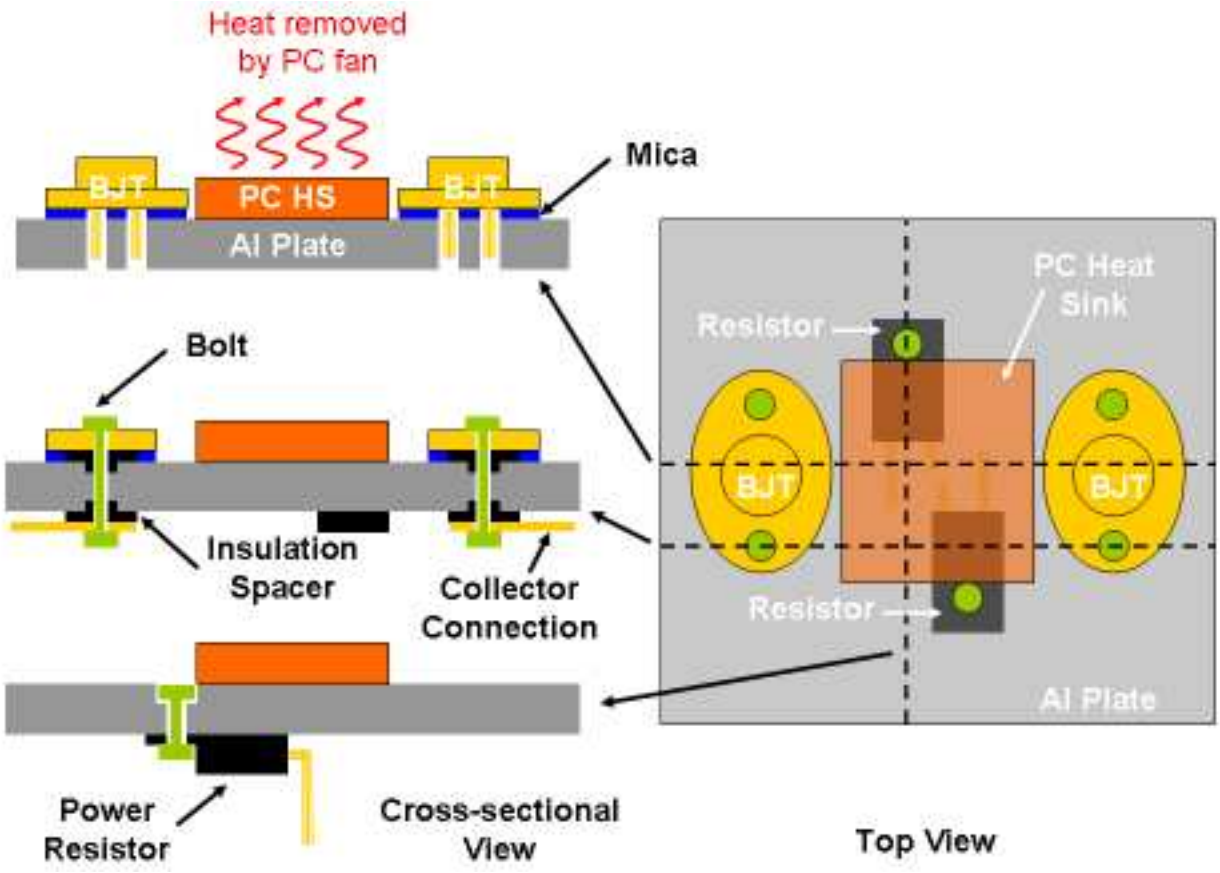

Figure 65. The top view shows the schematic layout of the BJTs and the power resistors on the heat sink. The three cross-sectional views show the details of the mounting of the BJTs and resistors.

When sizing the cooling fans and the aluminum plate, the thermal model shown in Figure 66 was used. Each BJT generates an average of about 65 W of heat with each resistor generating about 35 W. The maximum allowable junction temperature is 200 °C and 175 °C for the BJT and resistor for a case temperature of 25 °C respectively. The shown values for the thermal resistance are mostly found in the data sheets of the selected components. The Thermal resistance of the each power BJT is a reported 0.58 °C/W and 1.50 °C/W for the power resistors. The heat resistance of the aluminum plate is estimated using

$$R_{thermal} = \frac{\Delta T}{P_d} = \frac{d}{k_{AL} A} \tag{80}$$

where d is mean distance between the components, A is the average area the heat flux passes through, and k_{Al} is the thermal conductivity for aluminum (~ 205 W/m/°C). The thermal resistance of aluminum for the resistors is about 0.15 °C/W and 0.2 °C/W, respectively. The Mica insulator has a thermal resistance of about 0.1 °C/W and the thermal paste (applied between the aluminum plate and power components) has a thermal resistance of 0.05 °C/W.

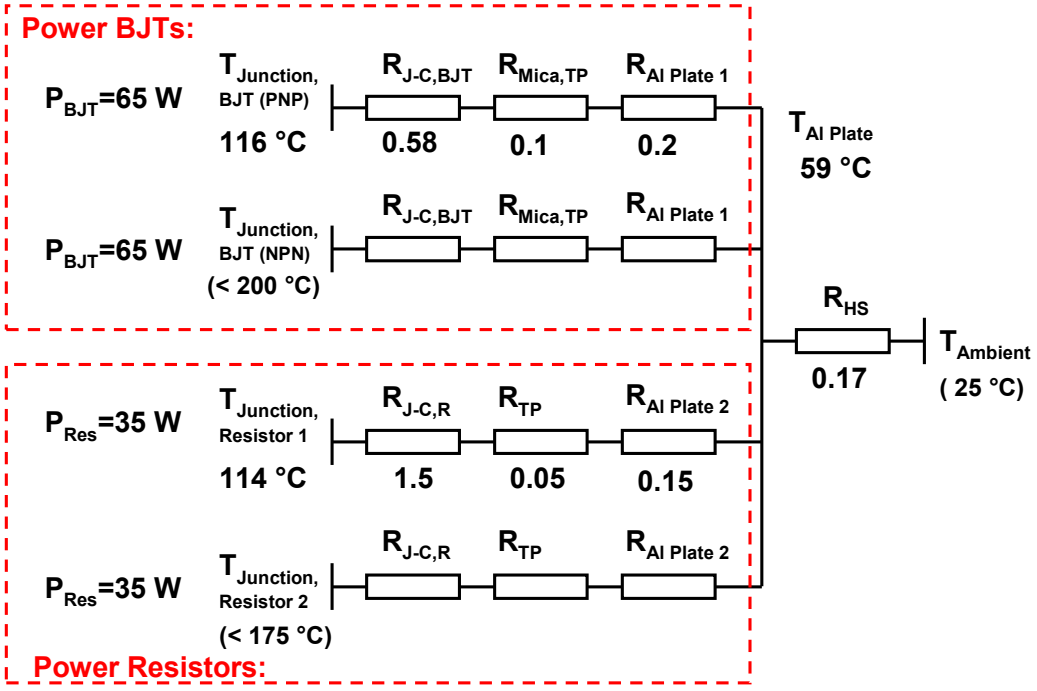

Figure 66. Lumped model of the power dissipation of the power stage.

The model suggests that the junction temperature of the BJTs reaches 116 °C which is lower than the 200 °C maximum allowable temperature. Similarly for the resistor, the junction

temperature of 114 °C is obtained which is lower than the 175 °C maximum allowable temperature. It is important to note that a de-rating of up to 20% is applied to the maximum power rating of the resistors which have a maximum power rating of 100 W. The design heat sink is therefore more than sufficient to dissipate all the heat generated by the power stage of a single amplifier. In order to maximize the performance in terms of heat dissipation of the amplifier, the heat sink was designed to accommodate six fans rather than the required four. In future, it is possible to increase the duty cycle of two of the amplifiers from 40% to approximately 80% by connecting another power stage in parallel to the existing amplifier.

2.3.3 Gradient Amplifier Construction

The CAD drawing of the assembled power stage on the heat sink and the printed circuit boards containing the rest of the electronics is shown in Figure 67. Each of the two printed circuit boards (PCBs) that is mounted on the aluminum plate contains the necessary electronics for driving the power stage of two amplifiers. The PCBs are connected to the power stage using separated wires. The cooling fans are power by a switching voltage regulator on the PCBs.

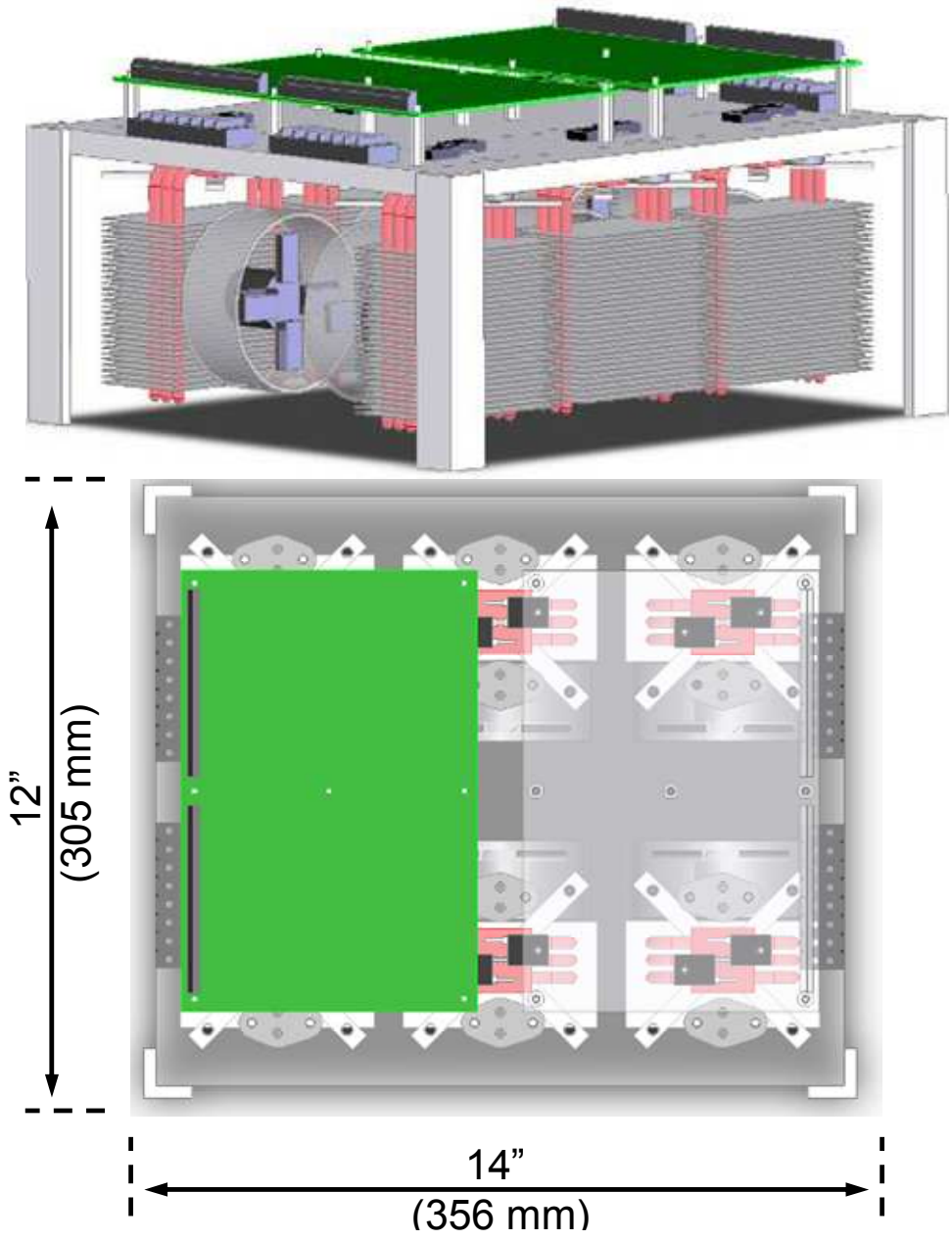

Figure 67. CAD drawing of the assembled power stage and the PCBs of all four amplifiers. The overall dimensions are also indicated.

For a detailed circuit schematic and PCB design for the complete amplifier refer to Appendix B. A photo of the heat sink with the power BJTs attached is shown in Figure 68a and the resistors on the back side in Figure 68b. The cooling fans are mounted on the same side as the power BJTs as shown in Figure 68c. The heat sink has an open design for maximum air flow.

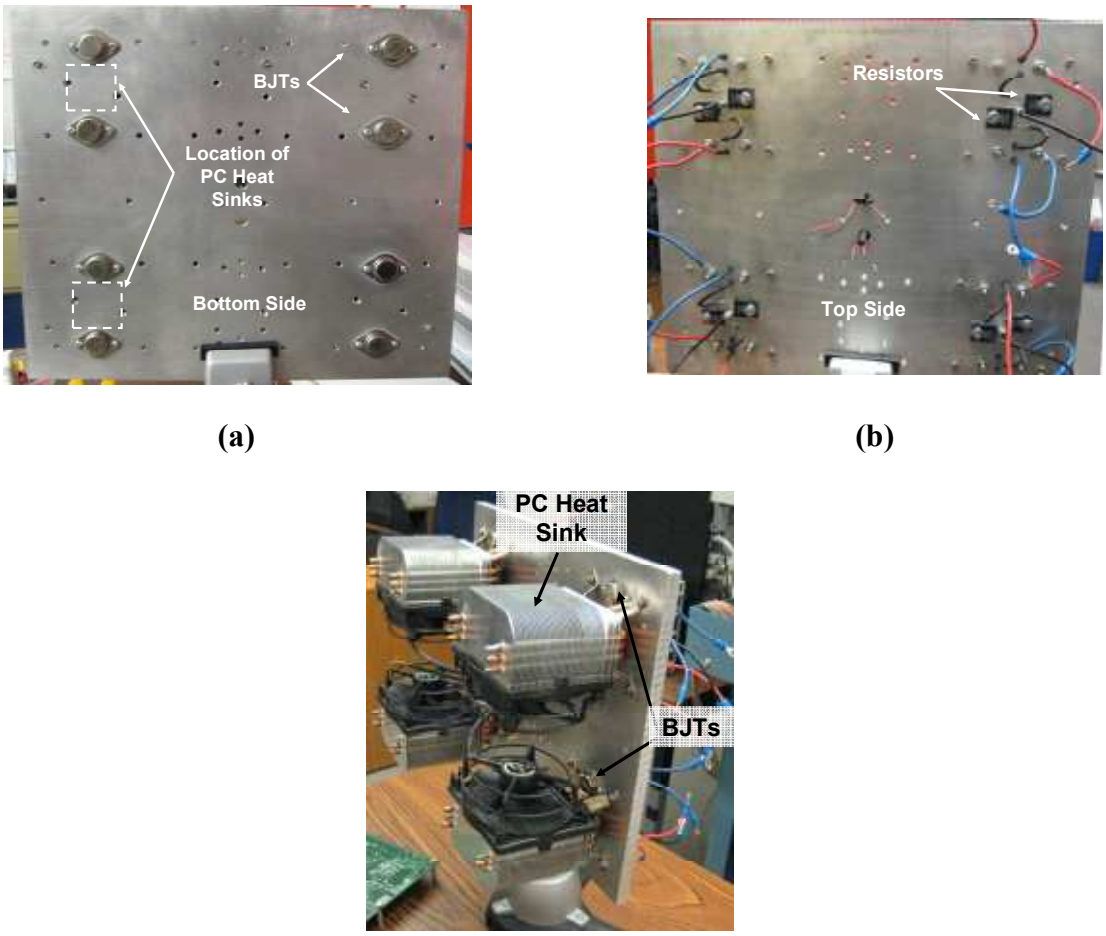

(a) **(b)**

(c)

Figure 68. Photos of the heat sink with the BJTs mounted on top (a) and resistors mounted on the bottom (b). The PC cooling fans are attached on the top side (c).

Photos of the assembled PCBs for all four amplifiers (as marked) are shown in Figure 69. Two 760W 19A 40V Agilent N5746A power supplies are used to generate the needed supply between

±20 to ±36V. The maximum voltage of the amplifiers is limited by the three voltage regulators ±18V and the cooling fan power supply).

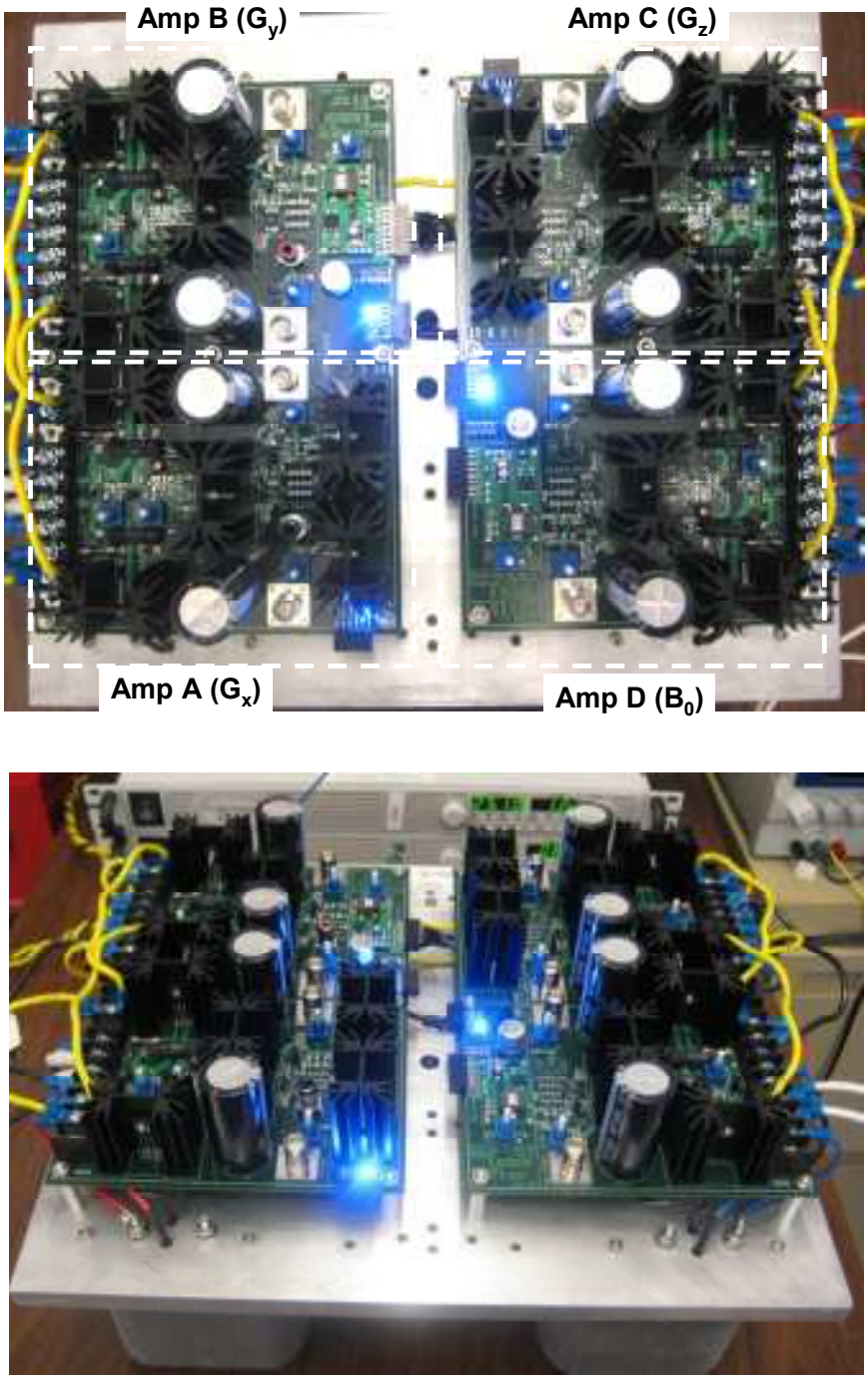

Figure 69. Photo of the assembled gradient amplifiers and the B_0 compensation amplifier (top). An angled view of the amplifier and the power supply is shown in the bottom photo.

2.3.4 Characterization and Testing of the Gradient Amplifiers

The assembled amplifiers were connected to a 1.0 Ohm low-inductive load for testing purposes. The current controller is then tuned by adjusting a variable capacitor; and the cross-over distortion was minimized by adjusting the potentiometers at the V_{BE} multipliers. A 30 kHz sine wave with ±0.5 V amplitude is connected to the input of the amplifiers. As expected a sinusoidal output current of ±1 A is observed on the oscilloscope as seen in Figure 70-a. The output closely follows the input with minimal cross-over distortion and offset. In Figure 70-b, a 10 kHz sine

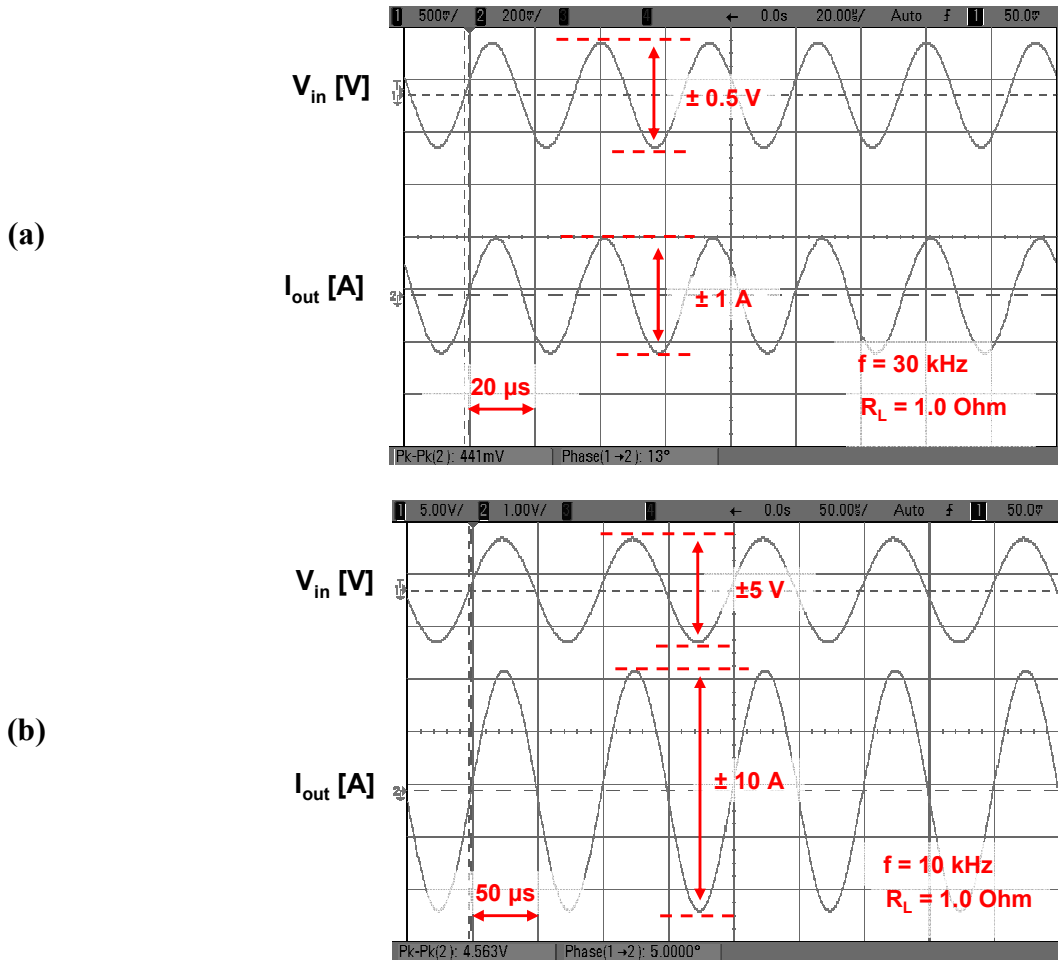

Figure 70. Measured response of the amplifiers for sinusoidal input (a) 1 A at ±30 kHz and (b) 10 A at ±10 kHz.

wave with ±5 V is input to the amplifier which is amplified to ±10 A, again with no offset and minimal distortion.

The measured frequency response is shown in Figure 71 for a 2 A peak-to-peak (±1 A) and 20 App (±10 A) sine waves. The output of the amplifier was a sine wave throughout the frequency sweep for 2 App, however for the 20 App signal significant cross-over distortion were observed above 40 kHz. The cross-over distortion can be minimized by adjusting the potentiometers of the biasing circuit, doing so however increases the power dissipation of the power stage which could cause permanent damage to the components in the power stage. Another reason for this distortion is that the amplifier was optimized for a 0.5 Ohm load (which was not available at the time of writing this thesis) and it is expected that the distortion is less for the designed load. Because this amplifier is mainly designed to be used mainly as a pulsed current amplifier, further adjustments to the biasing circuitry were not tested. The normalized magnitude (top) and the phase suggest that the amplifier has a -3 dB bandwidth exceeding 180 kHz which significantly exceeds the performance requirements (>50 kHz) described in the beginning of this chapter.

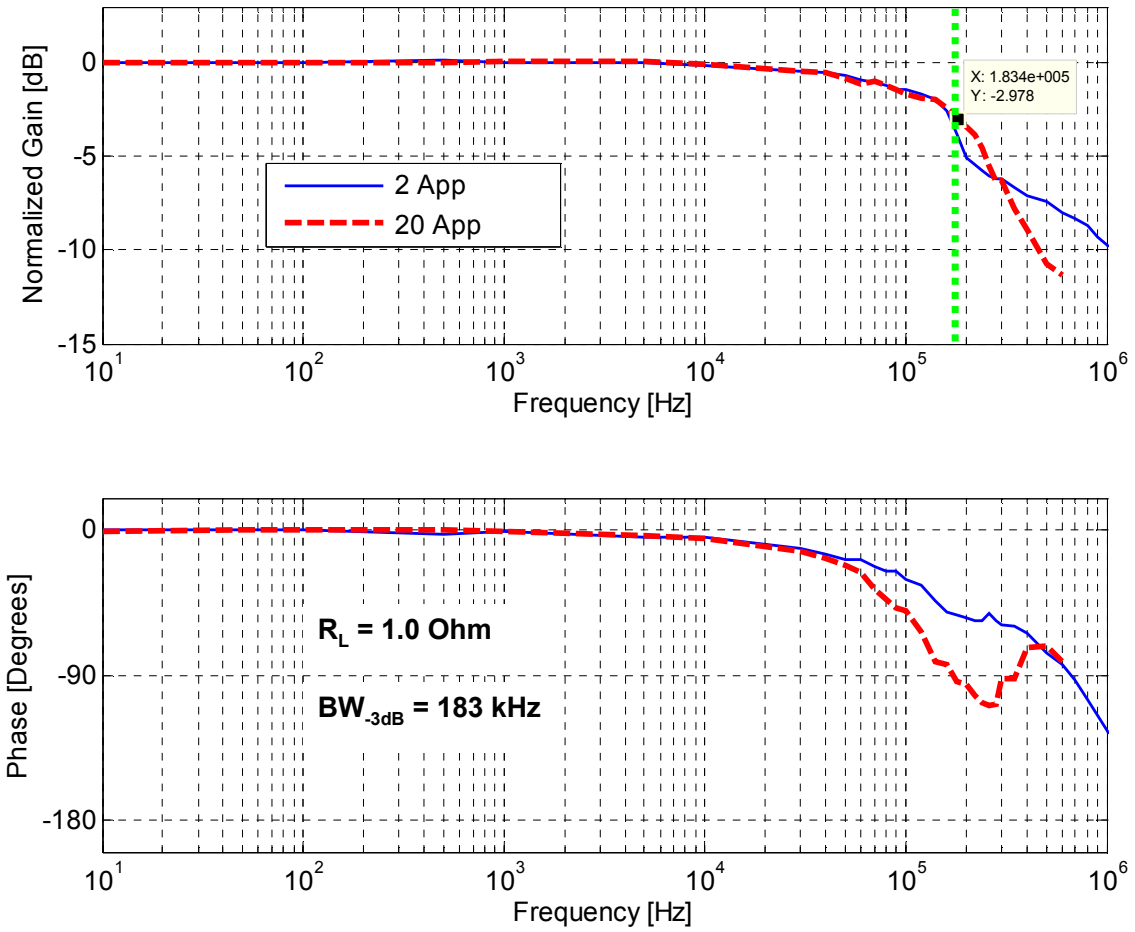

Figure 71. Measured frequency response of the amplifier into a 1.0 Ohm load is shown for current levels of ±1 A (= 2 App) and ±10 A (= 20 App). The -3 dB bandwidth (at 90° phase shift) is approximately 180 kHz which exceeds the performance requirements.

After the frequency response was measured, the amplifiers were connected to the actual gradient coils. The pulse response of the G_z amplifier for +20A and -20A pulses are shown in Figure 72-a and b, respectively. The input voltage is on the top of each plot and the output from the current monitor on the bottom. The maximum duty cycle for which this amplifier was tested for was 5% for the positive pulse and 20% for the negative pulse. Higher duty cycles are possible by increasing the fan speed, but were not tested. The rise and fall times are marked on the plots in Figure 72 and are generally less than 7 μs. The settling time is about 10-15 μs and can be

improved by further fine tuning the current controller.

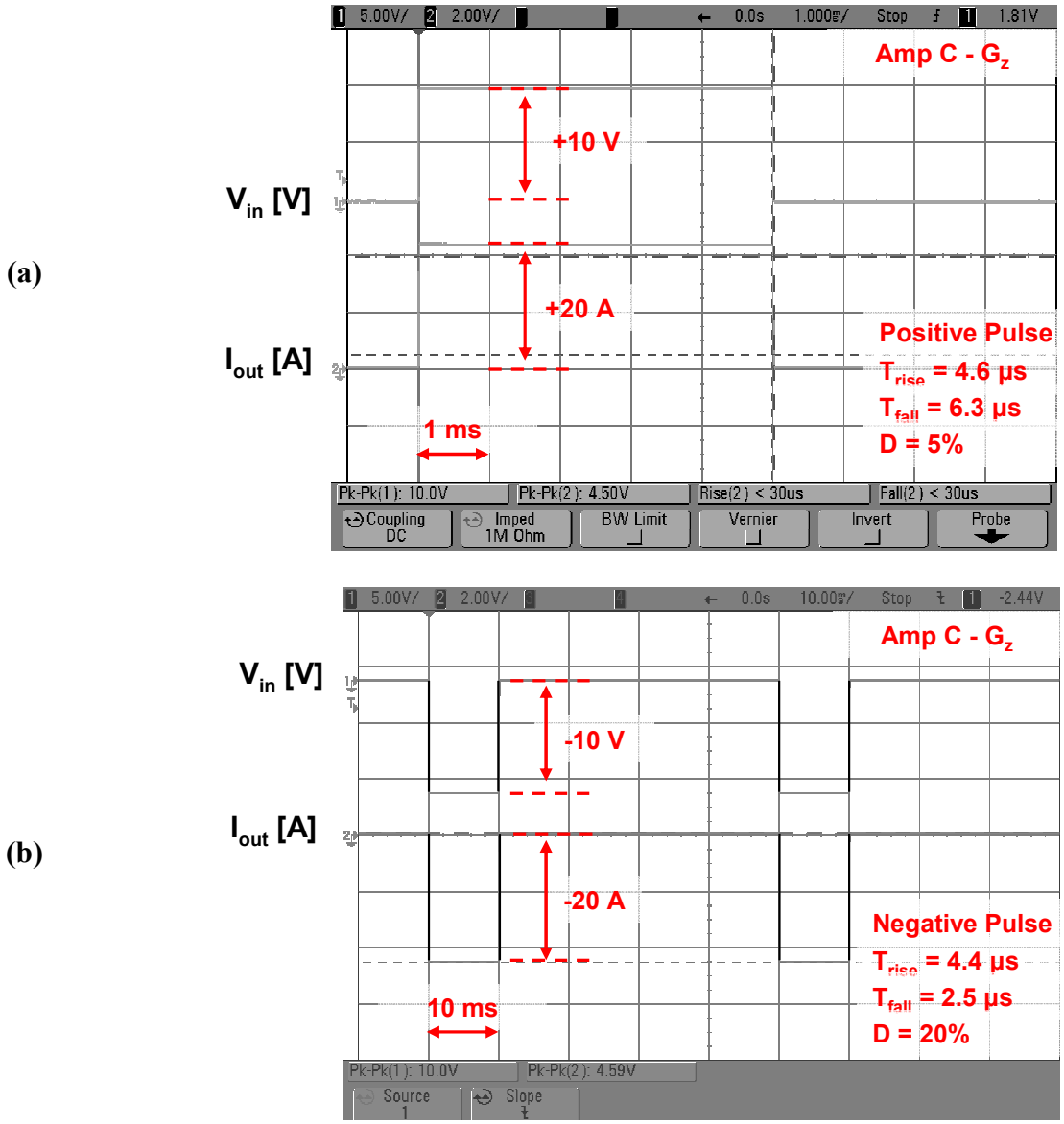

Figure 72. Measured response of the gradient amplifiers to a step input of (a) +10 A and (b) -10 A with the G_z coil attached. The rise and fall times are below 10 µs which exceed the performance requirements.

A close up of the rising edge of a +15 A is shown in Figure 73. The first channel on the top is the input, the second is the voltage at the load, and the third channel is the output from the current

monitor. The current on the load closely follows the expected shape predicted by simulation with minimal over shoot and oscillations. The small oscillations at the beginning of the pulse can be further minimized by fine tuning of the current controller (changing resistor values and adjusting variable capacitor)

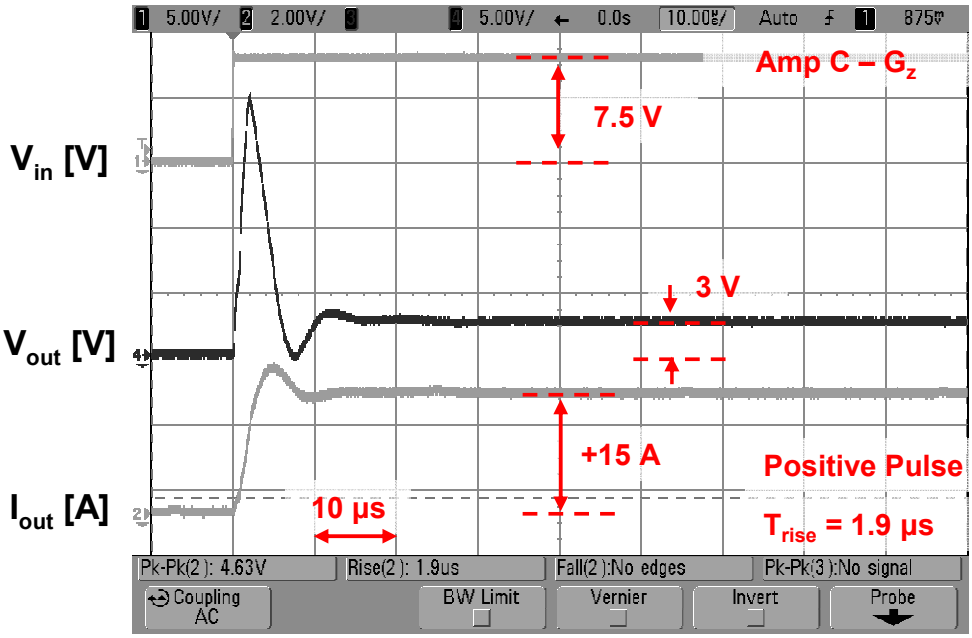

Figure 73. Measured transient response of the gradient amplifier to the rising edge of a +15 A pulse with the G_z coil attached attached. The Voltage at the load and its current are shown. The overshoot and the small oscillations can be further minimized by tuning the P-I current controller.

The other two gradient amplifiers (i.e., G_x and G_y) have similar performance characteristics and therefore not presented here. The rise and fall times exceed the required performance requirements (< 20 µs) described in the beginning of this chapter.

The response of the current amplifier for the B_0 compensation coil is also tested with the coils attached. The results are shown in Figure 74 for a +5 A and -5 A pulse with rise and fall times less than 10 µs. The bandwidth of this channel does not need to be higher than about 100 Hz as

its input is varied for each repetition of the imaging sequence; therefore, the bandwidth far exceed the requirement. Constant (DC) currents of ±3 A were tested with no problems.

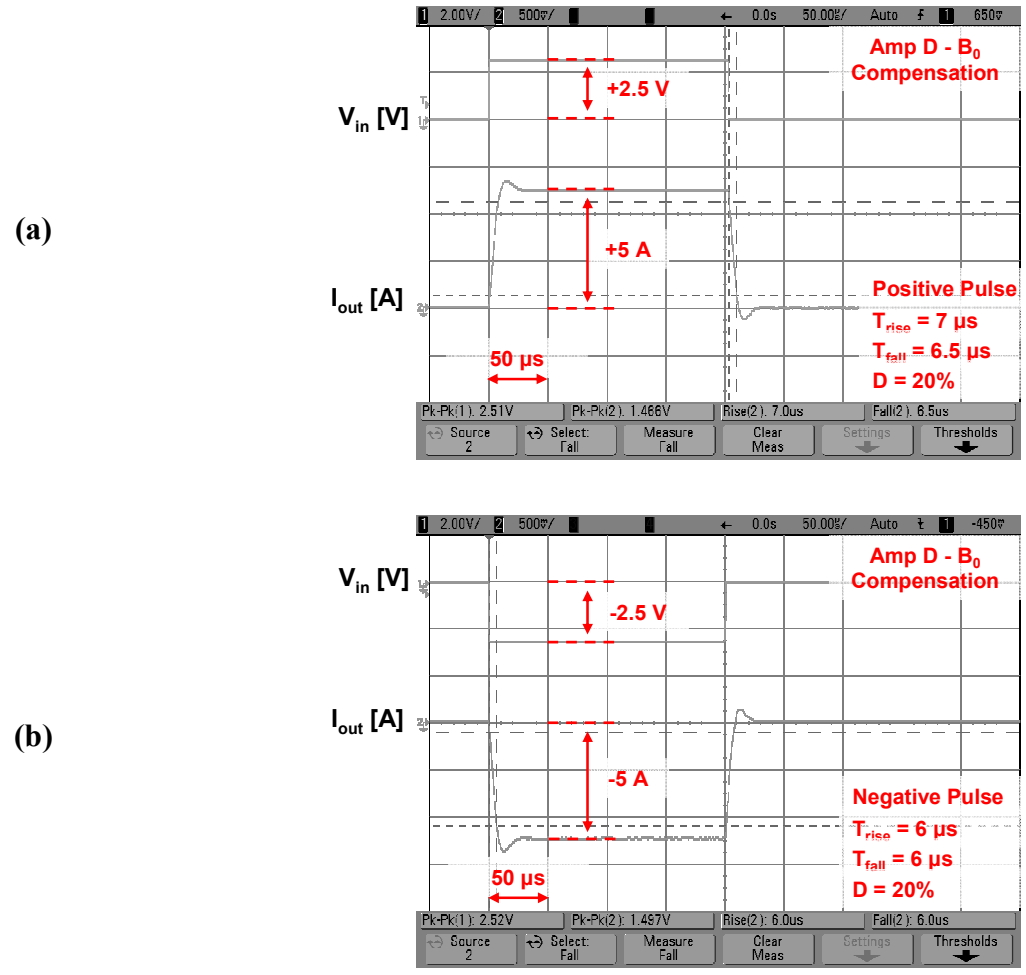

Figure 74. Measured response of the amplifiers to a step input of (a) +5 A and (b) -5 A with the B_0 compensation coil. The rise and fall times are below 10 µs which by far exceed the performance requirements of this amplifier.

2.3.5 Summary of the Gradient Amplifiers

In summary, three gradient amplifiers were designed and constructed mainly using discrete components which can drive bipolar currents up to ±20 A (duty cycles less than 5%) with rise

and fall times less than 10 μs into the gradient coils (0.4 Ohm and 3 μH). Also, the amplifiers are capable of continuous sine waves outputs of ±10A into a 1.0 ohm non-inductive load with a bandwidth exceeding 180 kHz. The supply range is ±25 V to ±36 V and the overall gain of the all the amplifiers is adjusted to 2 A/V. The measured results along with the required design specifications are given in

Table 12. Required and measured specification of the gradient amplifiers and the compensation coil amplifier

	Gradient Amplifier		**Compensation Coil Amplifier**	
	Requirement	**Measured**	**Requirement**	**Measured**
Current [A]	**±20**	**±20**	**±3**	**±5**
Max duty cycle [%]	**2**	**5**	**100**	**100**
Rise/Fall time [μs]	**< 20**	**<7**	**<10000**	**<10**
Settling time [μs]	**<100**	**<20**	**<1000**	**<50**

2.4 RF Electronics

The design and characterization of the radio frequency (RF) electronics for detection and excitation of the MR signal are described next. The design of RF electronics and some practical tips are extracted from [32, 38, 53, 56, 59, 88-101].

2.4.1 RF Electronics Requirements

There are three components to the RF electronics: the probe, transmitter and receiver.

The *probe* is a coil that generates and/or receives the time-varying magnetic field. In this work, both functions are performed by a single probe. The magnetic field generated by the probe must be orientated perpendicular to the main static magnetic field in order to flip the magnetization. Also, the generated magnetic field must be homogenous over the sample to excite all the spins in the sample by the same angle. Another requirement is that the impedance of the probe has to be matched to that of the transmitter and receiver, in order to ensure maximum power transfer from the transmitter to the probe for excitation, and from the probe the receiver for detection.

The *transmitter* supplies the time varying excitation signal to the probe with the desired shape and amplitude at the Larmor frequency. The shape of the RF excitation signal is determined by the imaging sequence. Refer to Chapter 1.4 for more information.

The *receiver* must detect and amplify the minute MR signals from the background noise. As a result, the receiver must have a high signal-to-noise-ratio (SNR). In addition the amplified voltage swing must be matched to the input voltage range of the data acquisition board. The receiver must also detect a wide range of amplitudes of the MR signal. For example, the receiver must detect a FID signal that has a larger amplitude at the start of the pulse sequence but much

smaller amplitudes a few T_2^* time constants later. Therefore, the requirements of the receiver can be summarized as: high SNR (i.e., low noise floor), high gain and high dynamic ratio.

Another important requirement is that the receiver must handle the large amplitudes of the transmitter pulse (= +30 dBm) while detecting a signal on the order of -100 dBm; a voltage difference of $3 \cdot 10^6$. Therefore, a protection scheme has to be implemented for the receiver.

2.4.2 RF Design

2.4.2.1 The Probe

The most commonly employed RF coils for similar applications are the solenoidal and Helmholtz coils [30]. The shape of the two coil types and direction of their magnetic field is depicted in Figure 75. A solenoidal RF coil is simply constructed by winding conductive material, such as copper, onto a cylindrical object. The optimum coil size and wire spacing is discussed in [88, 102, 103].The solenoidal configuration is also well suited for the compact integration of the gradient coils described in section 2.2. The Helmholtz RF coil consist of two equal rings of wires separated by a half the diameter of the rings.

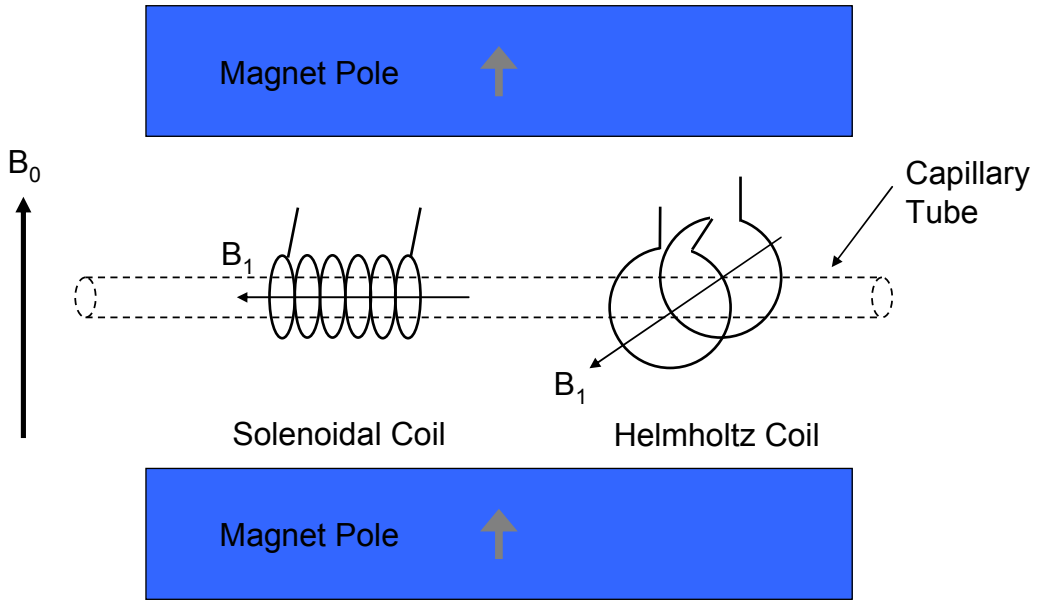

Figure 75. Orientation of the varying magnetic field (B_1) in Solenoidal and Helmholtz coils inside a static magnetic field B_0.

The Helmholtz coil has a larger access compared to the solenoidal coil. However, The SNR of the solenoidal coil is roughly three times greater when compared to the Helmholtz [25, 88, 102, 103]. Both coil types have a relatively homogenous region of excitation as long as the sample volume is sufficiently smaller than the diameter of the coil. A solenoidal coil is chosen for this work due to the simplicity of construction and better SNR performance.

It is important to match the impedance of the RF coil to that of the receiver and transmitter for optimum signal transfer. This is achieved by the adding two capacitors to the RF coil as shown in Figure 76. The tuning capacitor, C_{tune}, is connected parallel to the RF coil while the matching capacitor, C_{match}, is connected in series. By adjusting the capacitors the impedance can be matched (typically to 50 Ohms) to that of the transmitter and receiver. Other impedance matching techniques are described in [89].

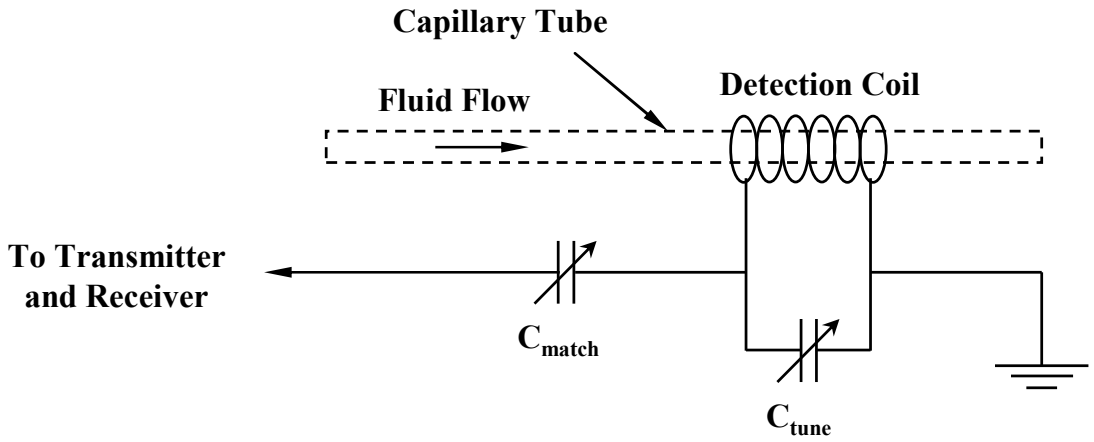

Figure 76. Impedance matching of the RF probe is achieved by adjusting the two capacitors.

There are SNR advantages when using micro coils [99], which will be necessary for high resolution imaging of micro capillaries.

Coil winding*:* To reliably wind coils with high repeatability with diameters less than 2 mm, a coil-winding machine was constructed by undergraduate students as a side project for this work. This apparatus is depicted in Figure 77. The capillary tube (flexible Teflon tube shown) is tensioned between two drive chucks which are rotated manually. The arm holds multiple wires which are wound on the capillary tube. All the wires are back-tensioned by passing a constant current through the motors attached to the arm. The spacing between the wires is controlled by selecting discrete sizes of fishing lines. The final coil is then glued in place using superglue.

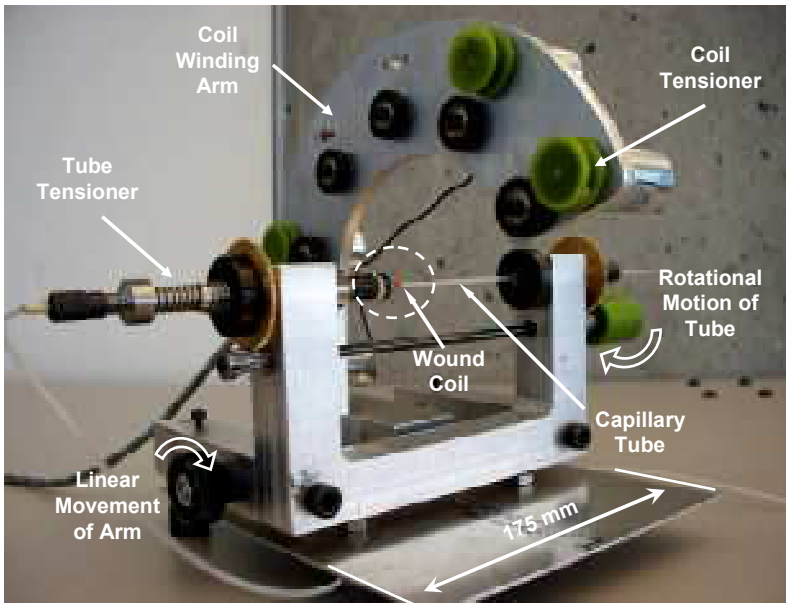

Figure 77. Coil winding machine capable of winding 20 µm wires onto 100 µm micro capillary tubes.

Integrated RF enclosure: An enclosure is machined out of polypropylene to hold the RF coil, the impedance matching capacitors, the capillary tube and also the gradient coils (described in section 2.2). The dimensions of the probe enclosure are 65 mm (H) x 80 mm (L) x 8.7 mm (T). It consists of two parts with milled slots that hold the capillary tube and the coaxial cable carrying the RF signals to and from the probe. The coaxial cable (RG-223) is of double shielded type and is used for its excellent noise shielding [98]. The directions of the time-varying magnetic field and the static magnetic field are marked in Figure 78-A. The RF coil is located in the middle of the enclosure and surrounds the capillary tube. The impedance matching capacitors, which are of non-magnetic type, are located as close as possible to the RF coil and are accessible for adjustment form the side of the enclosure. The two part of the enclosure are fastened to each other using plastic screws which also define the alignment of the two mirrored polypropylene components. The machined enclosure is shown in Figure 78-B. The final probe enclosure with its elements identified is shown in Figure 78-C. For prototyping purposes a tube with an outer

diameter of 5 mm was chosen. In the future, micro-capillary tubes will be used for visualization of flow at microscale.

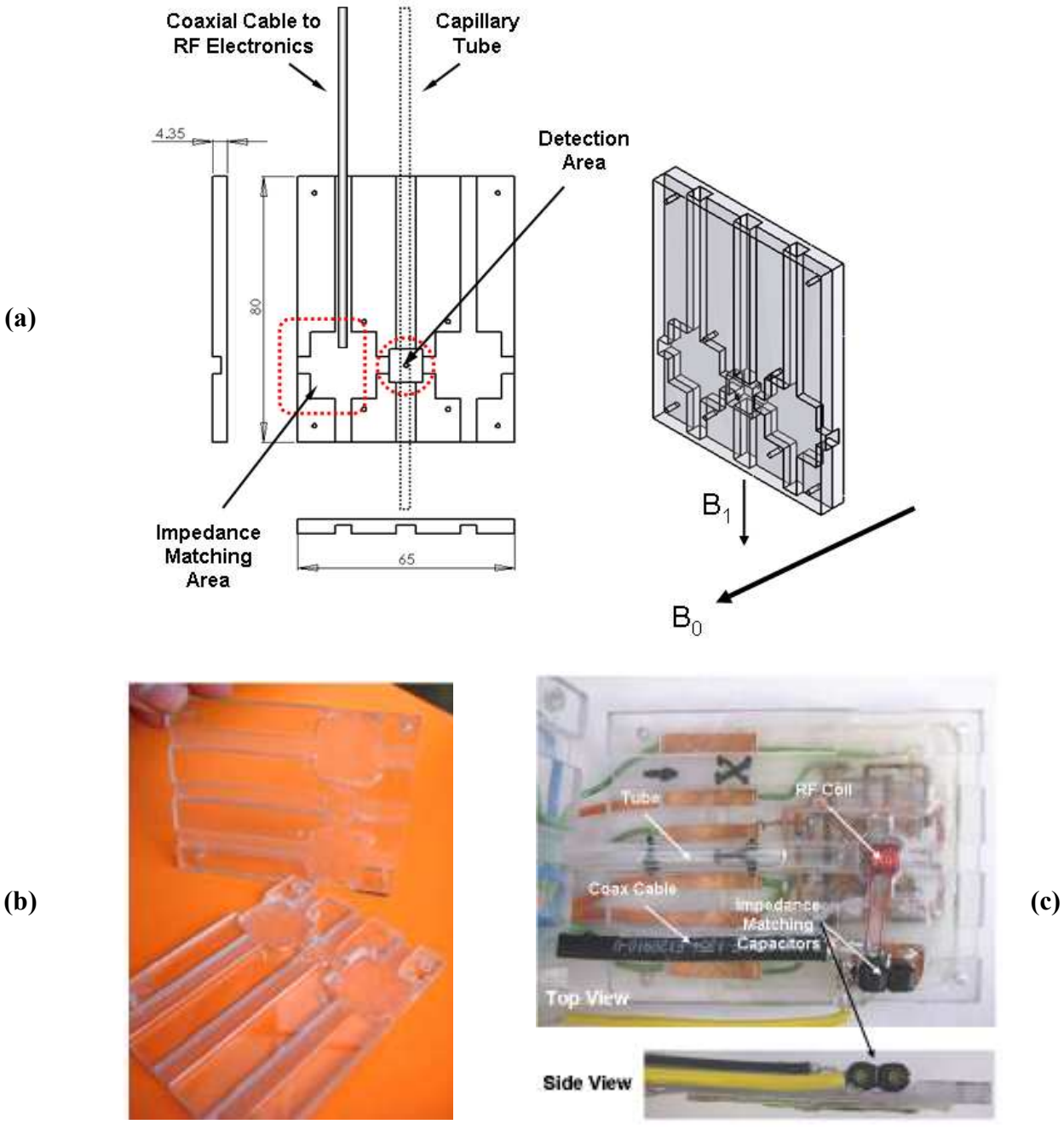

Figure 78. The CAD drawing of the enclosure for the RF probe along with the orientation of the magnetic fields is shown in (a). The machined enclosure and the components of the probe are shown in (b) and (c).

2.4.2.2 The Transmitter

To generate the excitation signal, a carrier frequency (pure sine wave) at the Larmor frequency is synthesized by an external source (a function generator specified later in this section). The carrier signal is modulated with the desired pulse shape and is then is then amplified. This is illustrated in Figure 17. The pulse shape is depicted in the top plot and the carrier signal is in the middle plot. The bottom plot shows the modulated carrier.

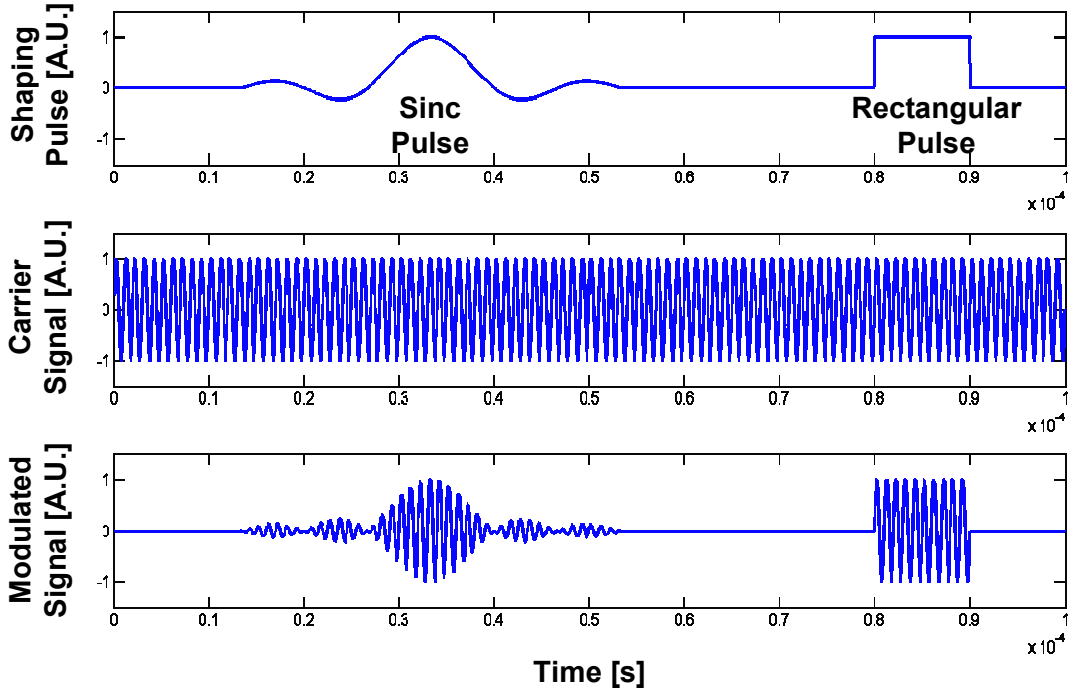

Figure 79. Pulse shaping of the excitation signal (bottom plot) is achieved by modulating a carrier sine wave (middle plot) with a pulse shaping signal (top plot).

The architecture of the transmitter is illustrated in Figure 80. The external sources are connected from the left side and not shown in the figure. The pulse shaping signal is digitally synthesized by a PC and output as an analog signal using a data acquisition board (NI-6259, National Instruments). The analog pulse shaping signal is then amplified by and SRS 560 (Stanford

Research Systems Inc., 1290-D Reamwood Avenue Sunnyvale, CA 94089, USA) amplifier. A 25 MHz carrier signal is synthesized by an Agilent 33250A function generator and is split between the transmitter and the receiver. The amplitude of the carrier signal is adjusted by an attenuator and is mixed (MXR-15, RF Bay Inc., 13111 Piney Knoll Lane., Suite B, Potomac, MD 20854, USA) by the pulse shaping signal. The modulated signal is passed through the RF switch (Mini-Circuits model ZYSWA-2-50DR, P.O. Box 350166, Brooklyn, NY 11235 USA) to the power amplifier (MPA-12-30, RF Bay Inc.) that amplifies the signal to +30 dBm (1 Watt). The output of the pulse shaping can be enabled or disabled using the "Pulse" signal. After the end of the excitation phase, the RF switch is disabled to minimize the noise sent to the power amplifier. The set of crossed diodes, placed after the power amplifier, are used to block the noise of the amplifier after the detection phase starts. The noise blocker effectively creates a threshold limit below which the noise (lower than 200 mV) is suppressed. The excitation signal is the sent to the probe via a splitter. The receiver is also connected to the probe via this splitter after passing through the protection electronics. The quarter wave line in addition to the crossed grounded diodes effectively creates high impedance which blocks the receiver form high powered pulses. For more information regarding the properties of the quarter wavelength refer to the book by Fukushima [89], and for other protection techniques refer to [59, 95, 97, 104-107].The grounded crossed diodes clip the incoming signal to the reverse biased voltage of the diodes (0.65 V). Thus, only low amplitude signal (such as MR signals) pass through the protection electronics once the high power excitation signal is turned off.

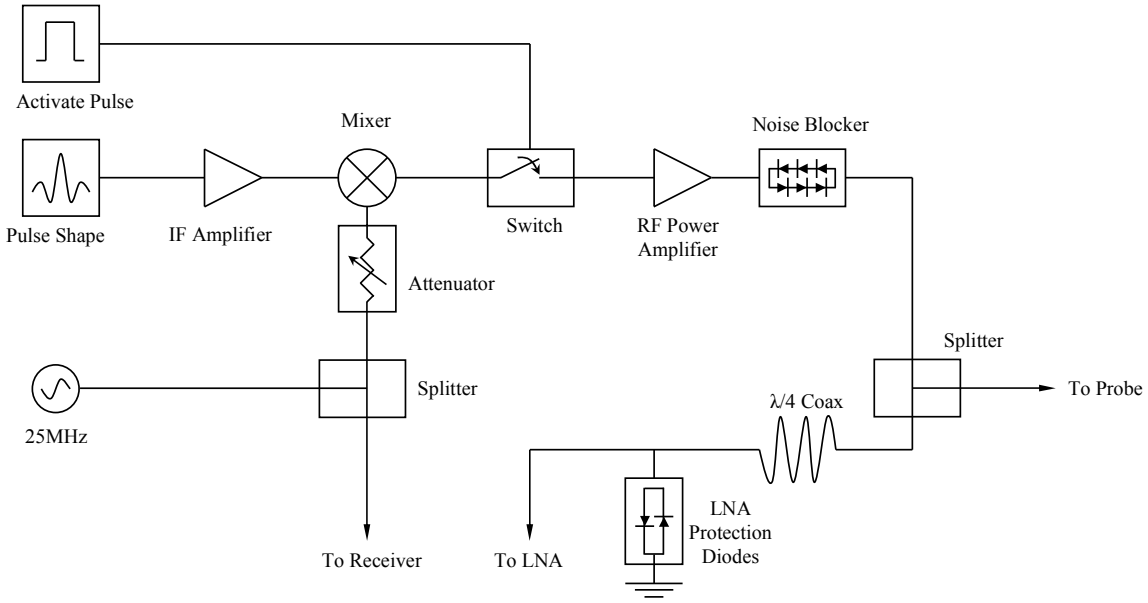

Figure 80. Architecture of the transmitter with pulse shaping capability and LNA protection.

2.4.2.3 The Receiver

To extract the small MR signals from all the background noise, a receiver with narrow bandwidth is used such that only the signal and the background noise of desired frequencies are amplified to maximize SNR. Various types of receiver architectures exist that are suitable for NMR and MRI applications and are discussed in [88, 89, 92, 93, 97, 100, 108]. To avoid aliasing of positive and negative frequencies, two quadrature channels (90° phase shift) are necessary. In this work, a direct phase-sensitive detection in quadrature architecture is used for its simplicity in design and construction.

The schematic of the receiver is shown in Figure 81. In the detection phase, the MR signal from the probe is first amplified using a low noise amplifier (LNA) with a gain of 41 dB and noise figure of 1.4 dB (LNA-605, RF Bay Inc.) and filtered using a homemade band-pass filter with a centered at 25MHz with a bandwidth of 1 MHz. The signal can be further amplified by another

LNA (LNA-1050, RF Bay Inc) with a gain of 51 dB and noise figure of 2.0 dB. The gain in this stage is adjusted by selecting appropriate attenuators (Mini-Circuits K1-VAT+). The amplified signal is then mixed down to audio frequencies using two level 7 mixers (MXR-15, RF Bay Inc.). The local oscillator input to each of the mixers is provided by a quadrature hybrid (ZMSCQ-2-50, Mini-Circuits) which generates and in-phase and quadrature reference signals. The audio frequency signals are then amplified by an audio amplifier and filtered using a third order Butterworth filter with a cut off of frequency of 70 kHz. The two channels are then sampled at 200 kS/s each and digitally filtered by a bandwidth defined by the pulse sequence.

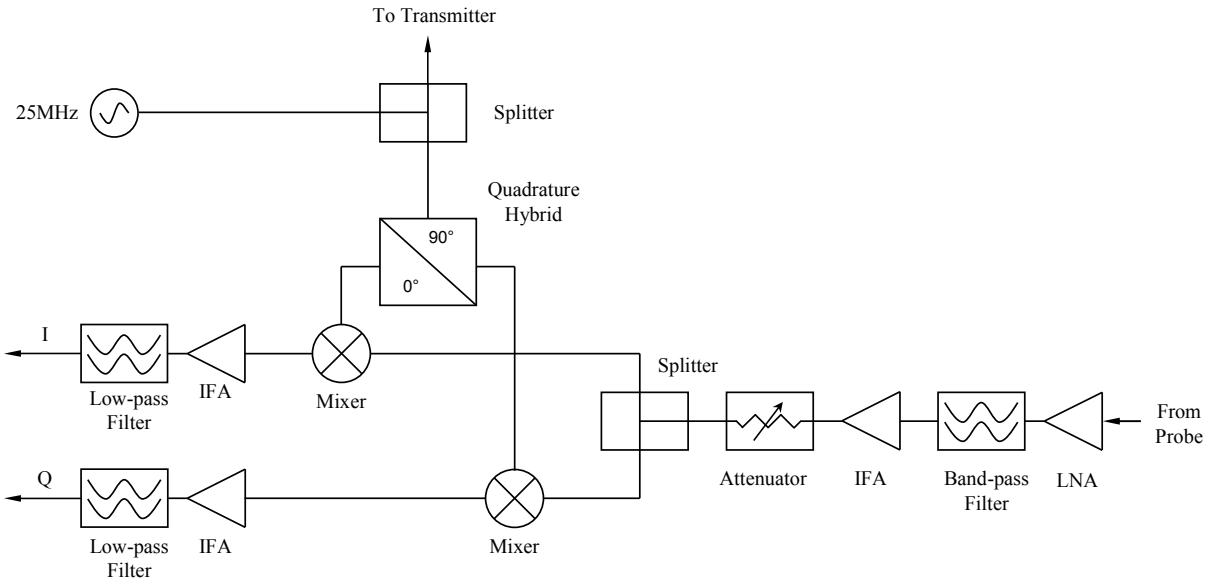

Figure 81. Architecture of the receiver with direct quadrature phase-sensitive detection.

2.4.2.4 Overall RF Design

The block diagram of the overall RF system including the probe, transmitter and receiver is displayed in Figure 82.

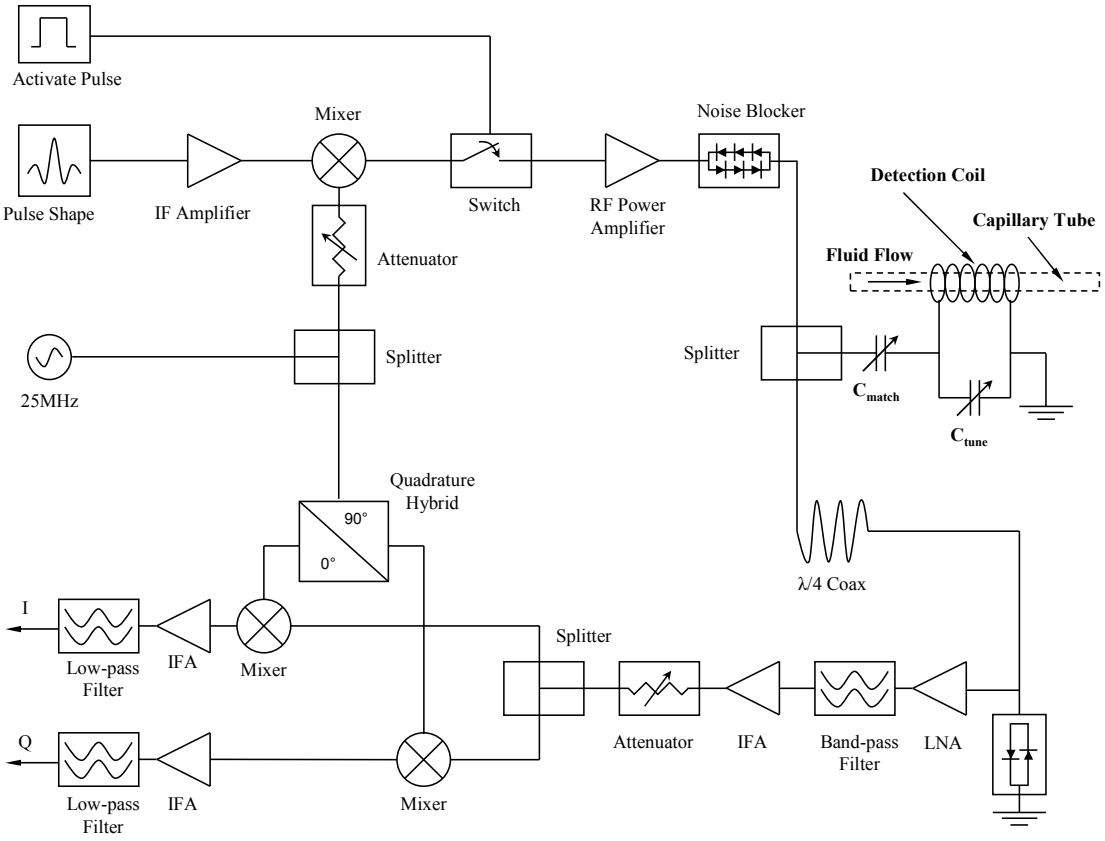

Figure 82. Architecture of the overall RF system for excitation and detection of MR signals.

Photographs of the implementation of the RF electronics are shown in Figure 83. The quarter-wavelength coaxial cable and the cable connecting the probe are not shown. The transmitter is marked on the right-hand side of Figure 83-A while the receiver is on the left side. The front panel of the homemade box is shown Figure 83-B. The RF components are interconnected using RG-316 coaxial cables.

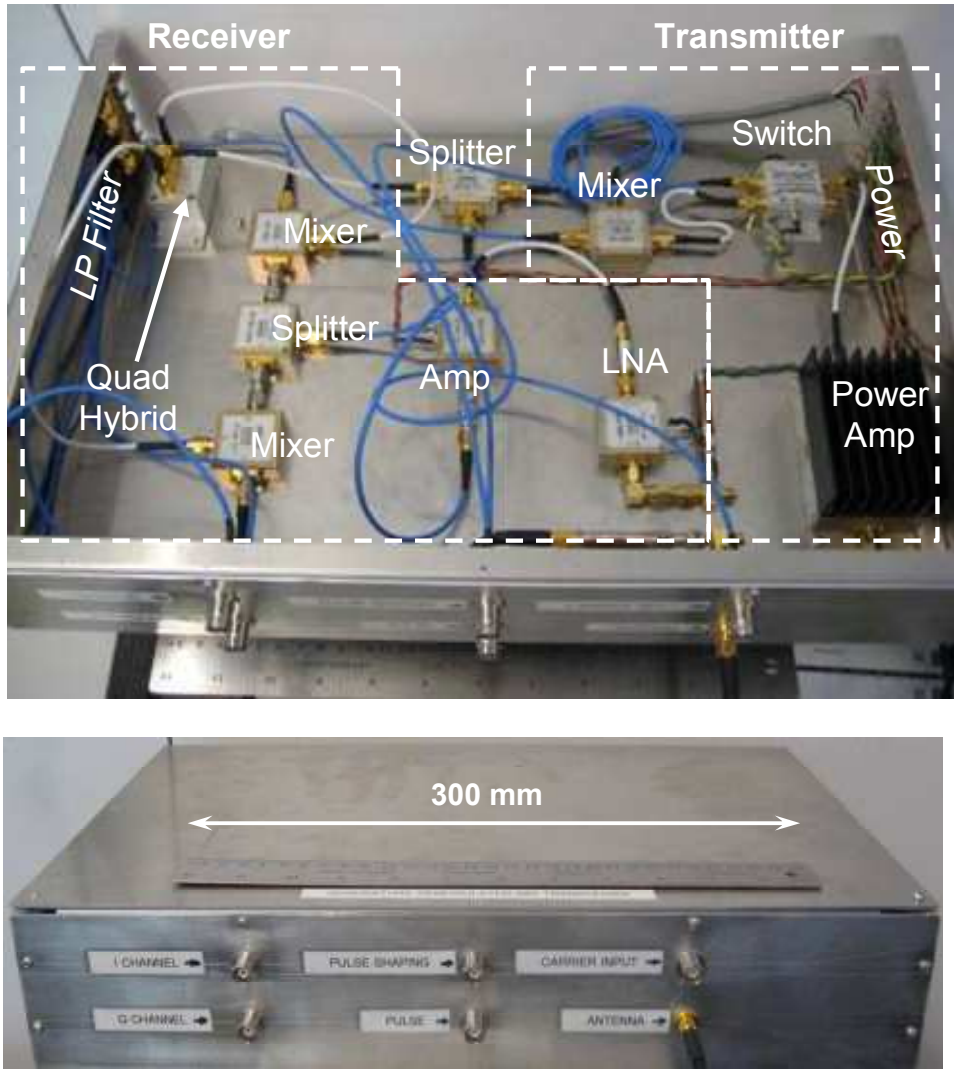

Figure 83. The RF electronics box implemented with off-the-shelf components.

2.4.3 Characterization of RF Electronics

The probe is made with an AWG 24 laminated copper wire with 7 turns with an inner diameter of 5.5 mm and 7.5mm length. The electrical properties are listed in Table 13.

Table 13. Properties of the RF probe.

Property	Value
B_1 [mT/A]	0.51
DC Resistance [mΩ]	17
Inductance [μH]	0.56
C_{tune} [pF]	10 - 120
C_{match} [pF]	10 - 120
Q	208

The tuning and matching is achieved by adjusting C_{tune} and C_{match} until the reflections by the probe are minimized [98, 109] at the Larmor frequency as described in the Appendix C. A snapshot of the screen of the oscilloscope of a matched and tuned probe at 25.2 MHz is shown in Figure 84. Channel one is an indicator of the frequency in sweep mode where the rising edge shows the starting frequency (10 MHz) and the falling edge is the marker frequency (Larmor frequency).

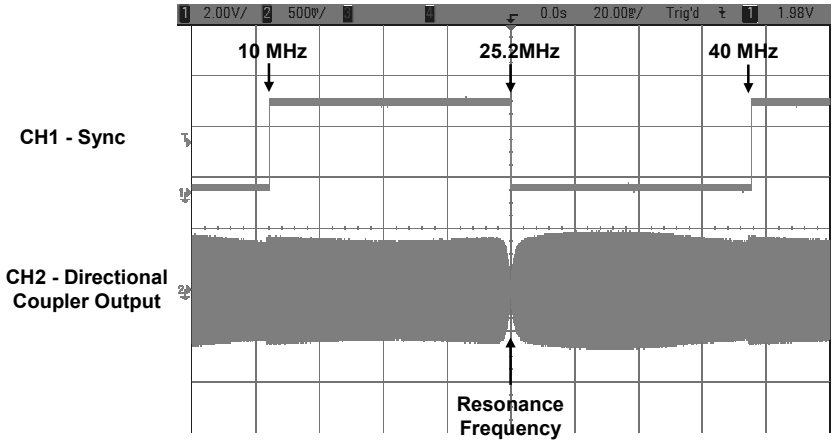

Figure 84. Scope screenshot of the tuned and matched probe. The probe is tuned to 25.2 MHz and matched to 50 Ohms.

Channel two is signal that is reflected from the probe. As visible in Figure 84, the reflections are minimum at the Larmor frequency (25.2 MHz).

The input versus output relation of the RF power amplifier in the transmitter is shown in Figure 85. The output power of the RF amplifier saturates at about 30 dBm which is more than sufficient to excite the sample by 90° flip angles with short (< 50 μs) rectangular pulses.

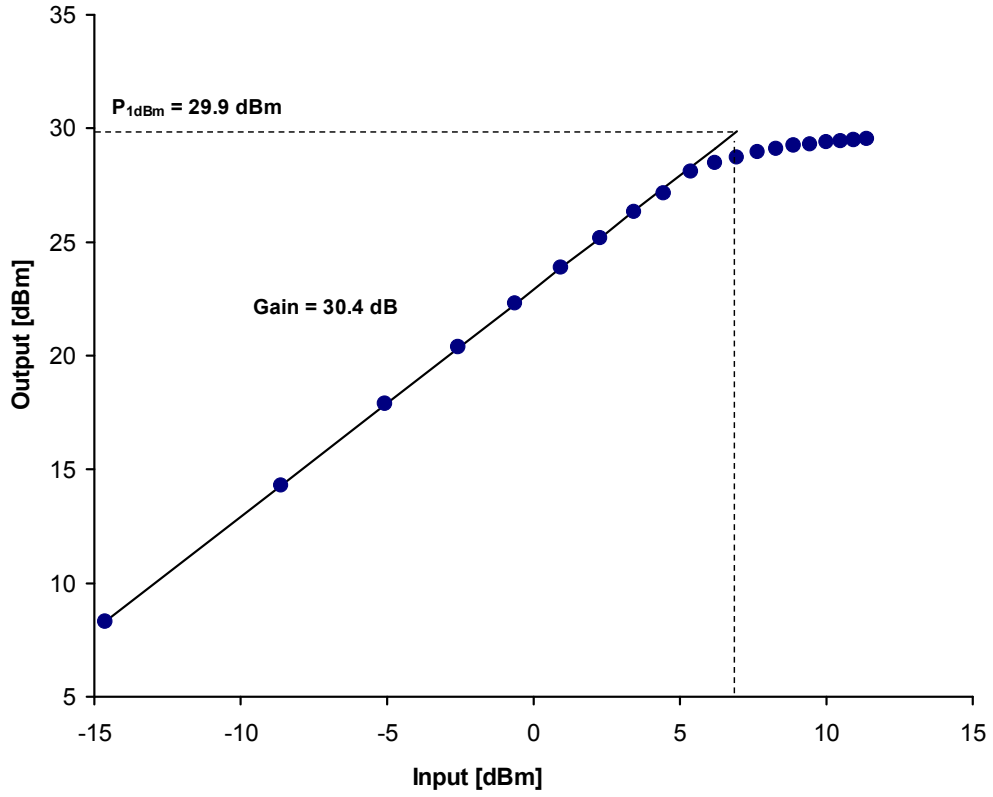

Figure 85. Output power of the power amplifier versus the input power. The amplifier has a gain of 30.4 dB and a 1-dB compression point of 29.9 dBm.

The results of the RF transmitter are summarized in Table 14.

Table 14. Properties of the RF transmitter.

Property	Value
$P_{1\ dB}$ [dB]	**29.9**
Gain [dB]	**30.4**
Frequency Range [MHz]	**25 - 1200**
Noise Figure [dB]	**4.2**

Snapshots of rectangular and sinc pulse shaping of the transmitter are shown in Figure 86-A and Figure 86-B respectively.

(a)

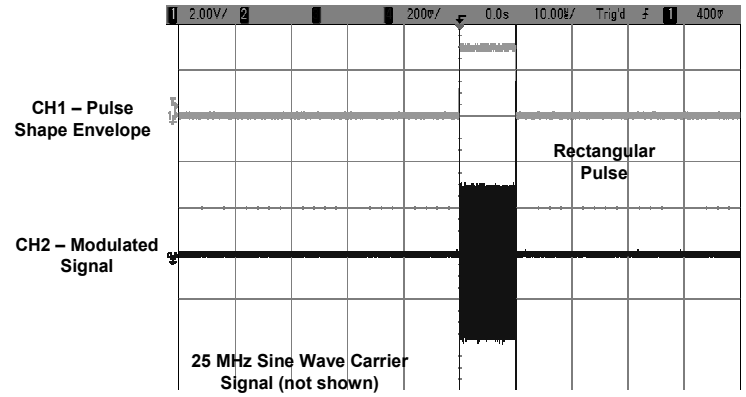

(b)

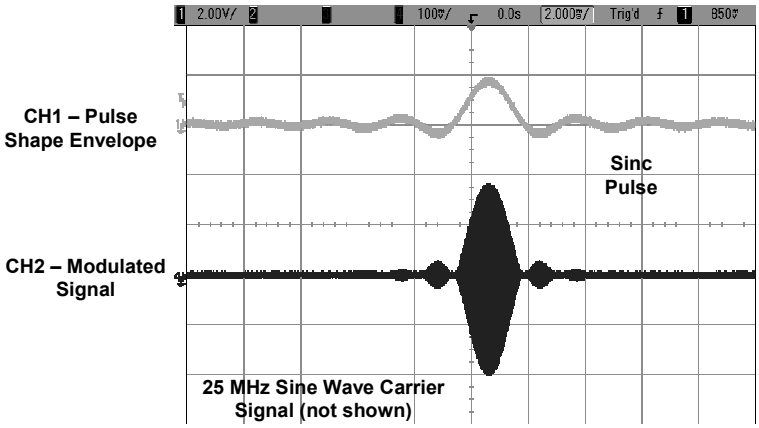

Figure 86. Scope screenshots of the pulse shaping for a rectangular (a) and sinc (b) pulse.

The pulse duration of the 90° flip angle for a free induction decay (FID) signal is

$$\tau = \frac{\pi/2}{\gamma B_1/2} = \frac{\pi/2}{(2\pi)\cdot(42.6\cdot10^6)\cdot(0.5)\cdot(0.51\cdot10^{-3})} \approx 23\,\mu s.$$

The factor of two in the B_1 term takes into account the fact that a solenoidal RF coil generates a field along the coil only. If a coil that could generate a circularly polarized field was used the factor of two is removed. This estimation was verified by measuring the amplitude of the FID signal for various pulse durations of rectangular shape. The result is shown in Figure 87. The amplitude of the MR signal is greatest at duration of about 24 μs. The variation of amplitude

with respect to pulse duration closely follows the expected cosine function as seen in Figure 87.

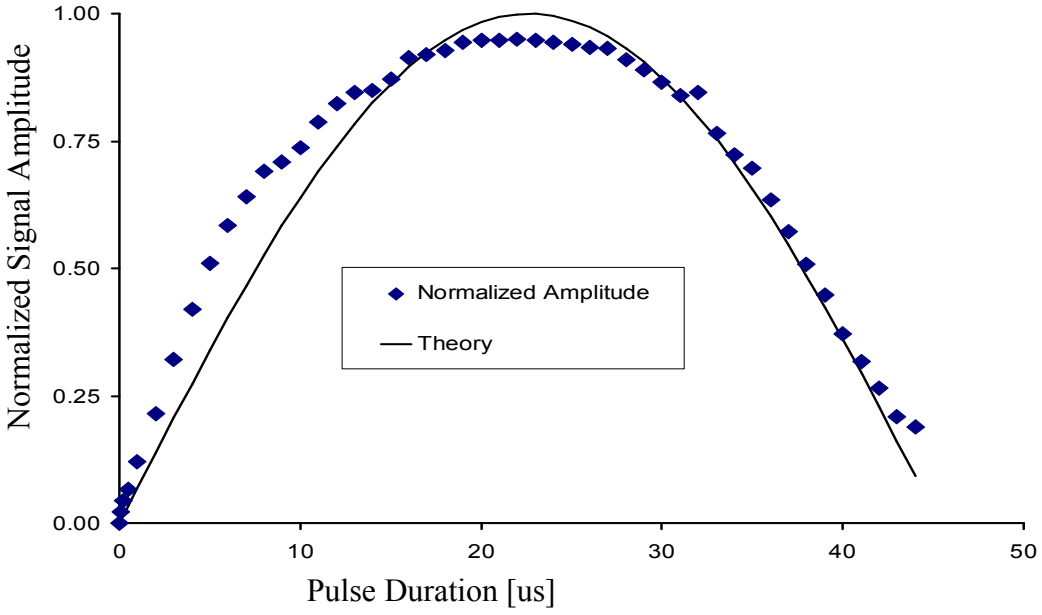

Figure 87. Amplitude of the FID signal versus the pulse duration of rectangular shape. The 90° flip is achieved for a pulse duration of about 24 µs.

The receiver is tested by injecting a -100 dBm sine signal at 25.010 MHz and a carrier frequency of 25.000 MHz. A snapshot of the received signal (averaged 16 times) of both quadrature channels is depicted in Figure 88. The received signal has an expected frequency of 10 kHz. The signal-to-noise ratio of the non-averaged signal is about 18 dB.

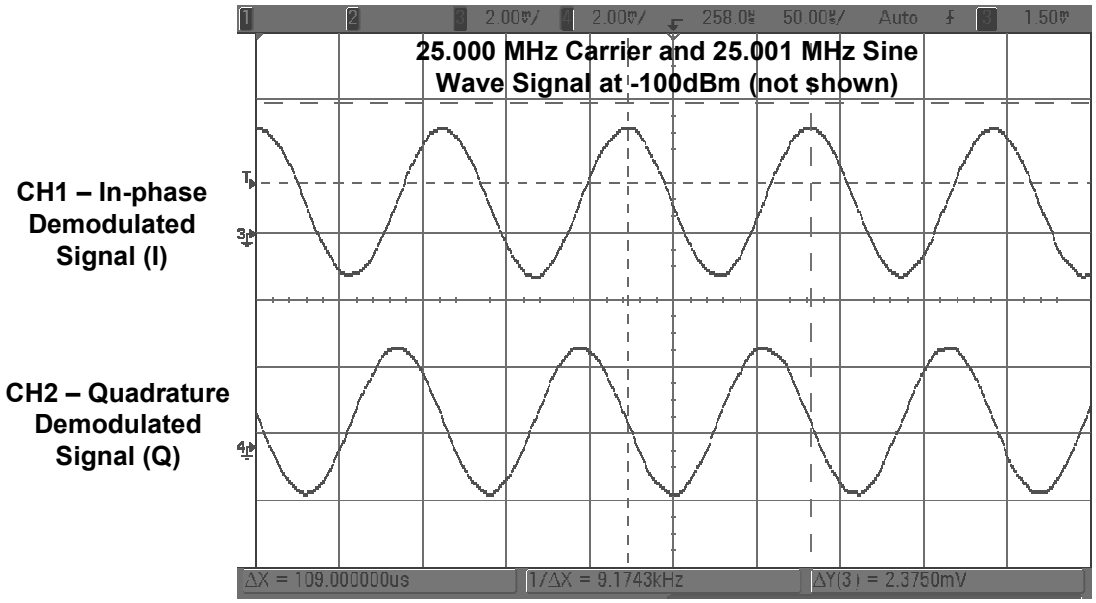

Figure 88. 10 kHz sample outputs of the both quadrature channels form the receiver for -100 dBm input signal. The output waveform is averaged 16 times. The SNR of the non-averaged signal is 18 dB.

The dynamic range depends on the expected amplitude of the MR signal, and is set by the correct combination of gains and attenuator in the receiver (see Appendix C for details). The dynamic range is limited by the dynamic range of the mixer (44 dBm). The performance characteristics of the receiver are summarized in Table 15.

Table 15. Properties of the RF receiver.

Property	Value
Max Gain [dB]	**130**
Frequency Range [MHz]	**25 - 50**
Dynamic Range [dB]	**44**
Noise Floor [dB]	**-120**
Dead-time [μs]	**100**

A sample snapshot of an NMR signal acquired by the described RF electronics is shown in Figure 89. The first channel shows a rectangular pulse that is used for triggering of the oscilloscope but is not visible because it has a very short pulse duration (20 µs). The second channel is the I-channel of the receiver detecting an NMR signal. The receiver dead-time is 100 µs as marked. The dead-time of the receiver is partially due to the ringing of the high resonant probe. The recovery time [95]

$$T_{Recovery} = \frac{Q}{\pi \cdot f} \ln\left(\frac{V_{out}}{V_{in}}\right) \tag{81}$$

can be calculated for this setup for a quality factor Q of 206, frequency, f (25.2 MHz), voltage of transmitter of +30 dBm (7.1 Vrms) and MR signal voltage down to -120 dBm (0.225 nV) to be 63 µs. This theoretical value is reasonably close to the measured dead-time of the receiver.

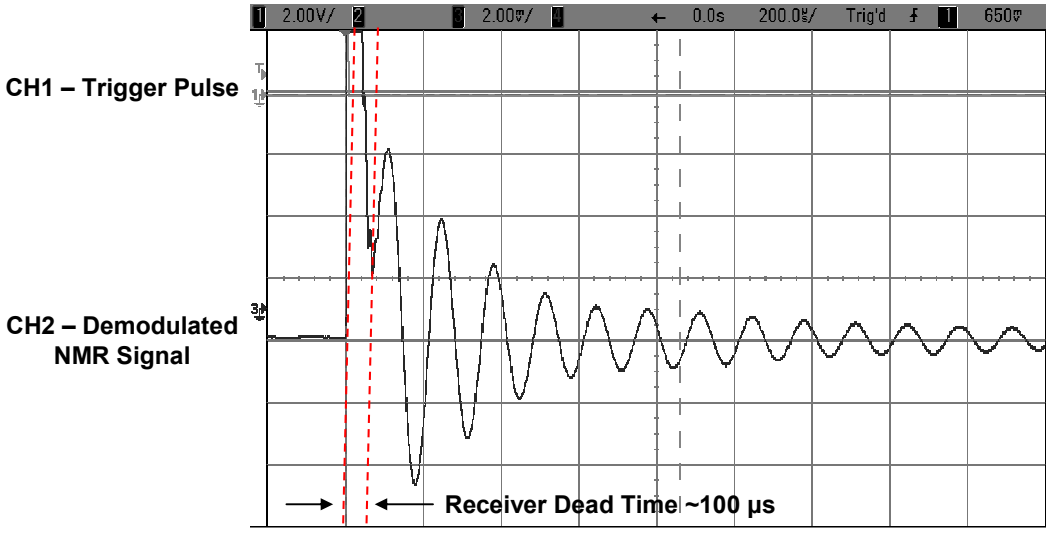

Figure 89. The dead-time of the receiver for a sample free induction decay MR signal is about 100 µs.

2.4.4 Summary of the RF Electronics

The design of the RF probe and the architecture of the transmitter and receiver were described. The transmitter and receiver were constructed out of off-the-shelf RF components. The RF probe has a quality factor of above 200 and is tuned and matched at the Larmor frequency (25 MHz). The transmitter has a gain of 30 dB and amplifies signals to + 30dBm that ranging from 25 MHz to 1.2 GHz. The transmitter can modulate the carrier signal with the desired pulse shape. The quadrature phase-sensitive receiver has a maximum gain of 130 dB and a measured noise floor of -120 dBm. The dynamic ratio of the receiver is 44 dB and has a dead time of approximately 100 μs. The RF electronics were successfully used to excite and measure MR signal of water inside a standard 5 mm NMR tube.

Chapter 3 - Overall System Design

This section describes how the various components are connected to each other and how they are synchronized. The synchronization of two data acquisition boards along with the signal acquisitioning of the raw MR signal is also described.

3.1 Overall Component Layout and Interconnections

The design and construction of each component of the MRI microfluidic visualization instrument was described in Chapter 2. A schematic of how the components are interconnected is shown in Figure 53. Depending on the desired imaging parameters (namely, FOV and receiver bandwidth, repetition rate, number of averages, etc) a pulse sequence is synthesized by a computer and saved as a text file. Next, the text file is loaded in a LabVIEW (by National Instruments) program that controls the six analog outputs of the two data acquisition boards (DAQ). Details regarding the LabVIEW program and the DAQ interconnections are described in the following sections. Three of the analog outputs are connected to the three gradient amplifiers that amplify the signal to the desired current level that drive the gradient coils. One analog output is connected to the fourth current amplifier that is used for compensating any drifts of the static magnetic field. The other two analog outputs are directed to the RF electronics; one channel controls the transmitter RF switch and the other channel is first amplified by an SR560 preamplifier (the bandwidth is set to 30 kHz) and then sent to the mixer for pulse shaping.

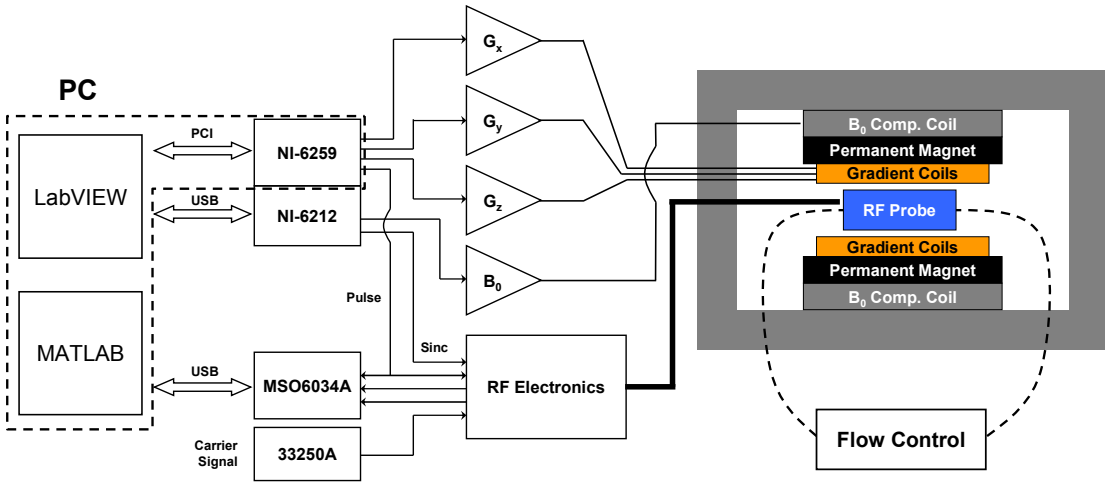

Figure 90. Schematic of the overall system indicating the connections between system components.

The carrier waveform is synthesized by an Agilent 33250A function generator which is connected to the RF electronics. The transmit signal is sent to the RF probe (see Figure 53) via a double shielded coaxial cable. This coaxial cable is also used to send the MR signal picked up by the RF probe to the quadrature phase-sensitive detector in the RF box. The two outputs from the receiver are sent to the Agilent MSO6034A oscilloscope for easy visualization of the raw signals. The oscilloscope is connected to the PC via USB and is configured to amplify and average the detected MR signals which are then sent to the PC for further processing. Details on how the MATLAB (master) and LabVIEW (slave) programs communicate are given in the following sections. A syringe pump (KD Scientific, Model 780210L) is used to control the flow inside the sample (a Teflon tube with an inner diameter of 1.67 mm) and is marked in Figure 53. A photo of the experimental MRI setup is shown in Figure 91.

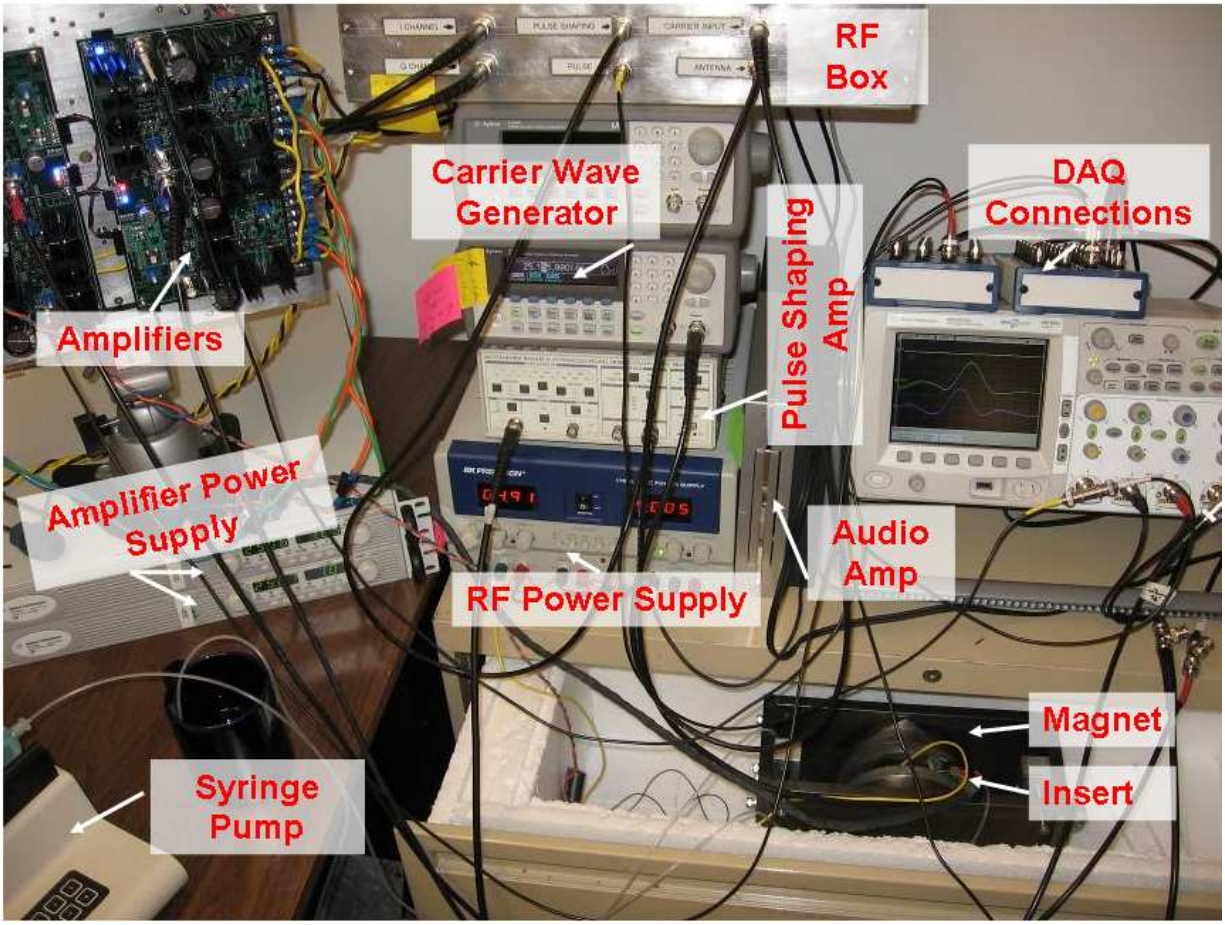

Figure 91. Experimental setup of the microfluidic visualization instrument with all the components connected.

3.2 Data Acquisition Software

The data acquisition software is programmed in LabVIEW 8.5 and controls the analog outputs of two data acquisition boards. The analog inputs are not used in this work, but can be used in future to acquire the MR signals as well.

The first DAQ is the NI6259 from National Instruments which has four analog outputs with a maximum sampling rate of 1.25 MS/s (for all four analog output channels together) and is connected to a PCI slot in the PC. It has programmable channels (called PFI) that can be used to

access the sampling clock signal and also be used for triggering. The internally generated sampling clock of 500 kHz is routed to the PFI 7. The external trigger is programmed to be on PFI 2. The digital triggering signal is also generated in the NI6259 DAQ using a counter (Cntr 0) which runs at 100 Hz with a 50% duty cycle (i.e., a square shaped waveform). The triggering signal (Cntr 0) must be physically connected to the trigger input of the DAQ (PFI 2) using a BNC cable. The physical connections of the DAQ are shown in Figure 92. The four analog channels of the NI6259 DAQ are connected to the three gradient amplifiers and the RF pulse signal going to the RF electronics box.

The second DAQ is the NI6212 also from National Instruments which has two analog outputs with a maximum sampling rate of 250 kS/s (for two analog output channels) and is connected to the PC via USB. This DAQ is programmed (PFI 0) such that the external clock is provided by the first DAQ (NI6259). Using this technique the sampling rate has been tested up to 900 kS/s (which is much higher than the reported specification) with no problems. The sampling rate is the same as the first DAQ which is set to 500 kS/s. The trigger is also programmed to be an external digital signal (PFI 2) which is supplied by the NI6259 DAQ. The physical interconnections between the two DAQs are also shown in Figure 92. The two analog outputs of the NI6212 DAQ are connected to the RF pulse shaping signal (connected to the SR560 pre-amplifier) and the B_0 compensation amplifier.

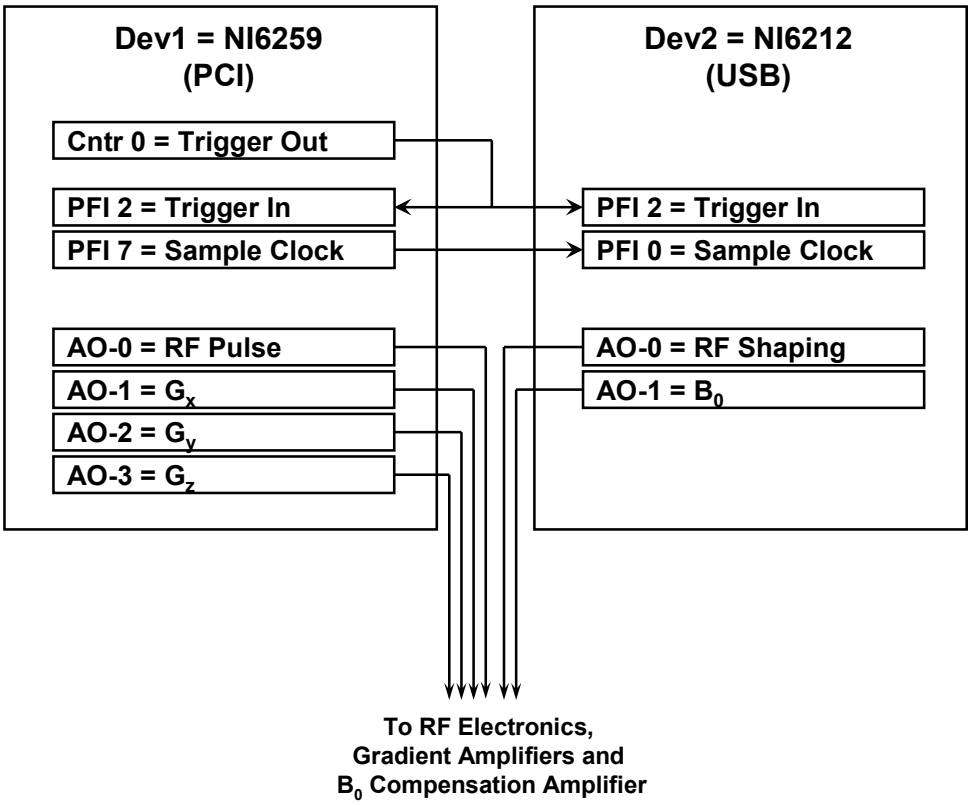

Figure 92. The synchronization between the DAQs is achieved by physically interconnecting them as shown.

A flow chart of the LabVIEW program controlling the two DAQs is shown in Figure 93. First, the triggering signal that is generated by the counter is initialized. Then, the channel properties (sampling frequency and triggering) of each DAQ is configured as explained before. The pulse sequence that is saved in a data text file is read. The pulse sequence data is then manipulated (i.e., an offset is added or a constant gain is multiplied to each channel) based on the data read from another text file called the MATLAB Link (ML) file. The ML file consists of a series of data, which specify the offsets and gains of the six analog outputs. This file is updated by a MATLAB program called the master. The master program is described in more detail in the following section. After the pulse sequence data is manipulated based on the data in the ML file,

the pulse sequence is again manipulated by gains and offsets available on the front panel of the LabVIEW program which are controlled by the user. The user adjustable gains and offsets are for fine tuning of the pulse sequence data. The analog waveforms output by the DAQs are updated every 100 ms. The LabVIEW (slave) program runs continuously until it is manually stopped by the user.

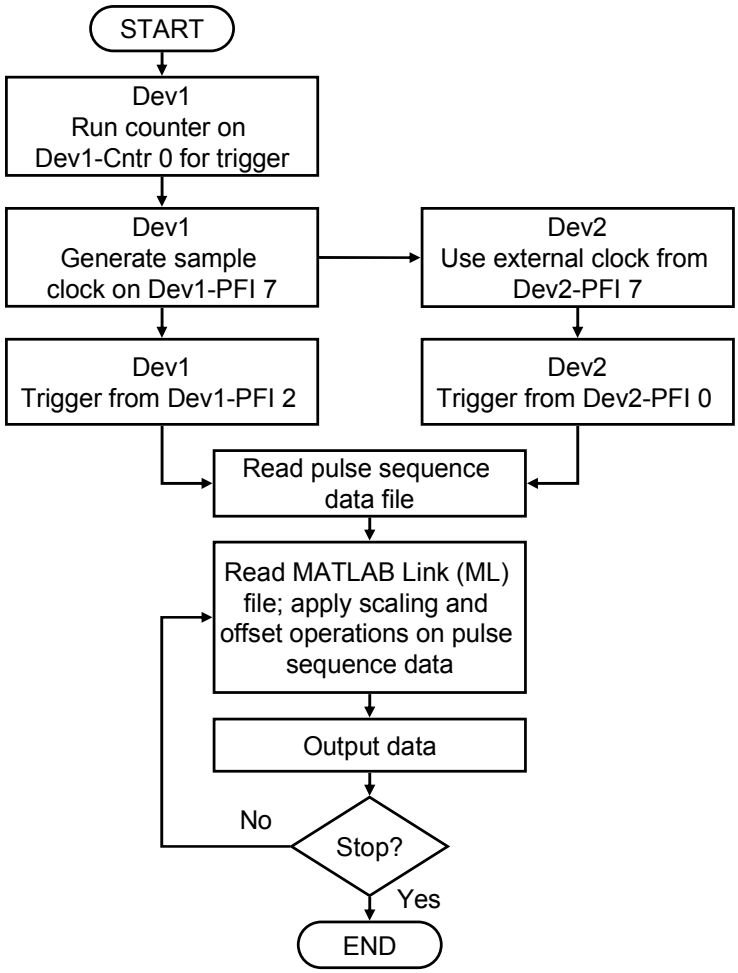

Figure 93. Flow chart of the LabVIEW program that synchronizes the two DAQs to output six analog waveforms read from a data file. The LabVIEW program is in slave mode and controlled by a MATLAB program (master).

The front panel with the graphical user interface (GUI) of the LabVIEW program is shown in

Figure 94. The location of the ML file and the pulse sequence data file are provided in a text box. The updated analog output waveforms of all six channels are shown on the six graphs on the front panel. The gains read in from the ML file are shown on the bottom left. The user configurable gains are located on the right.

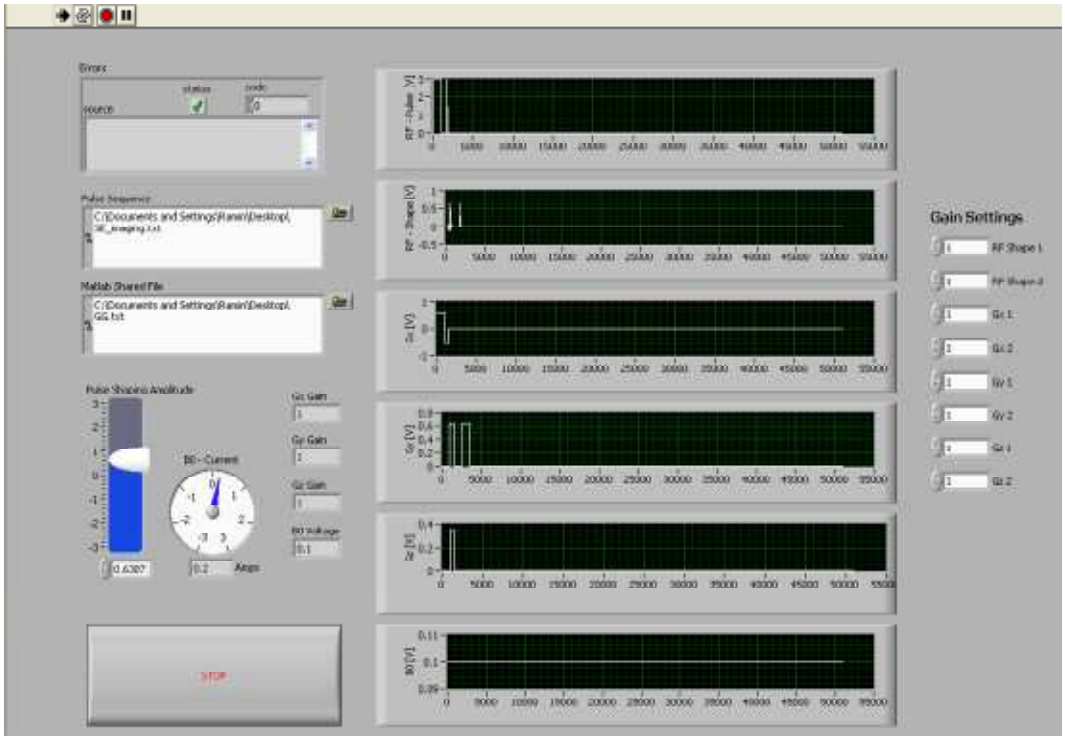

Figure 94. The LabVIEW program with a user friendly GUI in the front panel.

3.3 Frequency Shift Compensation and Signal Acquisition

A MATLAB program is written to control the analog outputs via the LabVIEW slave program and to perform the signal processing necessary to generate an MRI image. The sequence of program steps is summarized in the flow chart shown in Figure 95. After the user sets the imaging parameters (such and receiver bandwidth, number of averages, etc.) the program first initialized the ML file. Note that the LabVIEW program has to be running before the MATLAB

program is started. The oscilloscope is connected via USB to the PC and is configured to acquire the data from the receiver.

First, the magnetic flux density of the magnet is verified and controlled. For this purpose, an MR signal (second half of the echo) is acquired by the MSO6034A oscilloscope when the phase and frequency encoding gradients are turned off (their gains are set to zero in the ML file). The frequency shift of the signal is calculated after the offsets of the raw signal are removed and the data is phase corrected. The phase correction is a necessary step to ensure that the real and imaginary part can be both used for calculating the frequency shift. For more information regarding phase correction refer to [88]. The magnetic resonance frequency shift is calculated by taking a fast Fourier transform (FFT) of the phase corrected data. The zero crossing of the imaginary signal of the FFT corresponds to the resonance offset. The function that finds this zero crossing needs a starting point which is set to the maximum of the real part of the FFT. Based on the measured frequency shift, the ML file is updated to adjust the magnetic field in order to compensate for the frequency shift.

To acquire an image, the MR signal is acquired with no phase or frequency encoding gradients applied. The drift in the main magnetic field is calculated and a compensation signal is sent to the slave. If the magnet drift is too large (>100 Hz) this iteration is repeated. After the magnetic field is corrected, a single phase encoding step is performed. Again, the oscilloscope is configured to take the echo signal while the proper gradients are applied through the slave. After each phase encoding step, the compensation of the magnetic field is repeated. The averaged raw data (by the oscilloscope) are saved in k-space. After the imaging sequence is finished, the k-space is post processed (filtered and DC offsets removed) and a 2D FFT is performed to form an

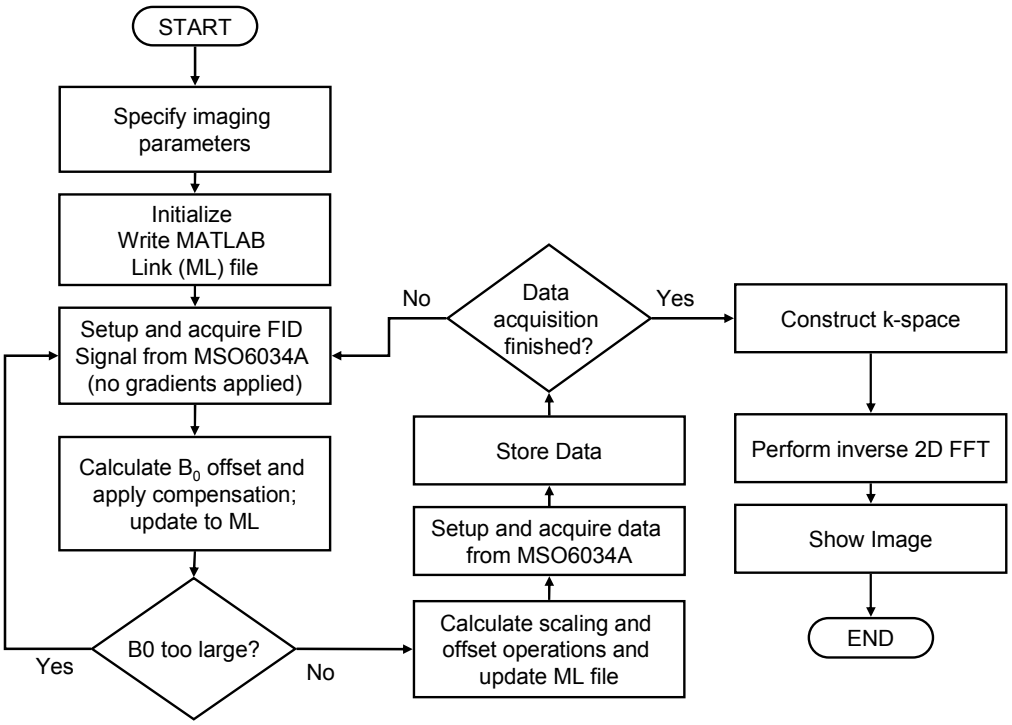

Figure 95. Flow chart of the MATLAB program (master) that controls the analog outputs via the LabVIEW program (slave).

image.

A performance of the B_0 compensation is shown in Figure 96 as a function of time. A simple integral controller is sufficient to compensate for the phase shift within ±150 Hz peak (average of 40Hz). The first plot shows the measured shift in the resonance frequency. The reference is set to zero Hertz for imaging. The second plot in Figure 96 shows that the error in the frequency shift is within ±150 Hz. The peak at time 6 min occurs because a lab chair (ferromagnetic) was purposely brought within 50 cm of the MRI setup for a minute and then removed.

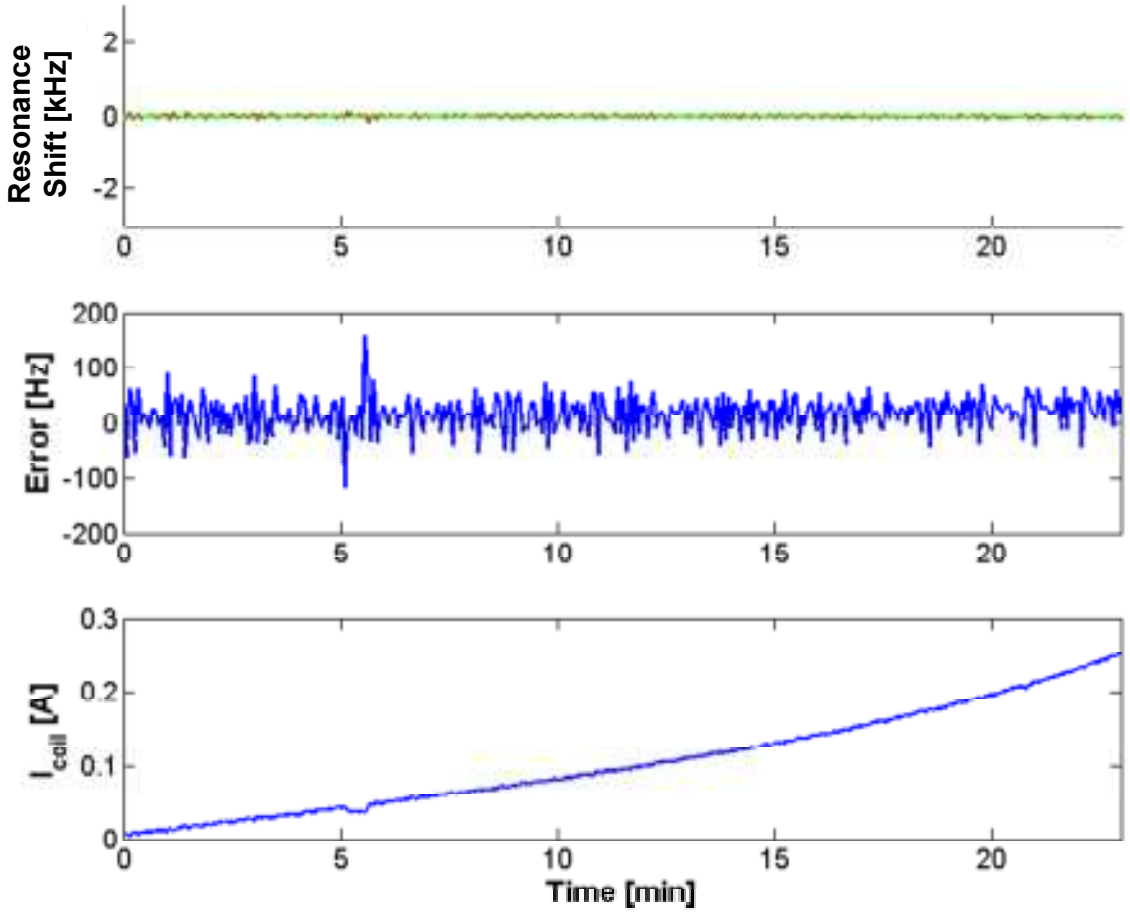

Figure 96. The performance of the B_0 compensation in terms of the shift of the magnetic resonance signal as a function of time is shown in the top figure with the reference is set to zero Hz. The error in the frequency shift is within ±150 Hz. The current inside the compensation coil is also shown as a function of time in the bottom plot. The peak of the error at time 6 min occurred because a lab chair was purposely brought close (50 cm) to the MRI setup.

The third plot in Figure 96 shows the current inside the B_0 compensation coil as a function of time. Without compensation, the resonance frequency would have shifted by 1.5 kHz over 24 minutes. The response of the compensation system is more clearly shown in Figure 97 where the reference resonance frequency was stepped to 2 kHz for testing purposes. The frequency shift is compensated for within two sampling points. The update rate is dependent on the repetition time of the pulse sequence, the SNR of the signal, the number of averages, and the delay introduced

by the data processing and acquisition (combination of the delays by the LabVIEW and the MATLAB programs and the setup time of the oscilloscope). Update rates between 0.01 to 0.5 Hz have been used in this work.

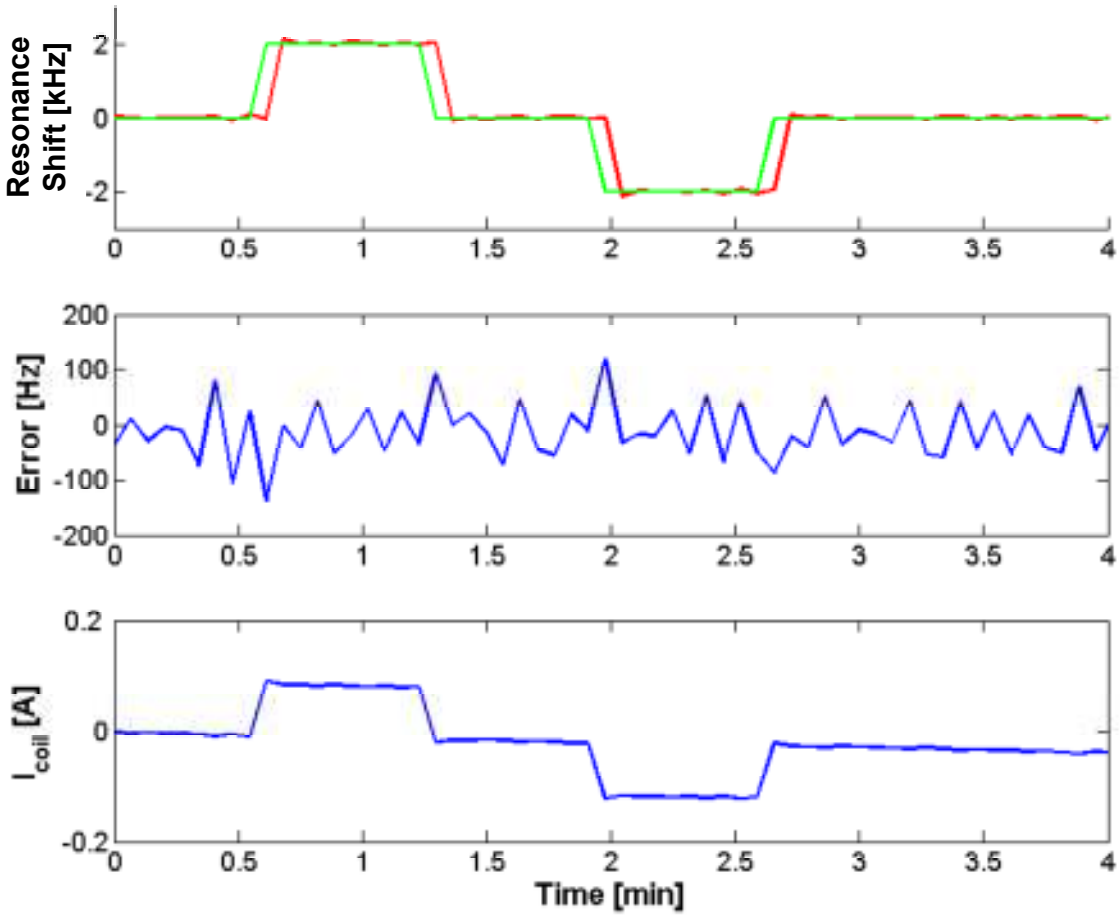

Figure 97. The performance of the B_0 compensation is shown in terms of the shift of the magnetic resonance signal as a function of time in the top figure with the reference changing by ±2 kHz. The error in the frequency shift is within ±150 Hz. The current inside the compensation coil is also shown as a function of time in the bottom plot.

The magnet compensation is applied until the frequency shift is within an acceptable range. After the magnet is compensated, the imaging sequence starts with a single phase encoding step. The phase encoding gain of in the ML file is updated. After a short pause the oscilloscope is configured to acquire data depending on the number of averages and the length of the pulse

specified by the user. The recorded data is store in a single line of k-space which is offset from the center depending on the phase encoding step. Then, the cycle for the magnet compensation is repeated before the next phase encoding step is performed. This cycle is repeated until the k-space is filled.

After the data acquisition is completed, the raw data in k-space is processed using MATLAB. First, the offsets are removed, and then the data is filtered by a third order Butterworth filter with a cut-off frequency equal to the receiver bandwidth specified by the user. A two-dimensional Fourier transform is then performed to generate the magnetic resonance image.

Chapter 4 - Micro MRI Static Imaging and Velocity Visualization

The pulse sequences to generate static and velocity encoded images using the described setup is presented next. Information regarding pulse sequence can be found in [15, 29, 30, 32, 88, 89]. A sample static image and a few velocity visualization plots that were obtained by the described instrument are presented.

4.1 Pulse Sequence for Static Imaging

The sample in this work is a tube filled with a fluid (water mixed with 40mM $CuSO_4$). For static imaging, the fluid is stationary and for velocity imaging the fluid is flowing at a flow rate set by the syringe pump. The coordinates adopted in this work are shown in Figure 98. The axis of the tube is along the x-axis with the flow moving in positive x-direction. The cross-sectional view of the tube is shown on the right-hand side of Figure 98 where the inner diameter of the tube is marked as D_i. The dimensions of the field-of-view (FOV) in the horizontal and vertical directions are marked as FOV_y and FOV_z, respectively.

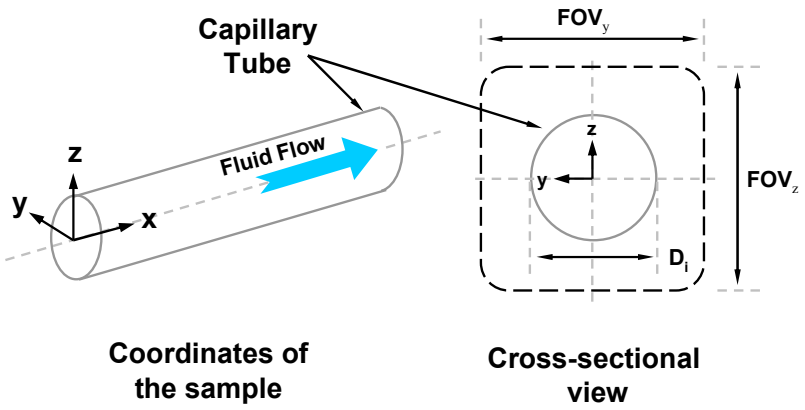

Figure 98. The coordinate system adopted in this work is shown for the sample. The field-of-view (FOV) is also defined in the cross-sectional view of the sample.

For basic 2D static imaging, the spin echo (SE) pulse sequence described in Chapter 1.4 is chosen for this work as it removes errors due to magnet in-homogeneities. A sample SE pulse sequence is shown in Figure 99 including the amplitude and duration of the each gradient. The echo signal, occurring at time TE, is recorded for imaging purposes. The FID signal immediately after the 90° is not used. To image the cross-section of the tube, a slice along the x-direction is needed. This is accomplished by a combination of a selective (Sinc) RF pulse of a an appropriate bandwidth and a slice selection gradient (G_x in this work). The bandwidth of the RF pulse (BW_{Sinc}) and the strength of the slice selection gradient (G_{slice}) define a slice thickness [m]

$$\text{Slice}_{TH} = \frac{2\pi \cdot BW_{Sinc}}{\gamma \cdot G_{slice}} = \frac{2\pi \cdot BW_{Sinc}}{\gamma \cdot G_{S,max}}. \tag{82}$$

The 180° RF pulse is non-selective but can be replaced by a selective pulse (in conjunction with a slice selection gradient) if desired.

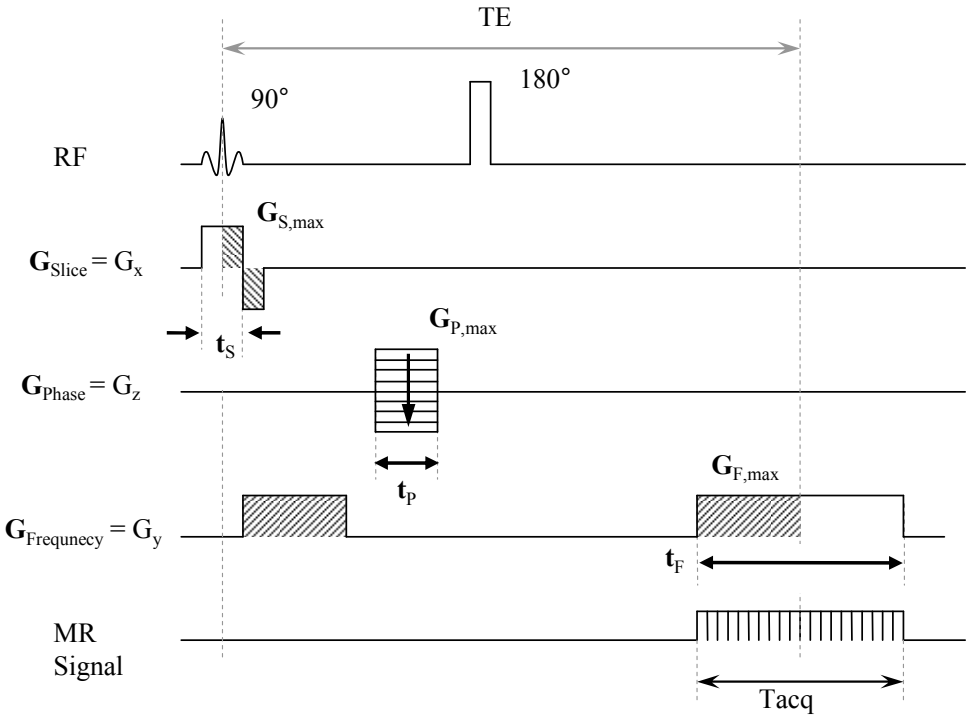

Figure 99. Basic spin echo (SE) pulse used for 2D imaging.

The phase encoding gradient is applied between the 90° and 180° RF pulse. The amplitude and duration of the phase encoding gradient are calculated based on the FOV and the spatial resolution in the phase direction. The gradient used for phase encoding is arbitrarily chosen to be in the z-direction in this work. The G_z gradient is given by

$$G_{z,max} = G_{Phase} = \frac{2\pi \cdot N_P}{FOV_P \cdot \gamma \cdot t_P}, \tag{83}$$

where N_p is the number of phase encoding steps (typically 128 or 256) and t_p is the duration for which the phase encoding gradient is applied. The FOV in the phase direction is the same as FOV_z defined in Figure 98. To minimize the echo time, TE, the pulse duration of the phase encoding gradient, t_p, is chosen to be as small as possible while respecting the restriction posed

by equation (83).

The de-phasing pulse of the frequency encoding gradient (G_y) is applied between the 90° and 180° RF pulses for a duration $t_F/2$. t_F is the pulse duration of the frequency encoding pulse applied during data acquisition of the magnetic resonance signal. This value is chosen based on the sampling frequency, $t_{Sampling}$, and the number of acquired samples $N_{Samples}$ (typically 128 to 512) given by

$$t_F = N_{Sampling} \cdot t_{Sampling}. \tag{84}$$

The gradient strength of the frequency encoding gradient is

$$G_{y,max} = G_{Frequency} = \frac{2\pi}{FOV_F \cdot \gamma \cdot t_{Sampling}}. \tag{85}$$

where FOV_F is the field of view in the frequency encoding direction (y-direction) as defined in Figure 98. Equation (85) can be re-written by substituting equation (84) given as

$$G_{y,max} = G_{Frequency} = \frac{2\pi \cdot N_{Sampling}}{FOV_F \cdot \gamma \cdot t_F}. \tag{86}$$

To minimize the echo time, TE, the duration of the de-phasing of the frequency encoding pulse is minimized. The frequency encoding gradient applied after the 180° RF pulse is shifted in time such that the rephrasing of the spins coincides with the echo time. The amplitude of this pulse defines the required bandwidth of the receiver given by

$$BW_{Receiver} = G_F \cdot FOV_F \cdot \gamma . \tag{87}$$

It is preferred to have a low bandwidth as the noise increases with bandwidth. A step by step procedure for calculating all the parameters for an imaging pulse sequence is outlined in the Appendix D.

The MR signal is recorded for a duration equal to the duration of the frequency encoding gradient with a sampling frequency $t_{Sampling}$. The raw data is then filtered using digital signal processing techniques (described in more detail in the following sections) and stored in k-space. The MR signal from each repetition of the phase encoding cycle occupies a single horizontal line in k-space as shown in Figure 100. The horizontal lines are offset from the center based on the duration and amplitude of the phase encoding gradient (i.e., the area underneath the phase encoding pulse). Each data point is horizontally spaced by

$$\Delta k_P = 1/FOV_P = \frac{\gamma \cdot G_{P,max} \cdot t_P}{2\pi \cdot N_P} \tag{88}$$

in the phase encoding-direction (vertical) and by

$$\Delta k_F = 1/FOV_F = \frac{\gamma}{2\pi} G_{F,max} t_{Sampling} \tag{89}$$

in the frequency-encoding (horizontal) direction.

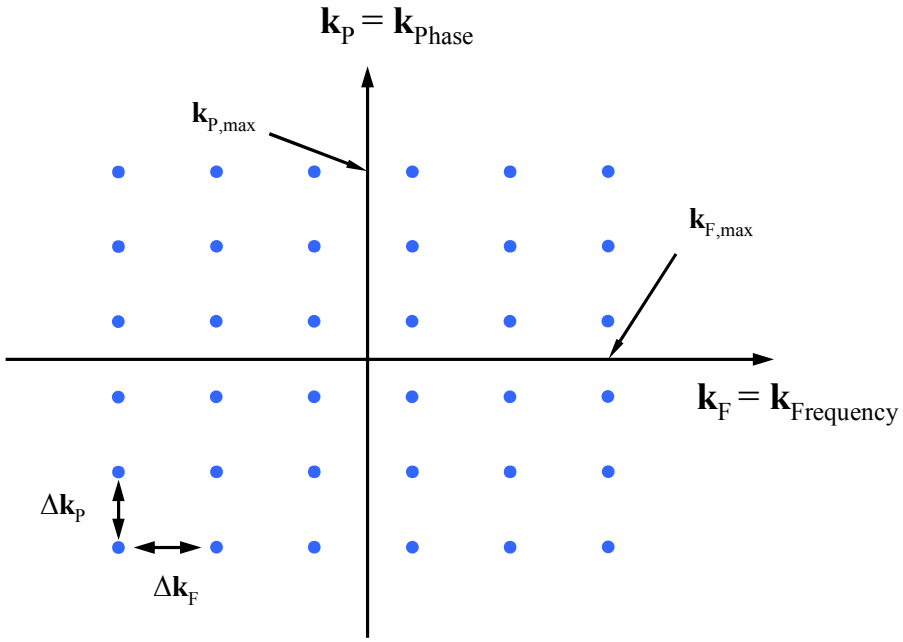

Figure 100. A sample k-space showing the points for which the raw data is stored. The recorded MR signal from each phase encoding step is stored in a horizontal line in k-space that is vertically offset from the center depending on the area of the phase encoding pulse.

4.2 Sample Static Image

A sample static 2D image of the circular cross-section of the tube (with an inner diameter of 1.67 mm) is shown in Figure 101. The number of averaging, NEX, is 128. The echo time, TE, is 5 ms with a repetition rate, TR, of 102 ms. The field of view for the phase and frequency encoding directions are 15 mm and 58 mm, respectively. A 128 x 1024 image is created by a 2D FFT. The image is cropped to 128 by 128 pixels. The receiver bandwidth is 500 kHz; thus every pixel represents approximately 500 Hz. The nominal resolution is 60 μm in frequency direction and 117 μm in the phase direction. A white/grey disc shaped image was expected to be seen in in the resulting image, which is clearly not the case in Figure 101. Due to time constrains, it was not determined why the image is not a representation of the sample.

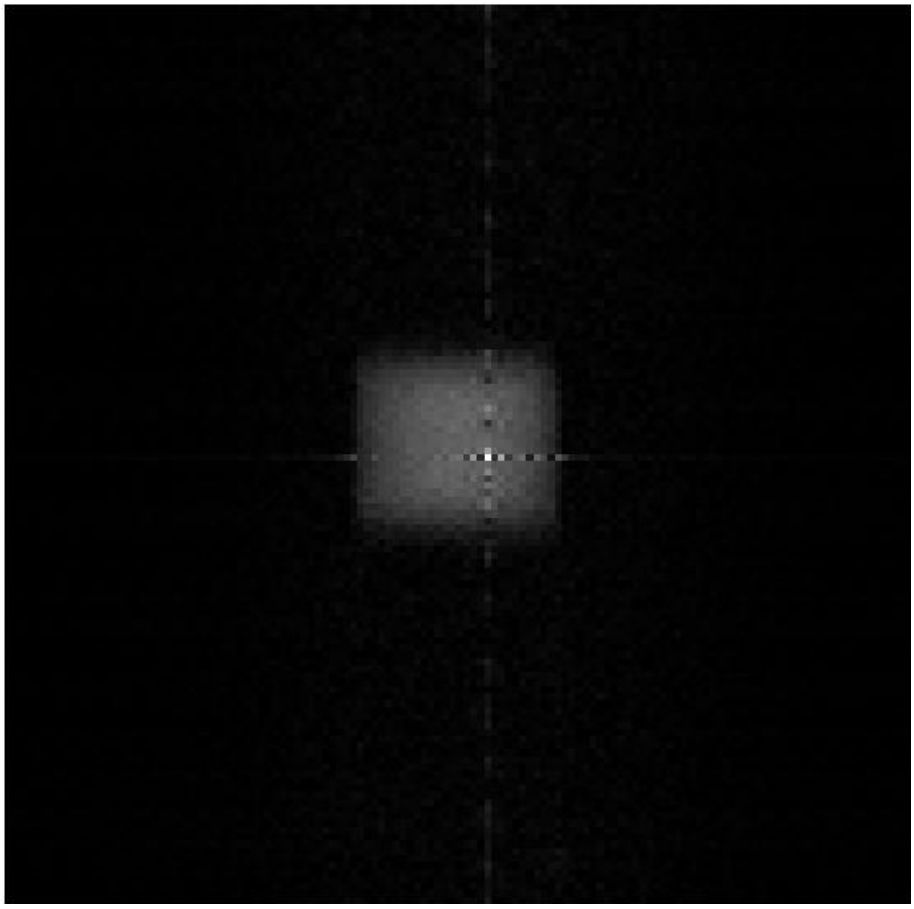

Figure 101. Sample static image featuring the (cropped to 128x128 pixels) cross-sectional view of the tube (inner diameter = 1.67 mm). TE/TR = 5/102 ms; NEX = 128; FOV_P = 15 mm; FOV_F = 58 mm.

Further effort was put on implementing the velocity encoded imaging because the primary purpose of this instrument is the visualization of velocity, rather than static imaging.

4.3 Pulse Sequence for Velocity Imaging

As discussed in Chapter 1.4, the two pulse sequence implementations for flow encoded imaging are time-of-flight (TOF) and phase contrast (PC) techniques. For PC flow encoded imaging, again a spin echo pulse sequence as shown in Figure 102 can be used. The pulse sequence is very similar to the static imaging case. The first notable difference is that the role of the gradients has changed. For example the slice selection gradient is now G_z which excites slice parallel to the fluid flow. The next difference is that the phase-encoding pulse is applied twice with a delay of *T* and duration t_P: once before and once after the 180° RF pulse.

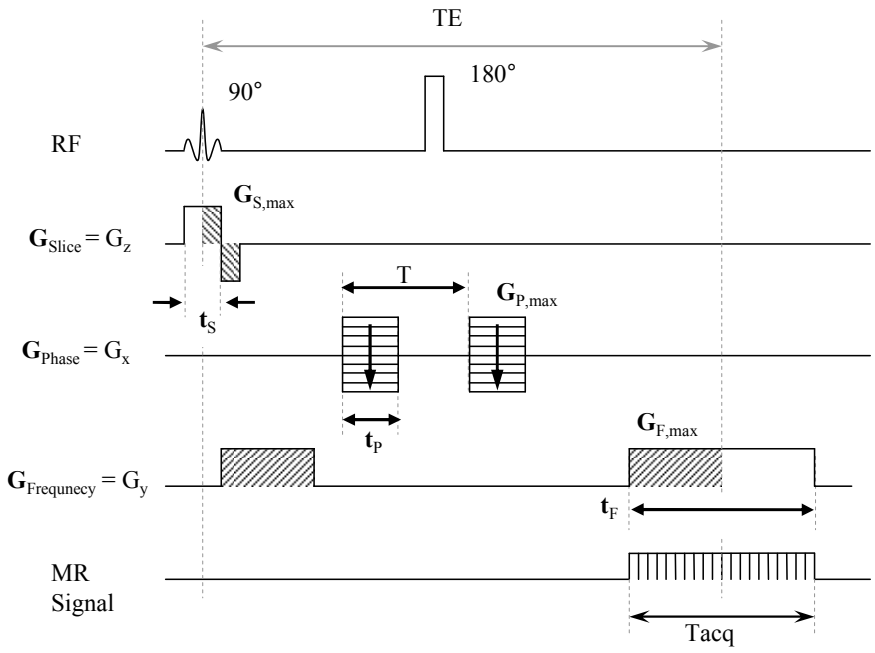

Figure 102. The basic modified spin echo (SE) pulse for phase sensitive velocity encoding.

The effect of this type on phase-encoding is that stationary spins do not experience any net phase shift; however, spins traveling with a speed *V* in the x-direction, experience a net phase shift

$$\Delta\phi_P = \gamma G_{P,max} t_P \cdot T \cdot V . \tag{90}$$

The pulse duration t_P and the time delay T are chosen based on the maximum expected velocity. To avoid any uncertainties due to phase warps greater than 2π, the parameters are chosen such that the maximum velocity is lower than

$$V < \frac{2\pi}{\gamma G_{P,max} t_P \cdot T} . \tag{91}$$

The k-space is filled similar to the static imaging case after the raw data is digitally processed.

Due to time constraints PC velocity imaging was not implemented. However, a TOF based velocity encoded pulse sequence was implemented for fast flows as a proof-of-concept that the experimental instrument is functional.

As described in Chapter 1.4, a one-dimensional plot of the velocity can be made using a SE pulse sequence shown in Figure 13a. A selective 90° RF pulse of with a bandwidth of 6 kHz was applied along with a slice selection gradient (G_x) with an amplitude of 0.06 T/m for a duration of 2 ms to excite a 2.3 mm slice. The rephrasing lobe of the slice selection gradient is applied for 1 ms with an amplitude of -0.06 T/m. The de-phasing pulse of the frequency encoding direction (G_y) can be applied anywhere between the 90° and 180° RF pulses. To minimize TE (5 ms) however, this pulse is applied when the re-phasing of the slice selection gradient starts. The amplitude of this gradient was 0.3 T/m and was applied for a duration of 1 ms. The frequency encoding gradient is applied again for a duration of 2 ms and sample amplitude after the 180° pulse, and is centered at the TE = 5ms. The phase encoding was not used in this experiment as only a 1D plot of bulk velocity in a slice was measured. The resulting echo was sampled during

the second pulse of the frequency encoding gradient at 500 kHz. A repetition rate of TR = 102 ms was used. The actual pulse sequence used in the instrument is shown in Figure 13b.

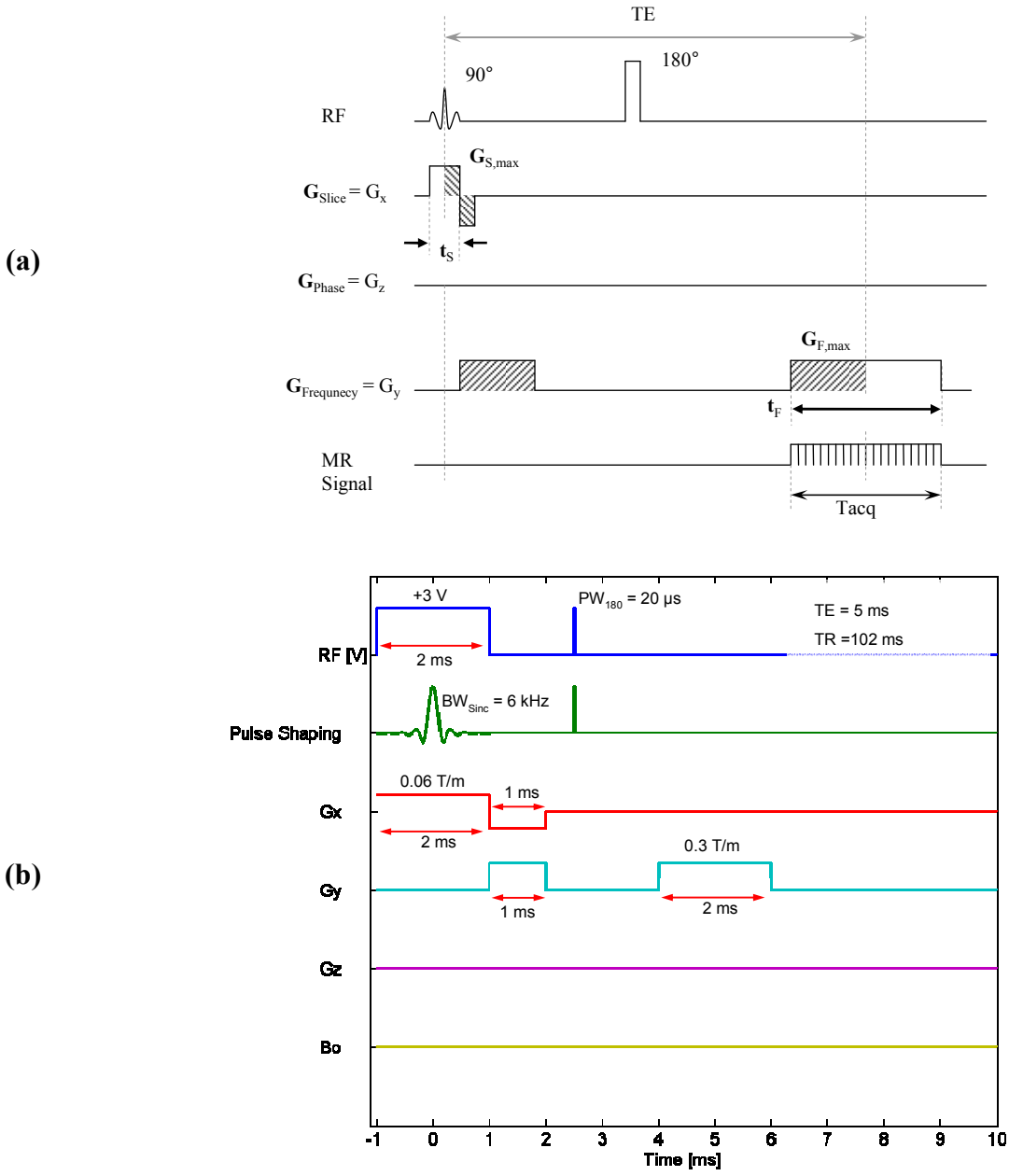

Figure 103. Simplified SE for 1D imaging of fast flow (a) and the sequencing diagram used for the instrument (b).

The pulse sequence shown in Figure 13 is repeated twice, once when the fluid in the tube is

stationary and once when the fluid is flowing at a certain flow rate (set by the syringe pump). The idea is that stationary spins produce and echo signal at time TE because the experience both RF pulses; however, moving spins (if sufficiently fast) do no experience the 180° pulse thus produce a reduced echo signal as they have moved out of the detection area (approximately 3 mm). A difference between the magnitudes of their Fourier transform is an indication of the velocity profile inside the tube. Sample 1D plots that show the flow field inside a tube are shown in the flowing section.

4.4 Sample Velocity Visualization Measurements

The normalized reduction of the echo amplitude as a function of the flow rate inside the tube is shown in Figure 104. As expected the echo amplitude is reduced as a function of flow rate for fast flows. The reduction in echo amplitude is observed for flow rates above 100 ml/hr, and it is semi-linear for flows up to 2,300 ml/hr. The echo amplitude further decreases (non-linearly) as a function of flow rate for flows above 2300 ml/hr. The average velocity is related to the flow rate was calculated to be 0.127 (mm/s) / (ml/hr). For example, a flow rate of 393 ml/hr corresponds to an average velocity of 50 mm/s inside the tube. The flow is still laminar for these experiments as the Reynolds number is approximately 85 which is below the critical value of 2300. This is true even for the maximum flow rate of 4000 ml/hr (0.5 m/s) where RE = 840.

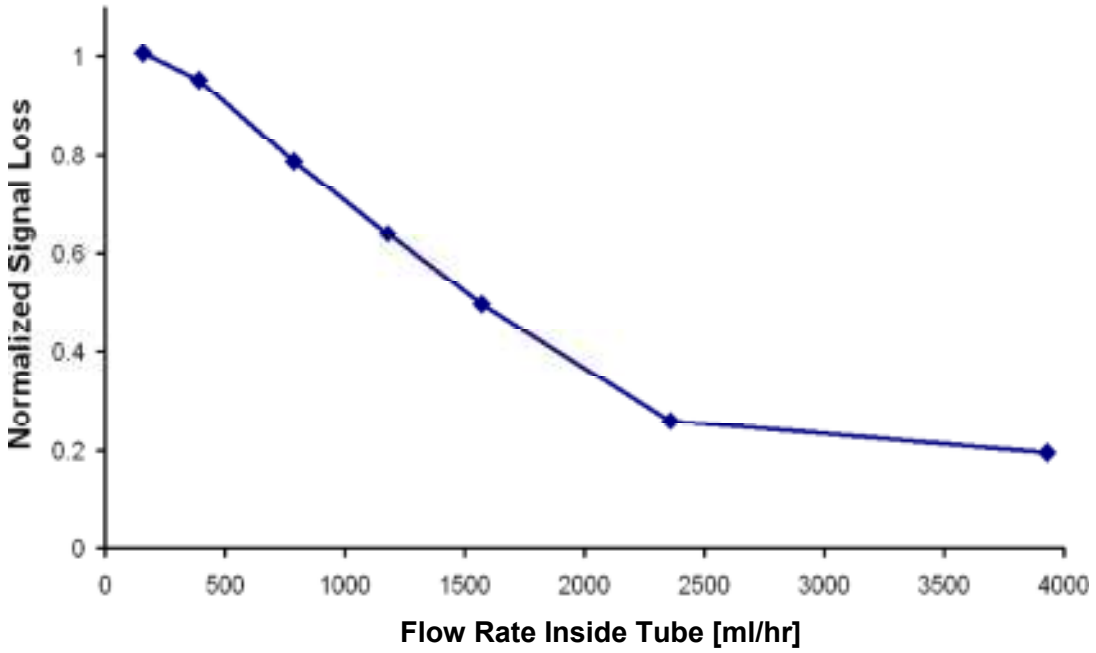

Figure 104. A reduction in the amplitude of the MR echo is observed as the flow rate is increased in the tube. The reduction in echo amplitude is observed for flow rates above 100 ml/hr, and it is semi-linear for flows up to 2,300 ml/hr.

The pulse sequence that was described in the previous section is used to extract one-dimensional bulk velocity information inside the 1.67 mm diameter tube, as shown in Figure 105. The flow rate was set to zero and the magnitude of the 1024-point Fourier transform was plotted as shown in the top plot of Figure 105a. The horizontal axis is the frequency where the bandwidth (22 kHz) of the signal is related to the gradient amplitude (0.3 T/m) and the diameter of the tube (1.67 mm). This corresponds to a FOV_F = 40 mm and a spatial resolution of approximately 40 μm. The center of the tube is offset from the center of the gradient which results in the offset observed in the spectrum shown in Figure 105. Also, at the zero-frequency a sudden dip in the magnitude is observed with a bandwidth of about 500 Hz which is due to the in-homogeneity of the magnet (20 ppm). After the initial experiment, the flow rate was set to 393 ml/hr (V_{mean} = 50 mm/s) and the experiment was repeated. The result is shown in the middle plot shown in Figure

105a. The difference between the first two plots is an indication of the velocity in the tube. This is shown in the bottom plot in Figure 105a where the vertical axis is in arbitrary units. As expected the maximum signal occurs in the center of the tube while the signal is zero at the walls of the tube. The experiment was repeated for a flow rate of 786 ml/hr (V_{mean} = 100 mm/s) as shown in Figure 105b. The residual signal shown in the bottom plot of Figure 105b has the largest signal (i.e., velocity), again, in the middle of the tube. The overall amplitude of the residual plot of this case (V_{mean} = 100 mm/s) is also larger than the one for the previous case (V_{mean} = 50 mm/s). The signal is zero at the walls of the tube as expected.

From laminar flow theory, the velocity profile in expected to be a parabolic with a shaped defined as [5]

$$V(r) = V_{max}\left(1-\left(\frac{r}{R}\right)^2\right) \tag{92}$$

where the velocity at each point *r* can be found if the maximum velocity *Vmax* is known.

(a)

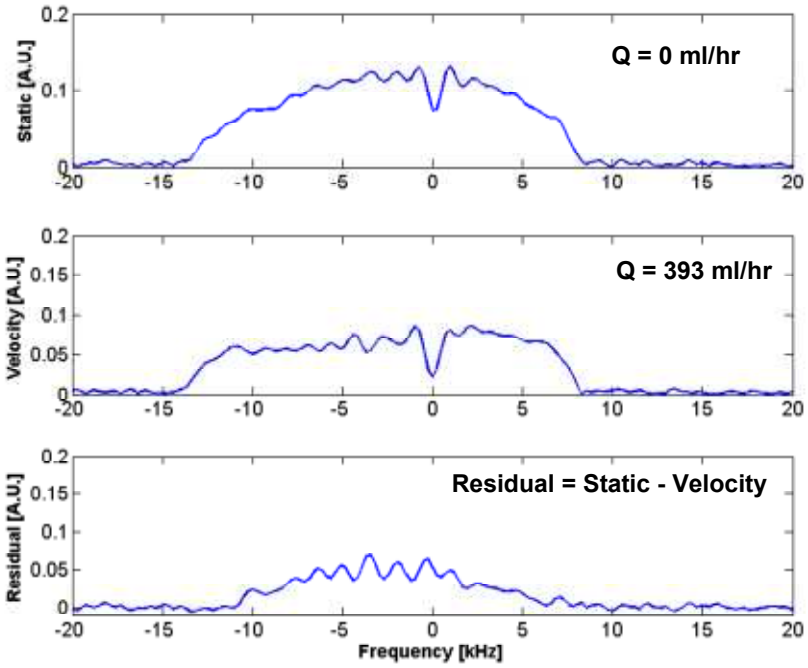

(b)

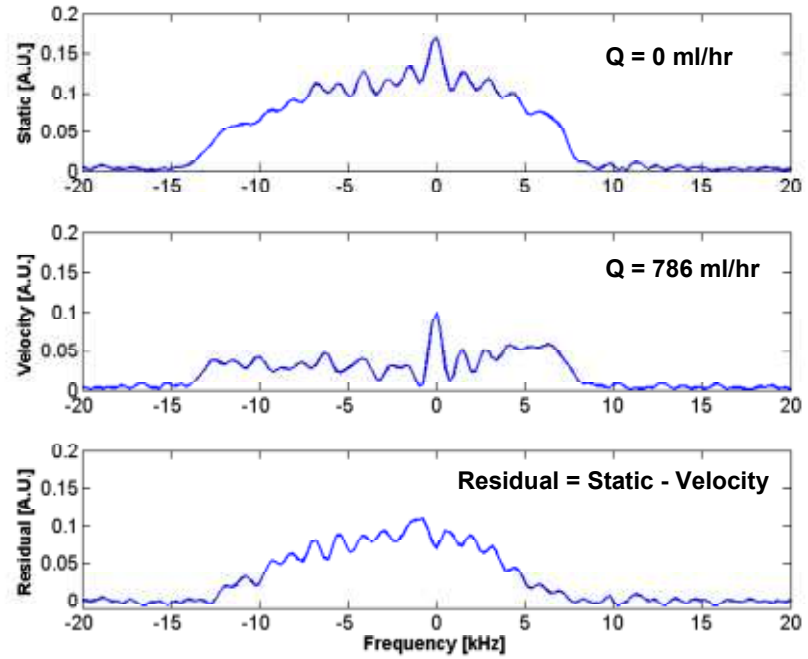

Figure 105. The 1D flow imaging experiment for a flow rate of 393 ml/hr (V_{mean} = 50 mm/s) in (a) and a flow rate of 786 ml/hr (V_{mean} = 100 mm/s) in (b). The residual plots in the bottom plot of (a) and (b) are an indication of the velocity profile in the tube.

The residual signals are presented in one plot and are fitted with a parabolic curve expected from laminar flow, as shown in Figure 106. The measured velocity profiles fit well with the parabolic curves expected by theory.

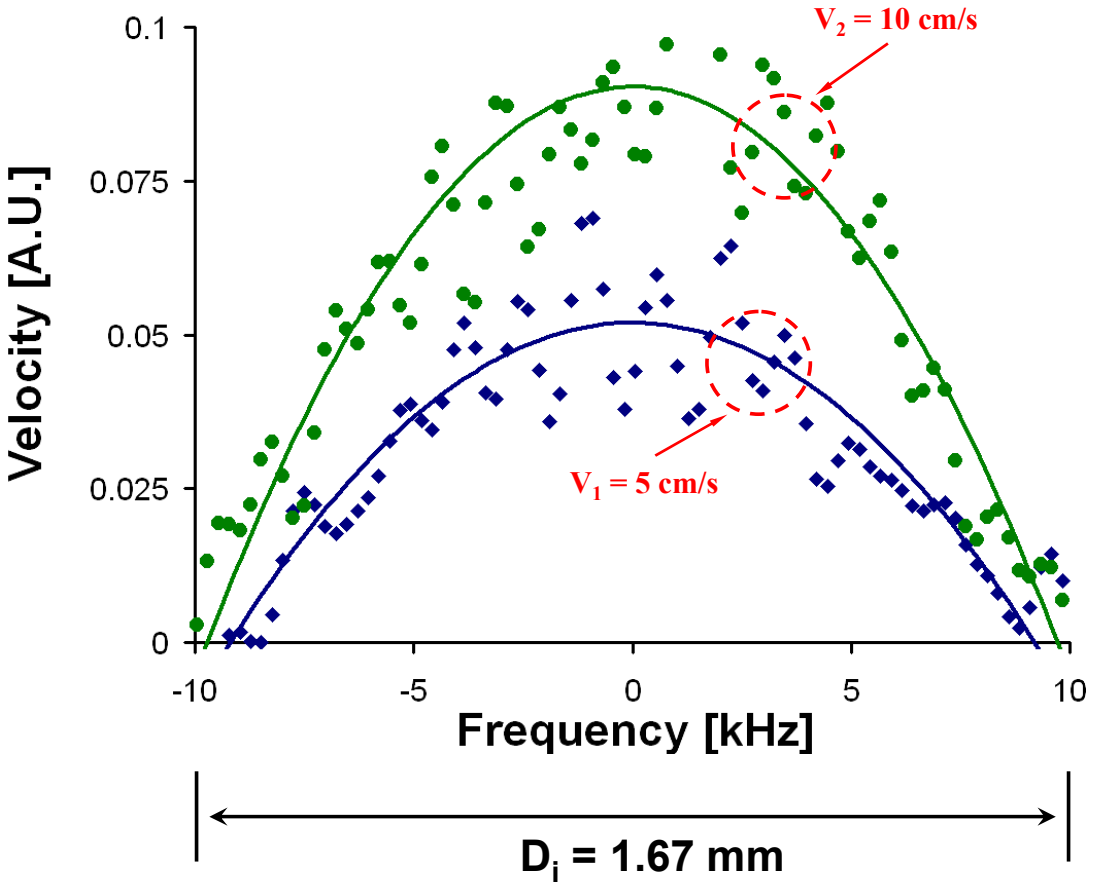

Figure 106. The velocity profile inside a 1.67 mm tube at flow rates of 393 ml/hr (V_{mean} = 50 mm/s) and 786 ml/hr (V_{mean} = 100 mm/s). The velocity profiles fit well with an expected parabolic profile of laminar flow.

As shown in Figure 106, this instrument can be used, at least for relatively fast flows, to visualize flow in one dimension. This result also suggest that the main components of this MRI imaging instrument are functional and can be used to set up more elaborate pulse sequences to accurately measure flow field of slower flows.

Chapter 5 - Conclusion and Future Work

5.1 Conclusion

In conclusion, the development of the world's smallest magnetic resonance imaging (MRI) instrument specifically designed for flow imaging is described. Static images can also be generated by this instrument. The hardware of this instrument has been developed for imaging resolutions approximately $(30\ \mu m)^3$ and velocity resolutions of 50 μm/s in all three spatial directions in a 2 mm diameter-spherical –volume (DSV). The work done in this thesis includes:

1. Analysis of requirements for high resolution magnetic resonance static and velocity encoded imaging (Chap 1.4)
2. Design, simulation and characterization of two permanent magnets (Chap 2.1) one of which was used for imaging at 0.6 T with a 20 ppm homogeneity over a 2 mm DSV.
3. Design, simulation and characterization of a triaxial gradient module capable of gradient fields up to 2.8 T/m with rise times below 50 μs, with integrated RF probe (Chap 2.2). A new fabrication process for MRI gradient coils was developed.
4. Design, simulation and characterization of four high-current gradient amplifiers capable of currents up 20 A with a bandwidth greater than 150 kHz at a combined power of 0.8 kW (Chap 2.3)
5. Design and characterization of a quadrature phase-sensitive detector capable of detecting magnetic resonance down to -120 dBm and RF transmitter with pulse shaping capability (Chap 2.4).

6. Implementation of the synchronization and timing of the overall magnetic resonance system (Chap 3).
7. Due to time constraints only a time-of-flight velocity encoded images were taken as a proof of concept. Visualization of flow inside a 1.67 mm diameter tube with average velocities of 50 mm/s and 100 mm/s were demonstrated in one-dimensional plots with a spatial resolution of approximately 40 μm. The images fit well with the parabolic curve expected from theory for laminar flows.

5.2 Future Work

The micro MRI for flow visualization has been built, the functionality of which was demonstrated. However, there are several improvements that can be made to this instrument for future which are discussed next.

5.2.1 Elimination of Noise in the Experimental Setup

The current setup is limited by to major noise sources: (1) the noise from the gradient amplifier and its power supplies which are picked up by the RF amplifier, and (2) noise from ground loop which deteriorates the signals received by the data acquisition system (the oscilloscope). A quantification of this noise was not made due to time constraints; qualitatively however, the voltage of the noise is about 30% of that of the MR signal which was partially reduced by averaging the signal over 128 repetitions.

The switching noise of the power supply is directly picked up by the RF electronics as they are very close to each other and are connected to the same power bar. This noise is observed when the power supply is turned ON while its outputs are disabled. The second way that switching

noise affects this system is when the noise from the outputs of the power supply travels through the current amplifier to the gradient coils. As the gradient coils are very close the RF probe, the noise is picked up from the RF probe and further amplified by the sensitive detector. The noise that is internally generated by the current amplifier also appears on the outputs which again couples through the gradient coils to the RF probe which again deteriorates the received signal The noise is at 60 Hz and was partially reduced by using common mode powder core filters connected to each output of the current amplifier.

Another major source of noise is ground loops in the current setup. It is very difficult to avoid ground loops as almost all RF components are one way or the other connected to ground. The ground of the power supplies (three for the RF electronics and two for the gradient amplifiers) are connected to a single point. The ground connections of the power supplies are also connected to the earth connection of the power bar. The ground of the audio amplifier, which is non-isolated, was connected to the system ground but is also connected to the ground of the power bar (which makes a ground loop by itself). The data acquisition boards are also non-isolated and therefore the grounds of all the connections to the DAQs are interconnected. In future this problem needs to be addressed by carefully interconnecting the components while keeping the ground loops to a minimum.

Ideally, the noise observed in the digitized signal on the PC is only the noise from the RF probe and the RF electronics.

5.2.2 Design of Optimized Pulse Sequences

In order to achieve the resolutions for which the components were designed for, the pulse sequence needs to be optimized. Due to time constraints only simple pulse sequences were

tested. For high resolution microscopy, typically phase encoding in all three spatial dimensions is used. Other elaborate pulse sequences exist for multi-echo acquisition which will speed up the imaging process significantly.

5.2.3 Improvements of the Magnet

The magnetic field and homogeneity of the 0.6 T permanent magnet can be improved by increasing the thickness of the iron plates of the efflux return path. According to simulations, the magnetic field will increase to 0.7 T for the same gap because the regions of saturation are reduced. This also has the effect of slightly improving the homogeneity. The homogeneity can be improved by another factor of 2-3 by using 2 mm thick high permeability material on the pole faces, according to simulations. Increasing the thickness of the Iron plates has the effect of reducing the leakage around the magnet which would make the magnet less susceptible to ferromagnetic objects around the magnet. In terms of temperature stability, it is probably best if a NMR lock was used to continuously control the magnetic field as opposed to the current implementation that compensates for the magnetic field every 10-20 seconds during which the magnetic field drifts. If an NMR lock is used, the imaging time would be approximately halved because the B_0 compensation software loop can be removed. The magnet also needs to be enclosed in a well insulated (thermal) and shielded (magnetic) area. This significantly reduces the image artifacts due to drifts and disturbances. All these improvements will be necessary to achieve high resolution images.

The main limitation for achieving higher resolutions is the magnet. With a higher magnetic field (SNR increases) it is possible to achieve higher resolutions. The magnetic field of the existing magnet can be improved such that saturation effects are minimized (by increasing the thickness

of the return path) and the area of the gap (i.e., the area of pole the pole faces) is reduced.

5.2.4 Improvements for Gradient Coils and Amplifiers

The existing triaxial gradient module and the gradient amplifiers should be sufficient for imaging resolutions of approximately $(30\ \mu m)^3$. If higher resolutions are desired the gradients coils can be redesigned to have a greater number of turns and/or have reduced dimensions. Reducing the dimensions also has the effect of reducing the volume over which the gradients are linear. Alternatively, the driving current supplied by the gradient amplifiers can be increased by redesigning the gradient amplifiers to allow for larger supply voltages.

A potentially problematic issue that was not fully investigated for the existing setup is the eddy currents that are generated in the conductive pole faces of the magnet by the rapidly switching gradient fields. This is especially true of large gradient strengths are used in the pulse sequence. A simple and effective fix for this to insert a few slotted conducting discs between the poles of the magnet and the gradients (discussed in Chapter 2.2). This will limit the eddy current in a smaller region where they are quickly diminished. Active shielding can also be used if additional sets of coils are added to the gradient module to cancel the effect of the gradient fields close to the magnet pole faces.

5.2.5 Improvements of the RF Electronics

The main performance limitations of the receiver are the dynamic range (i.e., SNR) and the rather large offsets on the outputs. The problem with large offsets at the output must be addressed as it introduces significant saturation in the RF components that leads to image artefacts. An effective solution is to use phase cycling [88, 89] to eliminate the offsets and other

common mode errors which would require a transmitter whose phase can be changed dynamically.

The home audio amplifier used as the final stage of amplification is also quite noisy with a limited bandwidth which must to be replaced by a suitable amplifier in near future.

The aforementioned problems can be avoided by replacing the existing analog receiver with a digital receiver. In a digital receiver, the signal picked up by the RF probe is first amplified by a low noise amplifier and then directly digitized by a fast analog-to-digital converter. The signal, now being in the digital domain, can be further processed using digital signal processing techniques with no additional loss or degradation of the signal. A digital receiver has the advantage of being more flexible in terms of signal bandwidth, choice of filtering, and operating frequency. It would make sense to change the transmitter also to digital if a digital solution is chosen for the receiver.

In foreseeable future it is necessary to develop a RF probe that is large enough to fit a typical microfluidics chip. This will be a necessary step if this instrument is to be used in industry and research institutes working on microfluidics.

Bibliography

[1] T. M. Squires and S. R. Quake, "Microfluidics: Fluid physics at the nanoliter scale," *Reviews of Modern Physics,* vol. 77, pp. 977-1026, 2005.

[2] D. Erickson and D. Li, "Integrated microfluidic devices," *Anal. Chim. Acta,* vol. 507, pp. 11-26, 2004.

[3] N. T. Nguyen and S. T. Wereley, "Fundamentals and Applications of Microfluidics," 2002.

[4] D. J. Beebe, G. A. Mensing and G. M. Walker, "Physics and Applications of Microfluidics in Biology," *Annual Reviews in Biomedical Engineering,* vol. 4, pp. 261-286, 2002.

[5] D. Sinton, "Microscale flow visualization," *Microfluidics and Nanofluidics,* vol. 1, pp. 2-21, 2004.

[6] K. P. Angele, Y. Suzuki, J. Miwa and N. Kasagi, "Development of a high-speed scanning micro PIV system using a rotating disc," *Measurement Science and Technology,* vol. 17, pp. 1639-1646, 2006.

[7] S. T. Wereley, L. Gui and C. D. Meinhart, "Advanced Algorithms for Microscale Particle Image Velocimetry," *AIAA J.,* vol. 40, pp. 1047-1055, 2002.

[8] D. Liu, S. V. Garimella and S. T. Wereley, "Infrared micro-particle image velocimetry in silicon-based microdevices," *Exp. Fluids,* vol. 38, pp. 385-392, 2005.

[9] S. J. Lee and G. B. Kim, "X-ray particle image velocimetry for measuring quantitative flow information inside opaque objects," *J. Appl. Phys.,* vol. 94, pp. 3620-3623, 2003.

[10] E. Fukushima, "Nuclear Magnetic Resonance as a Tool to Study Flow," *Annual Reviews in Fluid Mechanics,* vol. 31, pp. 95-123, 1999.

[11] P. T. Callaghan, "Rheo-NMR: nuclear magnetic resonance and the rheology of complex fluids," *Reports on Progress in Physics,* vol. 62, pp. 599-670, 1999.

[12] R. Frayne, "Velocity encoded pulse sequence design using phase-sensitive techniques," *PhD Dissertation,* 2007.

[13] P. G. Morris, "Nuclear Magnetic Resonance Imaging in Medicine and Biology," 1986.

[14] J. P. Hornak, "The Basics of MRI," 1996.

[15] M. A. Bernstein, K. F. King and Z. J. Zhou, *Handbook of MRI Pulse Sequences.* Amsterdam ; Boston: Academic Press, 2004, pp. 1017.

[16] R. Nezafat, P. Kellman, J. A. Derbyshire and E. R. McVeigh, "Real time high spatial-

temporal resolution flow imaging with spiral MRI using auto-calibrated SENSE," in *Engineering in Medicine and Biology Society,* 2004, pp. 1914-1917.

[17] A. J. Sederman, M. D. Mantle, C. Buckley and L. F. Gladden, "MRI technique for measurement of velocity vectors, acceleration, and autocorrelation functions in turbulent flow," *Journal of Magnetic Resonance,* vol. 166, pp. 182-189, 2004.

[18] D. Bonn, S. Rodts, M. Groenink, S. Rafaï, N. Shahidzadeh-Bonn and P. Coussot, "Some Applications of Magnetic Resonance Imaging in Fluid Mechanics: Complex Flows and Complex Fluids," *Annu. Rev. Fluid Mech.,* vol. 40, pp. 209-233, 2008.

[19] J. C. Bosshard, "Applications of MRI in Microfluidics: Single Echo Acquisition MRI towards Microfluidics," *Senior Honors Thesis,* 2006.

[20] K. Kose, Y. Matsuda, T. Kurimoto, S. Hashimoto, Y. Yamazaki, T. Haishi, S. Utsuzawa, H. Yoshioka, S. Okada, M. Aoki and T. Tsuzaki, "Development of a compact MRI system for trabecular bone volume fraction measurements," *Magn. Reson. Med.,* vol. 52, pp. 440-444, Aug. 2004.

[21] L. Sun, G. Amin, L. D. Hall, B. Wolf, W. J. Frith and S. Ablett, "A versatile thermostatted glass tube MRI rheometer," *Measurement Science and Technology,* vol. 10, pp. 1272-1278, 1999.

[22] H. Janeschitz-Kriegl and J. Meißner, *Polymer Melt Rheology and Flow Birefringence.* Springer-Verlag, 1983,

[23] J. Perlo, F. Casanova and B. Blümich, "Velocity imaging by ex situ NMR," *Journal of Magnetic Resonance,* vol. 173, pp. 254-258, 2005.

[24] Y. Uludag, M. J. McCarthy, G. A. Barrall and R. L. Powell, "Polymer Melt Rheology by Magnetic Resonance Imaging," *Macromolecules,* vol. 34, pp. 5520-5524, 2001.

[25] A. G. Goloshevsky, J. H. Walton, M. V. Shutov, J. S. Ropp, S. D. Collins and M. J. McCarthy, "Development of low field nuclear magnetic resonance microcoils," *Rev. Sci. Instrum.,* vol. 76, pp. 024101-1-024101-6, 2005.

[26] A. G. Goloshevsky, J. H. Walton, M. V. Shutov, J. S. Ropp, S. D. Collins and M. J. McCarthy, "Integration of biaxial planar gradient coils and an RF microcoil for NMR flow imaging," *Measurement Science and Technology,* vol. 16, pp. 505-512, 2005.

[27] P. T. Callaghan, "Rheo-NMR and velocity imaging," *Current Opinion in Colloid & Interface Science,* vol. 11, pp. 13-18, 2006.

[28] P. T. Callaghan, "Principles of Nuclear Magnetic Resonance Microscopy," 1991.

[29] D. G. Nishimura, "Principles of Magnetic Resonance Imaging," *Department of Electrical Engineering: Stanford University,* 1996.

[30] E. M. Haacke, R. W. Brown, M. R. Thompson and R. Venkatesan, "Magnetic resonance imaging : physical principles and sequence design," 1999.

[31] Z. Liang and P. C. Lauterbur, "Principles of magnetic resonance imaging : a signal processing perspective," 2000.

[32] P. Mansfield and P. G. Morris, "NMR Imaging in Biomedicine," vol. 2, 1982.

[33] E. L. Hahn, "Spin Echoes," *Physical Review,* vol. 80, pp. 580-594, 1950.

[34] W. A. Edelstein, J. M. Hutchison, G. Johnson and T. Redpath, "Spin warp NMR imaging and applications to human whole-body imaging," *Phys. Med. Biol.,* vol. 25, pp. 751-756, 1980.

[35] A. Kumar, D. Welti and R. R. Ernst, "NMR Fourier zeugmatography," *J. Magn. Reson.,* vol. 18, pp. 6983, 1975.

[36] L. Ciobanu, A. G. Webb and C. H. Pennington, "Magnetic resonance imaging of biological cells," *Prog Nucl Magn Reson Spectrosc,* vol. 42, pp. 69-93, 2003.

[37] A. Abragam, "The Principles of Nuclear Magnetism," 1961.

[38] D. I. Hoult and R. E. Richards, "Critical Factors in the Design of Sensitive High Resolution Nuclear Magnetic Resonance Spectrometers," *Proceedings of the Royal Society of London.Series A, Mathematical and Physical Sciences (1934-1990),* vol. 344, pp. 311-340, 1975.

[39] D. I. Hoult and R. E. Richards, "The signal-to-noise ratio of the nuclear magnetic resonance experiment," *J. Magn. Reson.,* vol. 24, pp. 71–85, 1976.

[40] R. K. Pathria, *Statistical Mechanics.* Butterworth-Heinemann, 1996,

[41] M. Jenkinson, "Fast, automated, N-dimensional phase-unwrapping algorithm," *Magnetic Resonance in Medicine,* vol. 49, pp. 193-197, 2003.

[42] T. Shirai, T. Haishi, S. Utsuzawa, Y. Matsuda and K. Kose, "Development of a compact mouse MRI using a yokeless permanent magnet," *Magn. Reson. Med. Sci.,* vol. 4, pp. 137-143, 2005.

[43] M. Kumada, I. Fujisawa, Y. Hirao, Y. Iwashita, M. Endo, M. Aoki, T. Kohda, I. Bolshakova and R. Holyaka, "Development of high field permanent magnet," *Applied Superconductivity, IEEE Transactions on,* vol. 12, pp. 129-132, 2002.

[44] S. R. Trout, "Understanding permanent magnet materials; an attempt at universal magnetic literacy," Magnequench International Inc., 1998.

[45] Anonymous "Soft magnetic materials and semi-finished products," Vaccumschmeze GMBH & Co. KG, Hanau, 2002.

[46] Anonymous "Datasheet: Carpenter high permeability 49 alloy," Carpenter, USA, 2003.

[47] H. Raich and P. Bluemler, "Design and construction of a dipolar Halbach array with a homogeneous field from identical bar magnets: NMR Mandhalas," *Concepts Magn. Reson.,* vol. 23, pp. 16-25, 2004.

[48] T. Miyamoto, H. Sakurai, H. Takabayashi and M. Aoki, "A development of a permanent magnet assembly for MRI devices using Nd-Fe-B material," *Magnetics, IEEE Transactions on,* vol. 25, pp. 3907-3909, 1989.

[49] K. Kose, T. Haishi, A. Nakanishi, S. Okada and T. Tsuzaki, "Development of a desktop MR microscope using a small permanent magnet," in *International Society for Magnetic Resonance in Medicine,* 2000, pp. 1380-1380.

[50] E. Katznelson and Y. Zuk, "Yoked Permanent Magnet Assemblies for use in Medical Applications," US Patent: 6150911, 2000.

[51] D. L. Y. Lee and R. D. Hay, "NMR Imaging Apparatus," US Patent: 4498048, 1985.

[52] R. L. Magin, A. G. Webb and T. L. Peck, "Miniature magnetic resonance machines," *Spectrum, IEEE,* vol. 34, pp. 51-61, 1997.

[53] G. Moresi and R. Magin, "Miniature permanent magnet for table-top NMR," *Concepts Magn. Reson.,* vol. 19, pp. 35-43, 2003.

[54] M. Kumada, E. Antokhin, Y. Iwashita, M. Aoki and E. Sugiyama, "Super strong permanent dipole magnet," *Applied Superconductivity, IEEE Transactions on,* vol. 14, pp. 1287-1289, 2004.

[55] M. Kumada, T. Fujisawa, Y. Hirao, M. Endo, M. Aoki, T. Kohda, Y. Iwashita, I. Bolshakova and R. Holyaka, "Development of a model 4 Tesla dipole magnet," *PAC2001,* pp. 18-22, 2001.

[56] S. M. Wright, D. G. Brown, J. R. Porter, D. C. Spence, E. Esparza, D. C. Cole and F. R. Huson, "A desktop magnetic resonance imaging system," *MAGMA,* vol. 13, pp. 177-185, Jan. 2002.

[57] S. M. Wright, D. G. Brown and D. C. Spence, "NMR Hardware and Desktop Systems," *Fourth Mexican Symposium on Medical Physics,* vol. 538, pp. 112-118, 2000.

[58] E. Esparza-Coss and D. M. Cole, "A low cost MRI permanent magnet prototype," in 1998, pp. 119-129.

[59] A. V. Sahakian, C. Hayes and B. Yalvac, "An inexpensive laboratory module to teach principles of NMR/MRI," in 2005, pp. 1-10.

[60] Y. Li, J. A. Nyenhuis, H. E. Pietsch, F. J. Friedlaender, R. L. Stroshine, W. K. Wai and G. W. Krutz, "Permanent magnet design for low field ^{1}H-MR," in 1993, pp. 1-2.

[61] T. Haishi, T. Uematsu, Y. Matsuda and K. Kose, "Development of a 1.0 T MR microscope

using a Nd-Fe-B permanent magnet," *Magn. Reson. Imaging,* vol. 19, pp. 875-880, Jul. 2001.

[62] A. Podol'skii, "Development of permanent magnet assembly for MRI devices," *IEEE Trans. Magn.,* vol. 34, pp. 248-252, 1998.

[63] A. Podol'skii, "Design procedure for permanent magnet assemblies with uniformmagnetic fields for MRI devices," *Magnetics, IEEE Transactions on,* vol. 36, pp. 484-490, 2000.

[64] A. Podol'skii, "Permanent-Magnet Assemblies for Magnetic Resonance Imaging Devices for Various Purposes," *IEEE Trans. Magn.,* vol. 38, pp. 1549, 2002.

[65] C. Li and M. Devine, "Efficiency of Permanent Magnet Assemblies for MRI Devices," *Magnetics, IEEE Transactions on,* vol. 41, pp. 3835-3837, 2005.

[66] Y. Yao, C. S. Koh and D. Xie, "Three-dimensional optimal shape design of magnetic pole in permanent magnet assembly for MRI taking account of eddy currents due to gradient coil field," *Magnetics, IEEE Transactions on,* vol. 40, pp. 1164-1167, 2004.

[67] J. S. Ryu, Y. Yao, C. S. Koh and Y. J. Shin, "3-D Optimal Shape Design of Pole Piece in Permanent Magnet MRI Using Parameterized Nonlinear Design Sensitivity Analysis," *Magnetics, IEEE Transactions on,* vol. 42, pp. 1351-1354, 2006.

[68] D. H. Kim, B. S. Kim, J. H. Lee, W. S. Nah and I. H. Park, "3-D optimal shape design of ferromagnetic pole in MRI magnet of open permanent-magnet type," *Applied Superconductivity, IEEE Transactions on,* vol. 12, pp. 1467-1470, 2002.

[69] N. Marks, "Conventional magnets I," *CERN European Organization for Nuclear Research,* pp. 867-867, 1994.

[70] L. R. Moskowitz, *Permanent Magnet Design and Application Handbook.* Krieger, 1986,

[71] G. P. Double, V. N. Kahwaty, J. D. Randall and F. M. Reinhart, "NMR Magnet Assembly With Pole Face Parallelism Adjustment," US Patent: 4093912, 1978.

[72] A. P. McCann, F. Smith, J. A. S. Smith and J. D. Thwaites, "Adjustment of the homogeneity of a permanent magnet for high-resolution nuclear magnetic resonance," *J. Sci. Instrum.,* vol. 39, pp. 349-351, 1962.

[73] R. Kimmlingen and R. Endt, "Method for compensating for a magnetic field disturbance affecting a magnetic resonance device, and a magnetic resonance device," 2006 0076954 A1, 2005,

[74] Y. Inoue, S. Nagano, T. Suzuki, H. Uno, Y. Higa and Y. Tsujii, "Magnetic field stabilization method, magnetic field generating apparatus and magnetic resonance imaging apparatus," US Patent: 6239680, 2001.

[75] R. S. Hinks, S. T. Mansell, M. J. Radzium, D. A. Purgill, A. M. Linz and D. L. Hallman, "Magnetic resonance imaging device having magnetic field disturbance compensation," US

Patent: 6396268, 2002.

[76] J. Jian-Ming, "Electromagnetic analysis and design in magnetic resonance imaging," 1998.

[77] D. A. Seeber, J. H. Hoftiezer, W. B. Daniel, M. A. Rutgers and C. H. Pennington, "Triaxial magnetic field gradient system for microcoil magnetic resonance imaging," *Rev. Sci. Instrum.,* vol. 71, pp. 4263-4272, 2000.

[78] W. A. Anderson, "Electrical Current Shims for Correcting Magnetic Fields," *Rev. Sci. Instrum.,* vol. 32, pp. 241-250, 2004.

[79] P. T. Callaghan, M. E. Komlosh and M. Nyden, "High Magnetic Field Gradient PGSE NMR in the Presence of a Large Polarizing Field," *Journal of Magnetic Resonance,* vol. 133, pp. 177-182, 1998.

[80] A. C. Wright, H. Bataille, H. H. Ong, S. L. Wehrli, H. K. Song and F. W. Wehrli, "Construction and calibration of a 50 T/m z-gradient coil for quantitative diffusion microimaging," *Journal of Magnetic Resonance,* vol. 186, pp. 17-25, 2007.

[81] F. Casanova and B. Blümich, "Two-dimensional imaging with a single-sided NMR probe," *Journal of Magnetic Resonance,* vol. 163, pp. 38-45, 2003.

[82] M. J. E. Golay, "Field Homogenizing Coils for Nuclear Spin Resonance Instrumentation," *Rev. Sci. Instrum.,* vol. 29, pp. 313-315, 2004.

[83] R. Bowtell and P. Robyr, "Multilayer Gradient Coil Design," *Journal of Magnetic Resonance,* vol. 131, pp. 286-294, 1998.

[84] P. Kozlowski, *Private Communication: Practical Information on Pulse Sequence Design and Receiver Design,* 2008.

[85] A. S. Sedra and K. C. Smith, "Microelectronic circuits," 1987.

[86] D. Sahebjavaher, "High current gradient amplifier," Dept. of Electrical and Computer Eng., Univ. of British Columbia, Vancouver, B.C., 2007.

[87] X. Lu, "Electromagnetically-Driven Ultra-Fast Tool Servos for Diamond Turning," *PhD Dissertation,* 2005.

[88] C. N. Chen and D. I. Hoult, "Biomedical magnetic resonance technology," 1989.

[89] E. Fukushima and S. B. W. Roeder, "Experimental pulse NMR : a nuts and bolts approach," 1981.

[90] D. A. Cornell, C. F. M. Clewett and M. S. Conradi, "Versatile pulsed NMR system and experiments for students," *Concepts Magn. Reson.,* vol. 12, pp. 257-268, 2000.

[91] S. Eroglu, B. Gimi, B. Roman, G. Friedman and R. L. Magin, "NMR spiral surface

microcoils: Design, fabrication, and imaging," *Concepts Magn. Reson.,* vol. 17, pp. 1-10, 2003.

[92] L. Gengying, J. Yu, Y. Xiaolong and J. Yun, "Digital nuclear magnetic resonance spectrometer," *Review of Scientific Instruments,* vol. 72, pp. 4460-4463, 2001.

[93] S. Jie, X. Qin, L. Ying and L. Gengying, "Home-built magnetic resonance imaging system (0.3 T) with a complete digital spectrometer," *Review of Scientific Instruments,* vol. 76, pp. 105101-1-105101-8, 2005.

[94] J. S. Lord and P. C. Riedi, "A swept frequency pulsed magnetic resonance spectrometer with particular application to NMR of ferromagnetic materials," *Measurement Science and Technology,* vol. 6, pp. 149-155, 1995.

[95] I. Lowe and C. Tarr, "A fast recovery probe and receiver for pulsed nuclear magnetic resonance spectroscopy," *Journal of Physics E: Scientific Instruments,* vol. 1, pp. 320-322, 1968.

[96] Y. Maguire, E. Boyden and N. Gershenfeld, "Toward a table-top quantum computer," *IBM Syst J,* vol. 39, pp. 823-839, 2000.

[97] C. A. Michal, K. Broughton and E. Hansen, "A high performance digital receiver for home-built nuclear magnetic resonance spectrometers," *Rev. Sci. Instrum.,* vol. 73, pp. 453-458, 2002.

[98] C. Michal, *Private Communication: Practical Information on Receiver Optimization and Impedance Matching of Probe,* 2008.

[99] T. L. Peck, R. L. Magin and P. C. Lauterbur, "Design and analysis of microcoils for NMR microscopy," *J. Magn. Reson. B,* vol. 108, pp. 114-124, Aug. 1995.

[100] K. Raoof, A. Asfour and J. M. Fournier, "A complete digital magnetic resonance imaging (MRI) system at low magnetic field (0.1 Tesla)," *Instrumentation and Measurement Technology Conference. IMTC 2002.,* vol. 1, 2002.

[101] D. A. Seeber, R. L. Cooper, L. Ciobanu and C. H. Pennington, "Design and testing of high sensitivity microreceiver coil apparatus for nuclear magnetic resonance and imaging," *Rev. Sci. Instrum.,* vol. 72, pp. 2171-2179, 2001.

[102] K. R. Minard and R. A. Wind, "Solenoidal microcoil design - Part I: Optimizing RF homogeneity and coil dimensions," *Concepts Magn. Reson.,* vol. 13, pp. 128-142, 2001.

[103] K. R. Minard and R. A. Wind, "Solenoidal microcoil design - Part II: Optimizing winding parameters for maximum signal-to-noise performance," *Concepts Magn. Reson.,* vol. 13, pp. 190-210, 2001.

[104] D. Bělohrad and D. Valúch, "High power switching unit for the MRI RF system," CERN, Switzerland, 2000.

[105] S. C. From and T. S. Damage, "PIN-limiter diodes effectively protect receivers,"

DesignFeature, 2004.

[106] D. A. Seeber, J. H. Hoftiezer and C. H. Pennington, "Positive-intrinsic-negative diode-based duplexer for microcoil nuclear magnetic resonance," *Rev. Sci. Instrum.,* vol. 71, pp. 2908-2913, 2000.

[107] D. G. Brown, D. Spence and S. Wright, "A transceiver for an inexpensive desktop MR microscope," *Engineering in Medicine and Biology Society, 2000.Proceedings of the 22nd Annual International Conference of the IEEE,* vol. 3, 2000.

[108] X. Wu, D. A. Patterson, L. G. Butler and J. B. Miller, "A broadband nuclear magnetic resonance spectrometer: Digital phase shifting and flexible pulse programmer," *Review of Scientific Instruments,* vol. 64, pp. 127-131, 1993.

[109] J. C. H. Tso, *Private Communication: Practical Information on Impedance Matching of the RF Probe,* 2008.

[110] O. Cakir, "Copper etching with cupric chloride and regeneration of waste etchant," *Journal of Materials Processing Tech.,* vol. 175, pp. 63-68, 2006.

Appendix A – Gradients

The fabrication process of the gradient coils is described next.

A.1 Gradient Fabrication Process

The designed assembly of the gradient coils and the mask is shown in Figure 107. The mask (positive) is printed on the shiny side of a toner transfer paper (TTS-5 from Pulsar) using a laser printer. The ink of the laser printer temporarily adheres to this special paper and is released when the printed side is pressured on the desired substrate and heated.

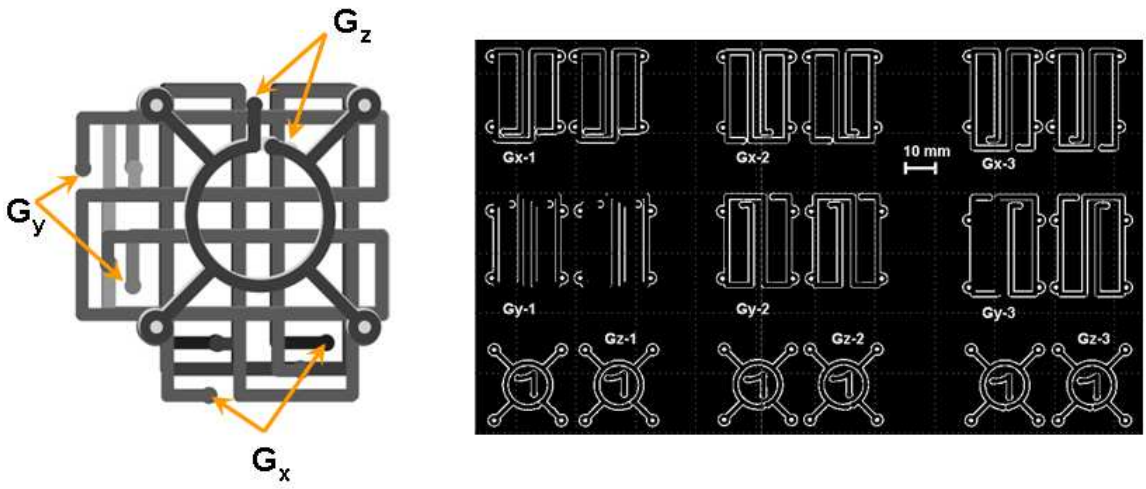

Figure 107. The assembly of the designed gradient coils (left) and its mask (right).

The fabrication process is schematically illustrated in Figure 108. In Step 1, a 0.01" (254 μm) thick copper sheet is cut (see Figure 109-1), flattened, cleaned using a Scotch-Brite® sponge and later cleaned again (see Figure 109-2) using a solvent (MG Chemicals Cat. # 827B-425G). In Step 2, the shiny side of the toner transfer paper which has the mask printed on it is laid on top of

the copper sheet. A completely black mask that is printed on a separate toner transfer paper is laid on the bottom of the copper sheet (see Figure 109-3). The masks are fastened by two strips of masking tape on each side; this is then sandwiched between to ¼" thick Aluminum plates that are used for applying pressure on this structure (see Figure 109-4). To ensure that a uniform pressure is applied on the mask and copper sheet, a few layers (~10) of paper are added (see Figure 108 Step 2) on each side. The two plates have are fastened to each other using five screws and baked for 30-45 minutes at 175 °C. After the backing process is finished, the plates are taken out of the oven (using pliers) and left in air to be cooled. The taped TTS-Copper-TTS is removed in Step 3 and placed in a bowl with warm water for 10 to 20 minutes (see Figure 109-5). The toner transfer paper is carefully pealed off. The mask is now transferred form the TTS paper to the copper sheet (see Figure 109-6). The texture of the transferred mask is relatively porous and will peal off if the etching is performed with no other intermediate step. To ensure that the mask adheres to the copper sheet, a green film (called Green TRF) is applied to both sides (see Figure 109-7) of the copper sheet using pressure and heat in Step 4 (same as Step 2). The only exception is that the film can be pealed off with no wetting step involved. The green TRF adheres to the mask only and it is repeatedly (usually 2 to 3 times) applied until the whole mask is covered (see Figure 109-9). In Step 5, the copper is etched in an etching solution typically containing 200 mL HCl, 100 mL H_2O_2 and 200 mL H_20. The etching solution is commonly referred to as Cupric Chloride ($CuCl_2$) and has an etching rate of up to 50 μm/min at 50° C and very high dissolved copper capacity. The main chemical reactions are [110]:

$$CuCl_2 + Cu \rightarrow 2CuCl \tag{93}$$

$$CuCl_2 + 2HCl + Cu \rightarrow 2CuCl + 2HCl\,. \tag{94}$$

The etching process also produces bubbles which ensure uniform and rapid etching. For easy handling of the sample a tape is attached to its back side. After the etching process is complete (see Figure 109-10), the sample is flushed with water for several minutes to clean it from any residual etchant (Step 6). To remove the mask in Step 7, either a degreaser or Acetone can be used (see Figure 109-11).

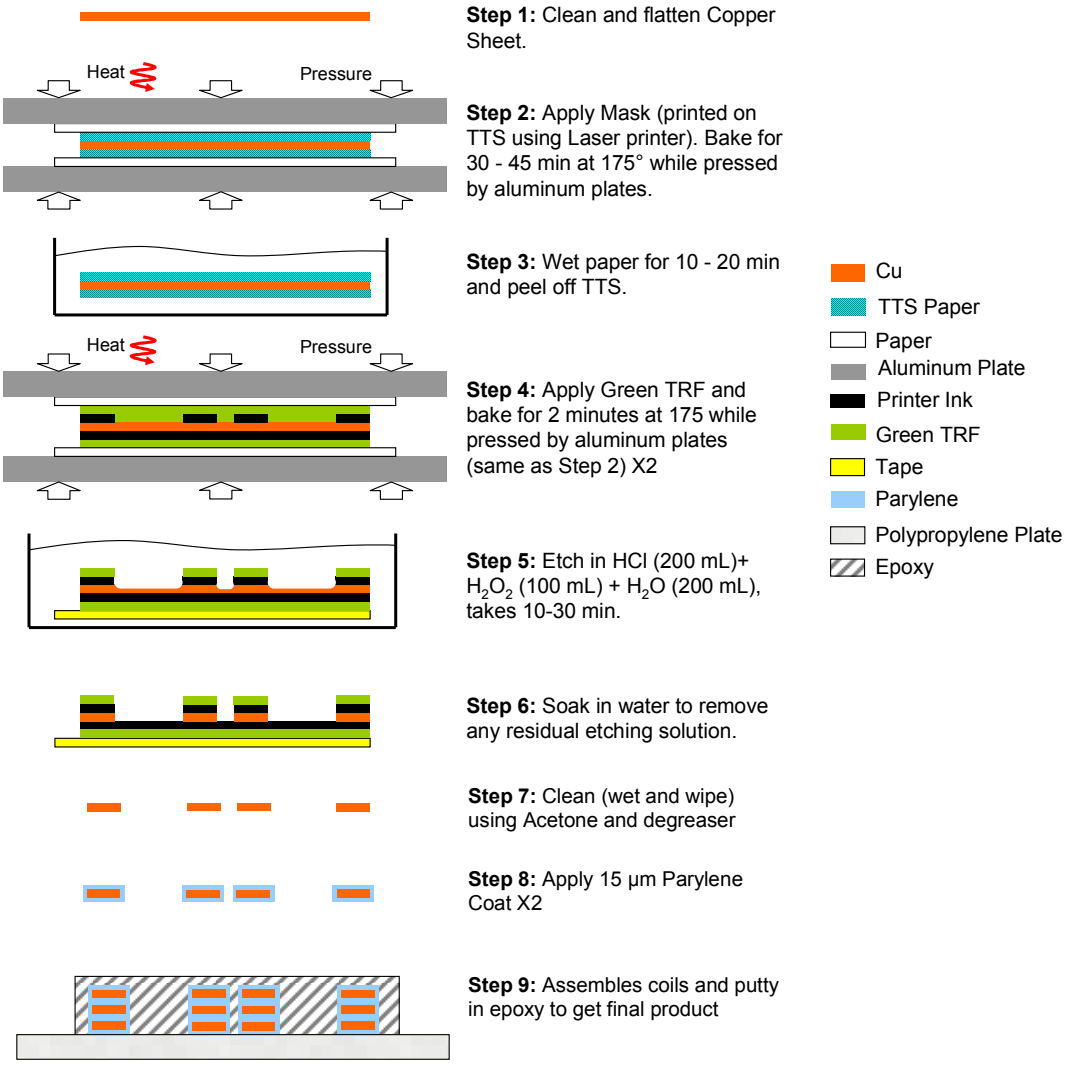

Figure 108. Fabrication process of the gradient coils is represented schematically from a cross-sectional point of view. For more information refer to the text.

In Step 8, each coil is coated with a 15 µm layer of Parylene for electrical insulation purposes

(see Figure 109-12 and Figure 109-13). After that, the coils are assembled and spaced using strips of cut transparency slides and another 15 μm Parylene coating is applied (see Figure 109-14).

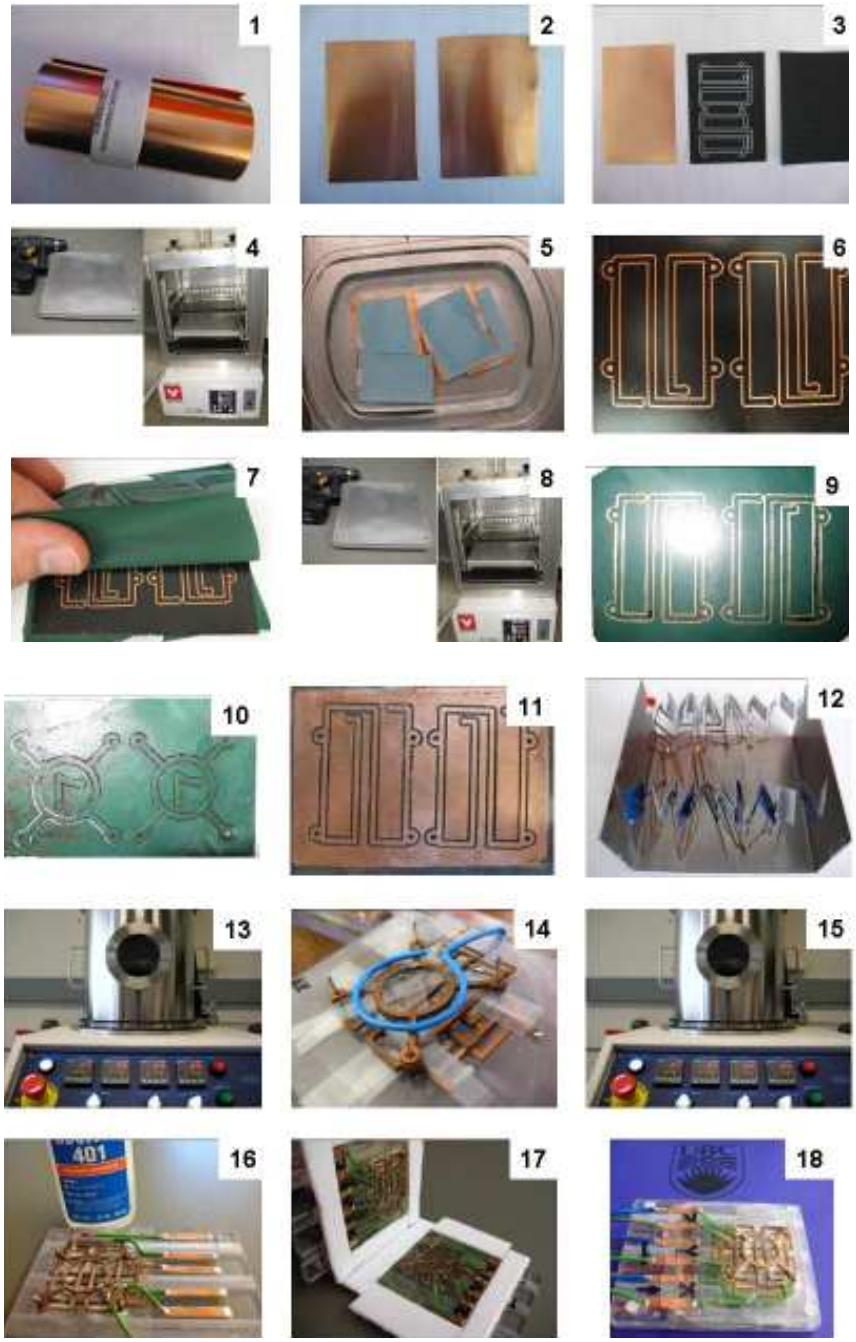

Figure 109. Photos of the fabrication steps. For more info refer to the text.

After the insulation is tested using a multimeter, all the coils are assembled using the four alignment pins and glued in place using super glue (see Figure 109-16). Unfortunately, the super glue reacts with the Parylene coating and the Polypropylene insert that produce a white coloured dust. The coils remain intact, however. In future other fast drying adhesives need to be explored to fix this (aesthetics) problem. In the final step (Step 8) the coils are puttied in a clear epoxy. Teflon strips are used to restrict the epoxy on each side (see Figure 109-17). The finished triaxial gradient insert is shown in Figure 109-18.

Appendix B – Gradient Amplifiers

B.1 Circuit Schematics of the Gradient Amplifiers

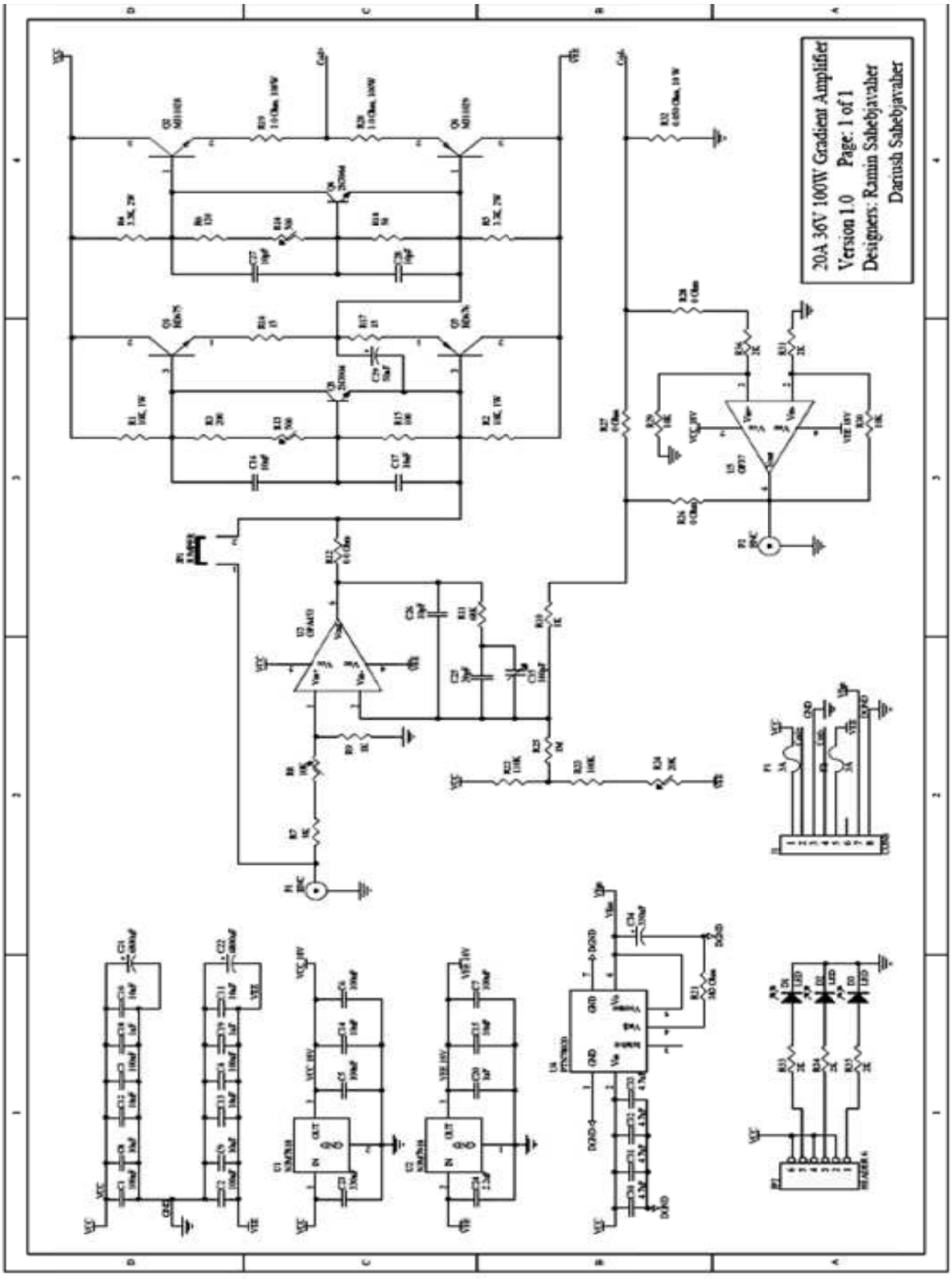
20A 36V 100W Gradient Amplifier
Version 1.0 Page: 1 of 1
Designers: Ramin Sahebjavaher
Daniush Sahebjavaher

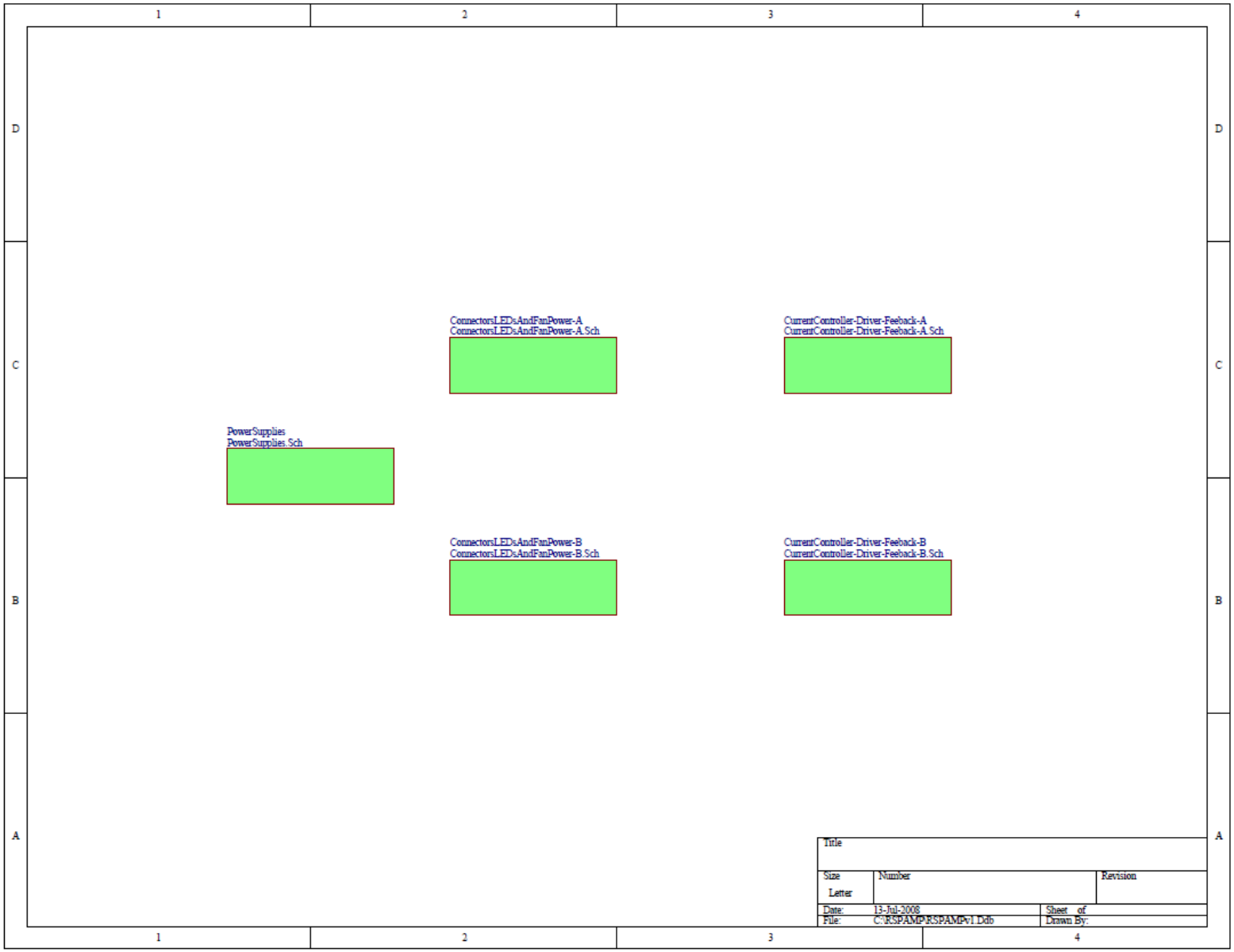
1
2
3
4
D
C
B
A
ConnectorsLEDsAndFanPower-A
ConnectorsLEDsAndFanPower-A.Sch
CurrentController-Driver-Feeback-A
CurrentController-Driver-Feeback-A.Sch
PowerSupplies
PowerSupplies.Sch
ConnectorsLEDsAndFanPower-B
ConnectorsLEDsAndFanPower-B.Sch
CurrentController-Driver-Feeback-B
CurrentController-Driver-Feeback-B.Sch
Title
Size
Letter
Number
Revision
Date:
13-Jul-2008
Sheet of
File:
C:\RSPAMP\RSPAMPv1.Ddb
Drawn By:

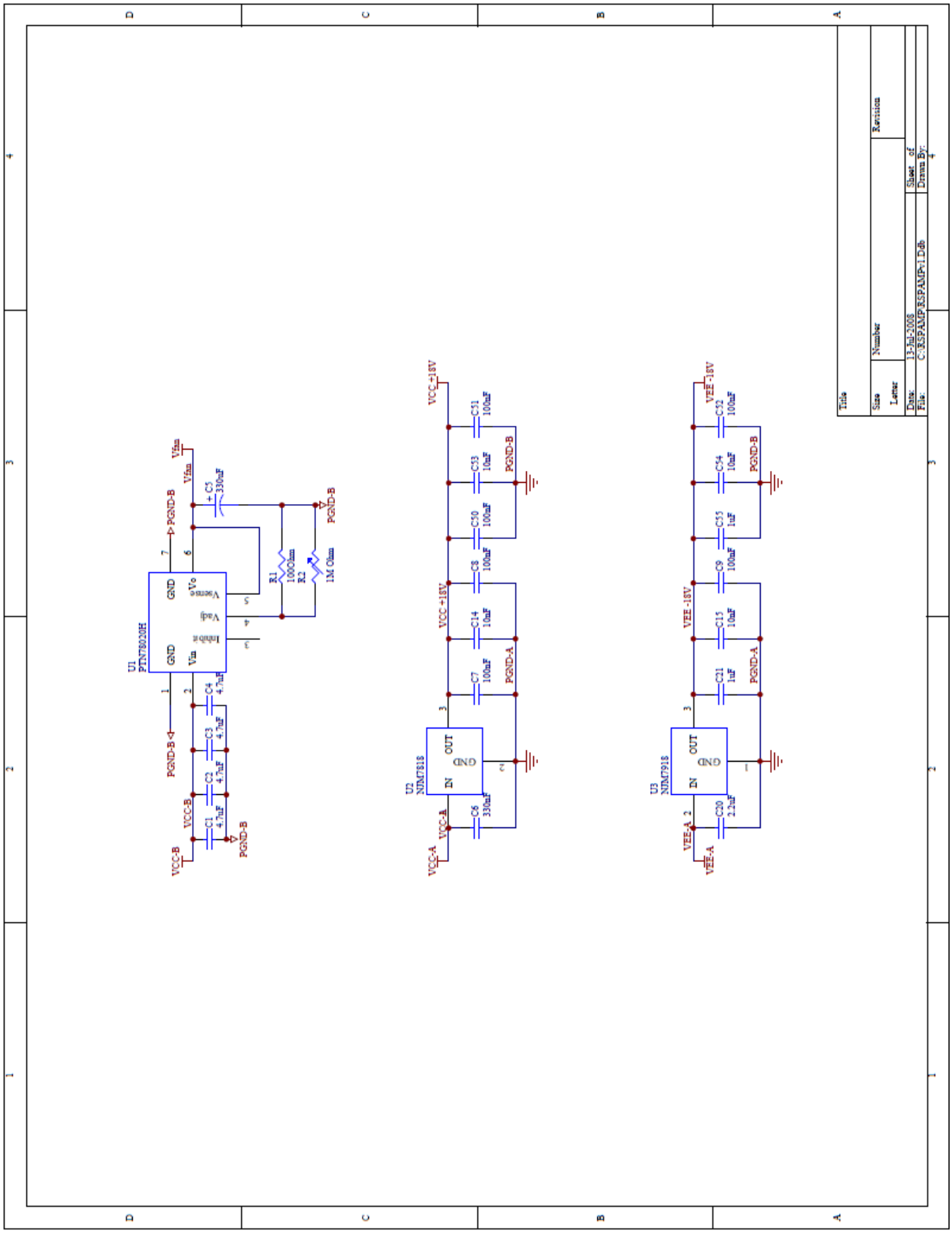
Title
Size
Number
Revision
Date: 13-Jul-2008
File: C:\RSPAMP\RSPAMP-1.DdB
Sheet of
Drawn By:
U1
PTN78020H
GND
Vin
Inhibit
Vadj
Vsense
Vo
GND
C1 4.7uF
C2 4.7uF
C3 4.7uF
C4 4.7uF
C5 330uF
R1 1000ohm
R2 1M Ohm
Vin
PGND-B
VCC-B
U2
NJM7818
OUT
GND
IN
C6 330uF
C7 100uF
C8 100uF
C14 10uF
C50 100uF
C51 100uF
C53 10uF
VCC-18V
VCC-A
PGND-A
U3
NJM7918
C10 2.2uF
C11 1uF
C15 10uF
C9 100uF
C52 100uF
C54 10uF
C55 1uF
VEE-18V
VEE-A

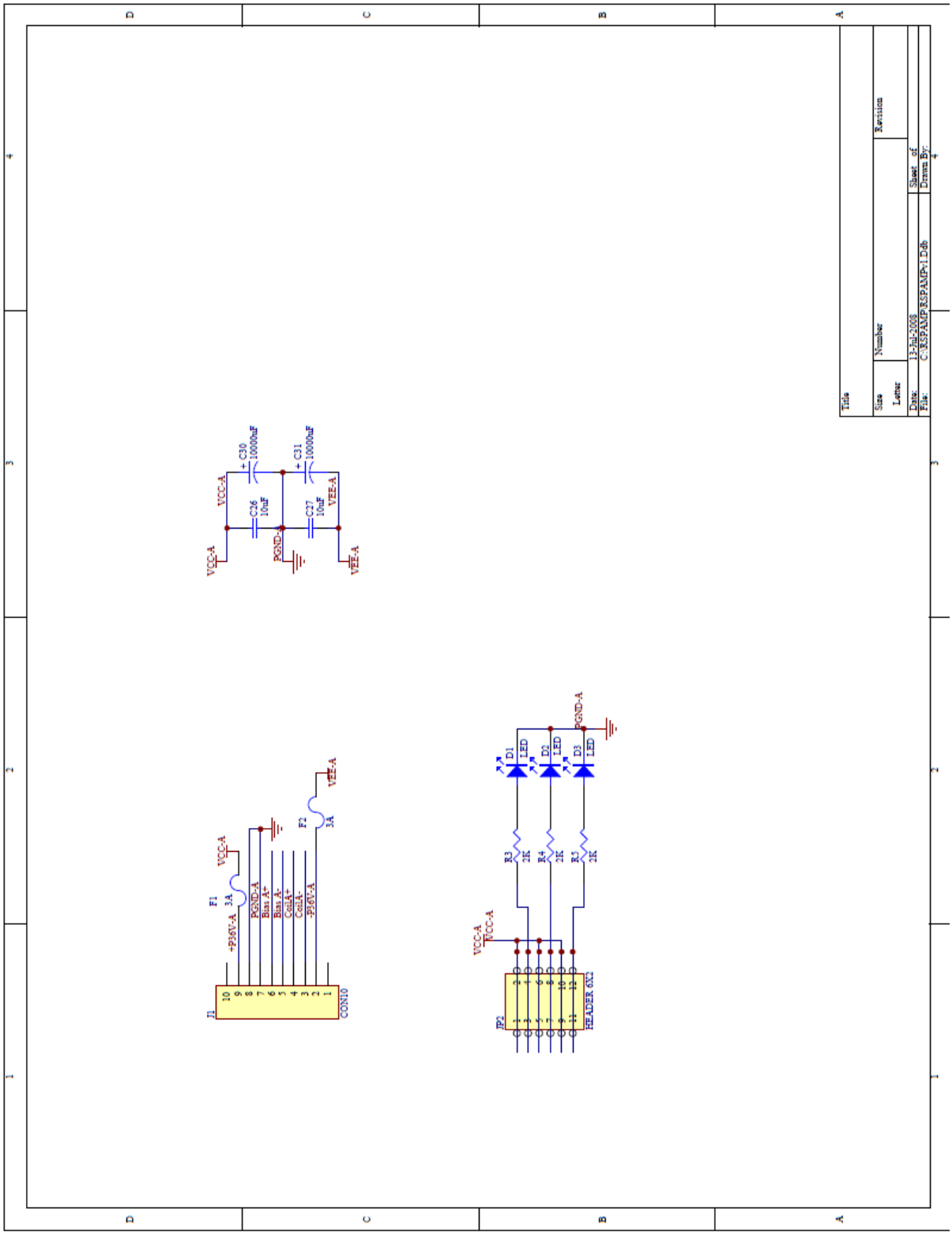
Title
Size
Letter
Number
Revision
Date: 13-Jul-2008
File: C:\85PAMP85PAMP-1.Ddb
Sheet of
Drawn By:
C30 10000uF
C31 10000uF
C26 10uF
C27 10uF
VCC-A
VEE-A
PGND-A
F1 3A
F2 3A
+P36V-A
-P36V-A
Bias A+
Bias A-
CoilA+
CoilA-
J1
CON10
D1 LED
D2 LED
D3 LED
R3 2K
R4 2K
R5 2K
JP2
HEADER 6X2

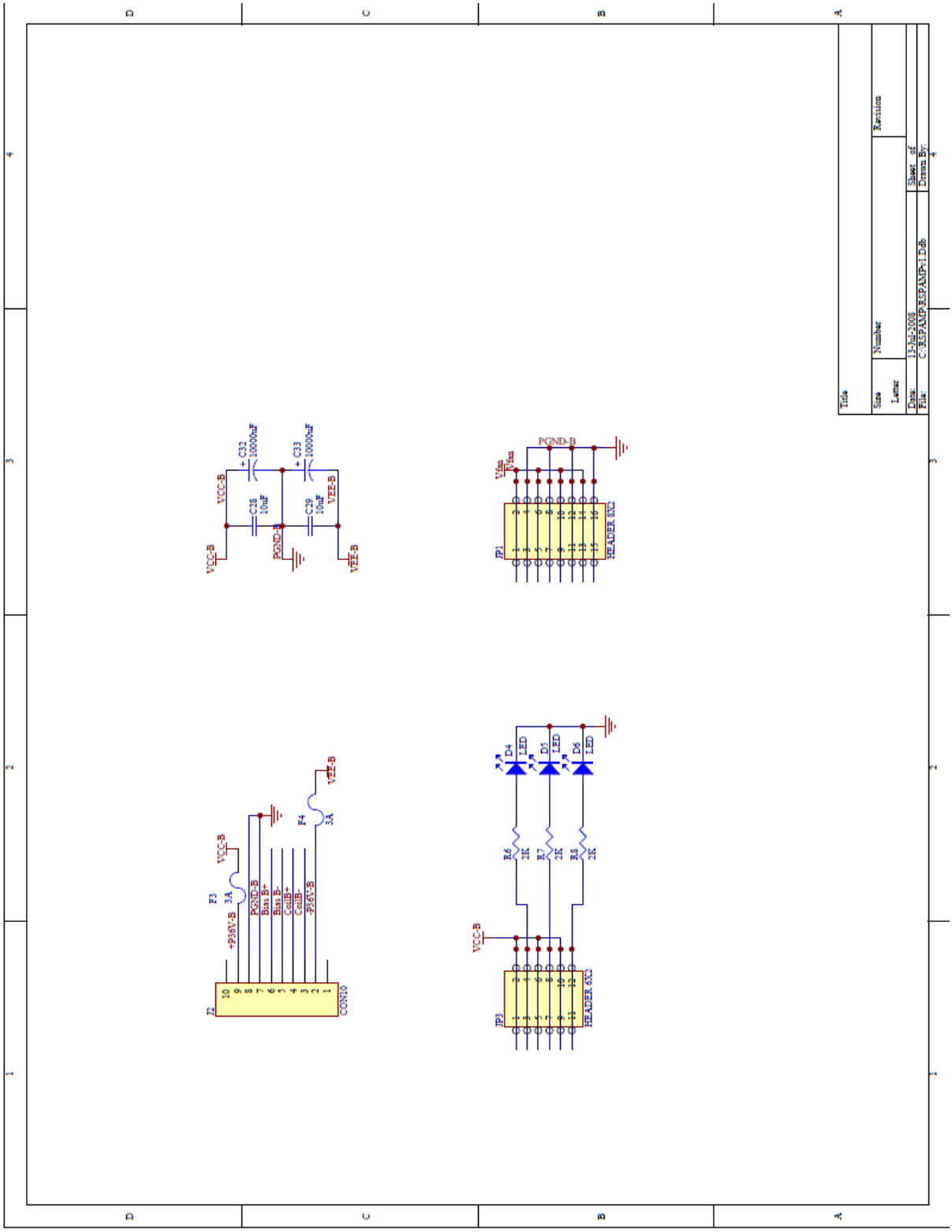
Title
Size
Letter
Number
Revision
Date: 13-Jul-2006
File: C:\835PAMP\835PAMP-1.Db
Sheet of
Drawn By:
C32
10000uF
C33
10000uF
C28
10uF
C29
10uF
VCC-B
VEE-B
PGND-B
JP1
HEADER 8X2
D4
D5
D6
LED
R6
R7
R8
2K
JP3
HEADER 6X2
F3
F4
3A
+P36V-B
-P36V-B
Bias B+
Bias B-
CoilB+
CoilB-
J2
CON10

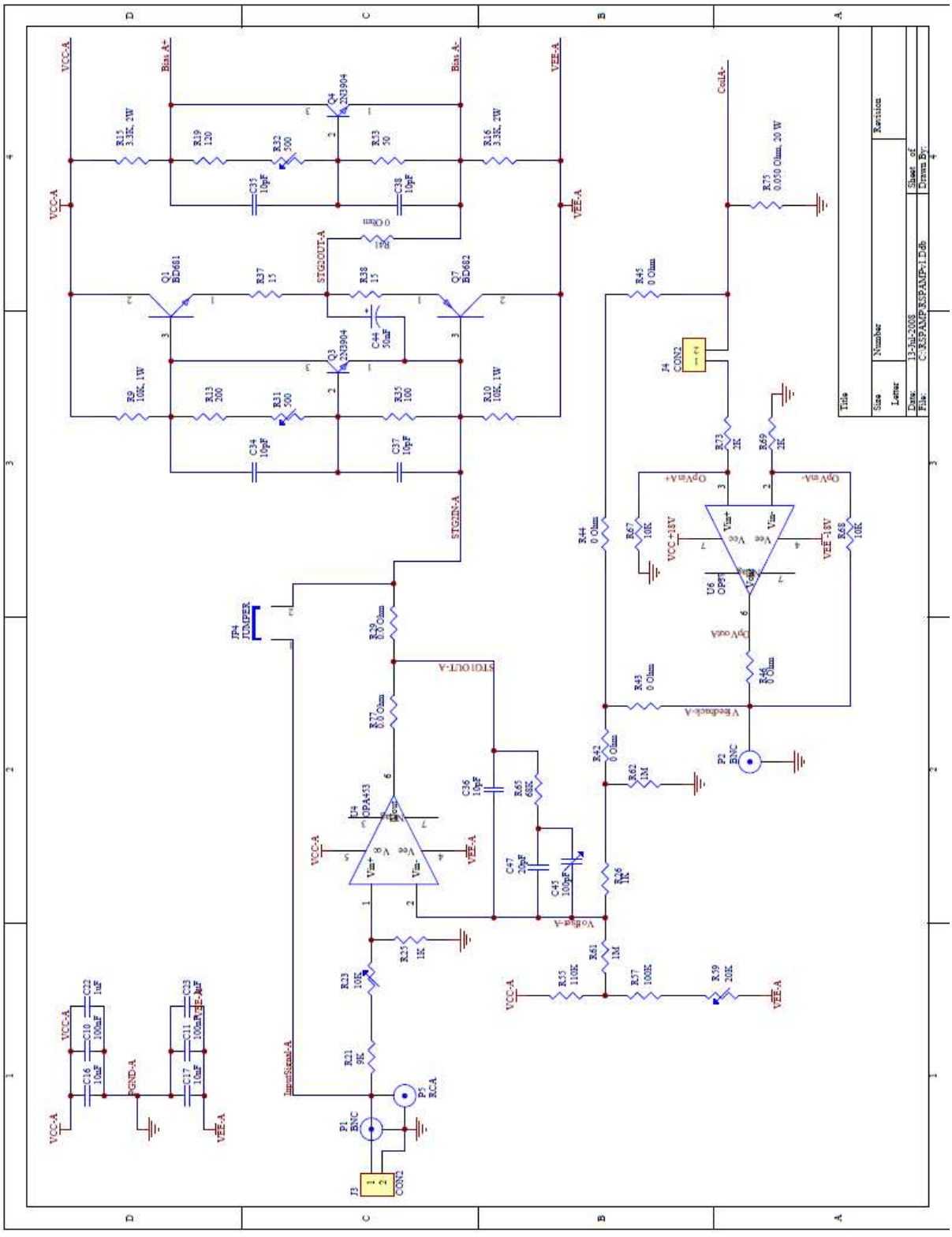

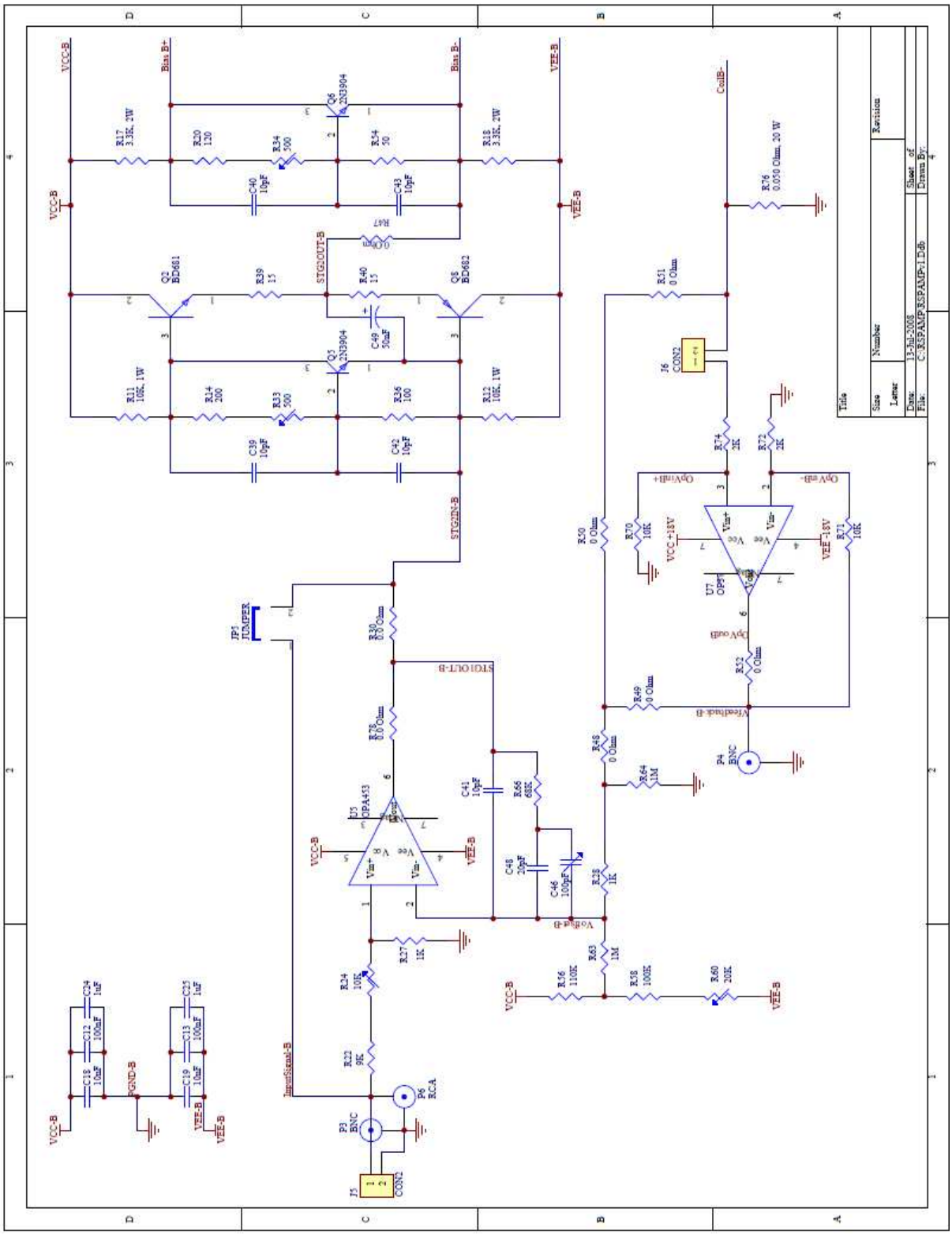

B.2 Printed Circuit Board (PCB) Layout of the Gradient Amplifiers

The driver and the current controller are implemented in a four-layered PCB that was fabricated by an outside vendor (Sierra Proto Express) and its components are soldered in-house. Each PCB contains the electronics for two of the amplifiers, power for cooling fans, and LEDs which can be connected to thermostats to indicate temperature spikes in the power stage (see Figure 110Figure). Each amplifier is powered separately such that in the event of a major failure of one amplifier, the rest of the amplifiers can be salvaged.

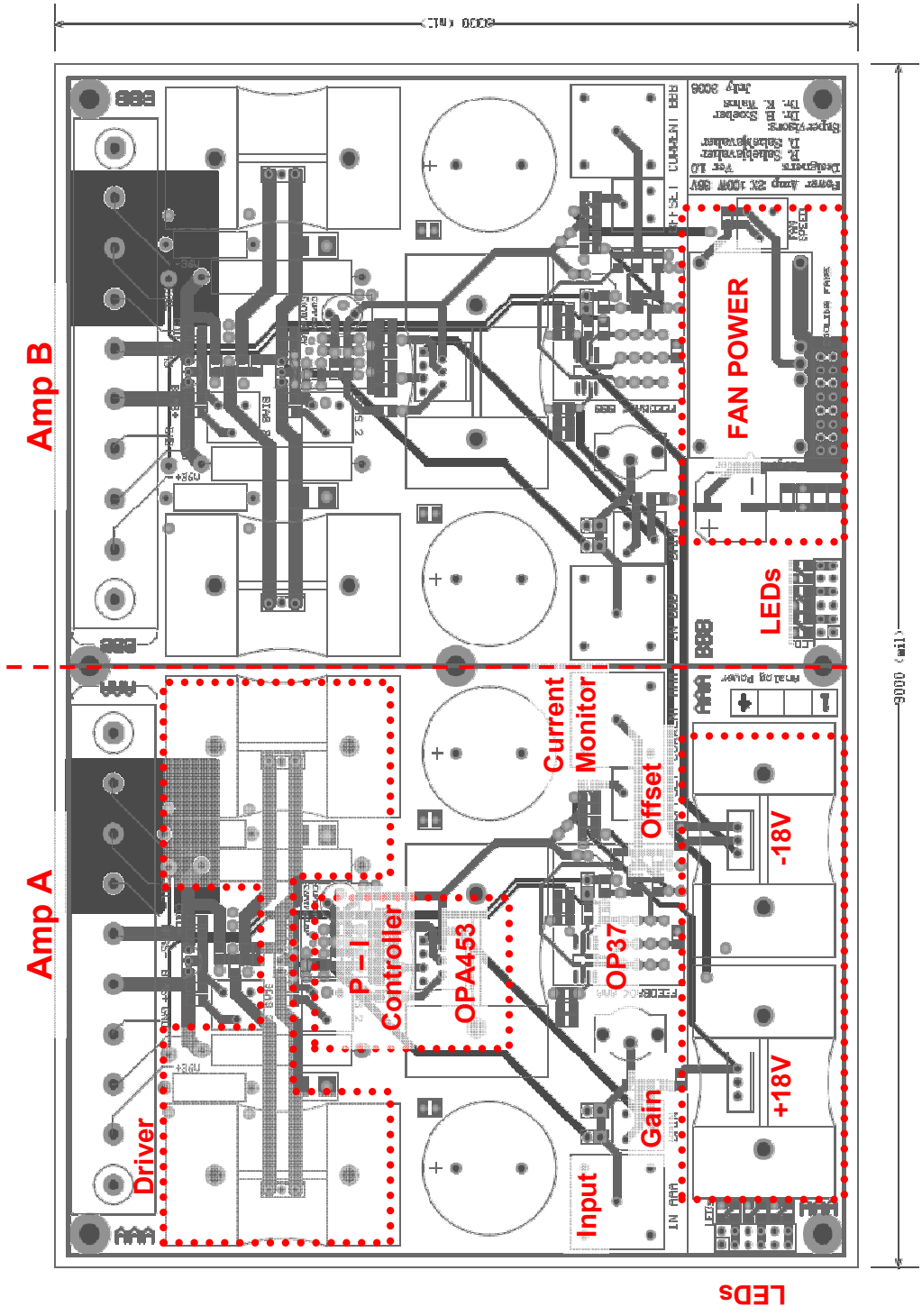

Figure 110. Final CAD drawing of the four-layered PCB design of two of the gradient amplifiers.

All 4 Layers

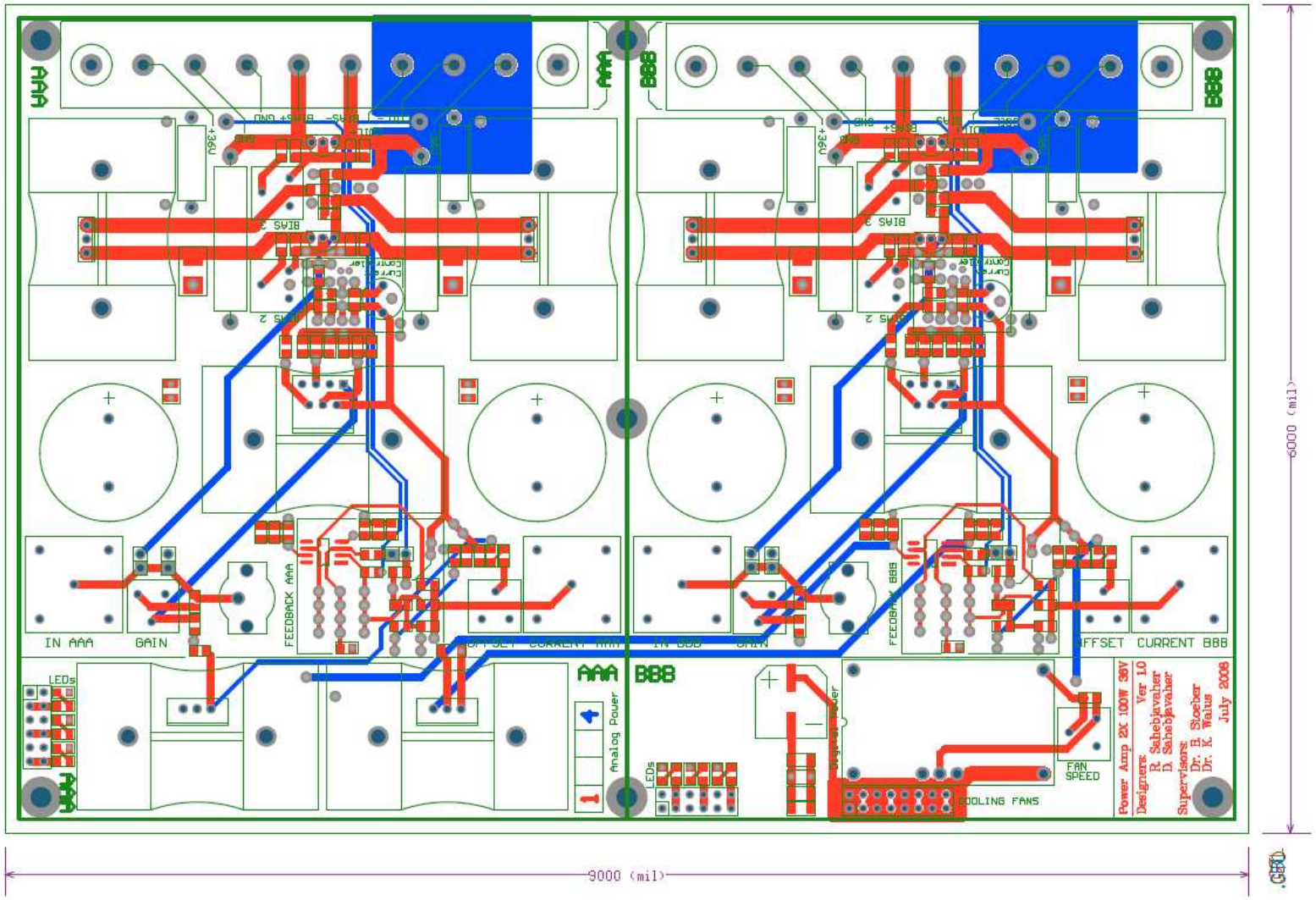
AAA
BBB
IN AAA
GAIN
FEEDBACK AAA
IN BBB
FEEDBACK BBB
OFFSET CURRENT BBB
LEDs
Analog Power
Digital Power
FAN SPEED
COOLING FANS
Power Amp 2X 100W 36V
Ver 1.0
Designers:
R. Sahebjavaher
D. Sahebjavaher
Supervisors:
Dr. R. Stoeber
Dr. K. Walus
July 2006
6000 (mil)
9000 (mil)

Top Layer

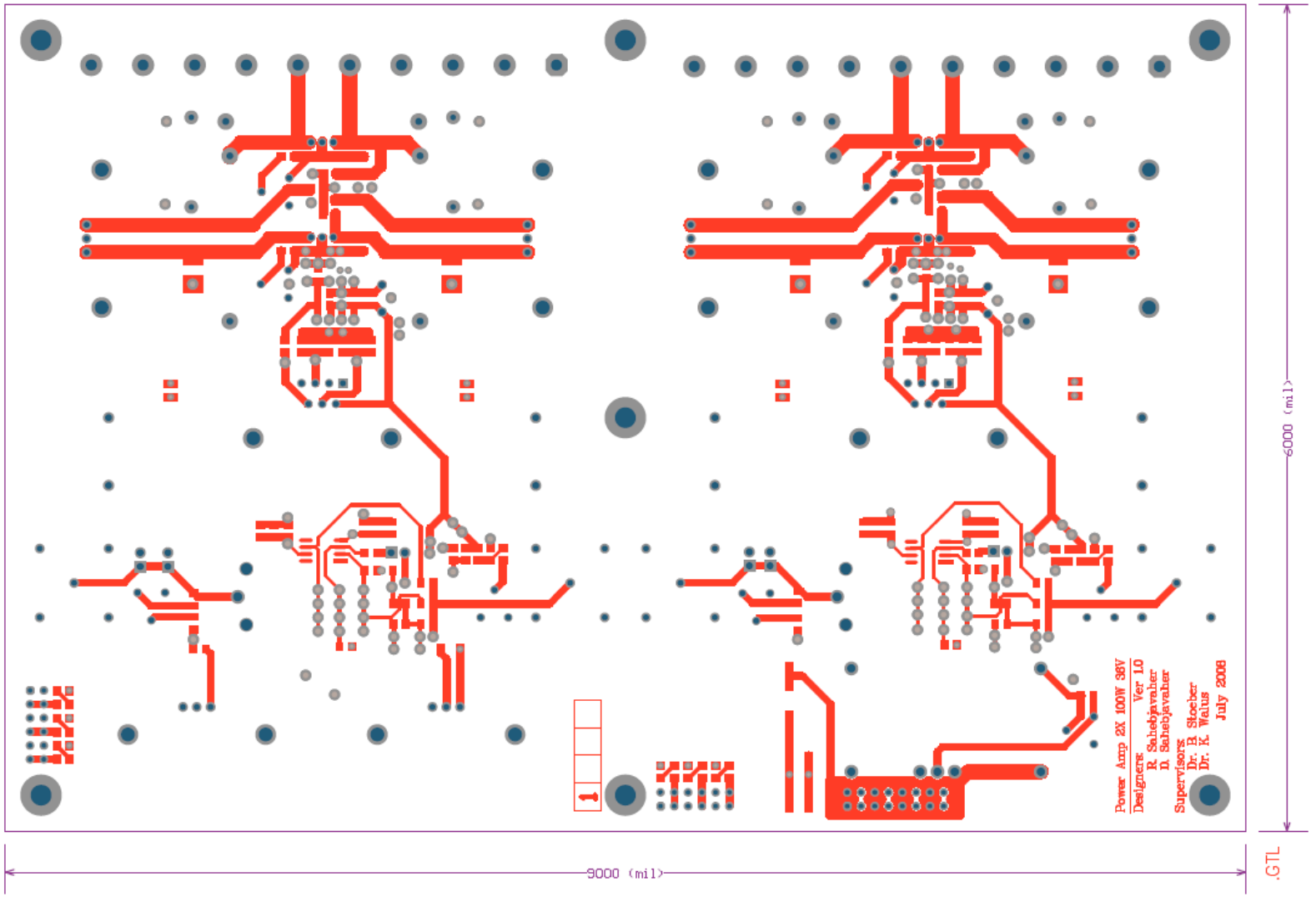
Power Amp 2X 100W 36V
Ver 1.0
Designers:
R. Sahebjavaher
D. Sahebjavaher
Supervisors
Dr. B. Stoeber
Dr. K. Walus
July 2008
6000 (mil)
9000 (mil)
.GTL

Bottom Layer

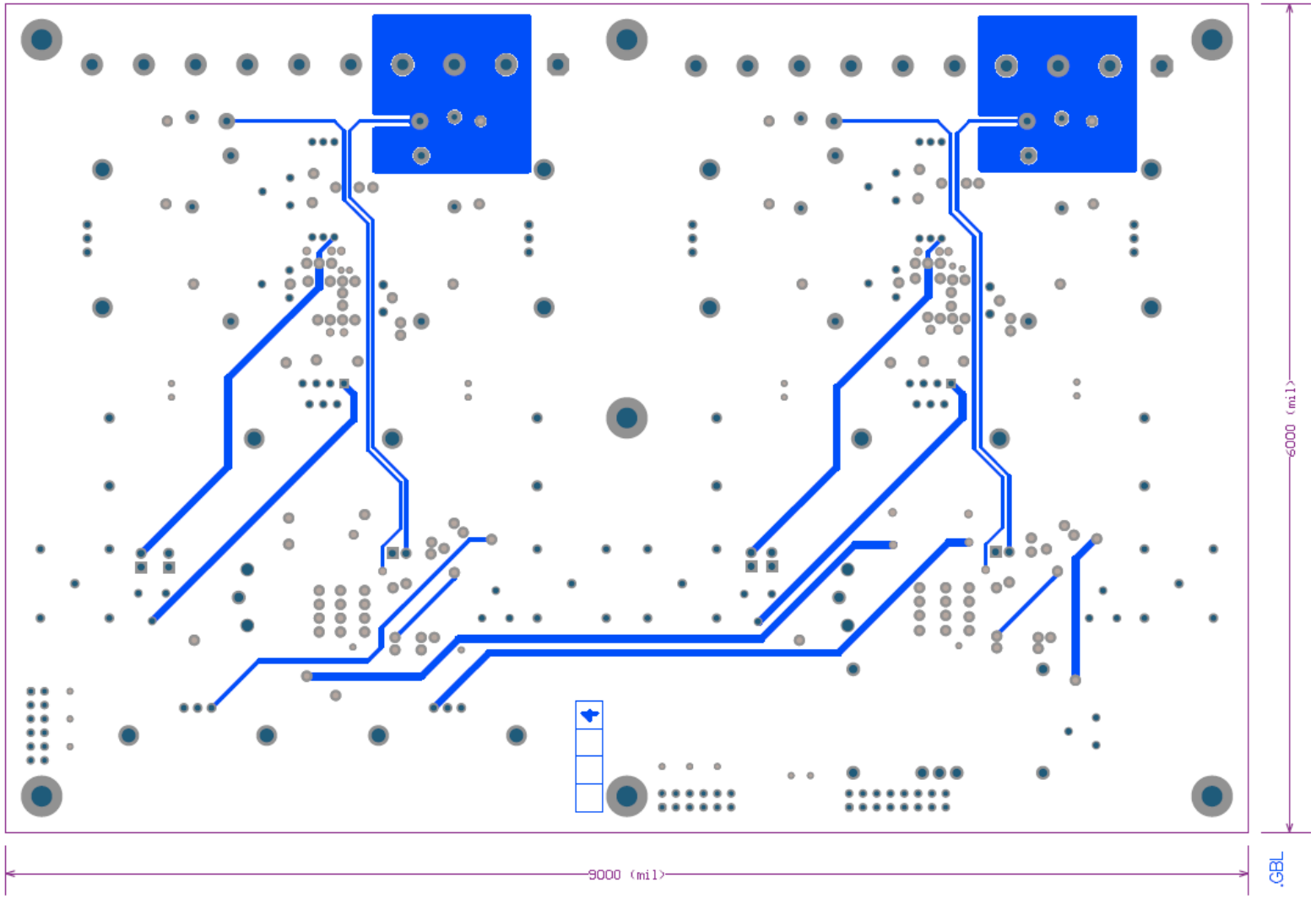

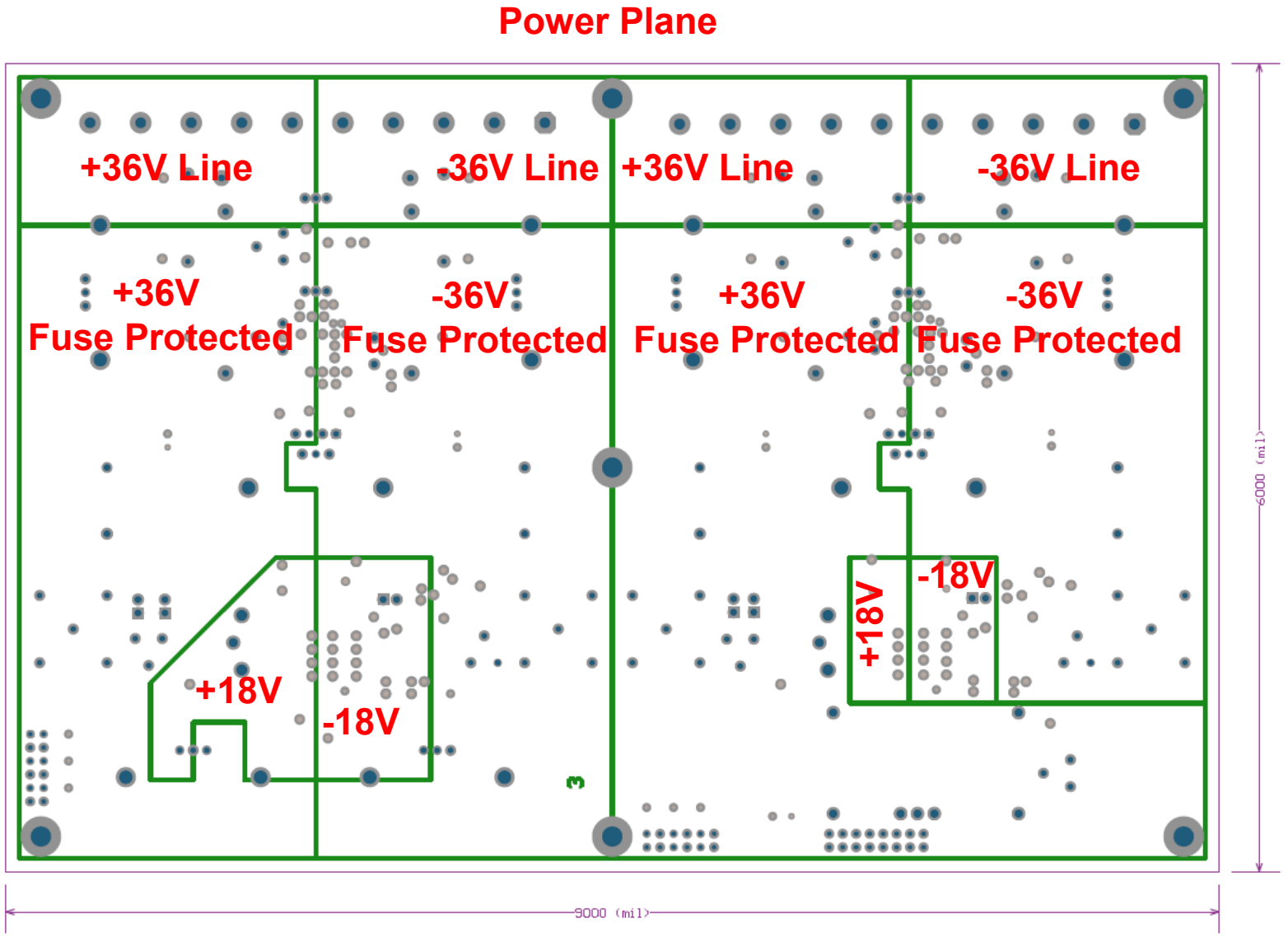
Power Plane
+36V Line
-36V Line
+36V Line
-36V Line
+36V
Fuse Protected
-36V
Fuse Protected
+36V
Fuse Protected
-36V
Fuse Protected
+18V
-18V
+18V
-18V
6000 (mil)
9000 (mil)

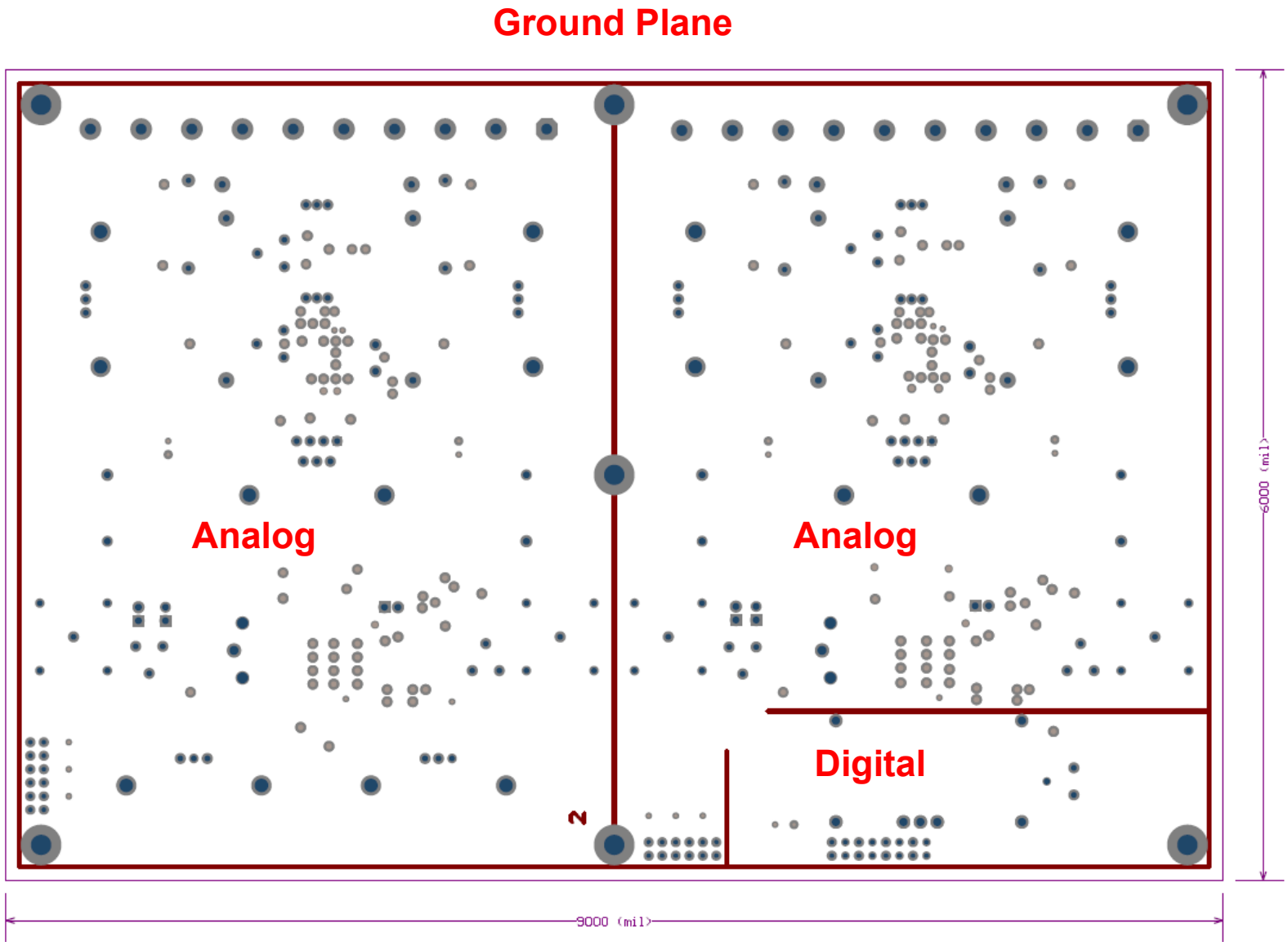
Ground Plane
Analog
Analog
Digital
2
6000 (mil)
9000 (mil)

PCB Construction Summary

Board Construction Summary

Board Construction Summary

Please review all the information below. It is all the data we're using to build your boards.

Click here if you face any issues with this order.	
Part : RSPAMP **/ Rev :** 1.0	**AFV # :** afv1-16910
Quantity : 3 **Boards**	**Turntime :** 10 **Days**

Below is how you assigned the layers when the file was submitted.

Layer Information for this 4 Layer board

File Name	Assigned Layer Type	Assigned Layer Side	Assigned Polarity	Layer Sequence Assigned
rspampv1.gtl	signal	top	positive	1
rspampv1.gp1	power_ground	inner	negative	3
rspampv1.txt	drill			
rspampv1.gbs	solder_mask	bottom	positive	
rspampv1.gts	solder_mask	top	positive	
rspampv1.gbo	silk_screen	bottom	positive	
rspampv1.gto	silk_screen	top	positive	
rspampv1.gp2	power_ground	inner	negative	2
rspampv1.gbl	signal	bottom	positive	4

Drill Information

Finished Hole Size(mils)	Quantity	Plated/Non-Plated
28.00	23	Plated
35.00	40	Plated
40.00	147	Plated
42.00	91	Plated
50.00	36	Plated
60.00	7	Plated
67.00	2	Plated
79.00	4	Plated
80.00	20	Plated
100.00	16	Plated
150.00	7	Plated

Other Information about your Boards

Quantity	Type	Feature
2	Solder Mask	Green
2	Silkscreen	White
	Board Thickness	0.062 inches
	Material Type	FR4
	Finish	HASL (solder)

B.3 Gradient Amplifier Bill of Material (BOM)

ALLIED ORDER

Order Information

Quantity	Description	Price	Ext. Price
4	**ON Semiconductor** BIP TO3 PNP 120A 60V FG **Mfr's part#:** MJ11033G **Allied Stk#:** 568-1000	$7.096 Each	$28.38
4	**ON Semiconductor** BIP TO3 NPN 50A 120V FG **Mfr's part#:** MJ11032G **Allied Stk#:** 568-0999	$6.209 Each	$24.84

DIGIKEY ORDER

Index	Quantity	Part Number	Description	Customer Reference	Backorder Quantity	Unit Price CAD	Extended Price CAD
1	50	P0.0ACT-ND	RES 0.0 OHM 1/8W 5% 0805 SMD	0 Ohm 0805	0	0.04460	$2.23
2	20	RHM15ARCT-ND	RES 15 OHM 1/8W 5% 0805 SMD	15 Ohm 0805	0	0.03600	$0.72
3	20	RHM49.9CRCT-ND	RES 49.9 OHM 1/8W 1% 0805 SMD	50 Ohm 0805	0	0.04000	$0.80
4	20	RHM100CRCT-ND	RES 100 OHM 1/8W 1% 0805 SMD	100 Ohm 0805	0	0.04000	$0.80
5	20	RHM120CCT-ND	RES 120 OHM 1/8W 1% 0805 SMD	120 Ohm 0805	0	0.04100	$0.82
6	20	RHM200CCT-ND	RES 200 OHM 1/8W 1% 0805 SMD	200 Ohm 0805	0	0.04100	$0.82
7	20	RHM1.00KCRCT-ND	RES 1.00K OHM 1/8W 1% 0805 SMD	1K Ohm 0805	0	0.04000	$0.80
8	20	RHM2.00KCCT-ND	RES 2.00K OHM 1/8W 1% 0805 SMD	2K Ohm 0805	0	0.04100	$0.82
9	20	RHM3.30KCRCT-ND	RES 3.30K OHM 1/8W 1% 0805 SMD	3.3K Ohm 0805	0	0.04000	$0.80
10	20	RHM4.99KCCT-ND	RES 4.99K OHM 1/8W 1% 0805 SMD	5K Ohm 0805	0	0.04100	$0.82
11	20	RHM9.09KCRCT-ND	RES 9.09K OHM 1/8W 1% 0805 SMD	9K Ohm 0805	0	0.04000	$0.80
12	20	RHM10.0KCCT-ND	RES 10.0K OHM 1/8W 1% 0805 SMD	10K Ohm 0805	0	0.04100	$0.82
13	20	RHM68.0KCCT-ND	RES 68.0K OHM 1/8W 1% 0805 SMD	68K Ohm 0805	0	0.04100	$0.82
14	20	RHM100KCRCT-ND	RES 100K OHM 1/8W 1% 0805 SMD	100K Ohm 0805	0	0.04000	$0.80
15	20	RHM110KCCT-ND	RES 110K OHM 1/8W 1% 0805 SMD	110K ohm 0805	0	0.04100	$0.82
16	20	RHM1.00MCRCT-ND	RES 1.00M OHM 1/8W 1% 0805 SMD	1M Ohm 0805	0	0.04000	$0.80
17	5	3310Y-001-102L-ND	POT 1.0K OHM 9MM SQ PLASTIC	1K Pot	0	2.76000	$13.80
18	5	3310Y-001-103L-ND	POT 10K OHM 9MM SQ PLASTIC	10K Pot	0	2.17000	$10.85

19	5	3310Y-001-203L-ND	POT 20K OHM 9MM SQ PLASTIC	20K Pot	0	2.76000	$13.80
20	5	3310Y-001-105L-ND	POT 1.0M OHM 9MM SQ PLASTIC	1M Pot	0	2.17000	$10.85
21	5	15FR050-ND	RES CURRENT SENSE .050 OHM 5W	0.050 Ohm Axial Current Sense	0	2.16000	$10.80
22	10	RHC2512-10KFCT-ND	RES 10K OHM 2W 1% 2512 SMD	10K 2W SMD	0	1.45700	$14.57
23	10	ALSR5J-3.3K-ND	RESISTOR SILICONE 3.3K OHM 5W	3.3K Wirewound 5W	0	1.56500	$15.65
24	10	MP9100-1.00F-ND	RESISTOR 1.00 OHM 100W 1% TO-247	1.0 Ohm 100W TO-247	0	10.55300	$105.53
25	30	709-1168-1-ND	CAP CER 10PF 50V NP0 0805	10pF 0805	0	0.04700	$1.41
26	20	399-1113-1-ND	CAP CERAMIC 22PF 50V NP0 0805	20pF 0805	0	0.10500	$2.10
27	20	399-1121-1-ND	CAP CERAMIC 100PF 50V NP0 0805	100pF 0805	0	0.05400	$1.08
28	20	399-1149-1-ND	CAP 1000PF 50V CERAMIC X7R 0805	1nF 0805	0	0.09000	$1.80
29	30	399-1158-1-ND	CAP 10000PF 50V CERAMIC X7R 0805	10nF 0805	0	0.03600	$1.08
30	20	399-1166-1-ND	CAP 47000PF 50V CERAMIC X7R 0805	50nF 0805	0	0.06600	$1.32
31	30	399-1170-1-ND	CAP .10UF 50V CERAMIC X7R 0805	100nF 0805	0	0.05000	$1.50
32	10	709-1195-1-ND	CAP CER .47UF 50V X7R 0805	470nF 0805	0	0.10500	$1.05
33	30	587-1308-1-ND	CAP CER 1.0UF 50V Y5V 0805	1uF 0805	0	0.09500	$2.85
34	10	490-3381-1-ND	CAP CER 2.2UF 50V Y5V 1206	2.2uF 1206	0	0.34100	$3.41
35	10	445-3472-1-ND	CAP CER 4.7UF 50V Y5V 1206	4.7uF 1206	0	0.41500	$4.15
36	10	PCC2308CT-ND	CAP 10UF 50V CERAMIC F 1210	10uF 1210	0	0.82800	$8.28
37	10	490-1957-ND	CAP 10.0-120.0PF 6MM TOPADJ BLK	120pF Variable Capacitor	0	0.86600	$8.66
38	5	565-2497-1-ND	CAP 330UF 50V ELECT MVY SMD	330uF Electrolytic	0	0.96200	$4.81
39	10	493-1119-ND	CAP 10000UF 50V ELECT VR RADIAL	10000uF Alum Cap	0	3.65500	$36.55
40	16	657-15ABPN	HEATSINK TO-220 W/PINS BLK 1.5"	6W Heat Sink TO-220	0	1.88800	$30.21
41	10	F2446-ND	FUSE 250V FAST 2AG 3.5A AXIAL	3.5A FUSE	0	0.84600	$8.46
42	2	CP-1406-ND	CONN RCA JACK METAL VERT BLK PCB	RCA Black	0	0.84000	$1.68
43	2	CP-1407-ND	CONN RCA JACK METAL VERT RED PCB	RCA Red	0	0.85000	$1.70
44	8	A33798-ND	CONN JACK BNC VERT 50OHM PCB	BNC Flange	0	4.47000	$35.76
45	4	A98501-ND	CONN BARRIER STRIP 10POS .375	Terminal Screw Block	0	2.95000	$11.80
46	2	S5561-ND	CONN FEMALE 16POSDL .1" R/A GOLD	8x2 Receptacle	0	1.24000	$2.48
47	4	S5559-ND	CONN FEMALE 12POSDL .1" R/A GOLD	6x2 REceptacle	0	1.24000	$4.96

48	10	S9001-ND	SHORTING GOLD FLASH	Jumper Shunt	0	0.09400	$0.94
49	5	OP37GSZ-ND	IC PREC OPAMP LN HS 8-SOIC	OP37	0	2.37000	$11.85
50	3	NJM#7918FA-ND	IC 18V NEGATIVE REGULATOR TO220F	-18V Regulator	0	0.84000	$2.52
51	3	NJM#7818FA-ND	IC 18V POSITIVE REGULATOR TO220F	+18V Regulator	0	0.65000	$1.95
52	10	2N3904FS-ND	IC TRANS NPN SS GP 200MA TO-92	2N3904 60v	0	0.12000	$1.20
53	12	BD681GOS-ND	TRANS DARL NPN 4A 100V TO225AA	NPN 4A 40W	0	0.69200	$8.30
54	12	BD682GOS-ND	TRANS DARL PNP 4A 100V TO225AA	PNP 4A 40W	0	0.69200	$8.30
55	10	754-1127-1-ND	LED 2X1.2MM 574NM GN WTR CLR SMD	Green LED 0805	0	0.12500	$1.25
56	10	754-1096-1-ND	LED 2X1.25MM LOPRO 610NM ORN SMD	Orange LED 0805	0	0.13300	$1.33
57	10	754-1133-1-ND	LED 2X1.2MM 650NM RD WTR CLR SMD	RED LED 0805	0	0.12500	$1.25
58	5	350-2046-1-ND	LED INGAN BLU WATER CLR 0805 SMD	Blue LED 0805	0	0.67000	$3.35
59	30	A31988-ND	CONN SOCKET 16-18AWG TIN CRIMP	Circular Contact 1.5mm 16-18AWG	0	0.57500	$17.25
60	10	4725K-ND	KIT MOUNTING HARDWARE TO-3CASE	TO-3 Mounting Kit	0	2.10800	$21.08
61	20	61454-1-ND	CONN RECEPT TAB 20-24 AWG CRIMP	Faston 1.58mm AWG20	0	0.25800	$5.16
62	20	8418K-ND	STANDOFF HEX M/F 6-32 1.00" ALUM	Alum Hex 1" Spacer #6-32	0	0.76100	$15.22
63	1	KE1804-ND	FLUX PEN FORMULA 951 NO CLEAN	Flux, Flux Remover	0	4.73000	$4.73
64	1	80-6-5-ND	SOLDER-WICK ROSIN .210" 5'	De-Soldering Braid	0	5.35000	$5.35
65	1	KE1109-ND	SOLDER RA FLUX 23AWG 63/37 1LB	Solder	0	32.62000	$32.62
66	2	350-2191-ND	LENS SPOT BASE MODULE 6DEG XLAMP	Reynald: Cree Xlamp 7090 LED Series, Round, 50mm	0	2.29000	$4.58
67	10	DN7692-ND	COIL 8.2UH MOLDED UNSHIELDED	7.96uH	0	0.71200	$7.12
68	10	DN7703-ND	COIL 220.UH MOLDED UNSHIELDED	227uH	0	0.90600	$9.06
69	10	DN7706-ND	COIL 560.UH MOLDED UNSHIELDED	530uH	0	1.13300	$11.33
70	20	P11408CT-ND	CAP 5PF 250VAC CERAMIC Y2/X1	5.1pF Disc Cap	0	0.23500	$4.70
71	20	490-4145-ND	CAP CER DISC 10PF 1KV SL RAD	10pF Disc Cap	0	0.12900	$2.58
72	20	490-4163-ND	CAP CER DISC 56PF 1KV SL RAD	56pF Disc Cap	0	0.12600	$2.52
73	20	478-4223-ND	CAP CER 100PF 1000V 10%DISC RAD	100pF Disc Cap	0	0.12200	$2.44
74	10	445-2727-ND	CAP CER DISC 1500PF 1KV 10% RAD	1.59nF Disc Cap	0	0.15100	$1.51
75	10	478-4275-1-ND	CAP CER .10UF 50V 20% DISC RAD	106nF Disc Cap	0	0.32000	$3.20
76	10	P4307-ND	.047 UFD 25V DISC CAP	45nF Disc Cap	0	0.14500	$1.45
77	5	490-2002-1-ND	CAP 8.0-45PF 2.5X3.2MM SMD	Trimmer	0	0.89800	$4.49

Appendix C - RF

C.1 Impedance Matching Setup

The electronics schematic for the RF probe is shown in Figure 111. The probe is modeled as an inductor (L_{coil}) with a given quality factor, a tuning capacitor (C_{tune}) and a matching capacitor (C_{match}).

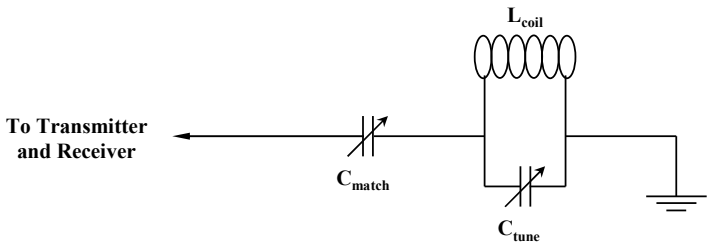

Figure 111. Lumped model of the RF probe.

The resonant frequency ω is tuned (to 25.2 MHz) when the resonance condition

$$\omega^2 L_{coil} C_{tune} = 1, \tag{95}$$

is satisfied and the input impedance (50 Ohms) is matched when the matching condition,

$$\frac{Q\omega L C_{tune}^2}{C_{tune} + C_{match}} = 50, \tag{96}$$

is satisfied [90, 99]. The quality factor of the coil can be estimated by approximation values found in [88]. An approximate value for the capacitors can be determined using (95) and (96). The matching capacitor is usually larger than calculated due to the parasitic capacitances of the

probe. To accurately tune and match the probe the test setup shown in Figure 108a is used. The function generator (Agilent 33250A) is used to generate a swept sine wave from 10 MHz to 40 MHz at 2 Vpp with a sweep rate of 0.2 seconds. The frequency marker (falling edge of Sync pulse) is set to the frequency (25.2 MHz) where to probe is tuned and matched. The Sync pulse is connected to CH1 of the oscilloscope (Agilent MSO6034A). The output of the function generator is connected to "RF Output" port of the directional couples (i.e., the "Magic T"). The "Coupled" is connected to CH2 of the oscilloscope and the "RF Input" port is connected to the probe as shown in Figure 108a. This setup measures the signal reflected by the probe. At the resonance frequency of the probe, most of the signal does not reflect from the probe provided that the probe is matched as well. The time axis of the oscilloscope is effectively related to frequency as shown in Figure 108b. The envelope of the signal seen on CH2 of the oscilloscope is an indication of the reflected signal from the probe at the range of selected frequencies. The tuning and matching capacitors are adjusted until the reflected signal form the probe is minimized at the Larmor frequency. The expected envelope of the reflected signal from a tuned and matched probe is shown in Figure 108b.

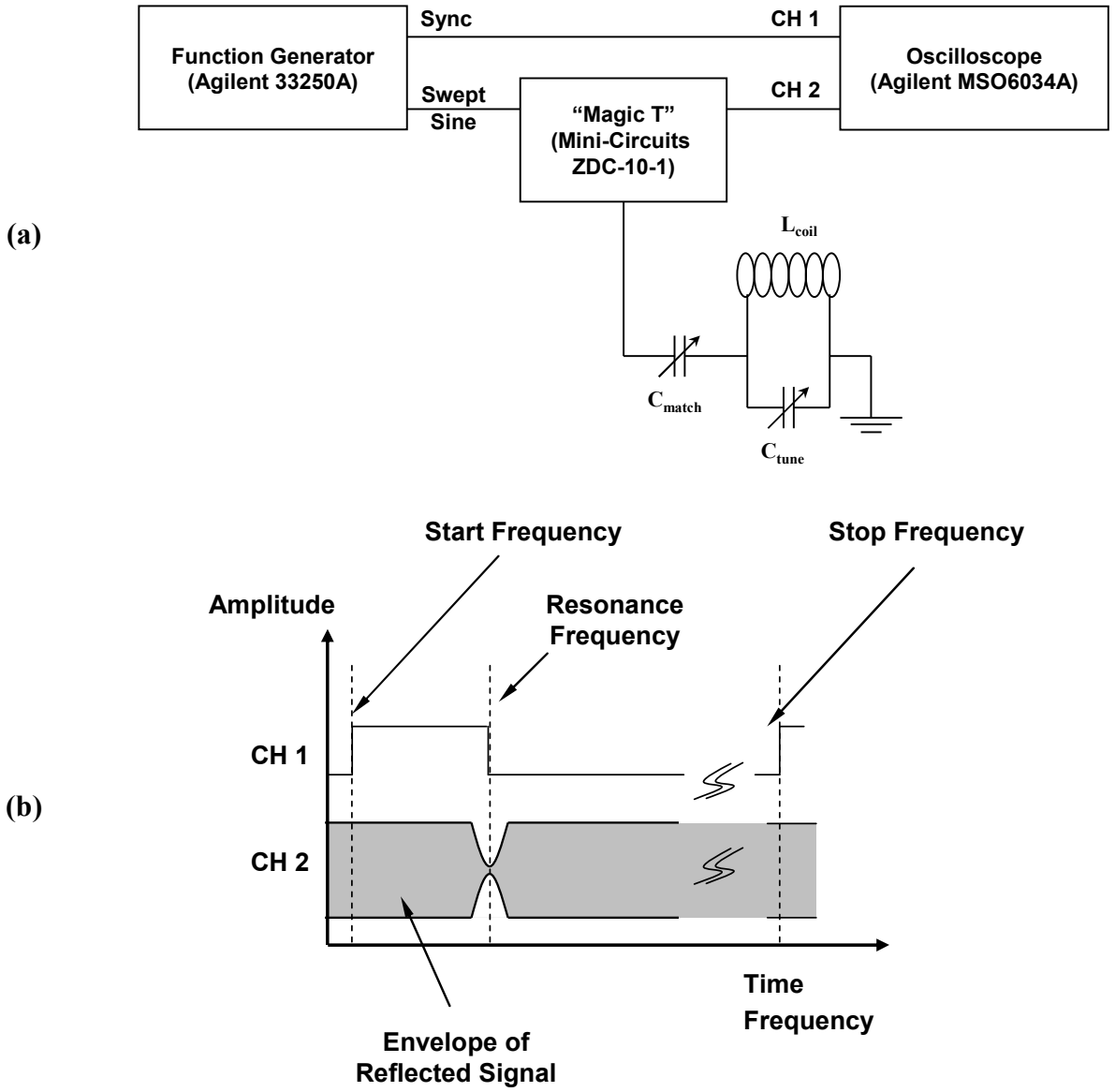

Figure 112. Test setup to measure reflections of the probe (a) and the resulting signals on the oscilloscope (b).

C.2 Selection of Gains in the Receiver

A simplified version of the components of the receiver are shown in Figure 113a.The signal path of the MR signal is shown in Figure 113b as it passes though various components. The signal

power of each stare is represented by the letter **P** and the gains and attenuators are represented by the letter **G**.

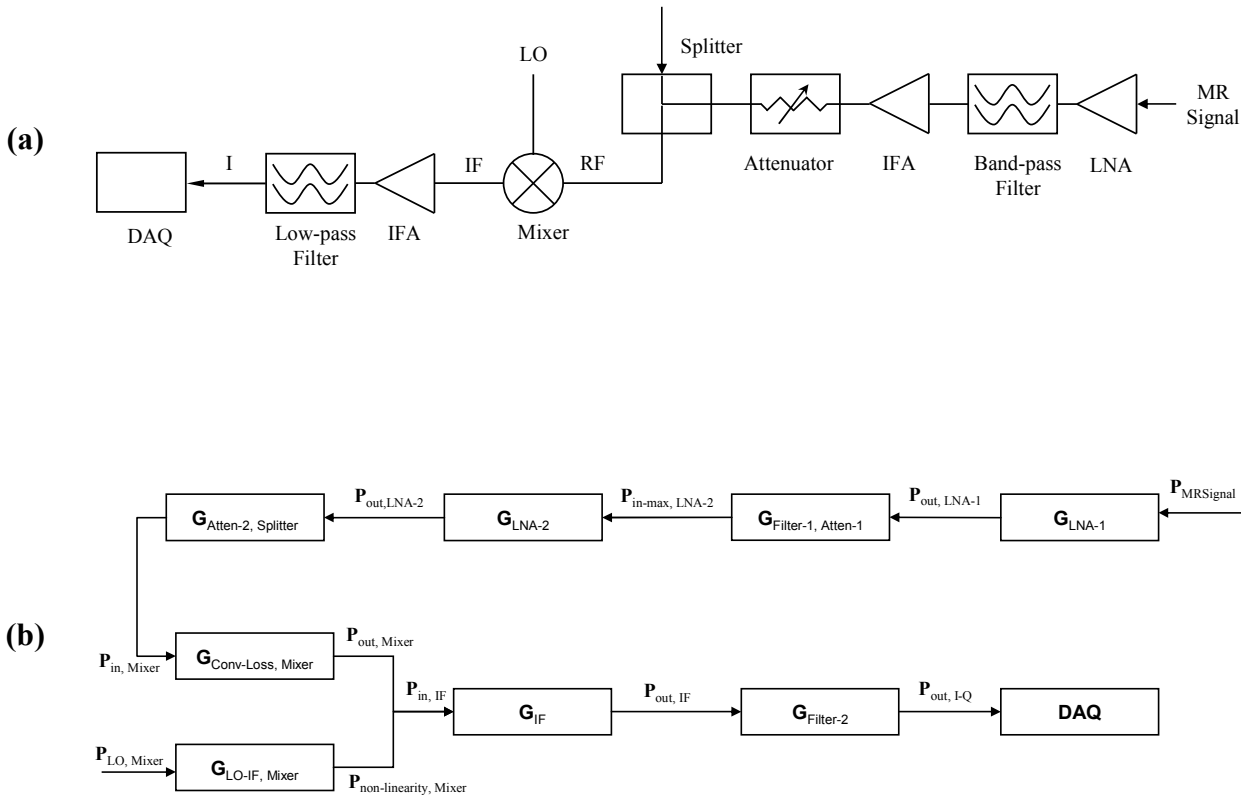

Figure 113. The components of the receiver are shown in (a), and the signal path of the MR signal is shown in (b).

The MR signal passes through the first LNA, the band pass filter, a second LNA, an attenuator and splitter, the down conversion mixer, the audio amplifier and filter, and finally the data acquisition board (DAQ). The dominant noise source of this particular receiver come from the noise picked up by the probe which is further amplified by th first LNA depending on its noise

figure. A signal distortion is also introduced at the mixer which comes from the leakage of the signal from the LO to IF ports of the mixer. The leaked signal of LO is at Larmor frequency and when mixed with the MR signal (also at Larmor frequency) results in a DC offset which could saturate the mixer and resulting in non-linearities. The proper selection of gains ensures that the noise level stays at the optimal value and no component of the receiver is overloaded and/or saturated. The combination is of gains and attenuator has to satisfy the following equations:

$$P_{out,LNA-1} = P_{MRSignal} + G_{LNA-1} < P_{1-dB,LNA-1} \quad \textbf{(97)}$$

$$P_{in,LNA-2} = P_{out,LNA-1} - G_{Filter-1,Atten-1} < P_{in-max,LNA-2} \quad \textbf{(98)}$$

$$P_{out,LNA-2} = P_{in,LNA-2} + G_{LNA-2} < P_{1-dB,LNA-2} \quad \textbf{(99)}$$

$$P_{in,Mixer} = P_{out,LNA-2} - G_{Filter-2,Atten-2} < P_{in-max,Mixer} \quad \textbf{(100)}$$

$$P_{out,Mixer} = P_{in,Mixer} - G_{Conv-Loss,Mixer} \quad \textbf{(101)}$$

$$P_{non-linearity,Mixer} = P_{LO,Mixer} - G_{LO-IF,Mixer} \quad \textbf{(102)}$$

$$P_{non-linearity,Mixer} < P_{out,Mixer} \quad \textbf{(103)}$$

$$P_{out,Mixer} < P_{in-max,IF} \quad \textbf{(104)}$$

$$P_{out,IF} = P_{in,IF} + G_{IF} < P_{1-dB,IF} \quad \textbf{(105)}$$

$$P_{out,I-Q} = P_{out,IF} - G_{Filter-3} \quad \textbf{(106)}$$

$$P_{in-min,DAQ} < P_{out,I-Q} < P_{in-max,DAQ} \quad \textbf{(107)}$$

$$G_{Receiver} = P_{MRSignal} + G_{LNA-1} - G_{Filter-1,Atten-1} + G_{LNA-2} - G_{Filter-2,Atten-2} - G_{Conv-Loss,Mixer} + G_{IF} - G_{Filter-3} \quad \textbf{(108)}$$

$$(P_{in-min,DAQ} + P_{Noise,Receiver}) < G_{receiver} < (P_{in-max,DAQ} + P_{Noise,Receiver} - DR_{Receiver}) \quad \textbf{(109)}$$

$$DR_{Receiver} = 1 - (P_{Conv-Loss,Mixer} - P_{LO-IF,Mixer}) \quad \textbf{(110)}$$

The constants of these equations can be found from the data sheets which have been summarized below in Table 13.

Table 16. Specification of the RF receiver.

$\mathbf{G_{LNA\text{-}1}}$ **[dB]**	51
$\mathbf{P_{1\text{-}dB,\ LNA\text{-}1}}$ **[dBm]**	17
$\mathbf{G_{LNA\text{-}2}}$ **[dB]**	42
$\mathbf{P_{in\text{-}max,\ LNA\text{-}2}}$ **[dBm]**	13
$\mathbf{P_{1\text{-}dB,\ LNA\text{-}2}}$ **[dBm]**	14
$\mathbf{P_{in\text{-}max,\ Mixer}}$ **[dBm]**	1
$\mathbf{G_{Conv\text{-}Loss,\ Mixer}}$ **[dB]**	7.5
$\mathbf{G_{LO\text{-}IF,\ Mixer}}$ **[dB]**	50
$\mathbf{P_{1\text{-}dB,\ IF}}$ **[dBm]**	30
$\mathbf{P_{in\text{-}min,DAQ} - P_{in\text{-}max,DAQ}}$ **[dBm]**	(-58) – (30)

Each component has to be checked for maximum input and output saturation which are given by (97)-(107). The total gain of the receiver can be calculated by (108) the information given in Table 13. The maximum gain has to be selected such that it satisfies (109), where the noise of the receiver is measured experimentally. Equation (109) ensures that the output swing of the receiver is match to the input voltage range of the DAQ. The dynamic range can be calculated as given by (110) and is limited to around 44 dB.

Appendix D - Pulse Sequence Design

The procedure to calculate the parameters of the static and velocity imaging pulse sequences is described in this section.

D1. Static Imaging

The SE pulse that is used for static imaging is shown in Figure 99. The SE pulse sequence is described in the text in Chapter 1 and 3 therefore not repeated here. However, the calculations of the pulse duration and the gradient amplitudes are detailed here. It is important to note that the

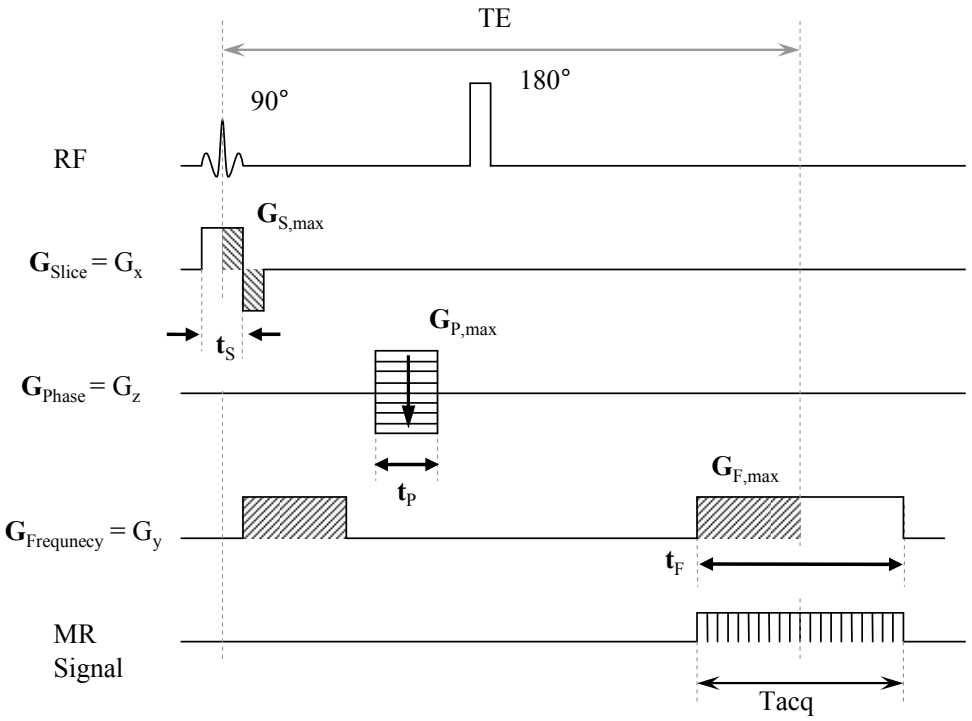

Figure 114. Basic spin echo (SE) pulse used for 2D imaging.

calculations presented here are valid for the pulse sequence shown in Figure 99 only and would

change if a different pulse sequence was used.

The bandwidth of the selective RF pulse (BW_{Sinc}) and the strength of the slice selection gradient (G_{slice}) define a slice thickness [m]

$$\text{Slice}_{TH} = \frac{2\pi \cdot \text{BW}_{\text{Sinc}}}{\gamma \cdot \text{G}_{\text{slice}}} = \frac{2\pi \cdot \text{BW}_{\text{Sinc}}}{\gamma \cdot \text{G}_{\text{S,max}}}. \tag{111}$$

To make the echo time as small as possible, the duration of the selective RF pulse is increased. This is achieved by increasing the bandwidth of the receiver (total length of the selective pulse is approximately $4/BW_{Sinc}$). The duration of the slice selection gradient, t_S, is equal to the duration of the selective pulse (approximately $4/BW_{Sinc}$). The rephrasing lobe of the slice selection gradient is $t_S/2$ if an equal but opposite ($-G_{S,max}$) is used. To reduce problem with eddy currents, the maximum gradient strength of the slice selection gradient is limited to about 0.3 T/m. In this work, the bandwidth of the slice selection was 6 kHz, which defines a 2 mm slice with a gradient amplitude of 0.07 T/m.

The bandwidth of the receiver, $BW_{Receiver}$, is a parameter that needs to be specified by the user. Ideally the bandwidth over a single pixel has to be greater than the errors due to the magnet in-homogeneities and the drifts. The average error of compensation of the magnetic resonance shift is approximately 100 Hz; therefore, for a 128 by 128 pixel image the received bandwidth has to be at least 12.8 kHz. The homogeneity of the magnet in this work produces a bandwidth of at least 350 Hz. This requires that the bandwidth of the receiver is better than 44.8 kHz. This bandwidth is too large for the RF electronics as the bandwidth is limited by the audio amplifier to about 30 kHz. Another limitation is that for larger bandwidth the SNR increases. Therefore, a bandwidth of 15 kHz was chosen for testing purposes.

The field of view of the phase encoding

$$\mathrm{FOV_P} = \delta_\mathrm{P} \mathrm{N_P} \tag{112}$$

Depends on the resolution in the phase encoding direction, δ_P, and the number of phase encoding steps N_P are specified by the user. A FOV_P of 5.12 mm was used for testing purposes for 128 phase encoding steps and a nominal resolution of 40 μm. The amplitude of the phase encoding gradient is given by

$$\mathrm{G_{z,max}} = \mathrm{G_{Phase}} = \frac{2\pi \cdot \mathrm{N_P}}{\mathrm{FOV_P} \cdot \gamma \cdot \mathrm{t_P}}, \tag{113}$$

where t_P is the duration for which this gradient is applied. To minimized *TE*, the pulse duration, t_P, needs to be minimized. To avoid eddy current problems which would distort the echo signal, the gradient was limited to about 0.3 T/m. For testing purposes the gradient was applied for 4 ms (t_P) with a maximum amplitude ($G_{P,max}$) of 0.148 T/m.

The FOV in the frequency encoding direction is given by

$$\mathrm{FOV_F} = \delta_\mathrm{F} \mathrm{N_{Sampling}}, \tag{114}$$

where the resolution in the frequency encoding direction, δ_F, and the number of acquired samples $N_{Sampling}$ are specified by the user. A FOV_F of 5.12 mm was used for testing purposes for a 128 samples in the frequency encoding direction and a nominal resolution of 40 μm.

The amplitude of the frequency encoding gradient is given by

$$G_{F,max} = \frac{2\pi \cdot BW_{Receiver}}{\gamma \cdot FOV_F}. \tag{115}$$

The amplitude of the frequency gradients is found to be 0.069 T/m for a receiver bandwidth of 15 kHz and a FOV_F of 5.12mm. The pulse duration of the frequency encoding gradient after the 180° RF pulse is equal to the total acquisition time, t_F, that is given by

$$t_F = \frac{2\pi \cdot N_{Samplig}}{FOV_F \cdot \gamma \cdot G_{y,max}} = \frac{N_{Samplig}}{BW_{Receiver}}. \tag{116}$$

For a total of 128 samples and a receiver bandwidth of 15 kHz, the acquisition time (equal to the duration of the frequency encoding gradient after the non-selective RF pulse) is approximately 8.5 ms.

The echo time can now be calculated based on the pulse durations found above. The echo time is approximately

$$TE \approx 2\left(\frac{2}{BW_{Receiver}} + \max\left(\frac{2}{BW_{Receiver}}, t_P, \frac{t_F}{2}\right)\right). \tag{117}$$

The first term is the half the duration of the selective RF pulse. The second term specifies the largest time among: the rephrasing time of the slice select gradient, duration of the phase encoding gradient, and half the duration of the frequency encoding gradient. The pulse duration of the non-selective RF pulse is very short (< 50 μs) compared to the duration of the gradients and therefore ignored. The echo time, *T*E, is set to 10 ms; this value is mainly defined by the duration of the frequency encoding gradient. The final pulse sequence is shown in where all the pulse durations and gradient amplitudes are marked.

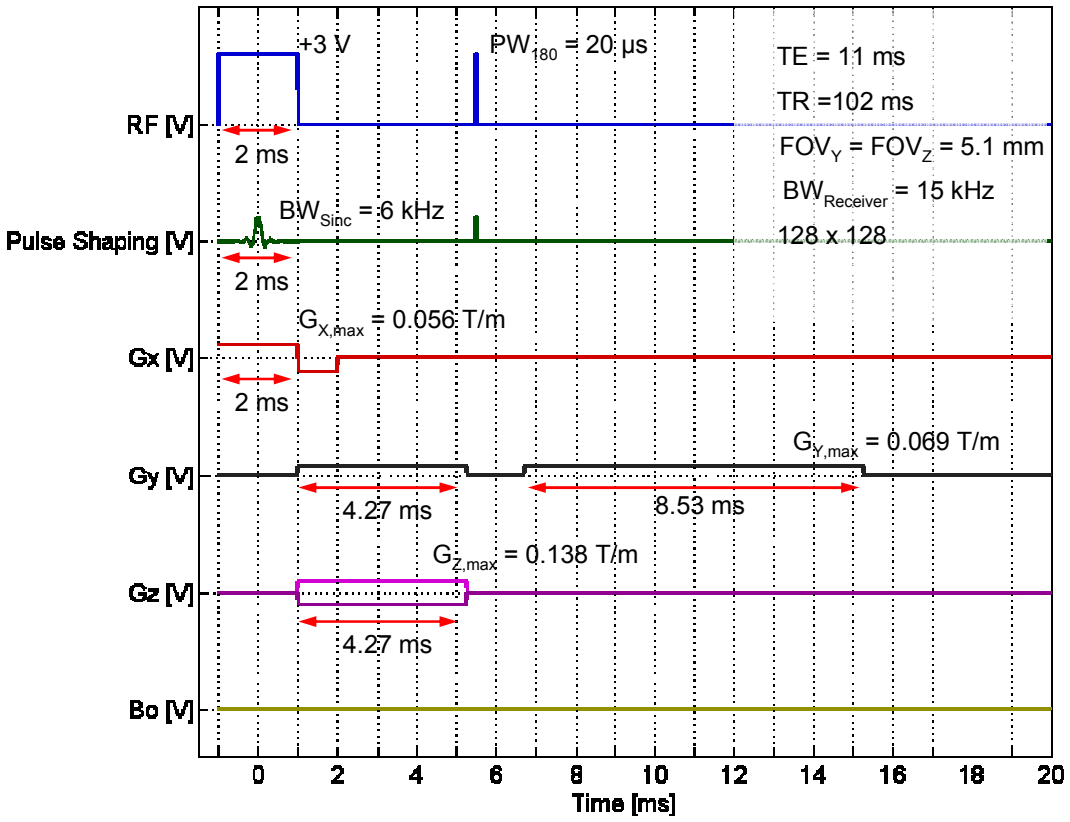

Figure 115. A sample spin echo (SE) pulse used for 2D imaging in this work.

D2. Velocity Imaging

For flow encoded imaging, again a spin echo pulse sequence as shown in Figure 102 can be used. The SE pulse sequence for flow imaging is described in the text in Chapter 1 and Chapter 4 therefore not repeated here.

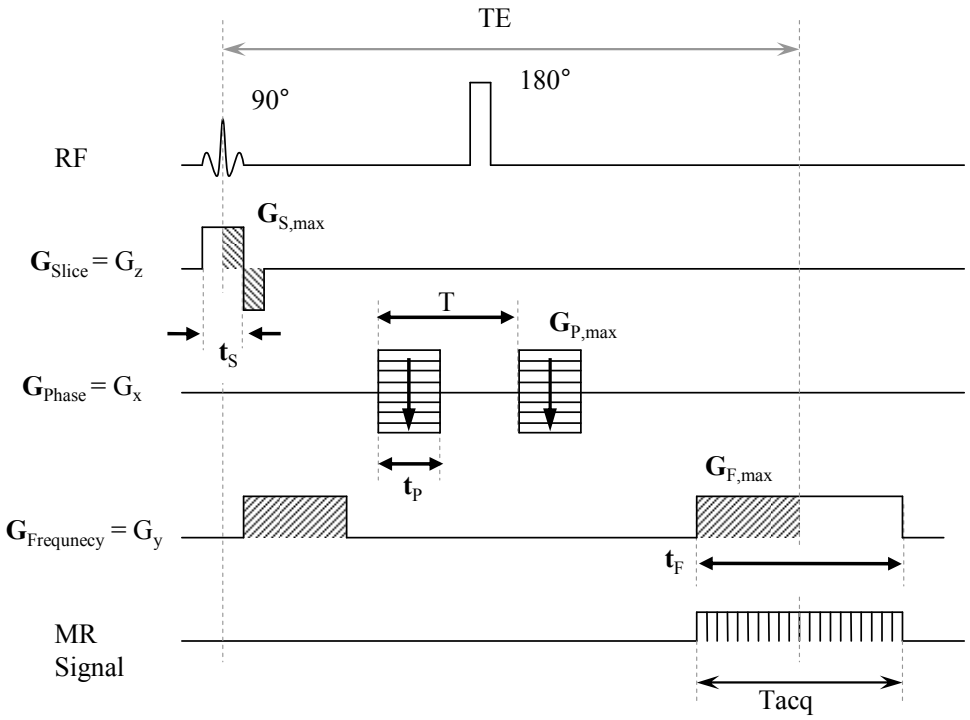

Figure 116. The basic modified spin echo (SE) pulse for phase sensitive velocity encoding.

All the parameters calculated for the static imaging case are valid for flow imaging except for the phase encoding direction and also the echo time.

The effect of this type on phase-encoding is that stationary spins do not experience any net phase shift whereas spins traveling with a speed *V* in the x-direction, experience a net phase shift

$$\Delta\phi_P = \gamma G_{P,max} t_P \cdot T \cdot V . \tag{118}$$

The pulse duration t_P and the time delay *T* are chosen based on the maximum expected velocity. To avoid any uncertainties due to phase warps greater than 2π, the parameters are chosen such that the maximum velocity is lower than

$$V < \frac{2\pi}{\gamma G_{P,max} t_P \cdot T}. \tag{119}$$

For testing purposes the maximum velocity was set to 13 mm/s. The maximum phase encoding (velocity encoding) gradient is set to about 0.3 T/m with a duration, t_P, of 2 ms and a delay, T, of 3 ms. The nominal velocity step resolution

$$\delta_v = \frac{V}{N_P} \tag{120}$$

depends on the number of phase encoding steps Np. For 128 phase-encoding steps the velocity resolution for this case is approximately 100 μm/s.

The echo time can now be approximated as

$$TE \approx 2\left(\frac{T - t_P}{2} + t_P + \frac{t_F}{2}\right) \tag{121}$$

The first term is the delay after the non-selective RF pulse needed for the re-phasing lobe of the phase encoding gradient. The second term is the pulse duration of the phase encoding gradient (needs to be applied before the frequency encoding gradient). The last term is half the duration for which the frequency encoding gradient is applied. An echo time, TE, of 13 ms is used for testing purposes.